Springer Tracts in Electrical and Electronics Engineering

Shanmuga Sundar Dhanabalan · Arun Thirumurugan · Ramesh Raju · Sathish-Kumar Kamaraj · Sridarshini Thirumaran *Editors*

Photonic Crystal and Its Applications for Next Generation Systems

Springer

Springer Tracts in Electrical and Electronics Engineering

Series Editors

Brajesh Kumar Kaushik, Department of Electronics and Communication Engineering, Indian Institute of Technology Roorkee, Roorkee, Uttarakhand, India

Mohan Lal Kolhe, Faculty of Engineering and Sciences, University of Agder, Kristiansand, Norway

Springer Tracts in Electrical and Electronics Engineering (STEEE) publishes the latest developments in Electrical and Electronics Engineering - quickly, informally and with high quality. The intent is to cover all the main branches of electrical and electronics engineering, both theoretical and applied, including:

- Signal, Speech and Image Processing
- Speech and Audio Processing
- Image Processing
- Human-Machine Interfaces
- Digital and Analog Signal Processing
- Microwaves, RF Engineering and Optical Communications
- Electronics and Microelectronics, Instrumentation
- Electronic Circuits and Systems
- Embedded Systems
- Electronics Design and Verification
- Cyber-Physical Systems
- Electrical Power Engineering
- Power Electronics
- Photovoltaics
- Energy Grids and Networks
- Electrical Machines
- Control, Robotics, Automation
- Robotic Engineering
- Mechatronics
- Control and Systems Theory
- Automation
- Communications Engineering, Networks
- Wireless and Mobile Communication
- Internet of Things
- Computer Networks

Within the scope of the series are monographs, professional books or graduate textbooks, edited volumes as well as outstanding PhD theses and books purposely devoted to support education in electrical and electronics engineering at graduate and post-graduate levels.

Review Process

The proposal for each volume is reviewed by the main editor and/or the advisory board. The books of this series are reviewed in a single blind peer review process.

Ethics Statement for this series can be found in the Springer standard guidelines here https://www.springer.com/us/authors-editors/journal-author/journal-author-helpdesk/before-you-start/before-you-start/1330#c14214

Shanmuga Sundar Dhanabalan ·
Arun Thirumurugan · Ramesh Raju ·
Sathish-Kumar Kamaraj · Sridarshini Thirumaran
Editors

Photonic Crystal and Its Applications for Next Generation Systems

Springer

Editors
Shanmuga Sundar Dhanabalan
Functional Materials and Microsystems Research Group
RMIT University
Melbourne, VIC, Australia

Ramesh Raju
Department of Electronics and Nano Engineering
Aalto University
Espoo, Finland

Sridarshini Thirumaran
Department of Electronics and Communication Engineering
College of Engineering Guindy Campus, Anna University
Chennai, Tamil Nadu, India

Arun Thirumurugan
Sede Vallenar
Universidad de Atacama
Vallenar, Chile

Sathish-Kumar Kamaraj
Unidad Altamira (CICATA-Altamira)
Instituto Politécnico Nacional (IPN)-Centro de Investigación en Ciencia Aplicada y Tecnología Avanzada
Altamira, Mexico

ISSN 2731-4200 ISSN 2731-4219 (electronic)
Springer Tracts in Electrical and Electronics Engineering
ISBN 978-981-99-2547-6 ISBN 978-981-99-2548-3 (eBook)
https://doi.org/10.1007/978-981-99-2548-3

© The Editor(s) (if applicable) and The Author(s), under exclusive license to Springer Nature Singapore Pte Ltd. 2023

This work is subject to copyright. All rights are solely and exclusively licensed by the Publisher, whether the whole or part of the material is concerned, specifically the rights of translation, reprinting, reuse of illustrations, recitation, broadcasting, reproduction on microfilms or in any other physical way, and transmission or information storage and retrieval, electronic adaptation, computer software, or by similar or dissimilar methodology now known or hereafter developed.
The use of general descriptive names, registered names, trademarks, service marks, etc. in this publication does not imply, even in the absence of a specific statement, that such names are exempt from the relevant protective laws and regulations and therefore free for general use.
The publisher, the authors, and the editors are safe to assume that the advice and information in this book are believed to be true and accurate at the date of publication. Neither the publisher nor the authors or the editors give a warranty, expressed or implied, with respect to the material contained herein or for any errors or omissions that may have been made. The publisher remains neutral with regard to jurisdictional claims in published maps and institutional affiliations.

This Springer imprint is published by the registered company Springer Nature Singapore Pte Ltd.
The registered company address is: 152 Beach Road, #21-01/04 Gateway East, Singapore 189721, Singapore

Preface

Photonics plays an important role in major domains such as high-speed networks, photonic integrated circuits, health care, sensors, energy, and environmental application. This technology development leads to the development of components and devices that support optics and photonics' growth. Though there is a significant development in each domain, still, there are certain demands and research gaps to be addressed. Photonic crystal-based development of optical components, such as splitters, encoders, decoders, and routers, will address the potential problems in obtaining high-speed networks using the photonic integrated circuits technology. These miniature chips can transmit data at a speed of Gb/s and Tb/s. Due to the development of these miniature chips, the bulky and large optical equipment have been replaced and outdated.

According to the United Nations, the elderly population is expected to grow by 56% by 2030 and is expected to double by 2050. Concurrently, advancements in diagnostic technologies have emerged creating new paradigms for customized health monitoring. Among these technologies, optical sensors present one of the most promising options for monitoring the health of patients and elderly people uninterruptedly and remotely. These handy sensors can overcome the limitations of the existing system, which seems to be rigid and requires complex integration of power supplies and circuit boards. Optics and photonics also have important applications in the energy and environment domain. They were employed to generate clean and renewable energy to overcome the energy crisis and significantly impact the environmental applications and support the development of a green future. The optical techniques and equipment were employed to sense, monitor, and transmit data concerning energy and environment applications. There is a need to advance and develop technology in each domain to provide miniature, high-speed, accurate, and efficient systems.

This book focuses on the recent advancement and applications of photonic crystals in our real-time applications. This book provides insight to the readers about the technological advancement, fabrication, challenges, application, and future perspective of photonic crystals in real-time applications. It also provides the vision to the

researchers, scholars, and industry persons about using photonic crystals in different applications.

At this time, we'd like to explicitly thank all of the contributors who worked so diligently on their respective chapters.

Melbourne, Australia — Shanmuga Sundar Dhanabalan
Vallenar, Chile — Arun Thirumurugan
Espoo, Finland — Ramesh Raju
Altamira, Mexico — Sathish-Kumar Kamaraj
Chennai, India — Sridarshini Thirumaran

Acknowledgements

In the first place, we want to give thanks to God for blessing us with good health and the ability to edit this book. Our deepest gratitude goes to the series editor and advisory board for believing in our work and accepting our book for publication. Thanks to everyone who helped make this book a reality—the authors, the reviewers, and everyone in between. We are grateful to the many publishers and authors who gave us permission to use their work, especially the figures and tables.

Shanmuga Sundar Dhanabalan would like to express his sincere thanks to Prof. Sivanantha Raja Avaninathan (Alagappa Chettiar Government College of Engineering and Technology, Karaikudi, Tamil Nadu, India), Prof. Marcos Flores Carrasco (FCFM, University of Chile, Chile), Prof. Sharath Sriram, and Prof. Madhu Bhaskaran (Functional Materials and Microsystems Research Group, RMIT University, Melbourne, Australia) for their continuous support, guidance, and encouragement. He extended his gratitude to Mrs. Preethi Chidambaram, and his family for support.

Arun Thirumurugan would like to express his gratitude to Dr. Justin Joseyphus (NIT-T, India), Prof. P. V. Satyam (IOP, India), Dr. Ali Akbari-Fakhrabadi (FCFM, University of Chile, Chile), and Prof. R. V. Mangala Raja (University of Adolfo Ibanez, Santiago, Chile) for their kindness and guidance. He thanks Dr. R. Udaya Bhaskar and Mauricio J. Morel (University of ATACAMA, Chile), Carolina Venegas, Yerko Reyes, and Juan Campos, Sede Vallenar, University of ATACAMA, Chile for their support. He acknowledges Agencia Nacional de Investigación y Desarrollo (ANID), Chile for the financial support through SA 77210070.

Ramesh Raju acknowledges the financial support from the Academy of Finland projects 319018 eVapor and 329406 CarbonSurf and the Photonics Flagship PREIN. He thanks Prof. Ilkka Tittonen, Department of Electronics and Nanoengineering Aalto University, Finland.

Kamaraj Sathish-Kumar would like to express his gratitude to the Director General of Instituto Politécnico Nacional (IPN) and Director of Centro de Investigación en Ciencia Aplicada y Tecnología Avanzada, Unidad Altamira (CICATA Altamira) for their constant support and facilities, able to promote the research activities. He extended his gratitude to the Secretaria de Invesigacion y Posgrado (SIP) for the

project number of 20231443. Further extensions to the funding agency of the National Council for Science and Technology (CONACyT-México) and Secretary of Public Education (SEP-México). He extended his gratitude to Mrs. Kamaraj Mounika for her family support.

Sridarshini Thirumaran would like to express her heartfelt gratitude to all the editors, the authors of each and every technical chapter, different teams of Springer publication, and the Magnificent Universe to make this book a successful one.

Contents

1 Hot Atomic Vapor for Photonic Crystal-Based Optical Components 1
Mahnaz Asadolah Salmanpour, Mohammad Mosleh, Reza Gholami, and Seyedeh Mehri Hamidi

2 Highly Efficient Graphene-Based Optical Components for Networking Applications 15
M. Soroosh, A. Farmani, M. J. Maleki, F. Haddadan, and M. Mansouri

3 A Nonlinear Optical Benzil Single Crystal for Photonic Applications 37
Thirupathy Jayapalan

4 Highly Efficient Materials for Photonic Crystal-Based Optical Components 53
Subramanian Thangarasu, Vadivel Siva, Sadasivam Kannan, and Anbazhagan Murugan

5 Fabrication of Unidirectional Grown 1, 3, 5-Triphenylbenzene Single Crystal for Nonlinear Optical and Fast Neutron Detector Applications 71
N. Durairaj, S. Kalainathan, and S. Moorthy Babu

6 Two-Dimensional Photonic Crystal-Based Filters Review 91
K. Rama Prabha and S. Robinson

7 Photonic Crystal-Based 2D Demultiplexer for DWDM Systems 113
V. R. Balaji, Richards Joe Stanislaus, M. A. Ibrar Jahan, R. G. Jesuwanth Sugesh, and Gopalkrishna Hegde

8 Investigation of Ultra-Small and Efficient Encoders and Decoders for High-Speed Optical Communication Systems 131
R. Arunkumar and S. Robinson

9 Photonic Crystal Fibers for Sensing Applications 155
Daniel A. May-Arrioja, Natanael Cuando-Espitia, Amado M. Velázquez-Benítez, and Juan Hernández-Cordero

10 Photonic Crystal Biosensors for Healthcare and Pathologic Diagnostic Application 171
Amir Reza Sadrolhosseini, Seyedeh Mehri Hamidi, and Farnaz Amouyan

11 High-Frequency Photonic Crystal-Based Terahertz Antenna for Medical Applications 187
Sathish Kumar Danasegaran, Elizabeth Caroline Britto, K. Sagadevan, and Susan Christina Xavier

12 Role of Photonics in Energy Crisis 205
L. Jerart Julus, A. Andrew Roobert, and J. Joshan Athanesious

About the Editors

Dr. Shanmuga Sundar Dhanabalan is an accomplished researcher with a proven track record in designing, developing, and translating micro- and nano-scale devices. His primary objective is to create next-generation products that enhance quality of life and well-being, making a significant contribution to society. He currently leading a team 'wearable and connected sensors' at RMIT University, with a focus on materials, flexible and stretchable devices, wearables, optics, and photonics. He graduated with a PhD in flexible electronics in June 2017 and secured a competitive postdoctoral fellowship from the Chilean government from 2018 to 2021. His studies have led to publications in referred international journals, book chapters, and books in progress as editor. He has presented plenary/keynote, invited talks and guest lectures, oral and poster presentations at scientific meeting at various universities world-wide. Several outcomes have been highlighted by scientific websites (such as Photonics Media, USA). His research work has led to securing grants from Australian government research schemes, such as the Cooperative Research Centres Projects, the ARC Research Hub for Connected Sensors for Health, Victorian Medical Research Acceleration Fund, and the Advanced Manufacturing Growth Centre's Commercialisation Fund. He has collaborations with universities from various countries, including India, Australia, Chile, Mexico, and Bangladesh. He has served as a reviewer for over 20 prestigious specialist journals. He also served as a topical editor for highly reputed journals including IEEE Transactions on Industrial Informatics, IEEE Instrumentation and Measurement Magazine, IEEE, Energies, Computer and Electrical Engineering. He is a part of the Editorial Board of American Journal of Optics and Photonics. In addition, he served as a session chair and technical committee member in various international conferences.

Researcher, Functional Materials and Microsystems Research Group, School of Engineering, RMIT University, Australia
e-mail: shanmuga.sundar.dhanabalan@rmit.edu.au
ORCID: https://orcid.org/0000-0001-5539-3380
Google Scholar: https://scholar.google.co.in/citations?user=SEmcvo4AAAAJ&hl=en

Dr. Arun Thirumurugan is a Academic Faculty at the University of ATACAMA working on the development of magnetic nanocomposite for energy storage and biological applications. He has completed his Ph.D. (2010–2015) at the National Institute of Technology (NIT), Tiruchirappalli, India. He has worked as a postdoctoral fellow (2015–2017) at the Institute of Physics, Bhubaneswar, India, and then worked as a FONDECYT postdoctoral fellow (2017–2020) at the University of Chile, Santiago, Chile. His research interests are synthesizing magnetic nanoparticles, surface modification of nanomaterials for the potential applications in detoxification, photocatalyst, energy storage, and biomedical applications. Dr. Thirumurugan acts as a reviewer for various journals from different eminent publishers. He is editing a topical issue on magnetic nanomaterials and carbonaceous nanocomposites in the Frontiers publishing group. He edited two books. He published more than 90 international journals, book chapters, and conference proceedings.

Assistant Professor
University of ATACAMA, Copiapo, Chile
e-mail: arun.thirumurugan@uda.cl
ORCID: https://orcid.org/0000-0001-7261-988X
Google Scholar: https://scholar.google.com/citations?user=wdA3v_gAAAAJ&hl=en

Dr. Ramesh Raju is a staff scientist at Aalto University. His research focuses on III-V materials growth and fabrication for optoelectronics applications and 2D materials growth and fabrication for photonics applications. During his Ph.D. at Anna University, Chennai, India, his research focused on III-Nitride materials growth by metal organic vapour phase epitaxy (MOVPE) for optoelectronics applications. After obtaining his Ph.D. degree, he moved to China, where he worked as a postdoctoral researcher at the Nanophotonics Laboratory, College of Physics, Hunan University (HNU), China. At HNU, he designed the growth setup for 2D material-based heterostructure for photonics applications. Since he is experienced in different growth, fabrication, and characterization skills, there is a natural scientific overlap with optoelectronics photonics, nanotechnology, and micro and quantum activities. In 2017, he started working with the optoelectronics and micro and quantum system group at Aalto University, Finland. At Aalto University, his research is towards III-Nitrides for optoelectronics and PEC water splitting applications. He published more than 35 research articles/conference proceedings based on his work in India and other international research at various universities. Dr. Ramesh Raju acts as a reviewer for various journals from different eminent publishers.

Staff Scientist,
Department of Electronics and Nanoengineering,
Aalto University, Espoo-02150, Finland
e-mail: ramesh.raju@aalto.fi
ORCID: https://orcid.org/0000-0002-1802-9077

Dr. Sathish-Kumar Kamaraj is a research professor at Instituto Politécnico Nacional (IPN), Centro de Investigación en Ciencia Aplicada y Tecnología Avanzada, Unidad Altamira (IPN-CICATA, Altamira). He would like to express his gratitude to, the Director General of Instituto Politécnico Nacional (IPN) and Director of Centro de Investigación en Ciencia Aplicada y Tecnología Avanzada, Unidad Altamira (CICATA Altamira) for their constant support and facilities, able to promote the research activities. Extended his gratitude to the Secretaria de Investigación y Posgrado (SIP) for project number 20231443. He received B.Sc. in Botany specialized in Industrial Microbiology, master's in Microbiology, and a postgraduate in Chemical Information Technology at Madurai Kamaraj University, Tamil Nadu, India. He obtained a Doctorate in Nanoscience and Nanotechnology (2010–2014) from The Centre for Research and Advanced Studies of the National Polytechnic Institute (CINVESTAV-IPN), CDMX, Mexico, with a scholarship from the General Directorate of International Relations-Secretary of Public Education Mexico (SEP-Mexico). During the academic period, he received the Best Student Competition Award at Battelle's Second International Symposium on Bioremediation and Sustainable Environmental Technologies (2013) in Jacksonville, Florida, USA. His thesis won the Best Ph.D. Thesis Award from the Mexican Hydrogen Society. His passion for sustainable natural systems triggers him to integrate his knowledge of the various fields to address the problems in the area of energy, environment, and health. He registered various patents in the Mexican Institute of Industrial Property (IMPI) and technology transfer to the industries. He also has relationships with government agencies and the private sector for circumstantial decision-making. He served as a guest editor and a reviewer in international journals. Extended his gratitude to Mrs Kamaraj Mounika and Bbg Aarudhraa for their family support. Research Professor, Instituto Politécnico Nacional (IPN)-Centro de Investigación en Ciencia Aplicada y Tecnología AvanzadaUnidad Altamira (CICATA-Altamira), Carretera Tampico-Puerto Industrial Altamira Km 14.5, C. Manzano, Industrial Altamira, 89600 Altamira, Tamps., Mexico
e-mail: skamaraj@ipn.mx,sathish.bot@gmail.com
ORCID: https://orcid.org/0000-0001-5145-6962

Dr. Sridarshini Thirumaran is currently working as an assistant professor in the Department of Electronics and Communication Engineering, College of Engineering Guindy Campus, Anna University, Chennai, India. She has completed her doctoral degree in the field of Photonics which mainly focuses on "Photonic crystals for passive optical components for optical communication systems" at Anna University, Chennai. Her areas of research are optical communication and networks and photonics. She has contributed about 20 papers in reputed international/national journals and 4 book chapters. Assistant Professor, Department of ECE, College of Engineering Guindy Campus, Anna University, Chennai, Tamilnadu, India.
e-mail: sridarshiniv@gmail.com
ORCID: https://orcid.org/0000-0001-9922-4378

Chapter 1
Hot Atomic Vapor for Photonic Crystal-Based Optical Components

Mahnaz Asadolah Salmanpour, Mohammad Mosleh, Reza Gholami, and Seyedeh Mehri Hamidi

Abstract Design and construction of advanced and new-born quantum devices and atomic chips motivated scientists to investigate atom–light interactions in miniaturized nanostructures. Miniaturization for lab on a chip requires enhancement in the interaction efficient volume and thus field enhancements between atomic media and the light. Field enhancement in photonic devices can be achieved in photonic crystal-based structures with defect modes, cavity states, Tamm modes, Bloch modes, and so on. Interaction of these mentioned modes with atoms can open new insights in the new-generation quantum devices. In this chapter, this interaction and applications in some quantum mechanical devices will be considered.

Keywords Photonic crystal · Bloch surface wave · Tamm mode · Hot atomic vapor

Introduction

Hot vapor of alkali metals like rubidium and cesium has wide applications in quantum technology (Ripka et al. 2018), metrology (Udem et al. 2002), and sensing (Sedlacek et al. 2013). Stability, accuracy, and sensitivity of transitions between state of atoms are the key feature which leads to realization of the devices like Rubidium atomic clocks and magnetometers (Kominis et al. 2003). Hot vapor-based atomic devices are almost bulky and need much amount of energy to run. Small size of atom–light interaction medium can decrease energy consumption while making assembly of multi-device chips possible. In recent years, miniaturized atomic cells, produced by MEMS technology, have provided the possibility of building integrated atomic clock and frequency reference systems (Schwindt et al. 2004).

M. A. Salmanpour · M. Mosleh · R. Gholami · S. M. Hamidi (✉)
Magneto plasmonic lab, Laser and Plasma Research Institute, Shahid Beheshti University, Tehran, Iran
e-mail: M_hamidi@sbu.ac.ir

© The Author(s), under exclusive license to Springer Nature Singapore Pte Ltd. 2023

S. S. Dhanabalan et al. (eds.), *Photonic Crystal and Its Applications for Next Generation Systems*, Springer Tracts in Electrical and Electronics Engineering,
https://doi.org/10.1007/978-981-99-2548-3_1

The optical energy confinement in nanostructures can improve photonic mode manipulating in addition to waveguiding and has drawn attention to nanophotonic–atomic states integration as a new paradigm for miniaturization of atomic devices. In atom–nanophotonic coupled devices, energy transferring between confined photonic modes of nanostructures and atomic states takes place by touch of atoms by evanescent tail of these modes and is completely dependent on characteristics of confined modes like inhomogeneous polarization states of evanescent waves. It is worth to mention that spin and pseudo-momentum transfer from evanescent waves to atom depends on geometry of nanostructures that host photonic mode, regarding inherent property of evanescent waves called spin-momentum locking (Matsudo et al. 1998; Mosleh et al. 2021b). In addition to complicated polarization states of evanescent fields, enhanced interaction of atom-confined photonic mode would result in nonlinearities in response of atoms (Ritter et al. 2016). Response of atoms in vicinity of nanostructures can be modulated through coupling of atomic states with resonant modes of nanostructures. For example, resonant coupling of Rb atoms with plasmonic modes results in Fano resonance and strongly modulates behavior of atoms comparing atoms in bulk (Mosleh et al. 2021a). Knowledge of physical phenomena arising from vapor atoms in vicinity of confined photonic modes is a necessary step in design of any miniaturized atom–nanophotonic device. There are numerous works which show spectroscopy of atoms by meta-surface (Chan, et al. 2018; Chang et al. 2009), waveguide (Zektzer et al. 2021), microcavity (Ritter et al. 2016; Naiman et al. 2020), plasmon-polaritons (Stehle et al. 2014; Aljunid et al. 2016), photonic crystal waveguide (Goban et al. 2014), and 2D photonic crystal (Yu et al. 2019). Choice of proper nanostructure depends on type of application which we consider. Guided electromagnetic modes have diffraction-free propagation and nanoscale effective mode area that can cause strong confinement of light field. Bloch surface waves (BSW) are propagating photonic modes in 1D-photonic crystals (Yeh et al. 1978) and fascinating candidate for integration with hot vapor of atoms. There is no doubt guided BSW mode characteristics strongly depends on properties of the substrate. In addition design on the surface of the truncation layer in 1D-photonic crystal would be used as a tool for atom–nanophotonic device manipulation. The goal of this chapter is to demonstrate the potential integration of surface modes sustained by 1D-PC with atomic transitions considering PC characteristics.

Tamm Plasmon in 1D-Photonic Crystal

Surface waves as specific type of waves are confined at the boundary between two different media which are used for many applications. The most considerable kinds of these surface waves are classified to surface plasmon and Tamm plasmons. Each of these waves can be formed at metal–dielectric interface or by the interface of two isotropic dielectric materials, at least one of which should be periodically nonhomogeneous (Chiadini et al. 2016) (usually the interface of two photonic crystals or a photonic crystal and a metal). Tamm states appear in the bandgap of the photonic

crystal or in the region in which the bandgaps of two photonic crystals overlap with each other. There is a main difference between these two important surface waves; in contrast to surface plasmons, Tamm plasmons have an in-plane wave vector within the light line, so direct optical excitation is possible. Also, they are formed in both polarizations and even in normal incidence.

This difference is the key parameter to drift scientists toward design of applicable devices based on optical modes (Shanmuga Sundar et al. 2018; Sathyadevaki et al. 2016) and Tamm plasmons such as optical switches (Zhang and Yu 2010), Tamm plasmon lasers (Kavokin et al. 2005; Symonds et al. 2013), for enhancement of magneto optical effects (Goto et al. 2008; Vinogradov et al. 2006; Liu et al. 2012) and also nonlinear optical effects (Lee et al. 2013). Furthermore, the controllable (Da et al. 2009; Merzlikin et al. 2007) and tunable (Chen et al. 2014, 2012) feature of these modes make them suitable for different applications such as sensing and filtering (Sasin et al. 2008). For these purpose, fine tunability and also adjustability of Tamm modes are very important.

Tunable Tamm Plasmon in one-dimensional photonic crystal (1D-PC):

Appropriate properties of 1D-photonic crystal and consequently Tamm plasmons could be designed through transfer matrix method (TMM), by tuning thickness and arrangement of dielectric layers covered by metallic thin film (as shown schematically in Fig. 1.1). TMM has been used in order to calculate the photonic bandgap and also the optical properties of the prepared samples by adjusting the matrix to each high and low refractive index.

In TMM-based calculation, assigned transfer matrix to each dielectric layer can be written as a function of phase difference in each layer, δ, and the refractive index of layer, n as

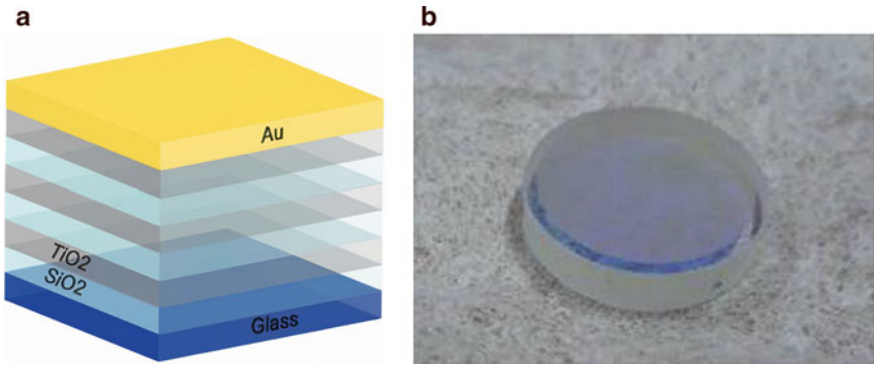

Fig. 1.1 **a** The 1D-PC structure with Au over layer as a main sample and **b** Fabricated 1D-PC ones

$$M = \begin{pmatrix} \cos\delta & \dfrac{i\sin\delta}{n} \\ in\sin\delta & \cos\delta \end{pmatrix} \tag{1.1}$$

In order to design 1D-PC, we must write this matrix for low, L, and high, H, refractive indices separately.

$$M_L = \begin{pmatrix} \cos\delta_L & \dfrac{i\sin\delta_L}{n_L} \\ in_L\sin\delta_L & \cos\delta_L \end{pmatrix} \text{ and } M_H = \begin{pmatrix} \cos\delta_H & \dfrac{i\sin\delta_H}{n_H} \\ inH\sin\delta_H & \cos\delta_H \end{pmatrix} \tag{1.2}$$

It is well known that to get the best interference in multilayer stacks like as 1D-PC, it's better to assign the optical thickness as quarter-wave layers, in which $\delta = \pi/2$ and thus

$$[H][L] = \begin{pmatrix} 0 & \dfrac{i}{n_H} \\ in_H & 0 \end{pmatrix}\begin{pmatrix} 0 & \dfrac{i}{n_L} \\ in_L & 0 \end{pmatrix} = \begin{pmatrix} -\dfrac{n_L}{n_H} & 0 \\ 0 & -\dfrac{n_H}{n_L} \end{pmatrix} \tag{1.3}$$

And the matrix for x pairs of these layers onto the substrate:

$$\begin{bmatrix} B \\ C \end{bmatrix} = \begin{pmatrix} \left(-\dfrac{n_L}{n_H}\right)^{\mathrm{X}} & 0 \\ 0 & \left(-\dfrac{n_H}{n_L}\right)^{\mathrm{X}} \end{pmatrix}\begin{bmatrix} 1 \\ n_{sub} \end{bmatrix} \tag{1.4}$$

It means

$$\begin{aligned} B &= \left(-\frac{n_L}{n_H}\right)^{\mathrm{X}} \\ C &= \left(-\frac{n_H}{n_L}\right)^{\mathrm{X}} n_{sub} \end{aligned} \tag{1.5}$$

Finally, the reflectance amplitude and phase of this mentioned multilayer as 1D-PC can be written as

$$\mathrm{r} = \frac{n_0 B - C}{n_0 B + C} \tag{1.6}$$

And thus

$$\mathrm{r} = \frac{n_0\left(-\frac{n_L}{n_H}\right)^{\mathrm{X}} - n_{sub}\left(-\frac{n_H}{n_L}\right)^{\mathrm{X}}}{n_0\left(-\frac{n_L}{n_H}\right)^{\mathrm{X}} + n_{sub}\left(-\frac{n_H}{n_L}\right)^{\mathrm{X}}}\ \varphi = \arctan\left(\frac{\mathrm{Im}[n_{sub}(BC* - CB*)]}{n_{sub}^2 BB* - CC*}\right) \tag{1.7}$$

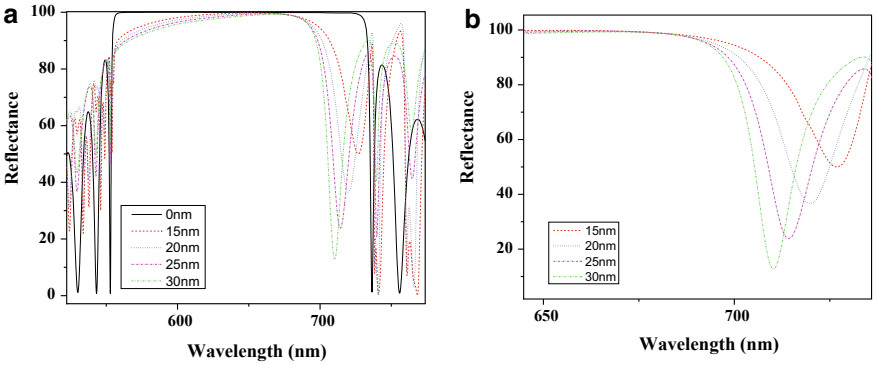

Fig. 1.2 **a** 1D-PC photonic bandgap for different gold cover layer thicknesses and **b** Tamm modes region in different thicknesses from 15 to 30 nm

We use these relations to design our PC and get the Tamm mode from that as follows.

The one-dimensional photonic crystal (1D-PC) comprising of 12 alternative layers of (TiO_2/SiO_2) was shown in Fig. 1.1. This 1D-PC was designed to exhibit a photonic bandgap centered at 635 nm and cover the main part of the visible spectral range. For this purpose, the thickness of TiO_2 and SiO_2 layers was set to the quarter of the designed wavelength, as 635 nm. At the first step, we design the 1D-PC with different thickness of gold cover layer as shown in Fig. 1.2. It is obvious that we have blue shift in the Tamm mode by enhancement in the gold layer thickness.

Depending on the main atom selection in atom–Tamm coupling, anyone can select one gold cover thickness to select the suitable wavelength. Now, Gold (Au) thin film with 30 nm thickness was selected and coated on top of the mentioned 1D-PC by DC sputtering method. This coated Au film played the role of Tamm plasmon exciter at our favorite region. Then, the sample was placed onto a rotating holder and its transmittance and reflectance spectra were measured as a function of incidence angle as shown in Fig. 1.3a, b. The optical branch consists of P- or S-polarized visible light which can be obtained by Glan–Taylor prism, sample, and a spectrophotometer for recording the response at various incidence angles.

In order to investigate Tamm plasmon (TP), transmittance (T), and reflectance (R) spectra of the 1D-PC samples before and after metallic layer deposition, (SiO_2/TiO_2)12 and (SiO_2/TiO_2)12/Au at normal incidence have been measured as shown in Fig. 1.4a, b. It can be seen, the bare 1D-PC shows a photonic bandgap (PBG) centered at 650 nm and after depositing the Au layer, TP can be observed for both T and R spectra at 670 nm, respectively.

In order to tune the TP resonance in the sample, we use angular modulation for both p and s polarizations in reflectance geometry (Fig. 1.4c, d). As one may know, the Tamm states offer the opportunity to allow both excitations in oblique incidence of angle. It can be clearly observed that the resonance wavelength of the TP has blue shift in the bandgap of PC by increasing the incidence angle. By changing the

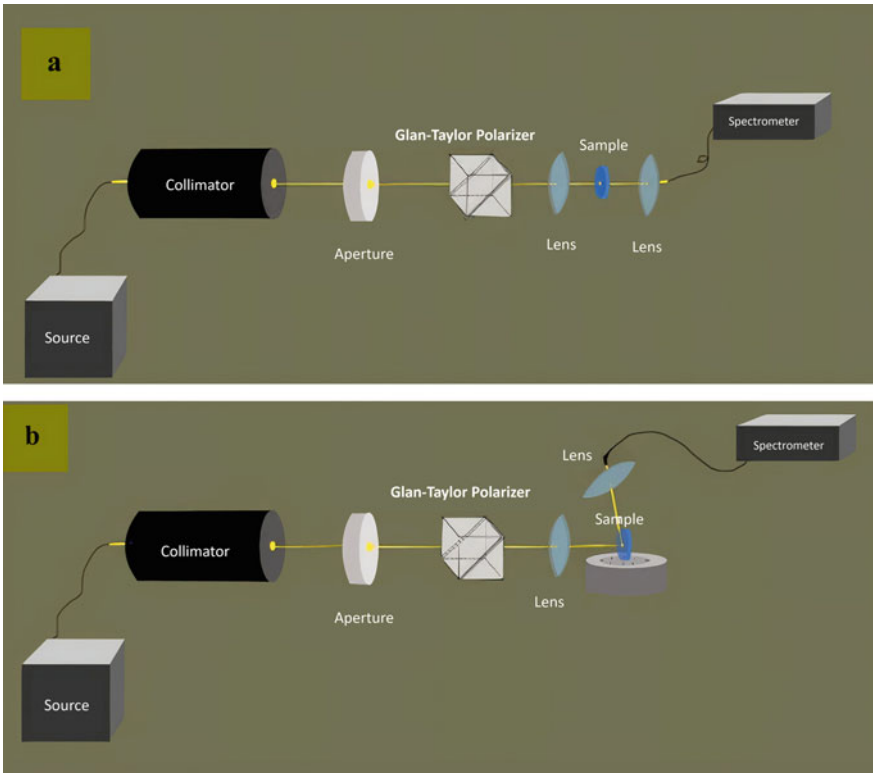

Fig. 1.3 A schematic diagram of the experimental setup to record the **a** reflectance and **b** transmittance spectra of the sample

incidence angle from 15 to 60° TP resonance can be tuned from 560 to 660 nm and this means that the existence of resonance plays an important role in the tunability.

The calculated electric field distribution for the TP mode compared with another wavelength has been shown in Fig. 1.5 in which light localization in Tamm state resonance wavelength has been confirmed in this figure.

Bloch Surface Waves in 1D-Photonic Crystals

For the first time in 1977, Yeh et al. studied the possibility of propagation of Bloch surface waves at the surface of periodic dielectric multilayer theoretically and experimentally (Yeh et al. 1978). Next Meade et al. (1991) showed that localization of electromagnetic surface modes at interface between external homogeneous medium and photonic crystal is because of interference states by consideration effect of terminating layer of photonic crystal.

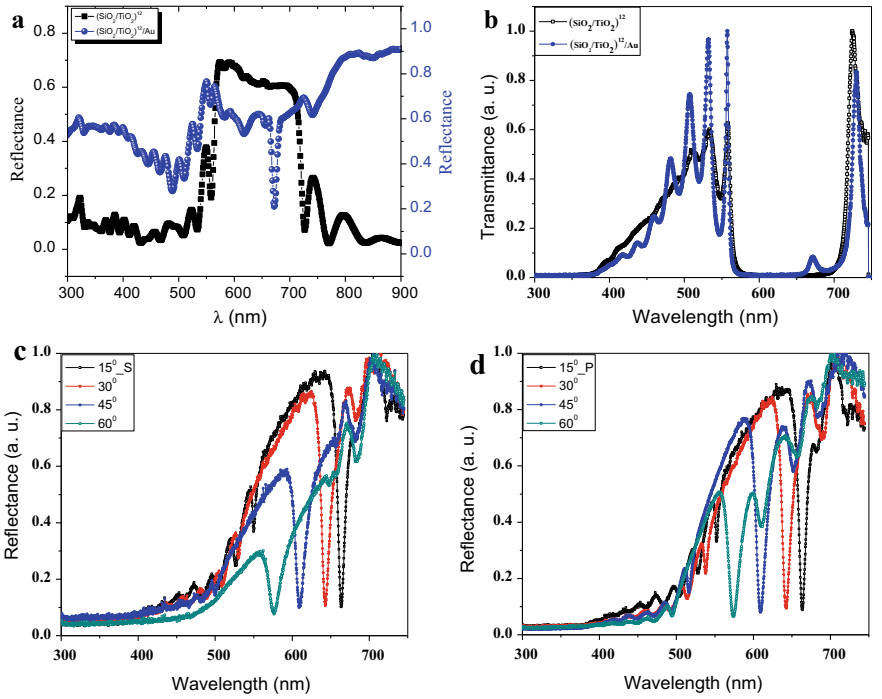

Fig. 1.4 **a** Reflectance and **b** Transmittance spectra of 1D-PC before and after Au layer deposition **c**, **d** Measured reflectance spectra of the sample at different incidence angles and polarizations

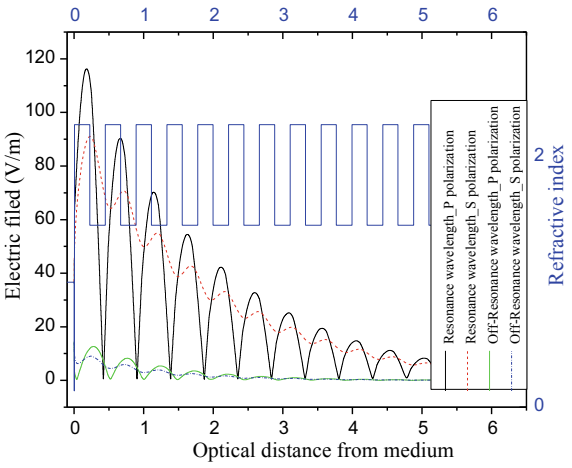

Fig. 1.5 Electric field distribution at resonance and off-resonance wavelength in each polarization accompanied by refractive index of structure

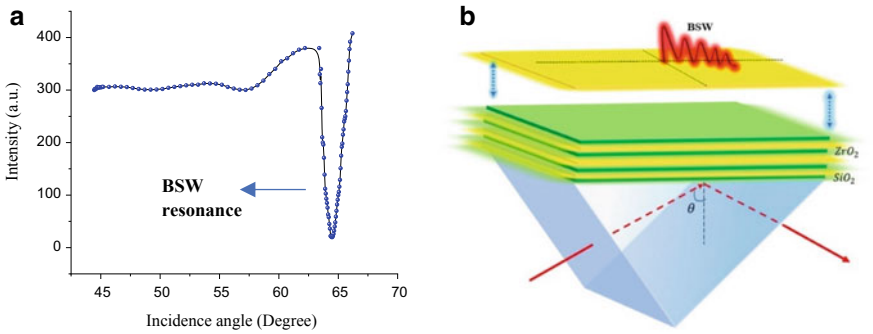

Fig. 1.6 **a** Angular reflectivity of multilayer at t the angles after the total internal reflection angle (42°). **b** schematic of the photonic crystal-coupled prism and interlink between vapor atoms and BSW mode

According to Bloch's theory, the electric field propagation in one-dimensional photonics crystal is as follows (Yeh et al. 1978).

$$E(x, z, t) = E_k(x)e^{ik_B x}e^{i(\beta z-\omega t)} \tag{1.8}$$

where k_B is Bloch wave number and β is propagation constant.

The photonic band structure of a 1D-PC can be straightly calculated by way of the TMM as follows:

$$\cos(k_B d) = \cos(k_1 d_1)\cos(k_2 d_2) - \frac{1}{2}\frac{k_1^2 + k_2^2}{k_1 k_2}\sin(k_1 d_1)\sin(k_2 d_2) \tag{1.9}$$

where d is the period of the unit cell which is constructed of two layers of thicknesses d1 and d2, and refractive indices n1 and n2, respectively. k_1 and k_2 are wavevector components along the stacking direction in the layers 1 and 2, respectively.

When $|\cos(k_B d)| < 1$ therefore k_B is real and thus corresponds to propagating Bloch waves in pc. In return, when $|\cos(k_B d)| > 1$ therefore $k_B = \frac{m\pi}{d} + ik_i$ is complex value which is having real and imaginary parts so Bloch wave is evanescent. These regions are identified as the "bandgaps" where no mode is allowed to propagate in pc because no pure real wave vector exists for any mode at that wavelength and only evanescent modes exist. The band edges are those where $|\cos(k_B d)| = 1$.

The surface modes were described in four categories as follows: EE modes (extend in both the pc and the external homogeneous medium), DE modes (decay in the pc and extend in the external homogeneous medium), ED modes (extend in the pc and decay in the external homogeneous medium), and DD modes (decay in both the pc and the external homogeneous medium) (Meade et al. 1991).

When an infinite periodic multilayer is truncated at the proper thickness, the fourth modes, DD mode, can appear at the interface between the truncated multilayer and the external homogeneous medium in such a way that maximum field intensity being

close to the truncation interface. These modes are known as Bloch surface waves (BSWS). Dispersion and propagation properties of these surface waves, such as effective refractive index and propagation length, can be controlled by choosing the proper thickness and refractive index of the truncation layer (Dubey et al. 2017a). Also, by choosing proper number, thickness, and material of the layers of the photonic crystal, the bandgap structure of the photonic crystal can be adjusted in a wide spectral range, and as a result Bloch surface waves can be excited at the desired wavelength (from UV to mid-IR) (Occhicone et al. 2020). Excitation of Bloch surface waves requires the fabrication of homogeneous thin layers with a thickness of several tens nanometers of dielectric materials. Therefore, various deposition techniques such as plasma-enhanced chemical vapor deposition (PECVD) (Batey and Tierney 1986), focused ion beam (FIB) (Orloff et al. 2003), and atomic layer deposition (ALD) (Leskelä and Ritala 2002) are used to make 1D-photonic crystals.

BSWs take advantage of inconsiderable ohmic loss with possibility to propagate at the interface between periodic dielectric multilayer and a surrounding medium in the scale of millimeter length. BSW's also represent chance to generate great enhancements of TE- or TM-polarized evanescent fields (Dubey et al. 2017a). Different dielectric materials are used to fabricate 1D-photonic crystals that support BSW excitation such as $(TiO_2)/(SiO_2)$, $(Ta_2O_5)/(SiO_2)$, $(Si_3N_4)/(SiO_2)$ (Da et al. 2009), $(ZrO_2)/(SiO_2)$, porous Si (p–Si), and amorphous silicon nitride (a–Si1–xNx:H).

BSWs in photonic crystals (PCs) are known as very broad applications in surface sensing because of high sensitivity to the refractive index variations of the external dielectric environment (Villa et al. 2002; Shinn and Robertson 2005; Konopsky and Alieva 2007). Another feature of Bloch surface waves is strong and local field enhancement at the multilayer surface that cause studies such as control and enhancement of emission properties of emitters (Liscidini et al. 2009), surface-enhanced Raman scattering (Pirotta et al. 2013; Angelini et al. 2013), enhanced fluorescence detection (Angelini et al. 2013), and trapping Au particles (Xiang et al. 2020).

BSW-based integrated photonic platforms

The long propagation length of BSWs gave rise to the interesting idea of light manipulation in two dimensions. It has been demonstrated that with implementation of dielectric strip on top of the truncated multilayer propagation of BSWs can be easily controlled by modification of local effective refractive index (Sfez et al. 2010). Photonic crystal ridges confined light based on the combination of a PBG effect from the photonic crystal side and TIR in the other sides. The interest in using polymeric ridges is extensive due to their relatively low cost, and chemical and mechanical stabilities. These structures can be fabricated by lithographic techniques, such as electron beam lithography (EBL) (Pala and Karabiyik 2016), direct laser writing (DLW) (Agrawal and Wang 2016), and focused ion beam (FIB) (Orloff et al. 2003). By designing different shapes and geometries of the ultra-thin polymer layer, BSW-based integrated photonic platforms, such as 2D lens (Yu et al. 2014), optical resonator (Dubey et al. 2016), flat reflector (Dubey et al. 2017b), and nanocoupler (Gulkin et al. 2021) have introduced. T. Kovalevich et al. have demonstrated experimentally the excitation of BSW through crisscrossed gratings which are fabricated

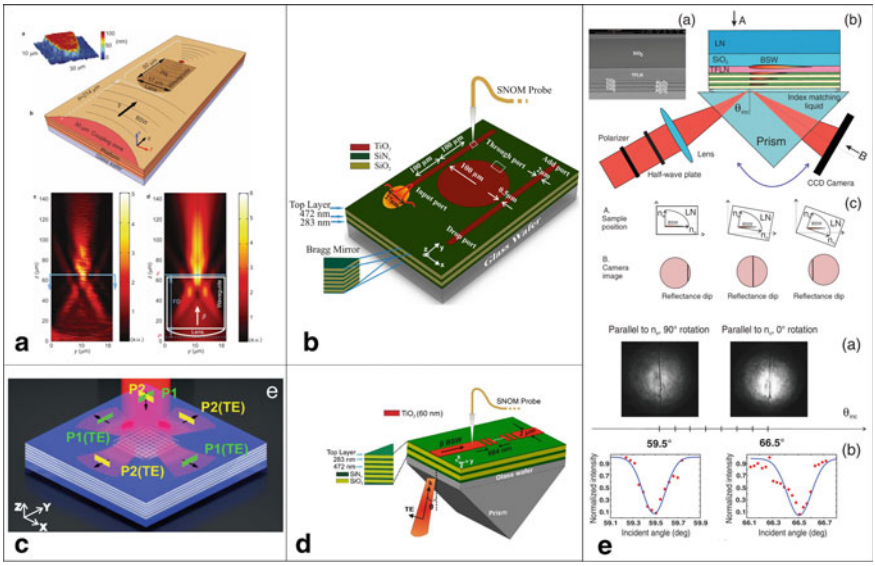

Fig. 1.7 **a** BSW propagating on the surface of photonic crystal can be focused by planoconvex lens-shaped photoresist layer (Yu, et al. 2014). **b** near-field interaction of the BSW with the resonator (Dubey et al. 2016). **c** gratings imprinted on a waveguide fabricated on top of 1D-photonic crystal operate as reflector (Dubey et al. 2017b). **d** tuning propagation direction of BSW with polarization of incident light with using 2D grating (Kovalevich et al. 2017). **e** tuneable Bloch surface wave with change sample orientation (Kovalevich et al. 2016)

with focused ion beam milling. At the normal incident, the direction of BSW propagation can be adjusted by changing of the incident light polarization so it can be introduced as a miniaturized BSW launcher and beam splitter for on-chip integrated systems (Kovalevich et al. 2017) (Fig. 1.7).

Toward fabrication of active BSW-based integrated systems has been introduced a 1D-pc that truncation layer is electro-optic thin layer of lithium niobate ($LiNbO_3$) (Fig. 1.6e). The electro-optical properties of $LiNbO_3$ and dependence of the refractive index on the sample orientation can be used to tune optical properties of BSWs. Different BSW coupling angles arising from ordinary and extraordinary refractive index (Kovalevich et al. 2016).

Interlink between BSW-based Integrated optics and hot vapor atomic

For many years, the investigation of the interaction of light and atoms has been carried out using bulky atomic vapor cells, which have many applications in quantum optics, magnetometry, sensing, and atomic clocks. The emergence of integrated optical devices provided the possibility of a manufacturing footprint and robust optical systems with the ability to manipulate light on the chip. Integrating these optical systems with atomic vapor allows the interaction of light and matter at the wavelength and sub-wavelength scales (Sedlacek et al. 2013; Kominis et al. 2003).

Recently, Salmanpour et al. investigated the coupling between the hot vapor of rubidium atoms with surface Bloch waves on one-dimensional periodic photonic crystal structure BK7/$(SiO_2/ZrO_2)^{12}$/SiO_2 (Asadolah Salmanpour et al. 2023). They made a vapor cell with the surface of the periodic photonic crystal structure located in the vicinity of the hot vapor of rubidium atoms. Decreased interaction volume of atom-BSWs can be a candidate to replace bulk vapor cells, especially in atomic vapor-based sensors. This study shows one of the main properties of surface waves to be considered in the design of surface wave–atom hybrid systems is the ohmic loss of hosting media of surface waves. In the case of BSWs, low ohmic loss of dielectric materials of photonic crystal helps BSWs to reject changes of resonance frequency by small deviation of incidence angle of laser light. Despite the coupling of the atom–BSWs, in the case of atom–SPP coupling strict dependence of resonance frequency and radiation loss of SPPs causes modulation of hybrid response of atom–SPPs by possible external effects modulating loss of plasmonic mode (Mosleh et al. 2022).

Another case that must be considered in the design of a surface wave–atom hybridized system is shifting in the frequency of atomic transition as a consequence of neighboring to the solid surface and effects like Casimir–Polder. In many applications based on atomic transitions, like atomic clocks, a distortion in atomic transition frequency will stop the work of the device and make miniaturization impossible. There are many studies that show evanescent fields can act as a mirror for atoms and change their straight path of ballistic flight in a gradient field of the electromagnetic field (Westbrook et al. 1998). Tuning the spatial distance of atoms from the solid surface can be used as a tool to eliminate the effects of transition-disturbing interactions. Considering the high local density of states of BSWs, modulation of the angle of incidence of light on the photonic crystal-vapor boundary can affect shifts in transition frequency. One of the differences between electromagnetic fields confined in surface waves compared with free space light waves is the sophisticated achievable phase and polarization states of surface waves. Considering the impact of spin transfer from surface wave to atoms in the design of the atomic vapor-based device, novel types of surface waves with specified properties can open the way for future applications. Periodic media such as photonic crystals are talented surfaces to realize the novel types of surface waves, predicted by topological band theory (Bliokh et al. 2023). Topological band theory enables prediction of novel types of surface waves, i.e., systems with wavelength-scale variations in their material parameters.

References

Agrawal R, Wang C (2016) Laser beam machining. Encyclopedia of nanotechnology, 2nd ed. Springer, Netherlands, pp 1739–1753

Aljunid SA et al (2016) Atomic response in the near-field of nanostructured plasmonic metamaterial. Nano Lett 16(5):3137–3141

Angelini A et al (2013) Fluorescence diffraction assisted by Bloch surface waves on a one-dimensional photonic crystal. New J Phys 15(7):073002

Asadolah Salmanpour M, Mosleh M, Hamidi SM (2023) Bloch surface wave-atom coupling in one-dimensional photonic crystal structure. Opt Express 31:4751–4759
Batey J, Tierney E (1986) Low-temperature deposition of high-quality silicon dioxide by plasma-enhanced chemical vapor deposition. J Appl Phys 60(9):3136–3145
Bliokh KY, Karimi E, Padgett MJ, Alonso MA, Dennis MR, Dudley A et al (2023) Roadmap on structured waves. arXiv:2301.05349.
Chan EA et al (2018) Tailoring optical metamaterials to tune the atom-surface Casimir-Polder interaction. Sci Adv 4(2):eaao4223
Chang D et al (2009) Trapping and manipulation of isolated atoms using nanoscale plasmonic structures. Phys Rev Lett 103(12):123004
Chen Z et al (2012) Study of optical Tamm states based on the phase properties of one-dimensional photonic crystals. Opt Express 20(19):21618–21626
Chen Y et al (2014) Effect of metal film thickness on Tamm plasmon-coupled emission. Phys Chem Chem Phys 16(46):25523–25530
Chiadini F et al (2016) Compound guided waves that mix characteristics of surface-plasmon-polariton, Tamm, Dyakonov-Tamm, and Uller-Zenneck waves. JOSA B 33(6):1197–1206
Da H-X, Huang Z-Q, Li Z (2009) Electrically controlled optical Tamm states in magnetophotonic crystal based on nematic liquid crystals. Opt Lett 34(11):1693–1695
Dubey R et al (2016) Near-field characterization of a Bloch-surface-wave-based 2D disk resonator. Opt Lett 41(21):4867–4870
Dubey R et al (2017b) Ultra-thin Bloch-surface-wave-based reflector at telecommunication wavelength. Photonics Res 5(5):494–499
Dubey R et al (2017a) Experimental investigation of the propagation properties of Bloch surface waves on dielectric multilayer platform. J Eur Opt Soc-Rapid Publ 13(1):1–9
Goban A et al (2014) Atom–light interactions in photonic crystals. Nat Commun 5(1):1–9
Goto T et al (2008) Optical Tamm states in one-dimensional magnetophotonic structures. Phys Rev Lett 101(11):113902
Gulkin DN et al (2021) Mie-driven directional nanocoupler for Bloch surface wave photonic platform. Nanophotonics 10(11):2939–2947
Kavokin A, Shelykh I, Malpuech G (2005) Optical Tamm states for the fabrication of polariton lasers. Appl Phys Lett 87(26):261105
Kominis I et al (2003) A subfemtotesla multichannel atomic magnetometer. Nature 422(6932):596–599
Konopsky VN, Alieva EV (2007) Photonic crystal surface waves for optical biosensors. Anal Chem 79(12):4729–4735
Kovalevich T et al (2016) Tunable Bloch surface waves in anisotropic photonic crystals based on lithium niobate thin films. Opt Lett 41(23):5616–5619
Kovalevich T et al (2017) Polarization controlled directional propagation of Bloch surface wave. Opt Express 25(5):5710–5715
Lee KJ, Wu J, Kim K (2013) Enhanced nonlinear optical effects due to the excitation of optical Tamm plasmon polaritons in one-dimensional photonic crystal structures. Opt Express 21(23):28817–28823
Leskelä M, Ritala M (2002) Atomic layer deposition (ALD): from precursors to thin film structures. Thin Solid Films 409(1):138–146
Liscidini M et al (2009) Strong modification of light emission from a dye monolayer via Bloch surface waves. Opt Lett 34(15):2318–2320
Liu H et al (2012) Optical magnetic field enhancement through coupling magnetic plasmons to Tamm plasmons. Opt Express 20(17):19160–19167
Matsudo T et al (1998) Pseudomomentum transfer from evanescent waves to atoms measured by saturated absorption spectroscopy. Opt Commun 145(1–6):64–68
Meade RD et al (1991) Electromagnetic Bloch waves at the surface of a photonic crystal. Phys Rev B 44(19):10961

Merzlikin A et al (2007) Controllable Tamm states in magnetophotonic crystal. Physica B 394(2):277–280
Mosleh M, Hamidi SM, Ranjbaran M (2021a) Ellipsometric spectroscopy of rubidium vapor cell at near-normal incidence, Sci Rep 0:17080
Mosleh M, Ranjbaran M, Hamidi S (2021b) Trace of evanescent wave polarization by atomic vapor spectroscopy. Sci Rep 11(1):1–9
Mosleh M, Hamidi SM, Ranjbaran M (2022) Multifunctional logic gates based on resonant transmission at atomic-plasmonic structure. Sci Rep 12:10734
Naiman A, Sebbag Y, Levy U (2020) Demonstration of on chip cavity to thermal Rb vapor strong coupling. In: 2020 Conference on lasers and electro-optics (CLEO). IEEE.
Occhicone A et al (2020) Spectral characterization of mid-infrared bloch surface waves excited on a truncated 1D photonic crystal. ACS Photonics 8(1):350–359
Orloff J, Swanson L, Utlaut M (2003) High resolution focused ion beams: FIB and its applications: Fib and its applications: the physics of liquid metal ion sources and ion optics and their application to focused ion beam technology. Springer Science and Business Media
Pala N, Karabiyik M (2016) Electron beam lithography (EBL). Springer, Dordrecht, The Netherlands
Pirotta S et al (2013) Surface-enhanced Raman scattering in purely dielectric structures via Bloch surface waves. J Phys Chem C 117(13):6821–6825
Ripka F et al (2018) A room-temperature single-photon source based on strongly interacting Rydberg atoms. Science 362(6413):446–449
Ritter R et al (2016) Coupling thermal atomic vapor to an integrated ring resonator. New J Phys 18(10):103031
Sasin M et al (2008) Tamm plasmon polaritons: Slow and spatially compact light. Appl Phys Lett 92(25):251112
Sathyadevaki R, Shanmuga Sundar D, Sivanantha Raja A (2016) Design of dual ring wavelength filters for WDM applications. Opt Commun 380:409–418
Schwindt PD et al (2004) Chip-scale atomic magnetometer. Appl Phys Lett 85(26):6409–6411
Sedlacek J et al (2013) Atom-based vector microwave electrometry using rubidium Rydberg atoms in a vapor cell. Phys Rev Lett 111(6):063001
Sfez T et al (2010) Bloch surface waves in ultrathin waveguides: near-field investigation of mode polarization and propagation. JOSA B 27(8):1617–1625
Shanmuga Sundar D, Sathyadevaki R, Sivanantha Raja A (2018) High-efficiency filters for photonic integrated networks: a brief analysis. Laser Phys 28:116203–116208
Shinn M, Robertson W (2005) Surface plasmon-like sensor based on surface electromagnetic waves in a photonic band-gap material. Sens Actuators, B Chem 105(2):360–364
Stehle C, Zimmermann C, Slama S (2014) Cooperative coupling of ultracold atoms and surface plasmons. Nat Phys 10(12):937–942
Symonds C et al (2013) Confined Tamm plasmon lasers. Nano Lett 13(7):3179–3184
Udem T, Holzwarth R, Hänsch TW (2002) Optical frequency metrology. Nature 416(6877):233–237
Villa F et al (2002) Photonic crystal sensor based on surface waves for thin-film characterization. Opt Lett 27(8):646–648
Vinogradov A et al (2006) Surface state peculiarities in one-dimensional photonic crystal interfaces. Phys Rev B 74(4):045128
Westbrook N, Westbrook CI, Landragin A, Labeyrie G, Cognet L, Savalli V et al (1998) New physics with evanescent wave atomic mirrors: the van der Waals force and atomic diffraction. Physica Scripta (T78):7
Xiang Y et al (2020) Trapping metallic particles using focused Bloch surface waves. Nanoscale 12(3):1688–1696
Yeh P, Yariv A, Cho AY (1978) Optical surface waves in periodic layered media. Appl Phys Lett 32(2):104–105
Yu S-P et al (2019) Two-dimensional photonic crystals for engineering atom–light interactions. Proc Natl Acad Sci 116(26):12743–12751

Yu L et al (2014) Manipulating Bloch surface waves in 2D: a platform concept-based flat lens. Light: Sci Appl 3(1):e124–e124
Zektzer R et al (2021) Atom-photon interactions in atomic cladded waveguides: bridging atomic and telecom technologies. ACS Photonics 8(3):879–886
Zhang W, Yu SF (2010) Bistable switching using an optical Tamm cavity with a Kerr medium. Optics Commun 283(12):2622–2626

Chapter 2
Highly Efficient Graphene-Based Optical Components for Networking Applications

M. Soroosh, A. Farmani, M. J. Maleki, F. Haddadan, and M. Mansouri

Abstract Graphene has been known as a fascinating material and has attracted much attention for different applications. Optical and electrical prominent features of graphene make the opportunity for designing graphene-based optical components. Zero bandgap and linear dispersion for electron energy in terms of wave vector are the characteristics of graphene. So, light absorption with any wavelength is possible. Besides, the band structure and the bandgap change by adding dopants and applying electric and magnetic fields. Propagation of surface plasmon polaritons is also possible at the graphene–dielectric material interface which helps in designing plasmonic-based optical devices. In this chapter, we focus on introducing some optical devices for network applications. Adjusting the graphene chemical potential and changing the Fermi energy level affect the graphene absorption coefficient for optical waves, and make the light manipulate and control in optical networks. The chemical potential changes in response to the applied voltage. We will discuss graphene, its electrical and optical properties, and some optical devices based on graphene. The graphene-based optical switches, decoders, and encoders will be considered. Guiding the optical waves and changing lines to transfer the optical data and reach the desired nodes will be also investigated in this chapter.

Keywords Decoder · Encoder · Graphene · Surface plasmon polariton · Switch

M. Soroosh (✉) · M. J. Maleki · F. Haddadan
Department of Electrical Engineering, Shahid Chamran University of Ahvaz, Ahvaz, Iran
e-mail: m.soroosh@scu.ac.ir

A. Farmani · M. Mansouri
School of Electrical and Computer Engineering, Lorestan University, Khoramabad, Iran

© The Author(s), under exclusive license to Springer Nature Singapore Pte Ltd. 2023

S. S. Dhanabalan et al. (eds.), *Photonic Crystal and Its Applications for Next Generation Systems*, Springer Tracts in Electrical and Electronics Engineering,
https://doi.org/10.1007/978-981-99-2548-3_2

Graphene

In recent years, graphene-based devices have been considered as a very important element in medical use for the treatment and diagnosis of diseases, energy production, military systems, rapid communications, rapid progress in response, etc.(Rezaei and Zarifkar 2021; Szunerits and Boukherroub 2015; Shvets and Tsukerman 2012). The new properties of plasmonic materials have led to the absorption and propagation of light by these materials in a special way which has led to unique properties in plasmonic detection. Among them, two-dimensional materials have a unique position. One of these materials is graphene. Graphene is a two-dimensional sheet of carbon atoms that has a hexagonal (honeycomb) configuration. Recently, graphene is one of the main materials in the hands of researchers because of its exceptional properties (Yildiz et al. 2021; Bagheri and Soroosh 2022; Mansouri et al. 2022). Graphene is classified as the newest family of multidimensional graphitic materials. In a graphene sheet, each carbon atom forms a covalent bond with three other atoms, and the angle between these atoms is 120°. In this network, the bond length of carbon atoms is equal to $a_{cc} = 0.142$ nm and its base vectors are defined as follows (Zhan et al. 2012):

$$\vec{a}_1 = \left(\frac{\sqrt{3}}{2}a, \frac{1}{2}a\right), \quad \vec{a}_2 = \left(\tfrac{\sqrt{3}}{2}a, -\tfrac{1}{2}a\right) \tag{1a}$$

$$\left|\vec{a}_1\right| = \left|\vec{a}_2\right| = |a| = \sqrt{a_{cc}^2 + a_{cc}^2 + 2a_{cc}a_{cc}cos(60)} = \sqrt{3}a_{cc} \tag{1b}$$

$$\vec{\delta}_1 = \left|\vec{a}_{cc}\right|cos(0) + \left|\vec{a}_{cc}\right|sin(0) = \left(\frac{a}{\sqrt{3}}, 0\right) \tag{1c}$$

$$\vec{\delta}_2 = -\left|\vec{a}_{cc}\right|cos(60) + \left|\vec{a}_{cc}\right|sin(60) = \left(\frac{-a}{2\sqrt{3}}, \frac{a}{2}\right) \tag{1d}$$

$$\vec{\delta}_3 = -\left|\vec{a}_{cc}\right|cos(60) - \left|\vec{a}_{cc}\right|sin(60) = \left(\frac{a}{\sqrt{3}}.0\right) \tag{1e}$$

Since the band structure of graphene is alternating, it has the same energy band structure as silicon. To calculate the band structure of graphene, we have to solve the time-independent Schrödinger equation. Here, we will avoid the long calculations of solving the Schrödinger equation and just express the final relation E(k) of graphene (Zhan et al. 2012).

$$E(k_x, k_y)^{\pm} = \pm\gamma\sqrt{1 + 4cos\frac{\sqrt{3}}{2}ak_x cos\frac{a}{2}k_y + 4cos^2\frac{a}{2}k_y} \tag{2.2}$$

where k is the wavevector and includes x and y indices in Eq. (2.2). For conventional calculations, we consider its experimental value which is equal to $\gamma = 1/3$eV (Zhan et al. 2012). The graphene band structure, the valence, and the conduction band

touch each other at the six points. Therefore, according to the form of interesting properties that can be observed in graphene and can be used, it is quasi-metallic behavior (semiconductor with zero bandgap) and its semiconducting behavior.

Graphene is the first two-dimensional material obtained from graphite using a simple method named as micromechanical cleavage. This method now provides high-quality graphene crystals of suitable size for research studies. Before presenting the micromechanical cleavage, it was generally believed that two-dimensional crystals were completely thermodynamically unstable and did not obtain in the free state. In addition to being used as a two-dimensional base system for materials science and dense matter physics, graphene has excellent electronic properties such as very high mobility, ballistic transmission, low thickness and stability, and quantum Hall effect. These unique properties of graphene make this material widely used in nano-electronic devices and other magnetic applications. Inherent graphene is a unique pseudo-metal or semiconductor without the bandgap. The outstanding electronic properties of graphene depend on the combined states of carbon and its unique topological structure. Basically, carbon has two 2S electrons and two 2P electrons. These four electrons produce different types of hybridization orbitals. In graphene, carbon atoms are arranged in a unique honeycomb lattice structure such that each carbon atom is surrounded by three neighboring axes. In fact, the honeycomb network can be defined as two triangular sub-networks that penetrate each other. As a two-dimensional crystal and symmetric honeycomb lattice model, the electrical structure and transport properties of graphene are predicted. Using density functional theory and the tight-binding method, the π bands and σ bands of graphene are appropriately described.

For the Γ point of the Brillouin zone (BZ), the gaps are 20 eV. Unlike most 3D materials whose electronic states are described using the Schrödinger equation, graphene's charges are described using the Dirac relation in quantum electrodynamics. According to the Dirac relation, one can obtain different properties of the graphene electronic structure. The first filled valence band is connected to the completely empty conduction band at points k and k' in the BZ. Therefore, the graphene bandgap disappears at the mentioned points. It is continuously adjusted due to p-type to n-type dopant applying an electro-static bias, resulting from the dipole field effect. On the other hand, zero bandgap and low density of electron states limit the graphene application in electronic and optical structures. Therefore, in different approaches, both theoretically and practically, it has been dedicated to introducing a limited bandgap for graphene. By using physical strategies such as graphene–substrate interaction, application of an external electric field on graphene, cutting graphene into nan-ribbons, and surface adsorption of graphene, a low adjustable bandgap up to 250 mV is opened. Adding a functional chemical group to graphene is known an efficient method to manipulate the electronic and magnetic features. The main issue in chemisorption on graphene, as a covalent modification of graphene, is to transfer the hybridization state of the host carbon atom from 2 to 3sp to break a π-bond and generate an additional σ-bond. Thus, the 3sp hybridization carbon is connected with other neighboring atoms using 4 σ-bonds. This 3sp hybridization

carbon can be seen as a monoatomic defect of the graphene crystal because it reduces the π electron to form a σ-bond (Aliofkhazraei et al. 2016).

The electrical conductivity of graphene comes from two physical mechanisms: intra-band and inter-band electronic transitions. In-band electronic transitions are described using the Drude frequency model which is a simple method implemented in finite difference time domain using the auxiliary differential equation (ADE). Inter-band transitions cannot be obtained directly by the ADE method. Graphene has the potential to modulate, transmit, and detect photonic signals, and also has a high optical damage threshold of 3×10^6 MW/cm^2, and many optical properties of graphene are stable in a large wavelength range. The frequency-dependent electrical conductivity spectrum of the graphene surface is a conjugate value. Graphene's electrical conductivity (σ) model uses Kubo's formula, and in the absence of an applied electric or magnetic field, it is obtained from the following equation (Deacon et al. 2007):

$$\sigma(\omega, \mu_c, \tau, T) = \frac{\frac{je^2}{\pi\hbar^2}}{\omega - j\frac{2}{\pi}} \int_0^\infty E\left(\frac{\partial f_d(E)}{\partial E} - \frac{\partial f_d E}{\partial E}\right) dE + \frac{je^2}{\pi\hbar^2}\left(\omega - j\left(\frac{2}{\pi}\right)\right) \int_0^\infty \left(\frac{f_d(E) - f_d(-E)}{\left(\omega - j\frac{2}{\tau}\right)^2 - 4\left(\frac{E}{\hbar}\right)^2}\right) \tag{2.3}$$

where ω is the angular frequency, e is the electron charge, μ_c is the chemical potential, and $1/\tau$ is equal to the carrier scattering rate. The Fermi–Dirac distribution function is defined by $f_d(E) = 1/\left(e^{(E-\mu_c)/K_BT} + 1\right)$ where K_B is the Boltzmann constant and T is the temperature in Kelvin. The first integral in the above equation describes the intra-band carriers and the other integral describes the inter-band carriers. The first integral is defined as follows:

$$\sigma_{intra}(\omega, \mu_c, \tau, T) = -j\frac{8\sigma_0 K_B T/h}{\omega - j2/\tau}\left[\frac{\mu_c}{k_B T} + 2ln\left(e^{(-\mu_c/K_BT)} + 1\right)\right] \tag{2.4}$$

From Maxwell's equations, the relationship between conductivity and electrical permittivity (ε) is obtained from the following equation (Deacon et al. 2007):

$$\varepsilon(\omega) = \varepsilon_r + \frac{\sigma_i(\omega)}{\omega} - j\left(\frac{\sigma_r(\omega)}{\omega}\right) \tag{2.5}$$

where ε_r is the relative permittivity, σ_i and σ_r are the imaginary and real parts of the conductivity, respectively.

As mentioned, graphene is an allotropic form of carbon, which is considered a single layer of carbon atoms. Concerning its excellent properties, graphene could be realized in various fields of industry including sensors, digital devices, routers, and

logic gates. In the following, we show some of the features of graphene that have recently attracted the attention of researchers.

The use of surface plasmonic resonators (SPRs) in optical routers offers a highly practical perspective. Therefore, the use of this mechanism in the router capability for high-speed, tunable, and compact optical devices was considered. The main feature of this structure over others is selectivity for frequency routing and reconfiguration based on plasmonic materials. In the σ-bond, the triangular hybridization of the shaped sp^2 orbitals with three neighboring carbon atoms shows coordination in three sites although there is an unpaired electron in the p-orbital to form a π-bond with one of the three neighboring carbon atoms, which is shown in Fig. 2.1a. Figure 2.1b illustrates a surface plasmonic optical router based on the graphene ring structure (Mansuri et al. 2020). Optical switches and routers are used in optical networks and communication systems. In parallel, the growth of plasmonic devices along with meta-materials has provided a way to integrate these two domains. Of course, high-capacity routers have caused the role of optical and optical technologies to be much considered (Tucker 2006; Farmani et al. 2017a; Xu et al. 2019). Fast path selection, nano-scale, precision, and sensitivity can be considered as advantages of this field. Currently, the focus is on plasmonic and resonant rings to develop devices with integration density and the ability to provide the functions of an optical router. By creating circles with different diameters based on the SPR mechanism, graphene causes each wavelength to be directed to its own output (as shown in Fig. 2.1c).

Transmission of terahertz waves in optical devices based on surface plasmons has received much attention in the last decade. The oscillations of the valence band electrons due to the application of a magnetic field cause the generation of surface plasmons (as shown in Fig. 2.1d for TM). The sub-wavelength dimensions enable the processing and transmission of waves in the terahertz range due to the confinement of surface plasmons in them. The surface electromagnetic waves that are coupled along the interface between the dielectric material and the metal emit polariton surface plasmons. Therefore, they can be used for optical integrated circuits based on surface plasmon polariton. For example, decoders, switches, encoders, and some devices have recently been proposed based on surface plasmon polaritons.

The need for high-speed data transfer is increasing day by day. All tools in this direction must have the necessary coordination. Light-speed transmissions require switches and routing for unrestricted transmission. Design in the terahertz range makes this possible because researchers have done a lot of research in this area recently (Mansuri et al. 2020; Farmani et al. 2017b; Xu et al. 2018; Derakhshi and Fathi 2017). Multiplexers and switches are among these that play an important role in this range (Mansuri et al. 2021; Udupi and Madhava 2021; Lima and Sombra 2017). The design structure is generally based on the metal–dielectric–metal configuration. Typically, SiO_2 is used as a dielectric and gold or silver as a metal on it. In a demultiplexer, an input signal is transmitted to three output ports. Of course, the same function can be used in reverse as a multiplexer. Routing and control in this design are based on the nonlinear phenomenon which is selected with different intensities of the desired path. The input signal is transmitted to a specific path based

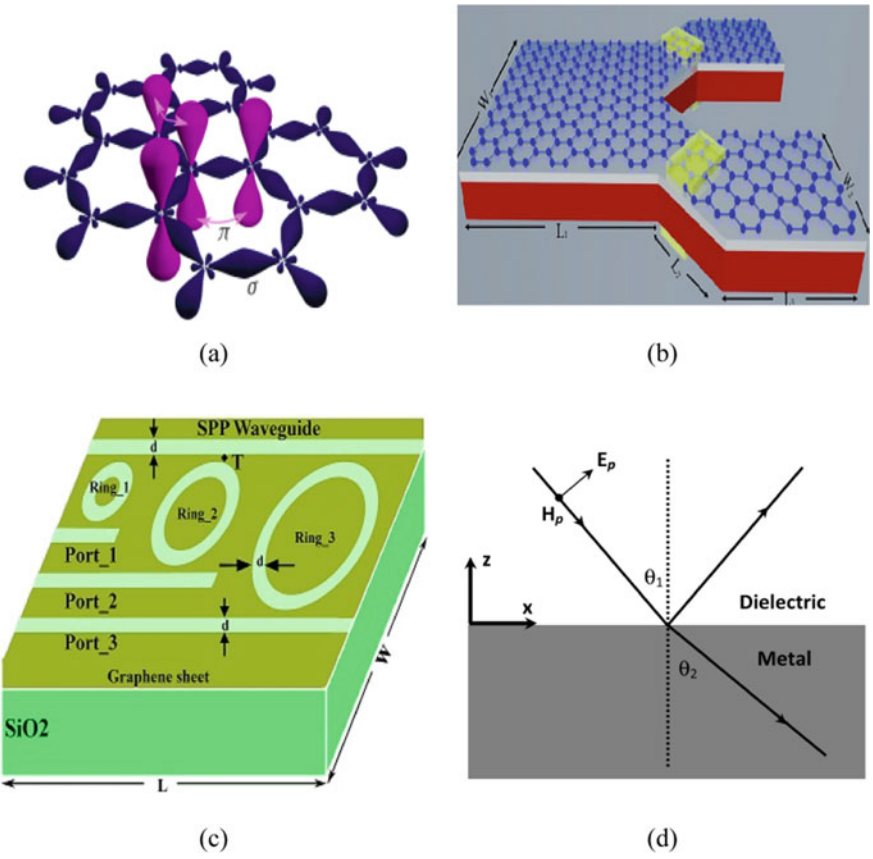

Fig. 2.1 **a** A graphene view of σ and π bonds (Mansuri et al. 2020) **b** a three-dimensional view of an optical logic gate. The hexagonal shapes provided by the graphene sheets with the voltage applied to the graphene control the amount of transmission in the two arms. (Farmani et al. 2017b) **c** a schematic of a graphene-based router including three resonant rings to drop the incoming waves toward ports 1, 2, and 3 (Mansuri et al. 2020) **d** TM illumination for SPP stimulation (Mansuri et al. 2020)

on the selected intensity. These devices are used in the processing of optical signals and plasmonic integrated circuits.

Analysis and processing are performed based on logic gates. In other words, they are the basis of technology for processing logic gates (Rezaei et al. 2019; Zhao 2017; Skidin 2018). Therefore, they have received a lot of attention for research and development of plasmonic technology (Lee 2020; Anguluri et al. 2021; Sharma et al. 2020). This field has changed in the direction of meta-materials and two-dimensional materials (Debu et al. 2019; Azar et al. 2020; Luo et al. 2020). Low volume and appropriate response are obtained by using this field. For example, in a recent study using hexagonal boron nitride(h-BN) and graphene based on plasmonic waveguides

at a wavelength of 7.5 μm (Rezaei et al. 2019). Logical operations such as XOR, AND, and OR have been introduced using this design based on the unique properties of graphene. The layout of this design is shown in Fig. 2.1b (Farmani et al. 2017b). Two inputs have been used for each gate and XOR, OR, and AND gates have been introduced. In other words, this gate is used as a multifunctional gate. Control over the inputs and outputs of this structure in ON and OFF modes is created by applying an external voltage. This application with an applied voltage to graphene as a 2D material provides control. As a result, the light applied to the inputs and outputs is controlled depending on the type of operation. The nano-scale of this design allows it to be used in integrated optical circuits and advances applications in this field. Like plasmonic memories that will take their place in the near future.

Graphene-Based Optical Switches

One of the main components in optical devices is optical switches, which are the basis of digital circuits. Two methods that can be used to design optical digital devices are plasmonic structures and photonic crystals. Photonic crystal-based devices such as adders, routers, and filters have been introduced, the main problem of which is their large dimensions and lack of integrability (Sundar et al. 2018a, 2018b; Sathyadevaki et al. 2018, 2016; Sivaranjani et al. 2020; Thirumaran et al. 2021). Solving this problem in plasmonic structures has received much attention from researchers in recent years. Here, two widely applicable types of graphene-based plasmonic waveguides are discussed (Rezaei and Zarifkar 2021; Haddadan et al. 2022). The transmission of terahertz waves in the waveguides can be adjusted by using a bias voltage to graphene. Applying a bias voltage changes the graphene chemical potential so the Fermi energy level changes. As a result, wave absorption varies for different values of the bias voltage. This feature causes the control of wave transmission and achieving the switching operation is possible. Accordingly, the graphene-based waveguides can be considered optical switches. Optical switches are widely used to design digital devices such as decoders and encoders. In the following, the switching operation of two types of graphene-based waveguides is discussed.

The basic graphene-based plasmonic waveguides including nano-ribbon (Rezaei and Zarifkar 2021) and ridge (Haddadan et al. 2022) are depicted in Fig. 2.2. The nano-ribbon waveguide made of a single graphene nano-ribbon which is placed on a stack of dielectric–metal substrate (as shown in Fig. 2.2a). The dielectric constant and thickness of the spacer are 3.9 and 20 nm, respectively. A gold layer with a thickness of 30 nm is used to intensify the wave confinement and also apply external voltage to electrodes.

Graphene nano-ribbon waveguides support two types of surface plasmonic modes, waveguide mode and edge mode (Rezaei and Zarifkar 2021). The waveguide modes propagate the electromagnetic waves through the graphene nano-ribbons while the edge modes transfer on the edges of the graphene nano-ribbons. In the narrow graphene nano-ribbons smaller than 50 nm, the edge mode of surface plasmons is

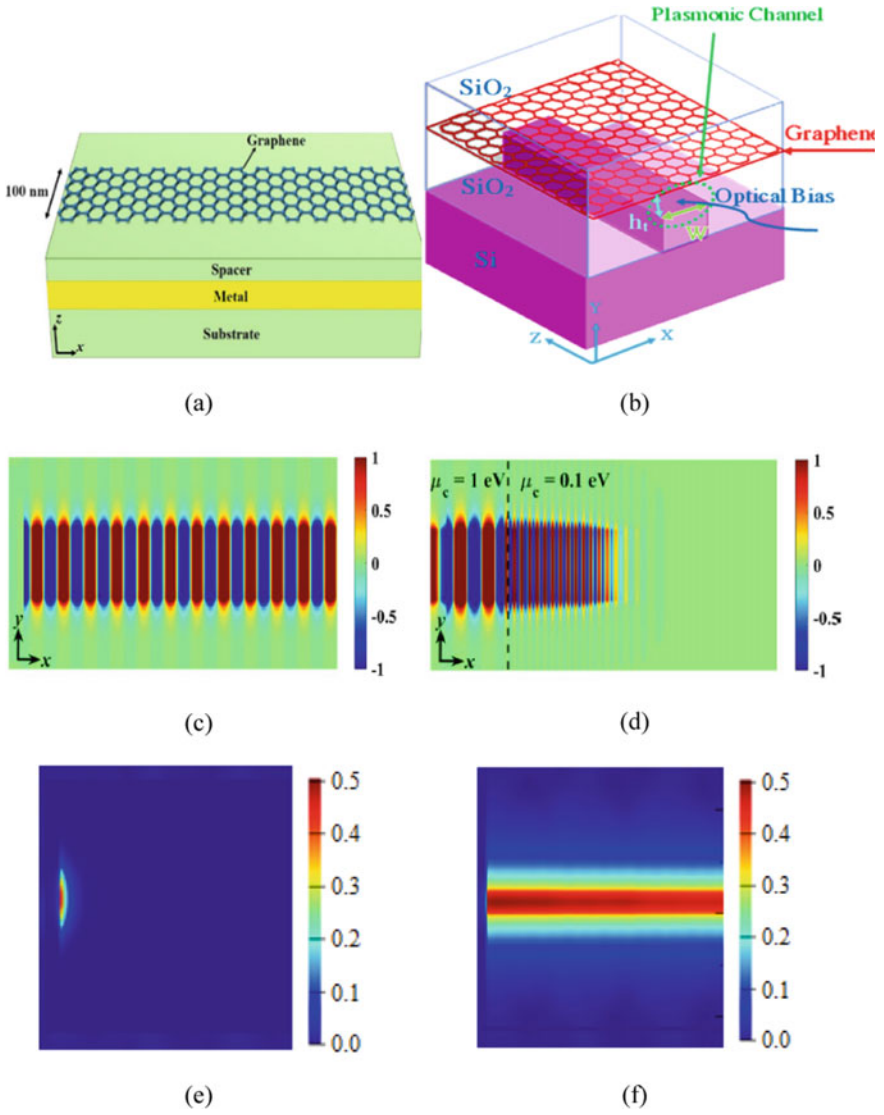

Fig. 2.2 Two types of the optical switches with **a** a graphene nano-ribbon on a spacer for SPP confinement (Rezaei and Zarifkar 2021), **b** a plasmonic channel sandwiched between a silicon ridge and a graphene monolayer (Haddadan et al. 2022). ON and OFF states of the graphene nano-ribbon structure are presented in sections **c** and **d**, respectively. A chemical potential of 1 eV allows the wave to pass while a chemical potential of 0.1 eV does not allow SPPs to transmit along the x-direction. Working states OFF and ON for the raised plasmonic channel are shown in sections **e** and **f**, respectively. The SPP propagation is allowed for $\mu_c = 0.5$ eV, and those are absorbed for $\mu_c = 0.1$ eV

stimulated. As the width of the graphene nano-ribbon widens, the waveguide mode is stimulated too.

Graphene has extraordinary electro-optical characteristics, especially in the far-infrared and terahertz frequencies, while noble metals are known as proper plasmonic materials for the visible and near-infrared applications. The optical properties of graphene are well defined by its surface conductivity. As the above mentioned, the surface conductivity consists of inter-band transitions and intra-band contributions depending on several parameters. The surface plasmon polariton wavelength (λ_{SPP}) and the propagation length are defined by Haddadan et al. (2022)

$$\lambda_{SPP} = \frac{\lambda_0}{Re(n_{eff})} \tag{2.6}$$

$$L_{SPP} = \frac{\lambda_0}{2\pi Im(n_{eff})} \tag{2.7}$$

By declining the real part of n_{eff}, the λ_{SPP} rises, and the higher the imaginary part of n_{eff}, which leads to less L_{SPP}. The electric field distribution along the z-direction for chemical potentials of 0.1 eV and 1 eV is shown in Figs. 2.2c and 2d. If the chemical potential equals 1 eV, the surface plasmons transmit through the waveguide as the ON state (see Fig. 2.2c). Furthermore, when the chemical potential alters to 0.1 eV, the surface plasmons are not allowed to propagate in the OFF state, and a significant amount of wave is lost and reflected (as shown in Fig. 2.2d) (Rezaei and Zarifkar 2021). This behavior enables the design of a plasmonic switch using graphene by adjusting a bias voltage.

Figure 2.2b illustrates a three-dimensional view of the silicon ridge waveguide (Haddadan et al. 2022). A 200 nm thickness of silicon is considered for the substrate. A silicon ridge with a height (h) of 50 nm and a width (W) of 80 nm is located on a substrate. Two layers of SiO_2 with a permittivity of 1.36 are located at the top and below the graphene sheet. The thicknesses of bottom and the top layer are equal to 10 and 20 nm, respectively, in the core region. Graphene and silicon ridge confine and transmit the incoming waves within the plasmonic waveguide. The distance between the ridge and the graphene is defined as the channel core, and the waves transmit in the z-direction.

By adjusting the graphene chemical potential, a mismatch between the surrounding and the ridge region radii is created. Therefore, the light is concentrated into the gap above the ridge by helping high electric field distribution at the plasmonic channel. The slot effect is related to by the confinement of plasmons in the channel (Haddadan and Soroosh 2023). A slot waveguide consisting of two strips with a high refractive index separated by a material with a low index transmits strongly confined waves in a low-index material due to the total internal reflection. A slot waveguide transmits the modes using discontinuity of the electric field at high refractive index contrast interfaces, and also the cohesion of the normal part of the electric field displacement at an interface in Maxwell's equations, the corresponding

electric field should penetrate a discontinuity with higher domain in the low-index material.

The values of Re(n_{eff}) for the five TM modes change from 61 to 78 for W > 430 nm. When W is less than 170 nm, there is only the fundamental mode in the channel. The simulation shows that α changes from 2.56 dB/μm to 2.98 dB/μm corresponding to Modes 0 to 4 at 0.3 eV. Also, by rising width, loss declines. The amounts of confinement and loss have negligible changes for W greater than 250 nm, and the channel behaves similarly to the slab waveguide. The height of the plasmonic channel is a key parameter in supporting TM modes in the channel. By rising ht, the substrate effect falls. When ht varies from 2 to 15 nm, the values of N and α decrease from 119 and 4.3 dB/μm to 67.3 and 2.6 dB/μm, respectively. By increasing ht, from 15 to 30 nm, N and α fall slowly again. Therefore, the mode confinement and loss decrease. The simulation results show N, α, and LGSP for $h_t = 12$ nm and W = 100 nm change greatly when the chemical potential varies from 0.1 eV to 0.5 eV. The steep slope of the α curve provides a possibility to reach the switching operation. When μ_c is 0.1 eV, α is obtained to be 486.3 dB/μm while α is 0.42 dB/μm for μ_c = 0.5 eV. In this case, two values of 0.5 eV and 0.1 eV are assumed for controlling the wave transmission in the channel. As a result, N = 44.06 and α = 0.42 dB/μm are considered as the ON state, and N = 300 and α = 486.3 dB/μm are related to the OFF state. Regarding $L_{GSP} = 10$ nm for $\mu_c = 0.1$ eV, the results recommend an optical sub-wavelength switch with a small length in nano-scale. By increasing μ_c, two parts of the refractive index decline so L_{GSP} rises.

Noble metals have a greater real index than silicon at terahertz frequency. These metals have high resistivity in the terahertz region, so they suffer from high plasmonic losses. They provide a high refractive index to confine the terahertz waves (Haddadan et al. 2022). Using noble metals, the ridge rises the index mismatch between the ridge and near regions. This issue leads to more mode confinement of plasmons into the gap area at the top of the ridge. Increasing the plasmon transmission within the gap declines the effects of cross talk.

Figure 2.2e, f illustrates the electric field distribution in the channel for W = 80 nm and $h_t = 10$ nm in response to $\mu_c = 0.1$ eV and 0.5 eV. As depicted in Fig. 2.2e, the loss in case of $\mu_c = 0.1$ eV is as great as 486.3 dB/μm. Therefore, the waves are not allowed to propagate within the channel. However, the waves are able to transfer through the channel for $\mu_c = 0.5$ eV, due to a low loss of 0.42 dB/μm (as shown in Fig. 2.2f). As a result, the presented ridge-base structure can be considered as an optical switch including OFF and ON states corresponding to $\mu_c = 0.1$ eV and μ_c = 0.5 eV, respectively.

Plasmonic Decoder

In this section, an electro-optical decoder based on a graphene waveguide is investigated (Rezaei and Zarifkar 2021). The fundamental graphene–dielectric–metal waveguide is shown in Fig. 2.3a. A single graphene nano-ribbon and a stack of

dielectric–metal substrate form the plasmonic waveguide. The thickness of the dielectric and metal is 20 and 30 nm, respectively. The metal is assumed as a contact to connect a bias. Also, the confinement of light in the dielectric is enhanced by helping the metal. For a narrow graphene nano-ribbon, the waveguide transfers only at the edge mode. So, power is focused at the graphene edges. If the graphene nano-ribbon widens, other modes can be stimulated and guided in the waveguide. The width of the graphene nano-ribbons (W) is considered to be 100 nm to reach a single-mode waveguide and transmit only the edge mode. Figure 2.3b illustrates the top view of the graphene nano-ribbon. In each arm, the ribbons are marked in a Y shape with an angle of 5 degrees.

By employing electron beam evaporation, the metal is deposited on the substrate. Designing the metal nano-electrode patterns is achieved by methods of standard photolithography and wet etching (Haddadan et al. 2022). Then, the deposition of the dielectric layer on top of the metal is done to reach a flat surface. By using the wet transfer method, the nano-ribbons grown on copper are transferred on the dielectric.

Y-branch splitters help to guide the surface plasmons toward the output ports. Four electrodes X, Y, $\overline{X}$, and $\overline{Y}$ are assigned to apply the electrical inputs (see Fig. 2.3c). The

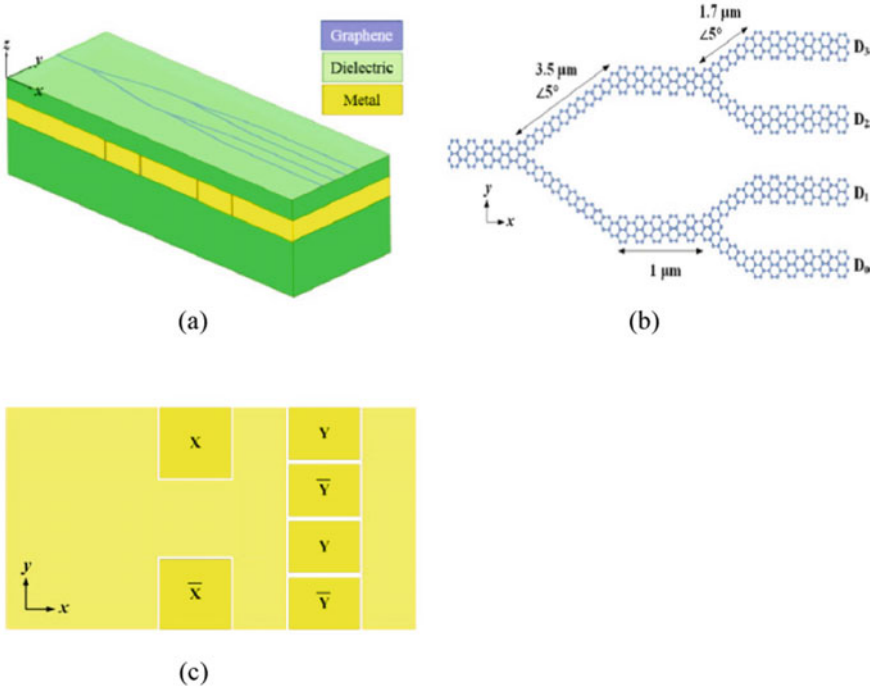

Fig. 2.3 **a** A three-dimensional view of 2 × 4 decoder including Y-shaped nano-ribbons on dielectric (Rezaei and Zarifkar 2021), **b** a top view of the nano-ribbon for guiding the waves by adjusting the chemical potential of graphene, **c** the assigned contact values to inputs X and Y for guiding SPPs toward the correct ports for working cases

electrical inputs control the surface plasmon propagation through the nano-ribbons. For the chemical potential of 1 eV, surface plasmons transmit on the plasmonic waveguide and result in the ON state at the output port. By applying $\mu_c = 0.1$ eV to graphene layer, surface plasmons are strongly attenuated, so they cannot propagate through the waveguide and make the OFF state at output. An external electrical inverter provides the $\overline{X}$ and $\overline{Y}$ electrode biases. Whenever electrode X becomes ON, electrode $\overline{X}$ equals OFF, and vice versa. This process is defined for Y electrical inputs. Illumination of a TM wave with $\lambda = 25$ μm stimulates the surface plasmons.

Figure 2.4 shows the distribution of the electric field for various states of the electrical inputs. In Fig. 2.4a, the inputs X and Y are in the OFF state so the complementary inputs are in the ON state. The surface plasmons transmit via the input waveguide to the arms of the first Y-branch splitter. For $X = 0$, a negligible amount of the incoming power reaches the output ports D2 and D3. Also, since that $\overline{X} = 1$, the plasmons travel to the second Y-branch splitter in the bottom arm. For $Y = 0$ and $\overline{Y} = 1$, the plasmons are attenuated for D1 and transmitted toward D0. A similar procedure also is illustrated for other states.

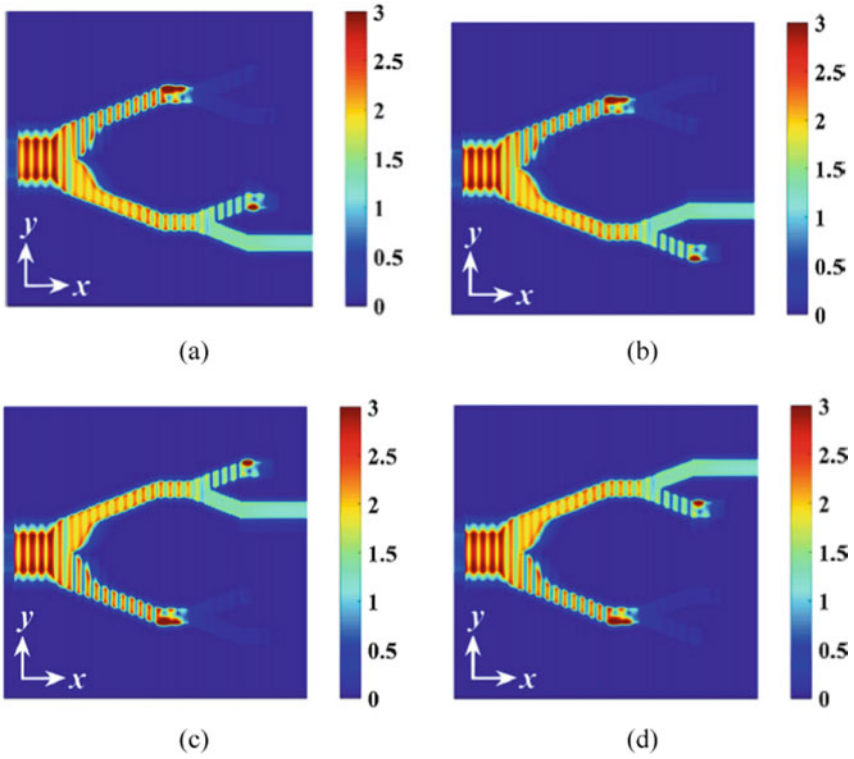

Fig. 2.4 Distribution of the electric field amplitude |E| for working states **a** XY = 00, **b** XY = 01, **c** XY = 10, and **d** XY = 11 (Rezaei and Zarifkar 2021)

Table 2.1 The calculated transmission at outputs for working states

Electrical inputs		Transmission at the output ports (dB)				ER (dB)
X	Y	D0	D1	D2	D3	
0	0	−5.65	−41.87	−42.01	−95.59	36.23
0	1	−41.90	−5.83	−62.32	−42.06	36.21
1	0	−42.06	−62.32	−5.83	−41.90	36.13
1	1	−95.59	−42.01	−41.87	−5.65	36.14

Table 2.1 gives the normalized power in dB for the various electrical inputs at a wavelength of 25 μm. The extinction ratio (ER) is calculated as follows (Rezaei and Zarifkar 2021):

$$ER_{(dB)} = 10log(\frac{P_1}{P_0}) \tag{2.8}$$

where P_1 (P_0) is power at the output port in the ON (OFF) state. The minimum value of ER is obtained higher than 36 dB for all outputs. The area of the designed structure is almost 8 μm^2.

Plasmonic Encoder

Figure 2.5a shows a view of the plasmonic ridge-based 4 × 2 encoder (Haddadan et al. 2022). Waveguides W1, W2, W3, W4, and W5 transmit the optical waves toward the outputs O0 and O1. Four single layers of graphene are placed on top of the waveguides. A silicon substrate and a silicon ridge are grown as the bottom layers. A SiO_2 layer is grown and followed by the graphene sheets. Finally, another SiO_2 layer is placed on the graphene. As shown in Fig. 2.5a, the chemical potentials μ_0, μ_1, μ_2, and μ_3 are adjusted for the graphene monolayers, and μ_4 is adjusted to 0.5 eV for possible states. The various chemical potentials to graphene layers correspond to the different applied bias voltages. The light transmission via the waveguides is controlled by changing the graphene chemical potential. When the distance between two waveguides is small, plasmons are easily coupled between them. So, a distance of 30 nm is assumed between the near waveguides. Figure 2.5b illustrates a modified structure for achieving the priority feature. This feature is obtained by changing the value of chemical potentials as shown in Fig. 2.5b.

Figure 2.6 shows the diagram of the electric field distribution for the introduced encoder in Fig. 2.5a. Four working states 00, 01, 10, and 11 have been shown for a channel width of 80 nm and a channel height of 5 nm. In the following, the mentioned states are investigated.

State 1: in this state, μ1, μ2, and μ3 equal to 0.1 eV while μ0 equals 0.5 eV. Because of a great loss, plasmons are not allowed to transmit through W1, W2, and W3, and

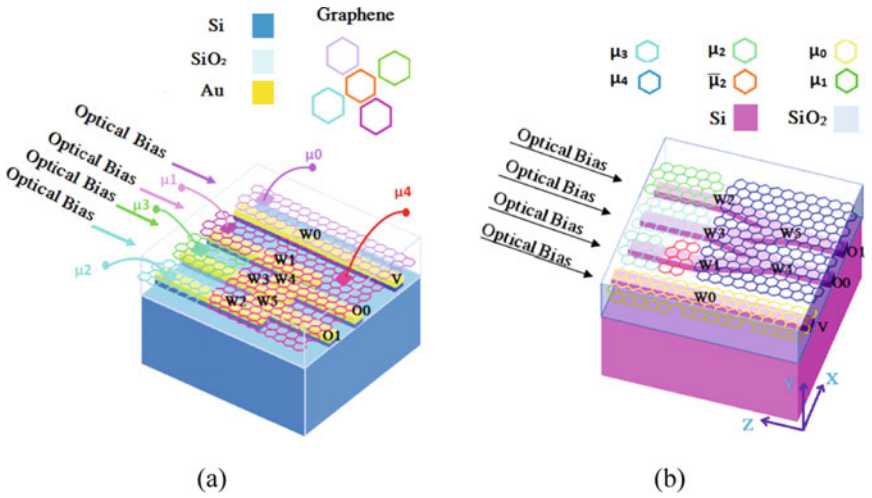

Fig. 2.5 **a** Aview of the plasmonic 4 × 2 encoder (Haddadan et al. 2022), **b** the modified structure for obtaining the priority feature (Haddadan and Soroosh 2023)

as a result, the plasmons do not propagate through W4 and W5 waveguides (as shown in Fig. 2.6a). Therefore, the terahertz waves do not reach the outputs, and O1O0 = 00 is obtained. Almost 88% of the incoming power through W0 reaches port V and it becomes ON.

State 2: $\mu 1$ and $\mu 4$ are selected 0.5 eV, and also $\mu 2$ and $\mu 3$ are considered as 0.1 eV. Due to the high loss, plasmons are attenuated and are not able to pass waveguides W2 and W3, so the plasmons do not travel through W5 waveguide, and the output power at port O1 is obtained almost zero (see Fig. 2.6b). Because of the low propagation loss, 62.2% of optical bias power transfers via W1, so the plasmons are coupled from W1 to W4 and transmitted through W4. Accordingly, the plasmons are available at port O0 and it becomes ON (O1O0 = 01).

State 3: if $\mu 2 = \mu 4 = 0.5$ eV and $\mu 1 = \mu 3 = 0.1$ eV are chosen, a high value of loss weakens plasmons so they do not pass W1 and W3 waveguides. As shown in Fig. 2.6c, the plasmons do not transmit via W4, and very low power is obtained at port O0. In this state, 62.2% of optical bias power transmits through W2 and is coupled from W2 to W5. As a result, the status of O1O0 = 10 is generated.

State 4: for $\mu 1 = \mu 2 = 0.1$ eV and $\mu 3 = \mu 4 = 0.5$ eV, the plasmons are not propagated via W1 and W2 as illustrated in Fig. 2.6d. Therefore, 32% of the bias power is equally coupled from W3 to W4 and W5 waveguides and transmits through W4 and W5. Accordingly, O1O0 is equal to 11.

Table 2.2 gives the normalized power at the outputs for four possible states. In each state, due to the assigned graphene chemical potential, the related outputs become ON. By choosing 0.5 eV for the graphene chemical potential, the bias light passes

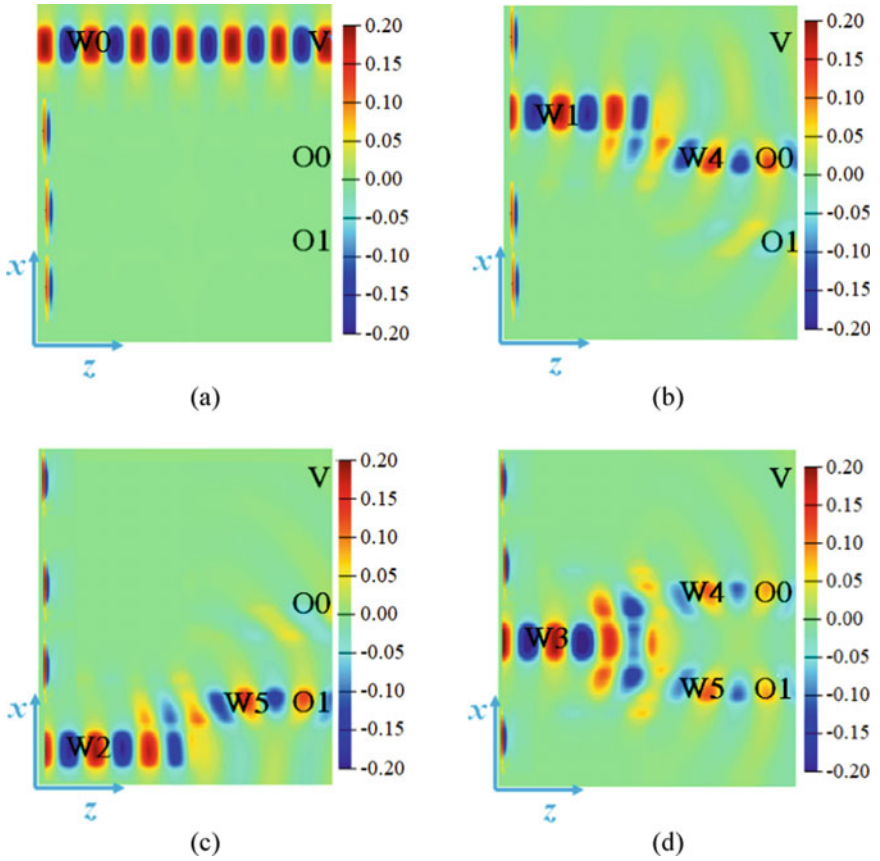

Fig. 2.6 The electric field distribution along the z-direction for working states **a** 00, **b** 01, **c** 10, and **d** 11 (Haddadan et al. 2022)

through the corresponding waveguides, while the incoming waves are not able to travel through the waveguides and do not reach the output ports for 0.1 eV. The extinction ratio of 17.33 dB for modes 2 and 3 is calculated in Eq. (2.8). Of course, the mentioned ratio is not calculated for modes 1 and 4 because it does not create a distinct logic.

As explained, the light transferring in the waveguide can be manipulated by applying a bias voltage to graphene. By employing the designed waveguide, an electro-optical priority structure is presented for encoding operation. As illustrated in Fig. 2.4b, the device consists of four input ports to income the optical signals, one activation port V, and two output ports O0 and O1 (Haddadan and Soroosh 2023). Two combiners with an angle of 30 degrees and a length of 0.5 μm have been used to travel light into the outputs O1 and O0. W0 transfers the waves toward V concerning μ0. W1 and W2 pass the terahertz waves to waveguides W4 and W5. Also, W3 transmits the incoming signals to W4 and W5. The transmission efficiency in W2

Table 2.2 The results corresponding states 1 to 4

State	Chemical potential (eV)					Output ports					
	$\mu 0$	$\mu 1$	$\mu 2$	$\mu 3$	$\mu 4$	Logic			Normalized power (%)		
						V	O1	O0	V	O1	O0
1	0.5	0.1	0.1	0.1	0.5	1	0	0	88	0	0
2	0.1	0.5	0.1	0.1	0.5	0	0	1	0	1.15	62.2
3	0.1	0.1	0.5	0.1	0.5	0	1	0	0	62.2	1.15
4	0.1	0.1	0.1	0.5	0.5	0	1	1	0	32	32

and W3 is adjusted by the chemical potentials of $\mu 2$ and $\mu 3$. The chemical potentials of $\mu 1$ and $\overline{\mu} 2$ control the light transmission through W1. Only two values of 0.1 eV and 0.5 eV are defined for the chemical potential. So, for $\mu 2 = 0.1$ eV, $\overline{\mu} 2$ is implied at 0.5 eV, and vice versa. The chemical potential of $\mu 4$ equals 0.5 eV for all working states. In this circumstance, the incoming waves from W1, W2, and W3 are able to transmit toward the output ports O0 and O1 through W4 and W5.

Among the five mentioned chemical potentials, $\mu 3$ and $\mu 0$ are considered the highest and the lowest priorities. According to the priority condition, if more than one input becomes logic 1 simultaneously, the binary code at output ports is related to the input with the higher priority. In this case, the lower priorities are known as the "don't care" states.

According to the priority feature, the structure works in 15 modes, which are simulated in the following. Working states are arranged and explained in four categories. Port V is defined as the activation port and distinct the state of $\mu 0 = 1$ (O1O0 = 00).

Case 1: By selecting 0.5 eV for the chemical potential $\mu 0$, the loss of the waveguide W0 becomes negligible; therefore, the incoming waves propagate toward port V (as demonstrated in Fig. 2.7a). For the chemical potential of 0.1 eV, the bias light is attenuated in waveguides W1, W2, and W3 so the light does not reach the outputs, and O1O0 = 00 is generated.

Case 2: With regard to $\mu 1 = \overline{\mu} 2 = 0.5$ eV, 88.34% of the incoming bias appears at O0 due to W1 and W4 as illustrated in Fig. 2.7b. Port O0 becomes logic 1 while a low portion of bias power appears in port O1. In this case, the binary code of O1O0 = 01 is provided.

Case 3: For $\mu 2 = 0.5$ eV, 88.34% of the optical bias appears at O1 due to W2 and W5 and O1 becomes ON as depicted in Fig. 2.7c. Applying $\overline{\mu} 2$ to W1 results in the don't care for $\mu 1 = 0.1$ eV and 0.5 eV. Therefore, the binary code 10 is considered to states of $\mu 1 = 0.1$ eV and 0.5 eV, $\mu 0 = 0.1$ eV, and 0.5 eV.

Case 4: When $\mu 3$ is adjusted to 0.5 eV, 43.11% of the terahertz waves appears at ports O0 and O1 due to waveguides W3, W4, and W5 (as illustrated in Fig. 2.7d), and the corresponding code 11 is obtained. In this case, the amounts of $\mu 0$, $\mu 1$, and $\mu 2$ are the don't cares, and the eight states for $\mu 0$, $\mu 1$, and $\mu 2$ can be simulated. The

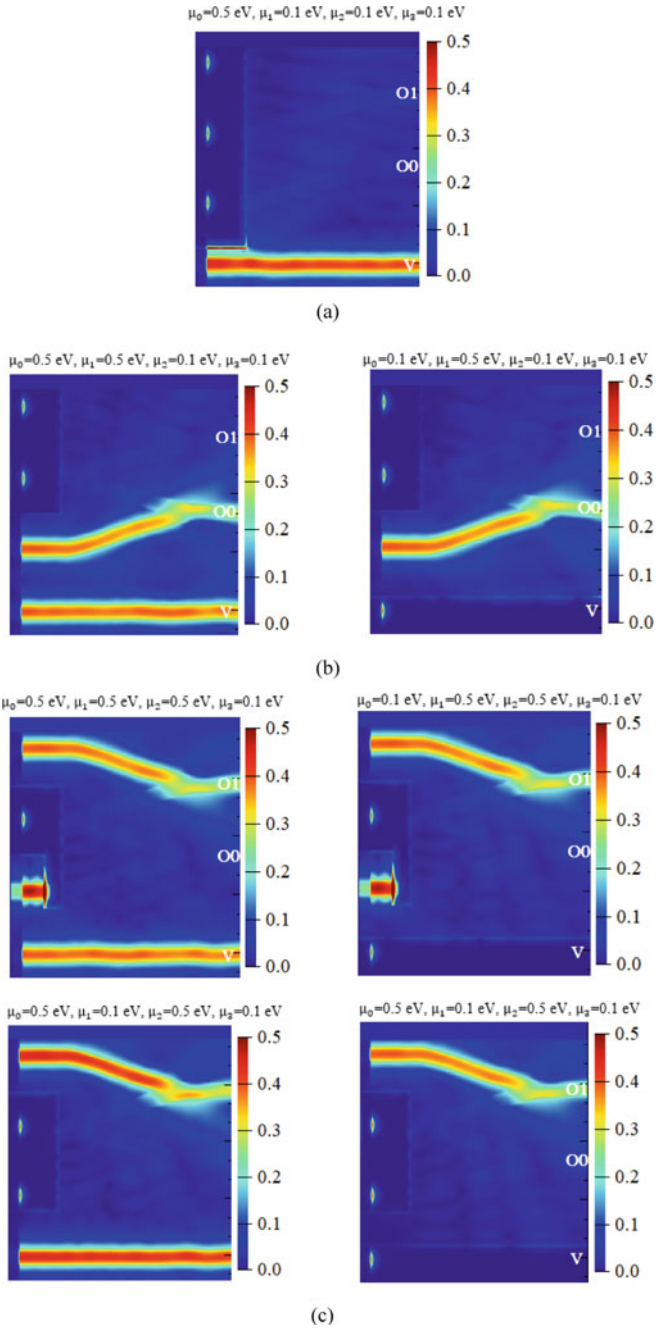

Fig. 2.7 The electric field distribution |E| for the binary codes **a** 00 for case 1 (including one state), **b** 01 for case 2 (including two states), **c** 10 for case 3 (including four states), and **d** 11 for case 4 (including eight states) (Haddadan and Soroosh 2023)

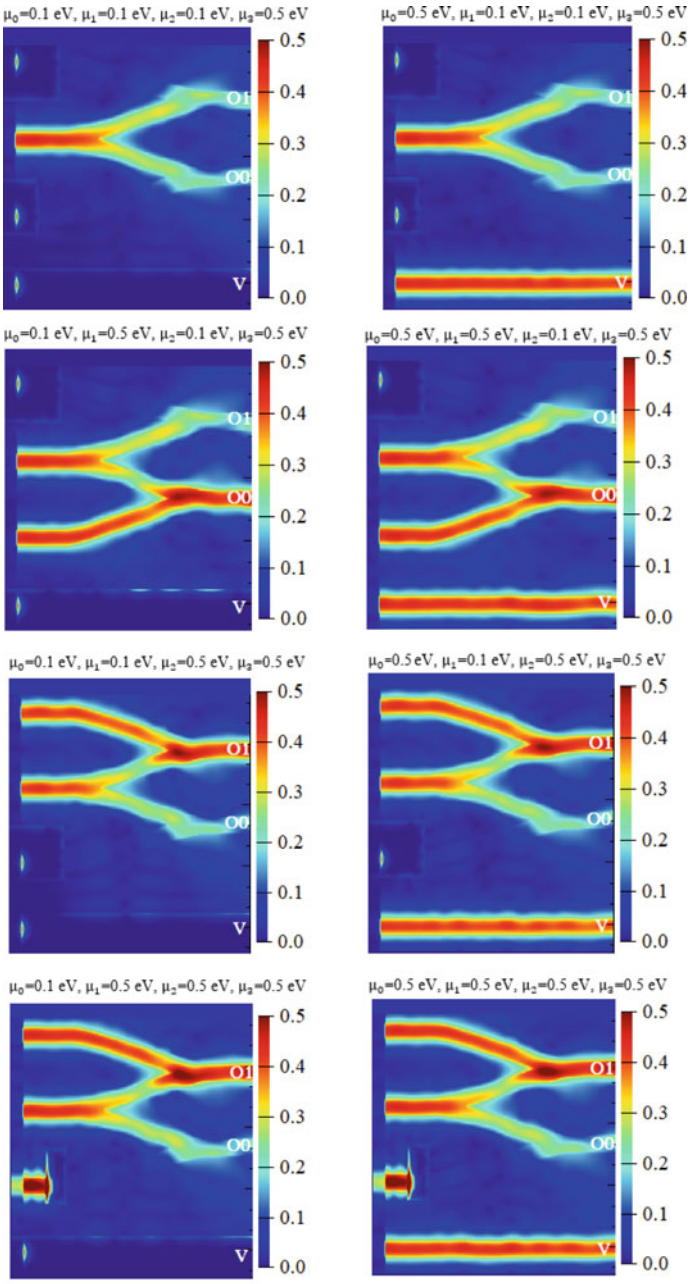

(d)

Fig. 2.7 (continued)

Table 2.3 The possible states calculated for powers at outputs

Case	Chemical potential (eV)					Output ports				Normalized power (%)	ER (dB)
	$\mu 0$	$\mu 1$	$\mu 2$	$\mu 3$	$\mu 4$	Logic		Normalized power (%)			
						O1	O0	O1	O0	V	
1	0.5	0.1	0.1	0.1	0.5	0	0	0	0	90	–
2	×	0.5	0.1	0.1		0	1	2.11	88.34	0 or 90	16.22
3	×	×	0.5	0.1		1	0	88.34	2.11	0 or 90	16.22
4	×	×	×	0.5		1	1	43.11	43.11	0 or 90	–

× don't care status

powers at ports O0 and O1 are presented for four cases in response to 15 states in Table 2.3.

Summary

The properties of graphene and its applications were briefly reviewed in this chapter. At first, the graphene waveguide that operates based on surface plasmon polariton guidance was introduced and investigated. One of the ways to control graphene is to adjust its chemical potential, which ultimately controls the transmission coefficient. Based on this, different tools have been presented, for example, the ON and OFF modes were investigated in a presented optical switch. Decoder and encoder are important components of digital circuits which were introduced and investigated based on surface plasmon polariton. Finally, an optical switch, which is one of the main components of digital circuits, was proposed as a practical method in devices with sub-wavelength dimensions.

References

Aliofkhazraei M, Ali N, Milne WI, Ozkan CS, Mitura S, Gervasoni JL (2016) Graphene science handbook, six-volume set. CRC Press

Anguluri SPK, Banda SR, Krishna SV, Swarnakar S, Kumar S (2021) The design, analysis, and simulation of an optimized all-optical AND gate using a Y-shaped plasmonic waveguide for high-speed computing devices. J Comput Electron 20(5):1892–1899

Azar MTH, Zavvari M, Zehforoosh Y, Mohammadi P (2020) Graphene plasmonic crystal: two-dimensional gate-controlled chemical potential for creation of photonic bandgap. Plasmonics 1–9

Bagheri F, Soroosh M (2022) Design and simulation of a compact graphene-based plasmonic D flip-flop. Opt Laser Technol 155:108436

Deacon R, Chuang K-C, Nicholas R, Novoselov K, Geim A (2007) Cyclotron resonance study of the electron and hole velocity in graphene monolayers. Phys Rev B 76(8):081406

Debu DT, Doha MH, Churchill HO, Herzog JB (2019) Gate voltage and doping effects on near-field radiation heat transfer in plasmonic heterogeneous pairs of graphene and black phosphorene. RSC Adv 9(50):29173–29181

Derakhshi M, Fathi D (2017) Terahertz plasmonic switch based on periodic array of graphene/silicon. Scientia Iranica 24(6):3452–3457

Farmani A, Miri M, Sheikhi MH (2017a) Analytical modeling of highly tunable giant lateral shift in total reflection of light beams from a graphene containing structure. Opt Commun 391:68–76

Farmani A, Zarifkar A, Sheikhi MH, Miri M (2017b) Design of a tunable graphene plasmonic-on-white graphene switch at infrared range. Superlattices Microstruct 112:404-414

Haddadan F, Soroosh M, Alaei-Sheini N (2022) Cross-talk reduction in a graphene-based ultra-compact plasmonic encoder using an Au nano-ridge on a silicon substrate. Appl Opt 61(11):3209–3217

Haddadan F, Soroosh M (2023) Design and simulation of a subwavelength 4-to-2 graphene-based plasmonic priority encoder. Opt Laser Technol 157:108680

Lee Y (2020) High-speed transmission control in gate-tunable metasurfaces using hybrid plasmonic waveguide mode. Adv Opt Mater 8(22):2001256

Lima AW, Sombra A (2017) Graphene-based Mach-Zehnder nanophotonics interferometer working as a splitter/switch and as a multiplexer/demultiplexer. Opt Quant Electron 49(11):1–17

Luo Z, Jia H, Lv L, Wang Q, Yan X (2020) Gate-tunable trion binding energy in monolayer MoS 2 with plasmonic superlattice. Nanoscale 12(34):17754–17761

Mansouri M, Mir A, Farmani A (2022) Design and numerical simulation of a MoS2 plasmonic pressure sensor based on surface plasmon resonance and Fabry-Perot interferometer. Plasmonics 17(6):2375–2384

Mansuri M, Mir A, Farmani A (2020) Numerical analysis of tunable nonlinear plasmonic router based on nanoscale ring resonators. Opt Quant Electron 52(10):1–15

Mansuri M, Mir A, Farmani A (2021) A tunable nonlinear plasmonic multiplexer/demultiplexer device based on nanoscale ring resonators. Photonic Netw Commun 1–10

Rezaei MH, Zarifkar A (2021) Realization of electro optical decoder, half adder, and half subtractor using graphene plasmonic waveguides. Opt Quant Electron 53:297

Rezaei MH, Boroumandi R, Zarifkar A, Farmani A (2019) Nano-scale multifunctional logic gate based on graphene/hexagonal boron nitride plasmonic waveguides. IET Optoelectron 14(1):37–43

Sathyadevaki R, Sundar DS, Raja AS (2016) Design of dual ring wavelength filters for WDM applications. Opt Commun 380:409–418

Sathyadevaki R, Sundar DS, Raja AS (2018) Photonic crystal 4×4 dynamic hitless routers for integrated photonic NoCs. Photon Netw Commun 36:82–95

Sharma S, Zafar R, Mahdieh MH, Singh G, Salim M (2020) High contrast ratio based all-optical OR and NOR plasmonic logic gate operating at E band, optical and wireless technologies. Lect Notes Electr Eng 546:325–332

Shvets G, Tsukerman I (2012) Plasmonics and plasmonic metamaterials: analysis and applications. World Scientific

Sivaranjani R, Sundar DS, Sridarshini T, Sitharthan R, Karthikeyan M, Raja AS, Carrasco MF (2020) Photonic crystal based all-optical half adder: a brief analysis. Laser Phys 30:116205

Skidin D (2018) Unimolecular logic gate with classical input by single gold atoms. ACS Nano 12(2):1139–1145

Sundar DS, Sathyadevaki R, Raja AS (2018b) High-efficiency filters for photonic integrated networks: a brief analysis. Laser Phys 28:116203

Sundar DS, Sathyadevaki R, Sridarshini T, Raja AS (2018a) Photonic crystal based routers for photonic integrated on chip networks: a brief analysis. Opt Quantum Electron 50:383

Szunerits S, Boukherroub R (2015) Introduction to plasmonics: advances and applications. CRC Press

Thirumaran S, Dhanabalan SS, Sannasi IG (2021) Design and analysis of photonic crystal ring resonator based 6 × 6 wavelength router for photonic integrated circuits. IET Optoelectron 15:40–47

Tucker RS (2006) The role of optics and electronics in high-capacity routers. J Lightwave Technol 24(12):4655–4673

Udupi A, Madhava SK (2021) Plasmonic coupler and multiplexer/demultiplexer based on nano-groove-arrays. Plasmonics 1–8

Xu Z et al (2018) Design of a tunable ultra-broadband terahertz absorber based on multiple layers of graphene ribbons. Nanoscale Res Lett 13(1):1–8

Xu P, Wan J, Zhang S, Duan Y, Chen B, Zhang S (2019) 2× 2 optofluidic switch chip with an air shutter. Appl Opt 58(17):4637–4641

Yildiz G, Bolton-Warberg M, Awaja F (2021) Graphene and graphene oxide for bio-sensing: General properties and the effects of graphene ripples. Acta Biomaterialia 131:62–79

Zhan D, Yan J, Lai L, Ni Z, Liu L, Shen Z (2012) Engineering the electronic structure of graphene. Adv Mater 24(30):4055–4069

Zhao K (2017) Surface charge tuneable fluorescent protein-based logic gates for smart delivery of nucleic acids. Chem Commun 53(82):11326–11329

Chapter 3
A Nonlinear Optical Benzil Single Crystal for Photonic Applications

Thirupathy Jayapalan

Abstract A nonlinear optical organic benzil single crystal with the size of 8 × 5 × 3 mm^3 was grown via using slow evaporation solution technique. UV–visible spectrum study was taken for the grown crystal to identifying the optical transmittance. The lower "cut-off" wavelength of benzil crystal is established to be 258 nm. An FTIR spectral analysis was utilized to find the existence of functional groups. Dielectric analysis of the grown crystal makes it known for the little dielectric loss, smaller defects, and enhanced optical properties, and hence it is apt for optical applications. Microhardness study reveals the crystal becomes a soft material category. Chemical etching analysis was confirmed the crystalline surface quality. "Differential Scanning Calorimetry" was made use of to study the thermal performance of the benzil crystal and is proposed for photonic application.

Keywords Organic crystal · Optical · Dielectric · Mechanical · Differential scanning calorimetry

Introduction

Achieving ultrahigh-speed information processing and all-optical logic computing based on micro- or nano-scale-integrated photonic devices is one of the development goals of integrated photonic technology. The development of integrated photonic technology is heavily reliant on microstructure photonic materials with the capacity to modulate photon propagation states. The emergence of photonic crystal raises a lot of hope for the accomplishment of these objectives. Photonic crystals, the semiconductor materials' counterpart in photonics, have distinct photonic band structures that include pass bands, stop bands, and defect states (Yablonovitch 1987; John 1987). As a result, photon behavior can be manipulated at will. Due to their distinct photonic

T. Jayapalan (✉)
Department of Physics, JCT College of Engineering and Technology, Pichanur, Tamil Nadu, Coimbatore 641 105, India
e-mail: thirupathyj1@gmail.com

© The Author(s), under exclusive license to Springer Nature Singapore Pte Ltd. 2023

S. S. Dhanabalan et al. (eds.), *Photonic Crystal and Its Applications for Next Generation Systems*, Springer Tracts in Electrical and Electronics Engineering,
https://doi.org/10.1007/978-981-99-2548-3_3

bandgap features, photonic crystals, also known as photonic bandgap materials, have been regarded as a crucial foundation for the creation of micro- or nano-scale-integrated photonic devices. Research into the physical characteristics and potential uses of photonic crystals has been intensive.

Brief Research History of Photonic Crystal

Yablonovitch and John first introduced the idea of a photonic crystal in 1987 (Yablonovitch 1987; John 1987). According to Yablonovitch, a three-dimensional periodic structure possesses an electromagnetic bandgap, and when the electronic band edge crosses the electromagnetic bandgap, spontaneous emission of atoms in the periodic microstructure can be strictly prohibited (Yablonovitch 1987). According to John, in a frequency range in specific disordered super-lattice microstructures with high enough dielectric contrast, photon localization could be substantial (John 1987). Photonic crystals offer several potential uses in the areas of optical computing, integrated photonic circuits, and ultrahigh-speed information processing because of their special capacity to control the propagation states of photons. Several scientists dedicate their time to the study of photonic crystals, which was inspired by the groundbreaking work of Yablonovitch and John. Physics and nano-photonics researchers are increasingly focusing on photonic crystals. The majority of research papers published between 1987 and the beginning of the 1990s (Yablonovitch and Gmitter 1989; Yablonovitch et al. 1991a, b; John and Akozbek 1993; Sievenpiper et al. 1996; Tarhan and Watson 1996; Anderson and Giapis 1996) concentrated on the mechanisms forming a photonic bandgap, the photonic band structures of different crystal lattice structures, the localized states of photons, and the wave-guiding characteristics of photonic crystals. In reality, nature contains very few examples of photonic crystals. To conduct research and develop practical applications, photonic crystals must be artificially created. As a result, it is essential that different methods for producing photonic crystals are devised in accordance with users' actual requirements. Later, in the 1990s, significant efforts were made to create various photonic crystal fabrication processes, control atoms' spontaneous emission utilizing the photonic bandgap effect, and investigate unique nonlinear optical phenomena of photonic crystals (Fan et al. 1997; Sievenpiper et al. 1998; Petrov et al. 1998; Berger 1998; Bertone et al. 1999). To create high-quality photonic crystals during this time, the self-assembly method and laser direct writing procedures using resin's two-photon absorption were developed (Vlasov et al. 1999; Sun et al. 1999). These two processes have recently grown to be crucial approaches for creating three-dimensional photonic crystals. Also, during this time, research was concentrated on the strategy for getting the entire photonic bandgap (Busch and John 1999; Li et al. 1998). The development of high-quality photonic crystals, research into physical processes in photonic crystals, and the creation of optical devices based on photonic crystals were the main focuses of photonic crystal research at the start of the twenty-first century (Joannopoulos 2001; Netti et al. 2001; Kopp et al. 2001; Notomi et al. 2001; Pokrovsky and Efros

2002; Chutinan et al. 2003). Using the vertical deposition method, laser direct writing method, and laser holographic lithography method, high-quality three-dimensional photonic crystals were produced (Vlasov et al. 2001; Campbell et al. 2000). During this time (Foteinopoulou et al. 2003; Cubukcu et al. 2003; Yanik et al. 2004), the novel phenomena of negative refraction effect and sluggish light effect in photonic crystals were also confirmed. The integrated photonic devices are based on photonic crystals, including a photonic crystal filter, photonic crystal optical switching, and photonic crystal laser (Jiang and Chen 2001; Mazurenko et al. 2001; Notomi et al. 2004). The creation of integrated photonic devices based on the novel physical processes and phenomena in photonic crystals has received a lot of interest recently (Chassagneux et al. 2009; Hu et al. 2008; Baker et al. 2010). Also, substantial research has been done on photonic metamaterials, surface plasmon polariton propagation and localization in metal photonic crystals, and the quantum electrodynamics of a high-quality photonic crystal microcavity coupled with quantum dots (Wang et al. 2008; Popa and Cummer 2008; Yu et al. 2008; Englund et al. 2010).

Fundamental Principles of Photonic Crystal

A type of microstructure photonic material having a spatially periodic distribution of dielectric constant is called a photonic crystal. The photonic bandgap effect, which results from the modulation of light by the spatially periodic distribution of dielectric constant, is what distinguishes photonic crystal from other materials. The frequency range where the density of photon states is zero in photonic band structures is designated as the photonic bandgap, also known as the stop band. The photonic crystal will totally reflect an incident electromagnetic wave with a resonance frequency dipping into the photonic bandgap. The cause is the absence of equivalent Bloch modes that can travel through the photonic crystal (Yablonovitch 1987; John 1987). A lattice defect will sustain an electromagnetic wave mode with a specific resonant frequency when it is added to a flawless photonic crystal structure. Defect states will consequently manifest in the photonic bandgap. The defect site will contain the defect mode's electric-field distribution (Guven and Ozbay 2005). High-quality microcavities can be created in photonic crystals by utilizing the lattice defect. The density of photon states in the defect mode's center is significantly higher than it is in the stop band. The interactions between light and matter are significantly improved in photonic crystal microcavities due to the strong photon confinement effect. As a result, photonic crystal microcavities allow for the observation of novel nonlinear optical phenomena as well as the potential for thresholdless laser emission in high-quality photonic crystal microcavity structures (Fatih et al. 2003; Colombelli et al. 2003). Based on the Bloch theory and the electromagnetic theories of Maxwell and Bloch, it is possible to calculate the propagation and confinement of light in a photonic crystal. The finite-different time-domain (FDTD) method, the plane-wave expansion method, the transfer matrix method, and others have all been developed to examine the photonic band structure, the photon confinement effect, and nonlinear

optical effects of photonic crystals (Okano and Noda 2004; Hsue et al. 2005; Li and Ho 2003). With the aid of these numerical calculation techniques, individuals may better comprehend the special characteristics of photonic crystals and create ideal photonic crystal structures for the production of integrated photonic devices. For the study and use of photonic crystals, a detailed grasp of their underlying concepts is very beneficial.

Fabrication of Photonic Crystals

The conventional approaches for creating one-dimensional photonic crystals, such as molecular beam epitaxy (MBE), chemical vapor deposition (CVD), and pulsed laser deposition (PLD), are based on pricey film growth processes. These procedures need a lot of time and complexity. One-dimensional photonic crystals may now be created using a variety of practical techniques, including the spin coating approach, the sol–gel method, and others (Komikado et al. 2006). This allows for the fast fabrication of one-dimensional photonic crystals using both organic and inorganic polymer materials. Two-dimensional photonic crystal manufacturing is more difficult than one-dimensional photonic crystal manufacturing. High-quality two-dimensional semiconductor photonic crystals can be created using the same micro-fabrication technology used in the microelectronics sector (Courjal et al. 2010). It is also possible to create two-dimensional organic photonic crystals and photonic quasi crystals using the laser holography lithography technique (Liang et al. 2006). The laser holography lithography technique can be used to create two-dimensional organic photonic crystals with a variety of intricate lattice configurations. A long-term objective and hope is still to produce large-size and single-crystal samples of three-dimensional photonic crystals. To obtain large samples of three-dimensional photonic crystals made of silicon dioxide or polystyrene nanoparticles, one can use the conventional self-assembling approach. Unfortunately, the three-dimensional colloidal photonic crystal has numerous structural flaws (Lee et al. 2004). Current developments in the fabrication of high-quality three-dimensional photonic crystals with different lattice configurations include the direct laser writing approach and the laser holography lithography method (Xia et al. 2008). To date, it has proven to be extremely difficult to realize large-scale single-crystal photonic crystals with the full photonic bandgap. In the study and practical use of photonic crystals, fabrication techniques are crucial. High-quality photonic crystal sample fabrication has seen significant advancements.

Photonic Crystal Optical Devices

Building and realizing micro- or nano-scale-integrated photonic devices is the main use of photonic crystals. Along with the significant progress made in the creation of high-quality photonic crystal samples in recent years, a number of integrated photonic

devices based on photonic crystals have been realized, including photonic crystal all-optical switching, photonic crystal lasers, photonic crystal sensors, and more (Chassagneux et al. 2009). Systems for optical computing and extremely fast data processing must have all-optical switching and logic devices. Scalora et al. suggested the idea of photonic crystal all-optical switching in 1994 (Scalora et al. 1994). The development of photonic crystal all-optical switching research was, however, relatively slow due to the low nonlinear optical coefficient of conventional materials. The nonlinear material's restriction was gradually overcome until recently. Recently, reports of ultrafast, ultralow-power photonic crystal switching have been made (Hu et al. 2008). This has significantly aided in the advancement of photonic crystal all-optical switching research. The photonic bandgap effect and the potent photon confinement effect of the photonic crystal microcavity can also be used to create logic circuits. As to date, there are few experimental reports of photonic crystal logic devices. In the creation of integrated photonic circuits and optical communication systems, micro/nano-scale photonic crystal lasers are crucial components. Low-threshold laser emission is possible when the gain medium is incorporated into the photonic crystal because of the sharp shift in the density of states of photons in photonic band edges and the potent photon confinement effect of the photonic crystal microcavity. Using the use of micro-fabrication etching technique, it has recently been able to create photonic crystal microcavities with an ultrahigh-quality factor of 106 orders (Deotare et al. 2009). Recently, low-threshold photonic crystal lasers were found (Chassagneux et al. 2009). Applications for photonic crystal filters in wavelength division multiplex (WDM) systems are quite promising. The photonic crystal microcavity mode has the potential to generate the filter's optical channel. Moreover, it is possible to create multichannel and narrowband filters using the coupling of several similar photonic crystal microcavities (Kohli et al. 2006). The filtering channel can be rapidly tuned when a nonlinear optical material is used to build photonic crystal filters (Schuller et al. 2005). This enables more adaptable uses for photonic crystal filters. The photonic crystal sensor is a type of micro/nano-scale-integrated photonic device that is extensively employed in the detection of the environment and biological processes. On the basis of high-quality factor photonic crystal microcavity structures, a variety of photonic crystal sensors, including fluid sensors, gas sensors, and biochemical sensors, can be achieved (Yang and Jiang 2011). On photonic crystal sensors, the real-time, labelless, and rapid detection is possible.

Photonic Benzil Single Crystal

Ever since nonlinear optical (NLO) materials found their way to numerous fields, right from science to engineering, its influence is very much being felt in the areas of communication, laser-based imaging, counter-measure systems, and remote sensing due to their ability to accomplish frequency conversion. The requirements of much improved quality NLO materials continue to be on the demand as they consistently

pave the way to open the overflow gates of emerging cutting-edge technology of today. Low-cost materials possessing comparatively superior efficiency and greater average power are at the doorstep of widespread acceptance as they fulfill the needed requirements of second harmonic generation and optical parametric amplification (Meredith and Symp 1983; Marder et al. 1991). Photonic crystals have huge potential for use as "laser-driven accelerator structures". Photonic crystals are a structure in permittivity episodic in many of its sizes. Though illustrated in Joannopoulos et al. (1995), optical forms in a photonic crystal as of bands, currently as electronic conditions do in crystalline solids. Correspondingly, a photonic crystal as well reveals single or additional photonic bandgaps, through frequencies within the gap are not competent toward disseminate in the crystal. A limited mode has been attained by establishing an imperfection keen on a photonic "crystal lattice". Because frequencies in the bandgap are not allowed to circulate into the crystal, it is restricted to the fault. Consequently, a linear imperfection acts as a waveguide. Elevated accelerating gradients are probable as photonic crystal able to be composed completely of dielectric materials and advantage as of their elevated breakdown threshold (Stuart et al. 1996). Photonic crystal waveguides also enable the detention of a form travelling at the speed of light into vacuum. An additional significant advantage of photonic crystal acts as accelerators is that merely frequencies contained by a bandgap be restricted. Generally, superior order forms can be agitated with the electron beam, which escape throughout the lattice. These benefits have motivated work on metallic photonic bandgaps structure on RF frequencies (Smith et al. 1994; Shapiro et al. 2001). Additionally, accelerating forms have been originated in a photonic bandgap fiber structures (Lin 2001). Generally speaking, a photonic crystal structure whose electromagnetic factors are specifically periodic, anywhere the length of every period is on the similar dimension scale as the operational wavelength of the structure (Cowan 2003). To develop the large efficiency of the accelerator, some residual laser power at the last part of the section is likely recycled for being utilized by the subsequent bunch train, a method explained in detail in Na et al. (2005). In the recent past, new complexes have been tried and successfully synthesized by mixing amino acids with organic or inorganic compounds with various proportions and combinations (Mallik and Kar 2005; Kandasamy et al. 2007) so as to obtain materials of much improved chemical stability, laser damage threshold (LDT), optical properties, and thermal properties. Mainly the benzil derivatives exhibit nonlinear optical properties individually as they have two phenyl rings as well as two carboxylic groups (Petrova et al. 2006). Most of the benzil family of crystals known so far crystallizes in noncentrosymmetric space group which is an essential embodiment for crystals to be accommodated in the field of nonlinear optics. Brown and Sadanaga had carried out single-crystal XRD analysis of benzil so as to solve the structure of the crystal (Brown and Sadanaga 1965) and Suthan et al. already reported the crystal growth with a few characterizations of benzil single crystal (Suthan et al. 2011). Nonlinear, optical, and piezoelectric behavior of benzil single crystal have been investigated and confirmed by Yadav et al. (2014). Unidirectional growth of benzil crystal by employing SR method was elucidated by Rajalakshmi et al. (2012). For the current work, benzil crystal has been grown by utilizing SEST by room temperature. The

grown crystal of benzil was utilized to single XRD study, powder XRD analysis, ultraviolet–visible–NIR, FTIR, dielectric studies, hardness, etching, photoacoustic spectroscopy, and laser damage threshold so that its effectiveness of applications as an NLO material can be asserted. Organic single crystals have acquainted themselves with a vital role for manufacturing a device and electronic components as a result of their better optical and electrical properties which are determined by their molecular configurations. Good noncentrosymmetric organic crystals of superior NLO properties than that of inorganic crystals have been already established. In the reported research papers, it has been found that benzil crystal possesses excellent dielectric, optical properties and also the SHG efficiency of benzil single crystal is known to be 7.5 times larger than that of standard KDP crystal (Rajalakshmi et al. 2012). To our knowledge, no one has so far reported photoacoustic analysis of benzil which is essential for laser, optical, and photonic applications. In the present work, we have reported benzil crystal with good optical and thermal properties. Hence, it is found to bet suitable for NLO and photonic applications.

Experimental Procedure

Growth of Benzil Crystal

By using the slow evaporation solution technique (SEST), single crystals of benzil were produced after being fully dissolved in ethanol and stirring vigorously for around 6 h with the aid of a magnetic stirrer. After obtaining the saturated solution, it was filtered using fine-quality filter paper (Whatman), and the filtrate was then transferred to a fresh beaker. The beaker was then covered with aluminium foil that had been punched with tiny holes, and it was set on a table set apart in a spotless environment for gradual evaporation to take place. A constant temperature bath was used to maintain the beaker's temperature at 30 °C throughout the whole experiment. Optically good quality parrot green color single crystals of size $8 \times 5 \times 3$ mm^3 were collected after a period of 18 days as depicted in Fig. 3.1.

Results and Discussion

UV–Vis Spectral Studies

As benzil single crystal has optical applications, the transmittance spectrum is imperative to be studied so that it was recorded for the wavelength ranging from 190 to 1100 nm using Perkin Elmer Lambda 35 double beam UV–Visible–NIR spectrophotometer and the observed spectrum is shown in Fig. 3.2a. For the study, a single crystal with a high degree of optical quality and a thickness of roughly 2 mm was chosen.

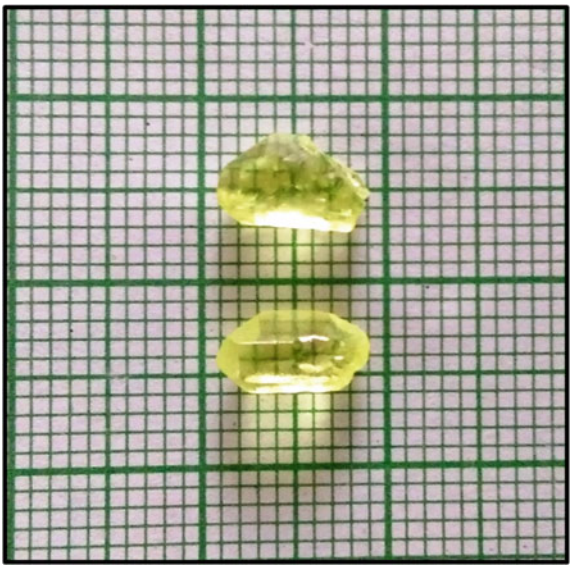

Fig. 3.1 A picture of a growing benzil crystal taken using the SEST method

Nonlinear behavior crystals should have the capacity to withstand high power intensities without getting any type of damage or breakdown (Rajalakshmi et al. 2012). It is very much essential for crystals to possess high transparency for a wide range of wavelength as they can be used for optical device fabrication which in turn imposes a huge demand for crystals of this kind (Sankaranarayanan and Ramasamy 2005). The formed crystal's UV lower cut-off wavelength is 258 nm. The transmittance spectrum was used to calculate the crystal's optical absorption coefficient (α) using the relation

$$\alpha = \frac{1}{t} \log\left(\frac{1}{T}\right) \tag{3.1}$$

where T is the transmittance and t is the crystal's thickness. Using Tauc's relation, the direct optical bandgap was determined as

$$\alpha = \frac{A(h\upsilon - E_g)^{1/2}}{h\upsilon} \tag{3.2}$$

If the bandgap energy $\left(E_g\right)$ A is constant, Planck's constant (h) governs the frequency (υ) of light.

The plot of $(\alpha h\upsilon)^2$ versus hυ is shown in Fig. 3.2b, and the value of Eg is approximated using extrapolation from the graph's linear region. The value of E_g for the crystal was identified to be 2.675 eV.

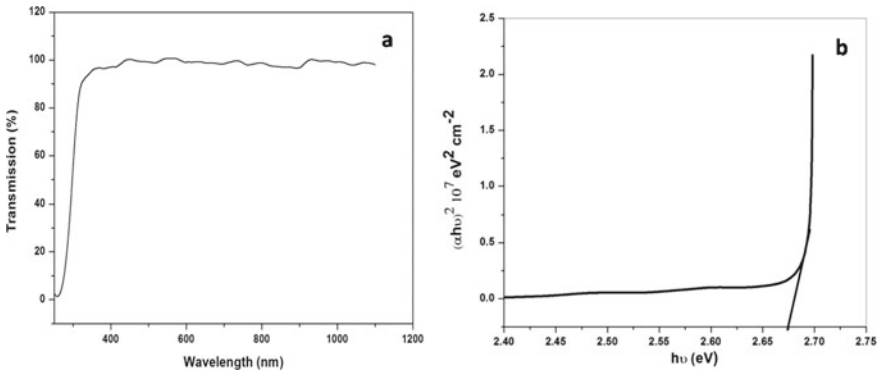

Fig. 3.2 **a** Transmittance spectrum in the UV–vis–NIR **b** Plot of $(\alpha h\upsilon)^2$ versus photon energy of the formed benzil crystal

FTIR Spectral Analysis

The grown benzil crystal was characterized to spectral analysis which was carried out using Perkin Elmer FTIR spectrometer via adapting KBr pellet method so as to obtain FTIR spectrum in the range between 400 and 4000 cm^{-1} that enabled to realize the presence of possible functional groups in the crystal. The recorded FTIR spectrum of benzil is depicted in Fig. 3.3. A peak appears at 1666 cm^{-1} that indicates the occurrence of C = O symmetric stretching. The sharp and quite intense band identified at 1169 cm^{-1} is allocated to N phenyl–C stretch in aromatic ketones (Nakamoto 1978; Socrates 2001). Aromatic C–H symmetric stretching is found at 3647 cm^{-1}. The peak at 2614 cm^{-1} arises due to C–H symmetric stretching. The band corresponding to C–O stretching is being found at 1489 cm^{-1} which is due to the aromatic ring stretching.

Dielectric Studies

By employing an impedance meter PSM1735 and a unique parallel plate capacitor approach, measurements of dielectric loss and dielectric constant for benzil crystal have been examined at a range of temperatures between 40° C and 60° C in the frequency range (1 Hz–1 MHz). A high-quality and well-shaped crystal was chosen, and the reverse faces were covered with silver paste to ensure the creation of ohmic contacts. This provided the growing crystal with a layer of good conducting surface. The dielectric constant versus frequency for various temperatures is shown in Fig. 3.4a, and the dielectric constant versus log F for various temperatures is shown in Fig. 3.4b.

Figure 3.4a, b implies that as and when frequency rises, the dielectric constant decreases and reaches to the value of saturation in the upper frequency region.

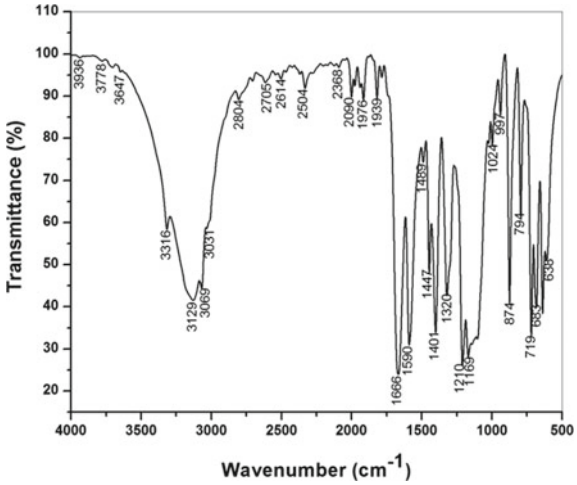

Fig. 3.3 FT–IR spectrum of benzil crystal

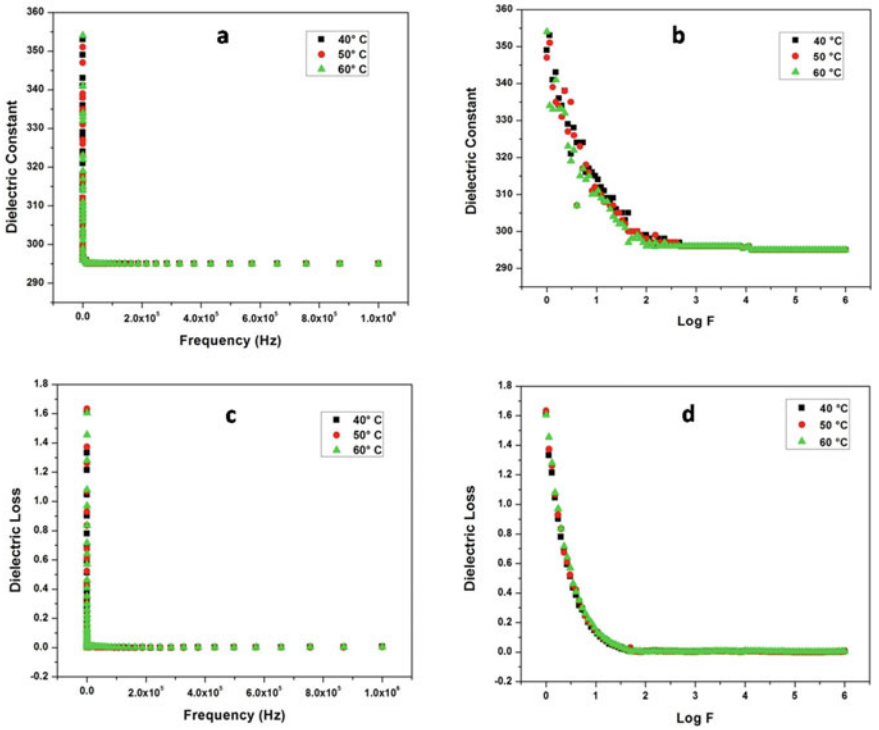

Fig. 3.4 **a** Dielectric constant of benzil crystal for different temperatures **b** Dielectric constant versus Log F of benzil crystal for different temperatures **c** Dielectric Loss of benzil single crystal for different temperatures **d** Dielectric Loss versus Log F of benzil single crystal for different temperatures

The presence of all known polarizations, including ionic, electronic, space charge, and orientation polarizations, results in an enhanced dielectric constant in the low-frequency domain. Space charge polarization is strongly influenced by the sample's quality and purity, which has a significant impact in high-temperature areas but has less impact in the low-frequency range. As the electric field exceeds a particular high frequency, the dielectric constant begins to steadily decrease as long as the typical behavior of dielectrics is taken into account. At this point, the dipoles no longer follow the alternating field. Crystals with high dielectric constant experience power dissipation, but materials with a lower dielectric constant suffer less because they have fewer dipoles per unit volume. As a result, compared to materials with greater values of the dielectric constant, these materials lose less power. Hence, it is very much evident that the grown benzil crystal can be utilized for high-speed electro-optic modulations (Rao and Smakula 1965). The changes occurring for dielectric loss versus frequency and dielectric loss versus Log F for dissimilar temperatures of benzil crystal are depicted in Fig. 3.4c, d. The characteristic nature of the crystal possessing low dielectric loss at the region of elevated frequency proposes that it has superior optical properties by smaller defects and these qualities are very much essential for NLO materials for their versatile applications (Rao and Samakula 1965).

Hardness Study

Microhardness study was analyzed by making use of Vickers micro-hardness tester supplemented by a diamond indenter. A 2-mm-thick, well-polished benzil crystal was kept on the Vickers micro-hardness tester's stage. With a consistent indentation period of every 10 s, the diagonal length of the indentation for various applied loads in grams was computed. Hardness of the materials is usually measured by the resistance that is rendered to local deformation (Mott 1956). Vickers micro-hardness number (H_v) was estimated by the relation (Mukerji and Kar 1999).

$$H_v = \frac{1.8544P}{d^2} \text{kg/mm}^2 \tag{3.3}$$

where d is the diagonal length of the impression expressed in mm and P is the applied load in Kg. Figure 3.5a shows the graph between the applied load (P) and the hardness number (Hv). The harness value is on the incremental effect as the load is increased in stages of 10 g, as can be seen from the plot. Breaks began to form as the weight was raised over 50 g due to the release of localized interior stress caused by indentation. It is well known that the hardness value increases with increasing load as a result of the impacts of reverse indentation size (RISE). Fig. 3.5b depicts the plot of log P vs log d as a straight line, which is in good agreement with Meyer's law (Mayer 1908)

$$P = Ad^n \tag{3.4}$$

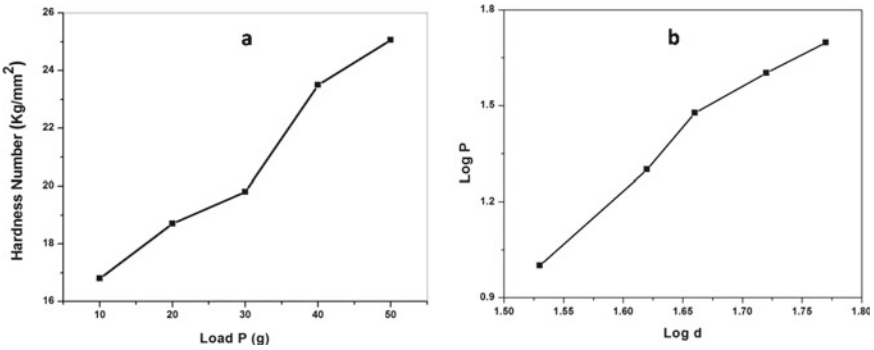

Fig. 3.5 **a** Variant of hardness versus functional load for benzil single crystal **b** Plot of log d versus log p for benzil single crystal

where A is denoted by the material constant and n is Meyer's index. The value (n) is provided by the graph slope, and it is found to be 3. In accordance with Onitsch (1947) and Hanneman (1941), n must lie between 1 and 1.6 for a material to be hard and for the values above 1.6, it is to be softer one. Hence, benzil crystal is considered to be the type of soft material.

Etching Studies

Etching is the exacting dissolution made on a crystal with the effect of an etchant so that it discloses the lattice defects and crystal symmetry (Sangwal 1987). The surface patterns, like hillocks, step patterns, spirals, etc., give us important details on the crystal's growth process and mechanism. In this instance, water was used as an etchant to erode the crystal's surface. The generated benzil crystal's etching analyses were investigated using a polarized high-resolution optical microscope. After being polished, the surface of the benzil crystal was etched for 5 and 10 s at room temperature using an etchant. The effect was then examined using an optical microscope and the reflection technique after it had been dried with a filter sheet. The typical etch patterns seen on benzil crystal are depicted in Fig. 3.6a, b. On the formed crystal, the etching primarily reveals pyramidal shapes, and it is evident that as the etching time is increased, so does the size of the etch pit. The crystal's etched surface has a consistent pit pattern. The arrangement of inclusions in the crystals is specifically impacted by the development of dislocations. The generated benzil crystals etch patterns, which represent it, confirm its crystalline quality.

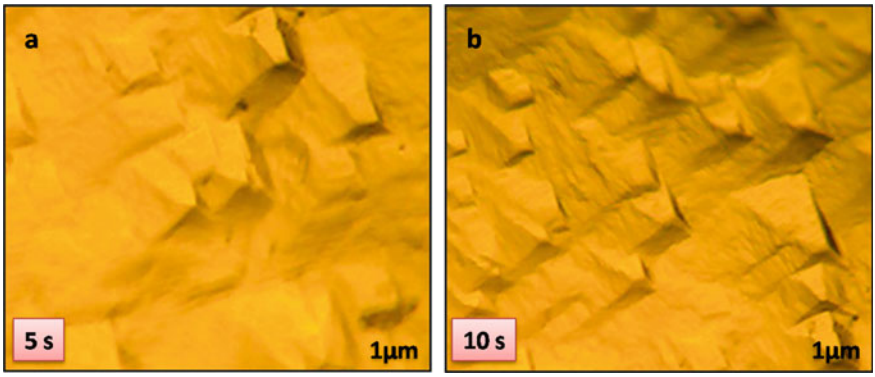

Fig. 3.6 **a** Etch pit pattern of benzil crystal (5 s) **b** Etch pits of benzil crystal (10 s)

Differential Scanning Calorimetry (DSC) Thermal Studies

The METTLER-TOLEDO DSC thermal analyzer was used to record the benzil grown crystal DSC data over the temperature ranges of 30 °C–160 °C. Depending on the type of material, DSC provides an account of information about a compound disintegrating farther than a specified degree of temperature. Figure 3.7 shows the grown crystal DSC plot, which was created using data collected at a heating rate of 10 °C/min. From Fig. 3.7, it is seen there is a sharp endothermic peak on the increase and the maximum peak arises at 97 °C owing to the sample's melting procedure in which it absorbs heat rapidly in order to melt so that benzil melting point is documented as 97 °C. The maximum peak value and height of the peak are persuaded by the weight of the sample and perhaps by encapsulation procedure for the reason that with the poor thermal contact, the result would be a broader peak with inferior peak height (Hatakeyama and Zhenhai 1998; Gabbot 2008). Analyzing the DSC plotted melting curve's structure allows one to assess a sample's purity. If there are many impurities in a sample, the melting point will be lower and the melting range will be wider. The sample's purity and crystallinity are therefore shown by the sample's higher melting point and sharper DSC melting peak. The intensity of the laser power employed has a significant impact on an NLO crystal's efficiency conversion for harmonic production. Hence, the usefulness for appropriate devices depends not only on its linear and NLO properties but also mainly on its capability to withstand the high power lasers (Glass and Guenther 1973). Therefore, the benzil crystal can be helpful for optical and photonic applications up to 97 °C.

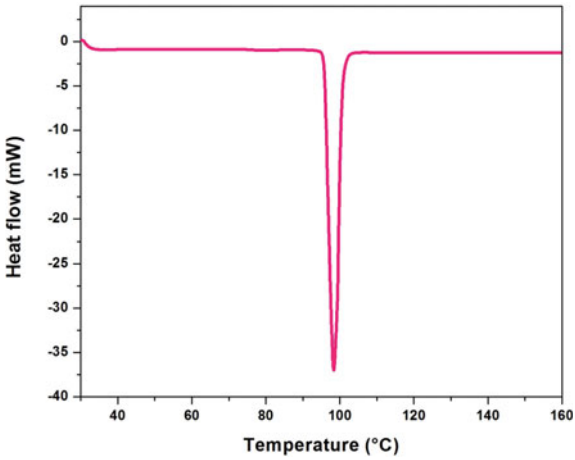

Fig. 3.7 DSC thermal analysis of benzil powder sample

Conclusion

Single crystal of benzil with the dimensions of $8 \times 5 \times 3$ mm^3 was grown via SEST method. From UV analysis, the cut-off wavelength of benzil crystal is experiential at 258 nm and the bandgap value (E_g) was identified to be 2.675 eV. The FTIR spectrum proved the occurrence of characteristic functional groups of the grown crystal. The dielectric studies make the materials have a less amount of power loss while comparing with the material of higher value of dielectric constant. It is so abundantly clear that the produced benzil crystal can be used for fast electro-optic modulations. A mechanical analysis shows that benzil crystals come into the category of soft materials. Major pyramidal formations can be seen in the formed benzil crystal, and it has been noticed that when the etching time is extended, the size of the etch pit also increases, as well as patterns that validate the crystal quality. Differential Scanning Calorimetry analysis shows that the grown benzil crystal is stable at 97 °C. From the different analysis results, the grown benzil single crystal has been utilized for selected applications like nonlinear optical and photonics.

References

Anderson CM, Giapis KP (1996) Phys Rev Lett 77:2949–2952
Baker SE, Pocha MD, Chang ASP, Sirbuly DJ, Cabrini S, Dhuey SD, Bond TC, Letant SE (2010) Appl Phys Lett 97:113701
Berger V (1998) Phys Rev Lett 81:4136–4139
Bertone JF, Jiang P, Hwang KS, Mittleman DM, Colvin VL (1999) Phys Rev Lett 83:300–303
Brown CJ, Sadanaga R (1965) Acta Cryst 18:158–167
Busch K, John S (1999) Phys Rev Lett 83:967–970
Campbell M, Sharp DN, Harrison MT, Denning RG, Turberfield AJ (2000) Nature 404:53–56

Chassagneux Y, Colombelli R, Maineult W, Barbieri S, Beere HE, Ritchie DA, Khanna SP, Linfield EH, Davies AG (2009) Nature 457:174–178
Chutinan A, John S, Toader O (2003) Phys Rev Lett 90:123901
Colombelli R, Srinivasan K, Troccoli M, Painter O, Gmachl CF, Tennant DM, Sergent AM, Sivco DL, Cho AY, Capasso F (2003) Science 302:1374–1377
Courjal N, Benchabane S, Dahdah J, Ulliac G, Gruson Y, Laude V (2010) Appl Phys Lett 96:131103
Cowan BM (2003) Phys Rev ST Accel Beams 6:101301
Cubukcu E, Aydin K, Ozbay E (2003) Phys Rev Lett 91:207401
Deotare PB, Mccutcheon MW, Frank IW, Khan M, Loncar M (2009) Appl Phys Lett 94:121106
Englund D, Majumdar A, Faraon A, Toishi M, Stoltz N, Petroff P, Vuckovic J (2010) Phys Rev Lett 104:073904
Fan S, Villeneuve PR, Joannopoulos JD, Schubert EF (1997) Phys Rev Lett 78:3294–3297
Fatih M, Fan S, Soljacic M (2003) Appl Phys Rev 83:2739–2741
Foteinopoulou S, Economou EN, Soukoulis CM (2003) Phys Rev Lett 90:107402
Gabbot P (2008) Principles and applications of thermal analysis. Blackwell, U.K., pp 1–50
Glass AJ, Guenther AH (1973) Appl Opt 12:637–649
Guven K, Ozbay E (2005) Phys Rev B 71:085108
Hanneman M (1941) Metall Manchu 23:135
Hatakeyama T, Zhenhai L (1998) Handbook of thermal analysis. Wiley, Chichester
Hsue YC, Freeman AJ, Gu BY (2005) Phys Rev B 72:195118
Hu XY, Jiang P, Ding CY, Yang H, Gong QH (2008) Nat Photon 2:185–189
Jiang W, Chen RT (2001) Phys Rev Lett 91:213901
Joannopoulos JD (2001) Nature 414:257–258
Joannopoulos JD, Meade RD, Winn JN (1995) Photonic crystals: molding the flow of light. Princeton University Press, Princeton NJ
John S (1987) Phys Rev Lett 58:2486–2489
John S, Akozbek N (1993) Phys Rev Lett 71:1168–1171
Kandasamy A, Siddeswaran R, Murugakoothan P, Kumar SP, Mohan R (2007) Cryst Growth Des 7:183–186
Kohli P, Christensen C, Muehlmeier J, Biswas R, Tuttle G, Ho KM (2006) Appl Phys Lett 89:231103
Komikado T, Yoshida S, Umegaki S (2006) Appl Phys Lett 89:061123
Kopp VI, Genack AZ, Zhang ZQ (2001) Phys Rev Lett 86:1753–1756
Lee W, Chan A, Bevan MA, Lewis JA, Langmuir PVB (2004) 20:5262–5270
Li ZY, Ho KM (2003) Phys Rev B 68:245117
Li ZY, Gu BY, Yang GZ (1998) Phys Rev Lett 81:2574–2577
Liang GQ, Mao WD, Pu YY, Zou H, Wang HZ, Zeng ZH (2006) Appl Phys Lett 89:041902
Lin XE (2001) Phys Rev ST Accel Beams 4:051301
Mallik T, Kar T (2005) Cryst Res Technol 40:778–782
Marder TB, Lesley G, Yuan Z, Fyfe HB, Chow P, Stringer G, Jobe IR, Taylor NJ, Williams ID, Kurtz SK (1991) ACS symposium proceedings. American Chemical Society, vol 455. Washington, DC, pp 605–615
Mayer E (1908) Z Phys 9:66–74
Mazurenko DA, Kerst R, Dijkhuis JI, Akimov AV, Golubev VG, Kurdyukov DA, Pevtsov AB, Selkin AV (2001) Phys Rev Lett 91:213903
Meredith GR (1983) ACS symposium series. American Chemical Society, vol 233. Washington, DC, pp 27–56
Mott BW (1956) Microindentation hardness testing. Butterworths, London
Mukerji S, Kar T (1999) Cryst Res Tech 34:1323–1328
Y. C. N. Na, R. H. Siemann, and R. L. Byer Phys. Rev. ST Accel. Beams 8, 031301 (2005).
Nakamoto K (1978) Infrared and Raman spectra of Inorganic and Coordination compounds. Wiley, New York
Netti MC, Harris A, Baumberg JJ, Whittaker DM, Charlton MBD, Zoorob ME, Parker GJ (2001) Phys Rev Lett 86:1526–1529

Notomi M, Yamada K, Shinya A, Takahashi J, Takahashi C, Yokohama I (2001) Phys Rev Lett 87:253902
Notomi M, Suzuki H, Tamamura T, Edagawa K (2004) Phys Rev Lett 92:123906
Okano M, Noda S (2004) Phys Rev B 70:125105
Onitsch EM (1947) Mikroscopia 2:131–151
Petrov EP, Bogomolo VN, Kalosha II, Gaponenko SV (1998) Phys Rev Lett 81:77–80
Petrova RI, Patel R, Swift JA (2006) Cryst Growth Des 6:2709–2715
Pokrovsky AL, Efros AL (2002) Phys Rev Lett 89:093901
Popa BI, Cummer SA (2008) Phys Rev Lett 100:207401
Rajalakshmi M, Shyiu TS, Indirajith K, Gopalakrishnan R (2012) Spectra Chem Acta A 86:27–32
Rao KV, Samakula A (1965) J Appl Phys 36:2031–2038
Rao KV, Smakula A (1965) J Appl Phys 36:3953
Sangwal K (1987) Etching of crystals. North Holland Physics Publishing, Amsterdam, The Netherlands
Sankaranarayanan K, Ramasamy P (2005) J Cryst Growth 280:467–473
Scalora M, Dowling JP, Bowden CM, Bloemer MJ (1994) Appl Phys Lett 73:1368–1371
Schuller C, Reithmaier JP, Zimmermann J, Kamp M, Forchel A, Anand S (2005) Appl Phys Lett 87:121105
Shapiro MA, Brown WJ, Mastovsky I, Sirigiri JR, Temkin RJ (2001) Phys Rev ST Accel Beams 4:042001
Sievenpiper DF, Sickmiller ME, Yablonovitch E (1996) Phys Rev Lett 76:2480–2483
Sievenpiper DF, Yablonovitch E, Fan S, Villeneuve PR, Joannopoulos JD, Schubert EF (1998) Phys Rev Lett 80:2829–2832
Smith DR, Shultz S, Kroll N, Sigalas M, Ho KM, Soukoulis CM (1994) Appl Phys Lett 65:645–647
Socrates G (2001) Infrared and Raman characteristic group frequencies. John Wiley, New York
Stuart BC, Feit MD, Herman S, Rubenchik AM, Shore BW, Perry MD (1996) J Opt Soc Am B 13:459–468
Sun HB, Matsuo S, Misawa H (1999) Appl Phys Lett 74:786–788
Suthan T, Dhanaraj PV, Rajesh NP, Mahadevan CK, Bhagavannarayana G (2011) Cryst Eng Commun 13:4018–4024
Tarhan I, Watson GH (1996) Phys Rev Lett 76:315–318
Vlasov YA, Yao N, Norris DJ (1999) Adv Mater 11:165–169
Vlasov YA, Bo XZ, Sturm JC, Norris DJ (2001) Nature 414:289–293
Wang Z, Chong YD, Joannopoulos JD, Soljacic M (2008) Phys Rev Lett 100:013905
Xia D, Zhang J, He X, Brueck SRJ (2008) Appl Phys Lett 93:071105
Yablonovitch E (1987) Phys Rev Lett 58:2059–2062
Yablonovitch E, Gmitter TJ (1989) Phys Rev Lett 63:1950–1953
Yablonovitch E, Gmitter TJ, Leung KM (1991a) Phys Rev Lett 67:2295–2298
Yablonovitch E, Gmitter TJ, Meade RD, Rappe AM, Brommer KD, Joannopoulos JD (1991b) Phys Rev Lett 67:3380–3383
Yadav H, Sinha N, Kumar B (2014) Cryst Eng Commun 16:10700–10710
Yang H, Jiang P (2011) Appl Phys Lett 98:011104
Yanik MF, Suh W, Wang Z, Fan S (2004) Phys Rev Lett 93:233903
Yu Z, Veronis G, Wang Z, Fan S (2008) Phys Rev Lett 100:023902

Chapter 4
Highly Efficient Materials for Photonic Crystal-Based Optical Components

Subramanian Thangarasu, Vadivel Siva, Sadasivam Kannan, and Anbazhagan Murugan

Abstract Photonic crystals (PhCs) are macroporous materials with interesting properties, especially physical, chemical, and optical properties. PhCs are highly ordered materials with properties that limit and control the propagation of light due to the photonic bandgap, with a band of frequencies where light propagation is restricted in a photonic crystal. PhCs have been the subject of many investigations. Due to the unique characteristics of photonic crystals, such as biosensors, gas sensing, optical filters, photonic papers, inkless printing and reflective flat displays, their potential applications are highly anticipated. PhCs are classified mainly into three categories according to their nature of structure and periodicity, namely, one-dimensional, two-dimensional and three-dimensional PhCs. 2D PhCs can be fabricated by photolithography or etching on a suitable substrate. These materials are also widely used as photonic crystal fibres, where microscale structures are used to control light with completely different properties compared to a conventional optical fibre. In this chapter, we discuss recent applications of PhC-based components coupled with emerging methodologies containing telemedicine, flexible and wearable sensing, smart materials and metamaterials. Finally, we discuss the current challenges and future applications of PhC-based optical devices.

Keywords Photonic crystals · Optical logic gates · Biosensors · Optical fibres · Optical diodes

S. Thangarasu · A. Murugan
Department of Physics, Kalasalingam Academy of Research and Education, Krishnankoil, Tamil Nadu 626 126, India

V. Siva (✉)
Department of Physics, Karpagam Academy of Higher Education, Coimbatore, Tamil Nadu 641 021, India
e-mail: siva33phy@gmail.com; siva.vadivel@kahedu.edu.in

Centre for Material Chemistry, Karpagam Academy of Higher Education, Coimbatore, Tamil Nadu 641 021, India

S. Kannan
Centre for High Computing, CSIR-Central Leather Research Institute, Chennai, Tamil Nadu 600 020, India

© The Author(s), under exclusive license to Springer Nature Singapore Pte Ltd. 2023

S. S. Dhanabalan et al. (eds.), *Photonic Crystal and Its Applications for Next Generation Systems*, Springer Tracts in Electrical and Electronics Engineering,
https://doi.org/10.1007/978-981-99-2548-3_4

General Introduction

All across the physical world, from the shifting colours of a crystal held up to the light to the patterns on a butterfly's wings, periodic structures' optical characteristics (Barrera-Patiño et al. 2020) can be seen. Although photonic crystals were used by nature for millions of years, humans have only just begun to recognize their potential. Photonic crystals are optical materials with periodic nanostructures; these structures (Högström and Ribbing 2004; Troia et al. 2013; Scullion et al. 2013) often take the form of periodic variations in refractive index, with occurrence periods on the order of optical wavelengths. As there is a significant difference in refractive indices, such as between glass or a semiconductor and air, in other instances there are relatively smaller differences. Certain authors propose for the requirement of high-index contrast for photonic crystals because some of the truly notable photonic crystal features, like entire photonic bandgaps, exits primarily in case with high-index contrast (Yablonovitch et al. 1991; Pendry 1996; Foresi et al. 1997). Thin film stacks have been researched as one-dimensional periodic structures for a long time, but Yablonovitch and John originally introduced the idea of 3D photonic crystals in 1987 (Yablonovitch 1987).

This broadening, which gave rise to the term "photonic crystal", spurred numerous other advancements in their production, theory and use, including integrated optics, negative refraction and optical fibres that direct light through air. PhCs have found extensive use in a variety of industries, including sensors, anticounterfeiting, information encryption, displays, light harvesting and energy conversion (Thylén and Wosinski 2014; Homola 2008; Barlen et al. 2007).

Their widespread use can be due to their simple, exact and adaptably tuneable self-assembly from a nanoscale building block assembly method as well as their unique optical characteristics, including its photonic stop bands (PSBs) and the slow light phenomenon (Yablonovitch 1993). In certain earlier reviews, the manufacturing of PhC and its uses in light harvesting (Wu et al. 2019), anticounterfeiting and sensing (Pan et al. 2019; Sc et al. 2014) were covered. Fenzl and colleagues have extensively described the application of stimuli-responsive PhCs for biological or chemical sensing of solvents, vapours, chemical substances and macromolecules (Fenzl et al. 2014), but the optical readout technique was restricted to reflection and diffraction shifts. When compared to other sensing concepts and materials such as electrochemical sensors that use functional nanomaterials (Ademgil and Haxha 2015), photoluminescence sensors that use quantum dots (Yuan et al. 2022) and optical sensors that use nanostructured nanophotonics, optical sensors (Wang and Ni 2014; Xavier et al. 2018) utilizing PhCs stand out because of their periodic structure and the ability to accurately control their respective optical characteristics.

A non-invasive, label-free and multiplexed analysis is made possible by the precise control. Here, the PhCs made of colloids stand out in particular. Colloid self-bottom-up assembly's method enables their low-cost fabrication with highly effective and high-resolution nanostructures. A simple comparison with electrochemical and photoluminescent sensors can be done to highlight the benefits of

PhC sensor. By measuring current, voltage or conductance, electrochemical sensors translate (Ghoumazi and Hocini 2021) a specific recognition incident to an appropriate electrical impulse. To increase their sensitivity and selectivity, scientists are turning to engineering nanomaterials from 0 to 3D and nanostructures (from arrays to hybrid systems).

Because each PhC can have unique characteristic spectrum due to Bragg diffraction, which is controlled by the size of the building blocks, PhC-based optical sensors offer simple possibilities for structure modification to acquire strong and specific analyte adsorption. However, they can also be used as barcodes. These barcodes are extremely stable and can be adjusted across a large portion of the visible spectrum, allowing for multiplexed experiments. In comparison to fluorescent dyes, CDs and QDs (Si et al. 2014), this represents a benefit. PhCs are transducers that also have improved optical signal-reading capabilities. These factors served as the foundation for the organization of this study. We initially go through PhC's optical characteristics before moving on to label-free PhC-based sensor applications (Freeman et al. 2009).

Optical Properties of Photonic Crystals

The laws that control how light behaves in the physical world are accurate representations of those laws. The law that defines transmissivity, absorptivity and reflectivity is one of the many that exist. Consider the crystal in the illustration below that is being illuminated by a light source generally from the top. According to the illustration above, when a light ray strikes a slab of the material, some of it is reflected back, some of it is absorbed and the remaining portion is passed through the material (Ciminelli et al. 2013). Typically, the equation below governs such an event:

$$\mathbf{A}(\boldsymbol{\lambda}) + \mathbf{R}(\boldsymbol{\lambda}) + \mathbf{T}(\boldsymbol{\lambda}) = 1 \tag{4.1}$$

Here "R" stands for the material's reflectance, "T" for its transmittance and "A" for its absorptance. In the field of optics, these three characteristics are most important. There are several methods to categorize them.

Reflectance

A sudden shift in a wave's propagation direction occurs when it encounters a barrier between two mediums (Sakoda 2004). The approaching wave disturbance is still present in the same medium, at least in part. At plane border, reflection happens regularly and follows a straightforward law.

Angles of incidence (between the approaching wave's direction of motion and a perpendicular to the reflecting surface) are identical to angles between the reflecting

wave's direction of travel and a perpendicular (angle of reflection). The ray will diffuse if it is reflected at an uneven or rough barrier. The portion of an incoming wave's energy that is rebounded by a surface material is known as its reflectivity. Structural colour is the term used to describe the reflected visible spectrum of light. Furthermore, the lattice constants of PCs are connected to their optical properties. A periodic structure with a millimetre-sized radius can act in the millimetre wavelength range; a submicrometre-sized structure in the visible light spectrum and a nanometre-sized structure in the X-ray spectrum. According to their lattice constants, the resultant PC therefore diffracts UV, visible or near-IR light.

Absorptance

In wave motion, energy is transferred from the wave to the matter as the wave moves through it. An acoustic, electromagnetic or other wave's energy is related to square of its amplitude or the maximum displacement or movement of a point on the wave. The amplitude of a wave continuously diminishes as it travels through a material. The medium is described as transparent to that particular radiation if just a tiny portion of the energy is absorbed, but opaque if all the energy is lost. Every known transparent substance exhibits some of absorption (Domínguez et al. 2012). For example, the ocean appears clear to sunlight when it is close to the surface, but as it goes deeper, it turns opaque.

Depending on the type of material and its thickness, radiation is partially absorbed when it passes through matter. It is possible to imagine that a homogeneous substance with a certain thickness is made up of numerous similarly thin layers. A similar portion of the energy that reaches each layer will be absorbed by it. The absorption coefficient of a material refers to the constant change in energy that occurs while a wave travels through a layer at a specific wavelength.

Transmittance

When a form of radiation is incident on a substance, wave energy is transferred through the medium, and this energy is what can be seen emerging from the material (Veronis et al. 2005). Now imagine that the material surface is not as smooth as it was in the previous scenario, but instead is rough. In this situation, the aforementioned equation is modified significantly to account for a process known as diffusion or scattering of light at the material's surface.

Types of Photonic Crystals

Photonic crystals are employed in a variety of industries, from optics to communications, and have undergone a number of treatments in recent years. One-dimensional photonic crystal (1D), two-dimensional photonic crystals (2D) and three-dimensional photonic crystals (3D) are the three basic categories into which photonic crystals can be divided (Lee and Wu 2010).

The periodical dielectric materials in 3D may have an electromagnetic bandgap, or a frequency range below which light cannot pass through the material in either direction. Additionally, he stated that it is possible to avoid unwanted spontaneous emission in semiconductor by arranging the material so that the emission frequencies occur within a photonic bandgap as no propagating states present at that frequency emission is in fact prohibited. Mostly the PhCs are that a lot of the characteristics of PhCs continue to exist even when the periodic lattice becomes disorganized. Strong light localization is still possible in certain structures if the index contrast is great enough, analogous to the electrical bandgaps of amorphous semiconductors. In addition to that explanation of the cavity modes that can be brought into a periodic structure by producing a defect or "phase slip" was perhaps more applicable to much of the PhC research that has proceeded. This method had previously been used to establish resonant cavities in distributed feedback lasers, but these modes could be localized in three dimensions and described the phenomenon in terms of defect states in the photonic bandgap. The idea of controlling light with periodic structures has quickly grown into a field of study on a global scale as a result of these findings and the earliest recommendations for limiting spontaneous emission.

From solid-state physics, where the existence of electronic bandgaps in semiconductors has modernized electronics, bandgaps in periodic materials had already been known. Photonic crystals have incorporated many solid-state research ideas, especially notation and nomenclature, and it is possible that this is why the subject has advanced so quickly in less than 20 years (Fig. 4.1).

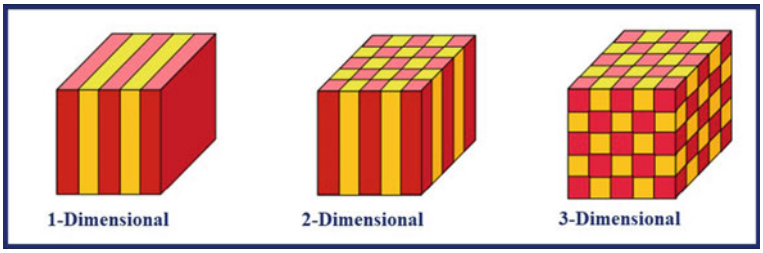

Fig. 4.1 Photonic crystals periodic in one, two and three orientations (From Open Access-Robinson S, Nakkeer R. Photonic Crystal Ring Resonator Based Optical Filters. Advances in Photonic Crystals [Internet]. 2013 Feb 13; Available from: http://dx.doi.org/10.5772/54533)

One-Dimensional PhCs

Despite the relatively recent invention of the name PhC, one-dimensional (1D) PhCs (Inoue and Ohtaka 2004) that take the shape of periodic dielectric stacks have been around for much longer. Optical filters, Fabry–Perot cavities, high-efficiency mirrors and distributed feedback lasers are just a few of the applications that make advantage of their wavelength-selective reflection capabilities. The simplest PhC is an alternate stack of two separate dielectric substances.

Every interface in such a stack reflects a portion of the field when light is incident on it. The reflected fields can merge in phase to produce constructive interference and intense reflectance, also referred to as Bragg reflection, if the thickness of each layer is set carefully. Contrary to 2D and 3D PhCs, 1D Bragg reflection occurs independent of the index contrast, though if the contrast is low, a significant number of periods are needed to produce a high reflectance. Dielectric stack mirrors are particularly effective and can be designed to reflect nearly 100% of the incident light within a narrow frequency range since the absorption in dielectric optical substance is relatively low. These dielectric mirrors' main drawback is that they can only function for a small range of angles that are near to normal incidence.

The fibre Bragg grating (FBG), which uses 1D PhCs (Elshahat et al. 2021) is another more modern use. In this device, the refractive index of the fibre core is periodically altered along its axis, often approaching a sinusoidal profile. Although the features are essentially the same, this instance is a little more complicated since the refractive index varies constantly rather than discretely as in the earlier example.

The key distinction is that thousands of periods are often needed to achieve the necessary reflectance qualities in the FBG since the refractive index contrast there is so minimal ($\Delta n \leq 0.5\%$). FBGs are currently a crucial component of fibre optic network and are utilized for a variety of purposes, including filters and dispersion compensation.

Two-Dimensional PhCs

Both two-dimensional (2D) and three-dimensional (3D) PhCs can be seen as specializations of the 1D case, where a complete 2D or 3D bandgap can only be observed if the 1D Bragg reflection criteria is satisfied concurrently met for all propagation orientations where the structure is periodic. This occurs for the majority of 2D periodic lattices if the index contrast is strong enough, but for 3D structures, only specific lattice geometries exhibit the required characteristics, and only in those cases when the index contrast is sufficiently large.

In 2D PhCs (Campanella et al. 2015) typically consist of an array of dielectric cylinder in a homogenous dielectric backdrop material rather than a stack of uniform dielectric layers, but there are numerous other potential geometries. For propagation in the plane of periodicity, which is perpendicular to the rods, 2D bandgaps can

develop if the refractive index contrast between the cylinders and the background is sufficiently high. The periodic array of cylinders causes Bragg reflection of light at a frequency within the bandgap in all orientations. In a 2D PhC, meanwhile, propagation can still take place in the non-periodic orientation, parallel to the cylinders, just as it did in the 1D example when light could still move in two dimensions. Therefore, a different method of confinement is needed in the third dimension to prevent diffraction and scattering losses from being too great.

Similar to semiconductor materials, a large portion of the fascination in photonic crystals comes from the ability to introduce a structural defect into an otherwise regular lattice, which allows for the creation of localized defect states inside the bandgap. For instance, removing a single cylinder from a 2D PhC can result in the formation of a point-like defect or resonant cavity, while removing a line of cylinders can result in the formation of a waveguide that can accommodate propagating modes. The special characteristics of the propagating phases that reside outside the bandgaps in defect-free PhCs are taken advantage of in a second class of 2D PhC usage. Strict phase requirements are imposed on the field distributions that PhCs support by their discontinuous translational symmetry. Because of this, only a limited set of modes may propagate at any fixed wavelength, and the characteristics of light in these Bloch modes might be considerably different from those of light in a homogeneous medium.

Three-Dimensional PhCs

The most difficult PhC structures to manufacture are three-dimensional ones. In contrast to 2D PhC research, which has benefited greatly from well-established 1D PhC thin-film and semiconductor production technologies like plasma deposition and electron-beam lithography, 3D PhC (Yokouchi et al. 2003) creation has necessitated the invention of completely new methods. Due to this, it took longer than 3 years following the initial suggestion for 3D bandgap substances until a structure was estimated to produce a bandgap for all orientations and all polarizations. At the corners of a diamond lattice, dielectric spheres made up the structure.

This was in response to experimental observations from the year before, in which a partial bandgap in a face-centred cubic (FCC) lattice of spheres was misclassified as a whole bandgap. The need for robust theoretical and computational methods capable of handling high-index contrast dielectrics was underlined by the latter discovery. Since these preliminary investigations, a large variety of 3D PhC geometries displaying full bandgaps have been shown in theory and practise. Early photonic crystal investigations were carried out at microwave and mid-infrared frequencies because it was difficult to fabricate high-quality structures with characteristics on the scale of visible frequencies. Smaller structures are now practical due to advancements in fabrication and material processing techniques, and in 1999 the first 3D PhC with a bandgap at telecommunications wavelengths was described. Since then, a number of lattice configurations for operating at comparable frequency have been proposed.

Waveguiding and the purposeful introduction of defects in 3D PhCs have not advanced as quickly as in 2D PhCs, primarily because 3D bandgaps need more complicated structure and challenging production. The potential for unique photonic circuit designs has been shown in theoretical research, but just a few experimental findings have been reported to date. Though telecommunication-related applications have garnered most of the recent attention in PhCs, the initial idea of reining in spontaneous emission has not been discarded. Recent research has shown that quantum dots placed in 2D and 3D PhCs can both prevent and promote spontaneous emission. The thermal emission characteristics of heated tungsten 3D PhCs have also been shown to be altered by the existence of a photonic bandgap at black-body radiation frequencies. Tunable bandgap phenomena have also been established via nonlinear (Lee and Wu 2010) and liquid crystal tuning, and superprism phenomena have been computed in 3D polymer PhCs.

Applications of PhCs

These photonic crystals, sub-wavelength imaging, scanning photon tunnelling microscopy and components like ultrahigh-sensitivity phase shifters and optical switches are only a few of the many uses. Photonic crystal fibres, which use a microscale structure to confine light with radically different properties compared to conventional optical fibre for applications in nonlinear devices and guiding exotic wavelengths, are already on the market as the first commercial products involving two-dimensionally periodic photonic crystals. The three-dimensional counterparts are still a long way from commercialization, but when some technological aspects like manufacturability and primary challenges like disorder are under control, they might offer additional features like optical nonlinearity needed for the operation of optical transistors used in optical computers (Bronnikov et al. 2013; Zhang et al. 2021). Intriguing optical materials for regulating and modifying light flow are photonic crystals. One-dimensional photonic crystals are already widely used in thin-film optics, which have uses ranging from colour-changing paints and inks to coatings for lenses and mirrors with low and high reflection. Two-dimensional photonic crystals are starting to find commercial uses, whereas higher dimensional photonic crystals are of significant interest for both basic and practical researches. Figure 4.2 depicts how photonic crystals are used in industry.

The multiplex detection, biomolecular screening and real-time monitoring of biomolecules are advantages of PhC-based biomaterials. PhCs also make excellent platforms for drug loading and biomolecule modification, which might be used with biological carriers and sensors. There are several ways to create PhC materials with changing structural colours that could be used in biomedicine today (Chen et al. 2017). Furthermore, PhC is used in biomedicine applications, including as drug administration, biodetection and tumour screening.

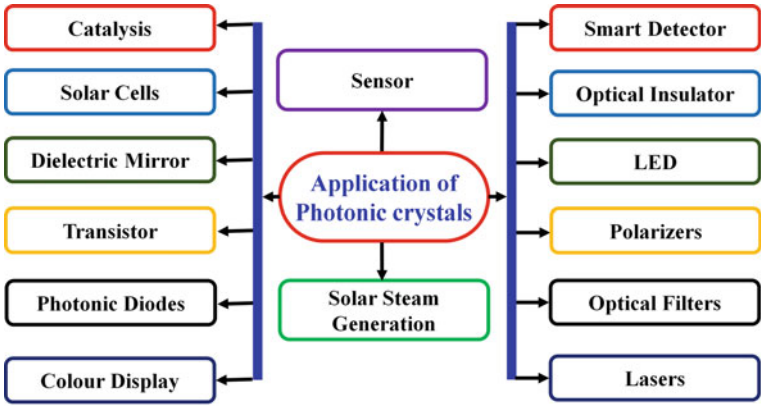

Fig. 4.2 Technological uses of photonic crystals

Because of the complexity of biomolecules and the difficult and expensive production methods, conventional techniques are insufficient. In the prevention and treatment of diseases, biomolecules including proteins, DNA and RNA must be found, delivered and expressed. As a result, numerous methodologies and procedures based on nanotechnology have been created in an effort to increase the sensitivity of these biomolecules' detection while also streamlining and cheapening the detection process. Hydrogels, nanoparticles and photonic crystals, among other nanomaterials, have significant promise as biosensor components (Fojo et al. 1986; Chen et al. 2017).

A biological response is transformed into electrochemical, optical, electrical or magnetic signals by signal transducers in biosensors, which are analytical tools made of biologically responsive materials. As they can perform remote sensing and offer essential and complementary information, optical biosensors play a significant role in biomedical research, healthcare, pharmaceuticals, environmental monitoring and homeland security. The encoding of typical fluorescent dyes is quickly quenched by light and heat, which results in encoding loss. The PhC-based encoding method, on the other hand, uses a physical encoding technique that can be utilized to microcarry encoded proteins with stable encoding. Moreover, the bead array's porous shape produces a high surface-to-volume ratio, which significantly boosts the sensitivity of detection in comparison to non-porous structures (Tang et al. 2021; Bian et al. 2019). This method's detection limit, which might be as low as 10^{-19} m, should enable the investigation of numerous genes' expression at once. One could conclude that PhC-based materials for biomedical applications have garnered a lot of interest recently. This is due to both the distinct photonic features of PhC materials and the advantages of merging chemistry and biology, which points the development of PhC materials in the right path. Lately, programmable structural colours in smart PhC materials have attracted increasing interest from the domains of material science and biomedicine. New molecular methodologies and techniques for material engineering can give synthetic PhC additional capabilities, and these have proven to be very beneficial for

biomolecular detection, tissue engineering, drug discovery and other applications (Li et al. 2020).

PhC-based Optical Components

This opens up new possibilities for information processing and technical applications, including chips, filters, lasers, waveguides, integrated photonic circuits, sensors and thin-film photovoltaic cells, to name a few. These qualities make it feasible to control and adjust light in PhCs. As is generally known, there are numerous types of materials that can be utilized to create tuneable PhCs, including liquid crystals, metals, semiconductors and superconductors.

Waveguides

Only one polarization state out of two orthogonal polarization states has a photonic bandgap in most conventional photonic crystal slab waveguides. Compact and high-performance optical waveguide devices have undergone significant development in recent years in order to establish high-speed and large-capacity photonic networks. In this situation (Clementi et al. 2021; Mbakop et al. 2020), various types of photonic crystals have been proposed as an artificial material, and photonic devices based on PhCs have garnered a lot of interest. A linear waveguide is yet another crucial optical component for integrated photonic electronics. The index of refraction differential between the waveguide core and the waveguide cladding in conventional dielectric waveguides serves to confine propagating beams. Most frequently, linear defects—a row of altered lattice unit cells—that are shaped onto high-index dielectric membranes—create photonic crystal waveguides (Shen et al. 2002).

The guiding in this case is due to a combination of scattered reflections from the photonic crystal in-plane and total internal reflection at the high-index membrane/low-index cladding contacts. Waveguide branches and bends with small bending radii can be used to obtain extremely low transmission losses since this confinement is not totally dependent on total internal reflection. Photonic crystal waveguides are most typically realized in two-dimensional photonic crystals produced in high-index dielectric slabs (Wen et al. 2008; Cerjan and Fan 2017; O'Brien and Kuang 2005). Typically, a substrate with a high index is placed a few microns below the membrane. Since the fields of the guided modes exponentially decrease outside of the membrane, the impact of a substrate few microns away is very nearly non-existent.

Multichannel Filters

To solve the problems of complex construction, single wavelength download and enormous size of multichannel filter, a novel ultrasmall, tunable multichannel filter based on photonic crystals was used. Multichannel optical filters and image sensors are the main building blocks of such an imaging system. To measure the precise feature of the spectra or to detect minute changes in the reflection or radiation spectrum of the object, several wavelength-elective filters with different features may be needed (Hu et al. 2022).

For certain applications, the transmission spectra of each wavelength channel must be contiguous within the specified wavelength band. Performance of the filter is influenced by how well information is transferred between the two waveguides. The full forward or backward transfer of the selected channel in the dropping waveguide without any forward transmission or backward reflection in the bus waveguide is referred to as perfect efficiency. The other channels are unaffected by optical resonators when they are present. As a result, optical filters are required to choose the requisite channel(s) at any destination (Sathyadevaki and Raja 2017; Mahmoud et al. 2013). The optical filters are the ideal tool for choosing one or more channels from multiplexed signals. Another innovative method for designing photonic crystal ring resonators is based on tunability.

A rising number of producers of photonic integrated circuits are showing interest in this technique, which acts as a tunable channel drop filter (Shanmuga et al. 2018; Sathyadevaki et al. 2018). The broad optical transmission bandwidth provided by the dielectric materials of ring resonators has led to a steady increase in the use of PhCs in all-optical fibre networks in international communication systems.

Logic Gates

Scientists are currently interested in photonic crystal logic gates, one of the most important optical media, for the purpose of creating optical computers. Photonic crystal designs can reduce the size of optical logic gates to the wavelength order. These devices also exhibit fast switching rates due to their response times of a few picoseconds or less and microwatt-level power consumption. All-optical photonic crystal logic gates are more likely to enable integrated optical circuitry. PhC logic gates are currently one of the most prominent optical media that draw researchers to develop optical processors. Using PhC structures, optical logic gates (OLGs) can have dimensions that are on the order of the wavelength (Salmanpour et al. 2015). These devices frequently consume only a few microwatts of power and respond in less than a few picoseconds, which increases switching speed. PhC OLGs increase the likelihood of fabricating integrated optical circuits. A digital processor can receive digital data at the speed of light using an optical cable. However, the greatest switching speed

for electrical logic gates is similar to 50 ps (2×10^5 Hz) with a typical one switching power of 0.5 mW.

PhC-based OLGs are exclusively bound by the speed of light through them, as opposed to semiconductor-based logic gates, which are also constrained by the p–n junction and interlinking capacitances. OLGs are skilled at performing a variety of logic operations and have numerous optical communication applications. For instance, address recognition, packet header adjusting and data integrity checking can all be done using the AND logic gate. In optical oscilloscopes, it can furthermore be utilized as a sampling gate.

Sensors

Photonic sensors have advanced significantly in recent years as a result of the rising need for sensing applications in a variety of sectors, including healthcare, defence, security, automotive, aerospace, the environment and food quality control, to mention a few. The development and integration of microfluidic and photonic technologies allow for the increase of sensing performance in terms of sensitivity, limit-of-detection (LOD) and detection multiplexing capability, with special reference to the CMOS-compatible silicon-on-insulator technology. In-depth research has been done on photonic sensors over the past 10 years, especially for the detection of a variety of biological and chemical contaminants (Mohammad Atiqullah et al. 2019; Arunbabu et al. 2011). Photonic lab-on-a-chip systems represent the state of the art in photonic sensing in this context because they are anticipated to have higher sensitivity and selectivity as well as high stability, immunity to electromagnetic interference and product improvements, like smaller integration sizes and lower costs. Some of photonic-based sensors are shown in Fig. 4.3.

Micro-structured optical fibres also known as photonic crystal fibres (PCFs) are a modern and intriguing type of optical fibre that can be used for a variety of sensing

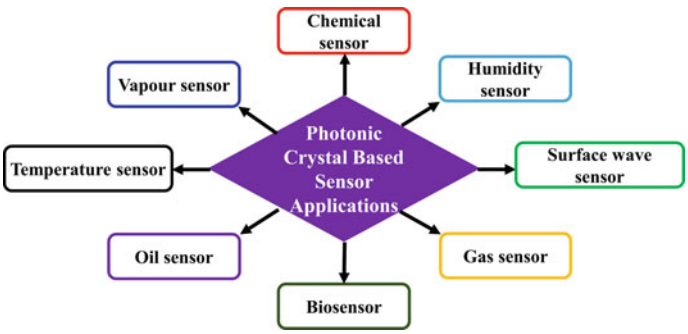

Fig. 4.3 Photonic crystals with various types of sensors

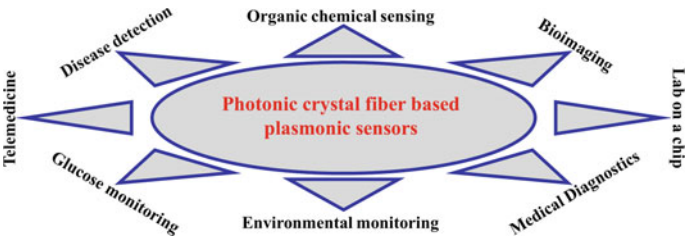

Fig. 4.4 Photonic crystal fibre-based plasmonic sensors

applications, including the measurement of strain, refractive index, pressure, temperature and magnetic field, to name a few. High sensitivity, small size, resilience, adaptability and the capacity for distant sensing are characteristics of PCF-based sensors (Nair and Vijaya 2010). Another benefit is the capacity to function in adverse environmental conditions, such as noise, powerful electromagnetic fields, high voltages, radioactive radiation, explosive or chemically corrosive substances, and at high temperatures.

Photonic crystals can be used to create chemical sensors that can measure the pH and ionic strength of liquids. Their use as sensors is made possible by their well-defined physical properties, such as reflectance and transmittance, high levels of sensitivity that produce precise detection limits and the beautiful visual quality they exhibit in the visible range of wavelengths. When using photonic crystal technology, measurements are accomplished by coupling the incident, reflected and transmitted light to optical fibres and analysing it at a distance. The sensor itself is quite small. For evaluating chemical and biological analytes, photonic crystal fibre surface plasmon resonance has become a highly sensitive portable sensing device and its corresponding uses are shown in Fig. 4.4. Due to their distinctive qualities, such as high sensitivity and diverse range of applications in environmental monitoring, food safety water testing, liquid detection, gas detection and medical diagnostics, including drug detection, bioimaging and biological analyte, surface plasmon resonance (SPR) sensors have generated a great deal of interest.

Lab-On-Chip Devices

Lab-on-chip (LOC) devices refer to small devices that are capable of carrying out common laboratory functions such as filtering, mixing and detecting the desired analytes. These gadgets are much more advantageous than other contemporary analysis technologies than just being smaller. Utilizing LOC devices results in lower sample volume requirements (mL/nL instead of mL as for laboratory procedures), which in turn lowers cost. Based on the needs of the application (Olyaee and Naraghi 2017), every single optical component needed to be incorporated in photonic integrated circuits can be specified and achieved using the photonic bandgap property

of photonic crystals. Using photonic crystals, numerous experiments have been conducted on various optical components.

Summary and Future Prospective

In this chapter, we have studied photonic crystals and their interesting properties, especially optical properties. The optical properties of photonic crystals were discussed in the aspect of reflectance, absorptance and transmittance. Generally, PhC materials are used to limit and control the propagation of light based on the photonic bandgap. Also, PhCs' classification is discussed, and PhCs were categorized according to its nature of structure periodicity into three types, that is, one-dimensional, two-dimensional and three-dimensional PhCs. PhCs have been used in many investigations. One-dimensional photonic crystals used in dielectric mirrors can create reflectors with extremely high reflectivity at a given wavelength. Fibre-optic communication is one use for photonic crystal fibres, which are two-dimensional photonic crystals. In the future, optical computers might use three-dimensional crystals, which might make photovoltaic cells more effective. The use of photonics spans a number of industries, including manufacturing, life sciences, health care, security and safety, as well as optical data transmission, imaging, lighting and displays. Especially, the PhCs have been used as biosensor, gas sensing, optical filters, photonic papers, inkless printing and reflective flat displays; their potential applications are highly anticipated. In this chapter, we discussed in detail application of lab-on-chip devices, sensors, logic gates, multichannel filters and waveguides.

Additionally, it is possible to create narrow linewidth lasers with photonic crystals made of photoemissive materials, such as III-V semiconductors and glasses doped with rare-earth elements, which may eventually be connected with other parts of an optical communication system. Filters that only transmit a very small range of wavelengths could also be made using photonic crystal microcavities made of passive components like silicon dioxide and silicon nitride. In a DWDM communication system, similar filters could be employed to choose a wavelength channel. Moreover, a channel demultiplexer that divides and short light pulses of various wavelengths may be built from arrays of these devices combined on a chip. The transmission of long-distance optical signals could be improved by materials with photonic bandgaps, which would speed up the Internet. One problem with conventional optical fibres is that varying optical wavelengths can move through the material at varying speeds. The field of photonics technology is vast. Applications for photonics include optical fibres that transfer data over the Internet, screens on smartphones and other electronic devices, improved military capabilities, higher manufacturing precision and a wide range of medical diagnostic tools.

Acknowledgements One of the authors V. Siva is grateful to the Management Karpagam Academy of Higher Education, Coimbatore-641021, Tamil Nadu, India for their support.

References

Ademgil H, Haxha S (2015) PCF based sensor with high sensitivity, high birefringence and low confinement losses for liquid analyte sensing applications. Sensors 15(12):31833–31842

Arunbabu D, Sannigrahi A, Jana T (2011) Photonic crystal hydrogel material for the sensing of toxic mercury ions (Hg^{2+}) in water. Soft Matter 7(6):2592–2599. https://doi.org/10.1039/C0SM01136C

Barlen B, Mazumdar SD, Lezrich O, Kämpfer P, Keusgen M (2007) Detection of Salmonella by surface plasmon resonance. Sensors 7(8):1427–1446. https://doi.org/10.3390/s7081427

Barrera-Patiño CP, Vollet-Filho JD, Teixeira-Rosa RG, Quiroz HP, Dussan A, Inada NM, Bagnato VS, Rey-González RR (2020) Photonic effects in natural nanostructures on Morpho cypris and Greta oto butterfly wings. Sci Rep 10(1):1–11

Bian F, Sun L, Cai L, Wang Y, Zhao Y, Wang S, Zhou M (2019) Molybdenum disulfide-integrated photonic barcodes for tumor markers screening, Biosens Bioelectron 133:199–204

Bronnikov S, Kostromin S, Zuev V (2013) Polymer-dispersed liquid crystals: progress in preparation, investigation, and application. J Macromol Sci, Part B 52(12):1718–1735. https://doi.org/10.1080/00222348.2013.808926

Campanella CE, De Leonardis F, Passaro VMN (2015) Investigation of coupling conditions for fiber Bragg grating ring resonators. In: Fotonica AEIT italian conference on photonics technologies. https://doi.org/10.1049/cp.2015.0155

Cerjan A, Fan S (2017) Complete photonic band gaps in supercell photonic crystals. Phys Rev A 96(5):051802. https://doi.org/10.1103/PhysRevA.96.051802

Chen H, Lou R, Chen Y, Chen L, Lu J, Dong Q (2017) Photonic crystal materials and their application in biomedicine. Drug Deliv 24(1):775–780. https://doi.org/10.1080/10717544.2017.1321059

Chen H, Lou R, Chen Y, Chen L, Lu J, Dong Q (2017) Photonic crystal materials and their application in biomedicine. Drug Deliv 24(1):775–780. https://doi.org/10.1080/10717544.2017.1321059

Ciminelli C, Campanella CM, Dell'Olio F, Campanella CE, Armenise MN (2013) Label-free optical resonant sensors for biochemical applications. Prog Quantum Electron 37(2):51–107. https://doi.org/10.1016/j.pquantelec.2013.02.001

Clementi M, Iadanza S, Schulz SA, Urbinati G, Gerace D, O'Faloain L, Galli M (2021) Thermo-Opt Induc Transpar Photonic Chip Light: Sci Appl 10(1):1–10. https://doi.org/10.1038/s41377-021-00695-3

Domínguez S, García O, Ezquer M, Rodríguez MJ, Lagunas AR, Pérez-Conde J, Bravo J (2012) Optimization of 1D photonic crystals to minimize the reflectance of silicon solar cells. Photonics Nanostructures-Fundam Appl 10(1):46–53. https://doi.org/10.1016/j.photonics.2011.07.001

Elshahat S, Abood I, Esmail MSM, Ouyang Z, Lu C (2021) One-dimensional topological photonic crystal mirror heterostructure for sensing. Nanomaterials 11(8):1940. https://doi.org/10.3390/nano11081940

Fenzl C, Hirsch T, Wolfbeis OS (2014) Photonic crystals for chemical sensing and biosensing. Angew Chem Int Ed 53:3318−3335

Fojo A, Chin JE, Roninson IB et al (1986) Human multidrug-resistant cell lines: increased mdr1 expression can precede gene amplification. Science 232:643–645

Foresi JS et al (1997) Photonic-bandgap microcavities in optical waveguides. Nature 390:143. https://doi.org/10.1038/36514

Freeman R, Finder T, Bahshi L, Willner I (2009) β-Cyclodextrin-modified CdSe/ZnS quantum dots for sensing and chiroselective analysis. Nano Lett 9(5):2073–2076. https://doi.org/10.1021/nl900470p

Ghoumazi M, Hocini A (2021) Photonic crystal based bio-sensor detection in nanophotonic structure using FEM method. Int J Sens Wirel Commun Control 11(2):216–224. https://doi.org/10.2174/2210327910666191218125109

Högström H, Ribbing CG (2001) Polaritonic and photonic gaps in SiO_2/Si and SiO_2/air periodic structures. Photonics Nanostructures-Fundam Appl 2(1):23–32. https://doi.org/10.1038/s41598-020-62770-w

Homola J (2008) Surface plasmon resonance sensors for detection of chemical and biological species. Chem Rev 108(2):462–493. https://doi.org/10.1021/cr068107d

Hu C, Ji J, Zhou T, Wan C, Xu C, Zhu A (2022) A tunable multichannel filter based on photonic crystal. Silicon 1–10. https://doi.org/10.1007/s12633-022-02159-8

Inoue K, Ohtaka K (eds) Photonic crystals: physics, fabrication and applications, vol 94. Springer Science & Business Media

Lee HM, Wu JC (2010) Transmittance spectra in one-dimensional superconductor-dielectric photonic crystal. J Appl Phys 107(9):094308

Li H, Low MX, Ako RT, Bhaskaran M, Sriram S, Withayachumnankul W, Kuhlmey BT, Atakaramians S (2020) Broadband Single-Mode Hybrid Photonic Crystal Waveguides for Terahertz Integration on a Chip. Adv Mater Technol 5(7):2000117. https://doi.org/10.1002/admt.202000117

Mahmoud MY, Bassou G, Taalbi A (2013) A new optical add–drop filter based on two-dimensional photonic crystal ring resonator. Opt-Int J Light Electron Opt 124(17):2864–2867. https://doi.org/10.1016/j.ijleo.2012.08.072

Mbakop FK, Tom A, Dadjé A, Vidal AKC, Djongyang N (2020) One-dimensional comparison of TiO_2/SiO_2 and Si/SiO_2 photonic crystals filters for thermophotovoltaic applications in visible and infrared. Chin J Phys 67:124–134. https://doi.org/10.1016/j.cjph.2020.06.004

Mohammad Atiqullah S, Palit A, Istiaque Reja M, Akhtar J, Fatema S, Absar R (2019) Detection of harmful food additives using highly sensitive photonic crystal fiber. Sens Bio-Sens Res 23:100275. https://doi.org/10.1016/j.sbsr.2019.100275

Nair RV, Vijaya R (2010) Photonic crystal sensors: an overview. Prog Quantum Electron 34(3):89–134. https://doi.org/10.1016/j.pquantelec.2010.01.001

O'Brien J, Kuang W (2005) Photonic crystal lasers, cavities and waveguides, encyclopedia of modern optics. Elsevier, pp 146–155. https://doi.org/10.1016/B0-12-369395-0/00929-5

Olyaee S, Naraghi A (2017) Recent progress in therapeutic diagnosis using photonic crystal nanostructures. Nanostructures for Novel Therapy 621–656. https://doi.org/10.1016/B978-0-323-46142-9.00023-2

Pan M, Wang L, Dou S, Zhao J, Xu H, Wang B, Zhang L, Li X, Pan L, Li Y (2019) Recent advances in colloidal photonic crystal-based anti-counterfeiting materials. Crystals 9(8):417. https://doi.org/10.3390/cryst9080417

Pendry JB (1996) Calculating photonic band structure. J Phys: Condens Matter 8(9):1085. https://doi.org/10.1088/0953-8984/8/9/003

Sakoda K (2004) Optical properties of photonic crystals, vol 80. Springer Science & Business Media

Salmanpour A, Mohammadnejad S, Bahrami A (2015) Photonic crystal logic gates: an overview. Opt Quant Electron 47(7):2249–2275. https://doi.org/10.1007/s11082-014-0102-1

Sathyadevaki R, Raja AS (2017) Photonic crystal-based optical filter: a brief investigation. Photon Netw Commun 33(1):77–84. https://doi.org/10.1007/s11107-016-0620-9

Sathyadevaki Shanmuga sundar D, Sivanantha Raja AR (2016) Design of dual ring wavelength filters for WDM applications. Opt Commun 380:409–418. https://doi.org/10.1016/j.optcom.2016.06.045

Sathyadevaki R, Sundar D, Shanmuga Raja, Sivanantha A (2018) Photonic crystal 4×4 dynamic hitless routers for integrated photonic NoCs. Photon Netw Commun. https://doi.org/10.1007/s11107-018-0758-8

Fenzl C, Hirsch T, Wolfbeis OS (2014) Photonic crystals for chemical sensing and biosensing. 53(13):3318–3335. https://doi.org/10.1002/anie.201307828 (C. Fenzl, T. Hirsch, O.S. Wolfbeis, Photonic crystals for chemical sensing and biosensing. Angewandte Chemie International Edition, 53(13) (2014) 3318–3335. https://doi.org/10.1002/anie.201307828)

Scullion MG, Krauss TF, Di Falco A (2013) Slotted photonic crystal sensors. Sensors 13(3):3675–3710. https://doi.org/10.3390/s130303675

Shanmuga sundar, D., Sathyadevaki, R., Sridarshini, T., Sivanantha Raja, A. (2018) Photonic crystal based routers for photonic integrated on chip networks: a brief analysis. Opt Quant Electron 50(11):383

Shen L, He S, Xiao S (2002) Large absolute band gaps in two-dimensional photonic crystals formed by large dielectric pixels. Phys Rev B 66(16):165315. https://doi.org/10.1103/PhysRevB.66.165315

Si Y, Sun Z, Zhang N, Qi W, Li S, Chen L, Wang H (2014) Ultrasensitive electroanalysis of low-level free MicroRNAs in blood by maximum signal amplification of catalytic silver deposition using alkaline phosphatase-incorporated gold nanoclusters. Anal Chem 86(20):10406–10414. https://doi.org/10.1021/ac5028885

Shanmuga SD, Sathyadevaki R, Sivanantha Raja A (2018) High-efficiency filters for photonic integrated networks: a brief analysis. Laser Phys 28(11):116203. https://doi.org/10.1088/1555-6611/aadf27

Tang L, Wang L, Yang X, Feng Y, Li Y, Feng W (2021) Poly(N-isopropylacrylamide)-based smart hydrogels: design, properties and applications. Prog Mater Sci 115:100702

Thylén L, Wosinski L (2014) Integrated photonics in the 21st century. Photonics Res 2(2):75–81. https://doi.org/10.1364/PRJ.2.000075

Troia B, Paolicelli A, De Leonardis F, Passaro VM (2013) Photonic crystals for optical sensing: a review. Adv Photonic Crystals 241–295. https://doi.org/10.5772/53897

Veronis G, Dutton RW, Fan S (2005) Metallic photonic crystals with strong broadband absorption at optical frequencies over wide angular range. J Appl Phys 97(9):093104. https://doi.org/10.1063/1.1889248

Wang Y, Ni Y (2014) Molybdenum disulfide quantum dots as a photoluminescence sensing platform for 2, 4, 6-trinitrophenol detection. Anal Chem 86(15):7463–7470. https://doi.org/10.1021/ac5012014

Wen F, David S, Checoury X, El Kurdi M, Boucaud P (2008) Two-dimensional photonic crystals with large complete photonic band gaps in both TE and TM polarizations. Opt Express 16(16):12278–12289. https://doi.org/10.1364/OE.16.012278

Wu Y, Lu J, Li M, Yuan J, Wu P, Chang X, Liu C, Wang X (2019) Bismuth silicate photocatalysts with enhanced light harvesting efficiency by photonic crystal. J Alloy Compd 810:151839. https://doi.org/10.1016/j.jallcom.2019.151839

Xavier J, Vincent S, Meder F, Vollmer F (2018) Advances in optoplasmonic sensors–combining optical nano/microcavities and photonic crystals with plasmonic nanostructures and nanoparticles. Nanophotonics 7(1):1–38. https://doi.org/10.1515/nanoph-2017-0064

Yablonovitch E (1987) Inhibited spontaneous emission in solid-state physics and electronics. Phys Rev Lett 58(20):2059. https://doi.org/10.1103/PhysRevLett.58.2059

Yablonovitch EJJB (1993) Photonic band-gap structures. J Opt Soc Am B 10:283–295. https://doi.org/10.1364/JOSAB.10.000283

Yablonovitch E, Gmitter TJ, Leung KM (1991) Photonic band structure: the face-centered-cubic case employing nonspherical atoms. Phys Rev Lett 67(17):2295. https://doi.org/10.1103/PhysRevLett.67.2295

Yokouchi N, Danner AJ, Choquette KD (2003) Two-dimensional photonic crystal confined vertical-cavity surface-emitting lasers. IEEE J Sel Top Quantum Electron 9(5):1439–1445. https://doi.org/10.1109/JSTQE.2003.819521

Yuan F, Xia Y, Lu Q, Xu Q, Shu Y, Hu X (2022) Recent advances in inorganic functional nanomaterials based flexible electrochemical sensors. Talanta 244:123419. https://doi.org/10.1016/j.talanta.2022.123419

Xu Y, Zhang X, Luan C, Wang H, Chen B, Zhao Y (2017) Hybrid hydrogel photonic barcodes for multiplex detection of tumor markers. Biosens Bioelectron 87:264–270

Zhang YS, Jiang SA, Lin JD, Yang PC, Lee CR (2021) Stretchable freestanding films of 3D nanocrystalline blue phase elastomer and their tunable applications. Adv Opt Mater 9(1):2001427. https://doi.org/10.1002/adom.202001427

Chapter 5
Fabrication of Unidirectional Grown 1, 3, 5-Triphenylbenzene Single Crystal for Nonlinear Optical and Fast Neutron Detector Applications

N. Durairaj, S. Kalainathan, and S. Moorthy Babu

Abstract The organic single-crystal 1,3,5-triphenylbenzene (TPB) is a favourable material for third-order nonlinear optical polarization and high-energy particle detection applications. Bulk size (25 × 150 mm) unidirectional (<100> plane) TPB cylindrical crystal was grown by the unidirectional solution growth technique and their physical properties were analysed. The UV absorption analysis determined the extinction coefficient, reflectance, refractive index, bandgap energy transmittance and confirmed the grown TPB cylindrical crystal's fitness to couple with light sensors and/or photomultiplier tube for detector device fabrications. The TPB crystal's second-order hyperpolarizability (γ) was determined to be 8.641110–34 esu. The third-order nonlinear optical (TNLO) characteristics were examined using the Z-scan method. It showed a negative refractive index and a lower absorption coefficient. The TPB single crystal's Laser Damage Threshold (LDT) was determined to be 2.1612 GW/cm^2. The gamma retorts of the grown cylindrical crystal were tested with various gamma energy sources ranging from 356 to 1275 keV. The Time-of-flight (TOF) experimental setup was constructed with a grown TPB crystal and neutron-gamma discrimination was demonstrated with a ^{252}Cf fission source. The developed TPB crystal exhibits strong timing characteristics which operates consistently and offers a great capability for discrimination over unwanted gamma and other radiations.

Keywords 1,3,5-triphenylbenzene · Nonlinear optical crystal · Organic scintillators · Neutron-gamma discrimination · Fast neutron detector

N. Durairaj (✉) · S. M. Babu
Crystal Growth Centre, Anna University, Chennai, Tamil Nadu 600025, India
e-mail: duraimady@gmail.com

S. Kalainathan
Centre for Nanotechnology Research, VIT University, Vellore, Tamil Nadu 632014, India

© The Author(s), under exclusive license to Springer Nature Singapore Pte Ltd. 2023

S. S. Dhanabalan et al. (eds.), *Photonic Crystal and Its Applications for Next Generation Systems*, Springer Tracts in Electrical and Electronics Engineering,
https://doi.org/10.1007/978-981-99-2548-3_5

Introduction

Organic Molecules for NLO Applications

Organic molecules possess a greater role in radiation detection, fibre optical communication, optical switch, photonic and optical computing. Since they have molecular flexibility and large structural diversity (Clark and Lanzani 2010), these materials have fast response times and high electronic susceptibilities (Ledoux and Zyss 1994). Inorganic materials have a high melting point, are chemically inert and have good mechanical strength but relatively poor NLO properties than organic materials. Also, the NLO property in organic materials can be tuned during synthesis (Semin et al. 2021). The nonlinearity of organic materials is the presence of conjugated systems of the bonds giving rise to π-electrons delocalization, which can be improved by donor and acceptor functional groups (Gao et al. 2022). For various NLO applications, bulk single crystals are needed, which is difficult in the case of organic crystals since they are more brittle in nature, so an attempt is made from the solution growth technique to grow a bulk-size organic single crystal. Organic compounds having aromatic systems in conjugated places lead to transfer charges (Xu et al. 2019). These compounds are non-centrosymmetric in nature for the applications of nonlinear optical effects. The substituted derivatives of benzene are good for NLO properties.

Organic Molecules for Scintillators

Detecting invisible radioactive particles via scintillation spectroscopy is an especially sensitive technique (Lecoq 2020). During the middle of the 20th century, new organic molecules were analysed it emission, light output and decay times for the suitability of radiation detector device fabrications (Marchi et al. 2019; Sato et al. 2022). Two decay (prompt and delayed) fluorescent molecules allow for subatomic distinction, such as neutron-gamma separation in a diverse radiation field. Many researchers have concluded that the organic molecules with existing two-decay fluorescence are utilized for high-energy particle discrimination (Selvakumar et al. 2008; Jordan, et al. 2005). Some of the organic compounds are listed below:

- Anthracene.
- Stilbene.
- Salicylamide.
- p-terphenyl.
- Diphenylacetylene.
- 1,3,5-triphenylbenzene.
- Aspirin.
- Pyrene.
- Tetraphenyl butadiene.

- Triphenylmethane.
- 9,10-diphenyl anthracene.
- 2-methoxybenzoic acid.
- Phenylanthranilic acid.

It is thought to be rapid industrialization in several uses, including radiological medicine, surveillance systems and environmental monitoring structures (Lawrence et al. 2016; Shin et al. 2017; Hamel et al. 2017; Baker et al. 2007). However, the conventional crystal growth system has several unavoidable problems, including high manufacturing costs, specialized tools' necessity and challenges in locating vast area scintillators. To resolve these problems, numerous scientists have come across novel organic scintillators and developed low-cost methods for growing massive single crystals. Hence to overcome these issues, many researchers have found new organic scintillators and grown larger single crystals with low-cost techniques.

Properties of Scintillator Materials

The need for radiation-detecting materials has been at the forefront of materials research in recent years due to applications in national security, medical imaging, X-ray detection, oil well logging and high-energy physics (Lecoq 2020; Clarke et al. 2017; Wimmer-Schweingruber et al. 2020; Matsuya et al. 2022). There has been a growing interest in the development of scintillator materials with the following properties (Knoll 2010).

- Minimal optical self-absorption.
- High light yields the transformation of invisible radiation energy to visible light.
- Emission wavelength (typically 300–500 nm) matching the photodetector.
- Fast emission timing (1–30 ns).
- Particle separation between the complex of radiation.
- Good energy spectroscopy/resolution.
- Flexibility to grow the crystal in large size, low cost, strength and stability.

Importance of the Scintillation Crystals

For fast neutron detection, several known organic scintillator materials were tested. However, the trans-stilbene (t-stilbene) is currently used in various radiation detection devices (Knoll 2010). This is one of the best materials for this purpose which exhibits excellent pulse shape discrimination properties to separate the neutron pulses from the gamma-induced pulses (Quang et al. 2022; Cieślak et al. 2017; Sosa et al. 2019; Sun et al. 2023). However, other materials are being surveyed due to flammability,

toxicity, environmental anxieties, bulk production and cost issues. Other known scintillators, such as $LaBr_3$:Ce, NaI:Ti and BaF_2, also show a poor response in one or more of these properties.

There is a need for the development of high-efficiency neutron detectors that can function under reasonably large gamma fields. The currently available liquid and gas detectors are required maintenance and give problems due to leakages. These problems could be avoided with the use of scintillator crystals which are known to function for long times without any intervention. Hence, the current study aims at the fabrication of large transparent low-cost crystals that could serve as replacements for liquid and gas scintillator detectors for fast neutron detection against difficult radiation environments.

Among the well-known organic molecules, TPB ($C_{24}H_{18}$) single crystals are one of the most dynamic materials to distinguish neutrons in the gamma-ray circumstantial (Zaitseva et al. 2011). An important property of neutron detectors is the ability of the detector to record all the neutron pulses while discriminating against the pulses caused by gamma radiation. It has been recently reported that TPB has shown excellent neutron-gamma discrimination. Organic scintillation crystals are noted for their high light output efficiency. TPB has been identified as a crystal for potential use as a neutron detector. This crystal has been reported to show a good response to neutrons. It also has been shown to have good discrimination against gamma radiation. Neutron detectors fabricated using these crystals have a fast scintillating response and offer the advantage of higher efficiency. The proposal involves an investigation of the growth and characterization of TPB. This crystal is expected to have better scintillation properties and high radiation stability compared to the other crystals used for the same purpose.

For basic research and numerous applications, large cylindrical shape crystals are required for coupling with a photomultiplier tube (PMT) for detector fabrication. But the conventional solution growth crystals having multiple planes must be processed by cutting and polishing for device fabrication (Zaitseva et al. 2011; Zaitseva and Glenn 2015; Bourne et al. 2016). But the crystals grown by the unidirectional method are cylindrical and therefore suitable for coupling with PMT without major cutting and polishing (Durairaj et al. 2016). Furthermore, the significance of unidirectional/uniaxial growth can also be tested by acquiring information about the anisotropy of the crystal, which influences the light output and pulse shape responses (Schuster and Brubaker 2016; Dioni, et al. 2018). The ampoule design, cylindrical dimension of unidirectional solution growth of TPB single crystal and its initial studies for device assembly were reported (Durairaj et al. 2016). The grown TPB crystal structural properties were studied by XRD analysis. To find the growth mechanism and the nature of defects in the crystal, etching studies, thermal behaviour and mechanical properties were performed and reported (Durairaj et al. 2016). The linear optical property of TPB was discussed and reported (Durairaj et al. 2017).

Further, the NLO properties by Z-scan technique and laser damage threshold were performed for NLO applications. This work also includes the response of these laboratory-grown TPB crystals to the gamma rays of different energies emitted by radioactive sources. The timing property of the crystal is also tested to utilize it for

neutron-gamma discrimination by the time-of-flight (TOF) technique. The present work aims to discuss the TPB crystal growth methodology elaborately for producing various diameters of cylindrical crystal. This work could be useful for the bulk production of similar crystals in industry.

Experimental Details

Crystal Growth

Growth of the Single Crystal

Crystals were grown from toluene solutions using a method earlier developed for the growth of large water-soluble crystals (Zaitseva et al. 2011). As a result, the purchased chemicals have a light yellow colour that becomes further concentrated on dissolution and heating. Initial TPB powders have always been purified by being first stirred in acetone in a closed container at ambient temperature before being re-crystallized from solvents toluene seven times or until the forming crystals were entirely colourless. Then, the resulting growing saturated solution was prepared using dehydrated toluene.

Initial crystals of TPB were grown using the slow evaporation technique described in Farag et al. (1954). Under scientific realism, the finest of these tiny crystals was chosen to serve as the seeds for the development of bulk crystallization. First, TPB solid material was dissolved in toluene to create the initial solutions. Then, the solutions were permitted to stir at ambient temperature in covered containers for a few days until they reached saturation. The slow evaporation method appears simple, but creating a self-contained crystal about cm in size isn't easy.

Spurious nucleation, which causes the random growth of numerous crystals, resulting in deformation and crystal size restrictions, is the primary challenge in this task. The issue is particularly severe when growth is carried out using toluene-like volatile organic solvents. The prepared saturated TPB solution was transferred through filtering into a new growth vessel with a cover with a tiny hole in the centre to lessen the impact of these occurrences. The solution was then heated to a temperature 5–10 °C above saturation temperature after the opening had been sealed. The resilience of the solutions to random nucleation was significantly increased by overheating the solution without causing it to evaporate. This helped break up big crystalline formations. In order to avoid further formation just on dry surfaces, cooling the enclosed solution encouraged condensation on the interior vessel walls. For the introduction of a tiny seed dropped into the bottom of the jar, the sealed hole was opened to just a few degrees above ambient temperature in that the solution hit the before saturation point; the seed needed to be slightly dissolved to get rid of crystalline dust and damaged surfaces and then the saturated solution started to evaporate

slowly. The evaporation and growth rates were controlled by making tiny holes in the lid cover, which typically do not beat 1 mm/day.

In general, seed crystal for the unidirectional technique is prepared from the faster growth plane of the crystal grown from the conventional slow evaporation technique. The rapid growth plane mainly depends on the molecular interaction and packing density along the axis of the unit cell. Zaitseva et al. (2011) and Farag (1954) have reported the TPB molecule interaction and packing along the crystallographic axis of the unit cell, whereas the presence of all planes was enlightened from the layered arrangement of TPB molecules. The uniaxial growth plane was selected from a well-faceted conventional crystal faster growth plane of a particular axis (*a*-axis). The crystal morphology and indexed planes using the powderX software have been reported previously (Durairaj et al. 2016). Unidirectional TPB single crystal has been grown by mounting a seed crystal along an *a*-axis <100> plane in a glass ampoule (borosilicate material). 5 mm (Length) × 5 mm (diameter) of the seed crystal was used for the bulk growth of TPB crystal.

An optimized crystal growth procedure was demonstrated for the TPB crystal. The solubility of TPB was reported were shown in Durairaj et al. (2016), and according to that the saturated TPB solution was made at 40 °C. The existing unidirectional growth setup utilized for isothermal solvent evaporation provides a temperature gradient (39 °C in the top ring heater and 35 °C in the bottom ring heater) across the solution and growth zone. The temperature variation along the growth ampoule creates the concentration gradient and maximum supersaturation at the growth zone transporting the nutrition for the bulk growth of TPB. The maximum supersaturation was maintained throughout the growth period. By modifying the growth zone diameter of the glass ampoule, 10 to 30 mm of cylindrical TPB crystal was grown. The crystals were skillfully extracted from the glass and cut into circular discs for characterization. The growth direction of the TPB crystal was established by XRD analysis and established to be <100> plane as reported (Durairaj et al. 2016). The glass ampoule design, grown crystal with glass ampoule and cylindrical shape crystals are shown in Fig. 5.1.

Z-Scan Technique TNLO Property

The Z-scan technique analysed the TNLO property of unidirectional grown TPB single crystal (Sheik-bahae et al. 1989). The TPB crystal acts as a comparatively tiny lens in the Z-scan technique, and its focal length tends to vary as the crystal moves along the propagation of laser light. Throughout the examination, the crystal is exposed to varying strengths of an electric field at various places over the optical axis (Z-axis). As a result, the transmission (Tz) of light as a function of Z-position provides precise information about nonlinear refraction (n) and absorption (β). Consequently, the laser beam transmittance intensity can increase or decrease depending on the sample's absorption nature and refractive index.

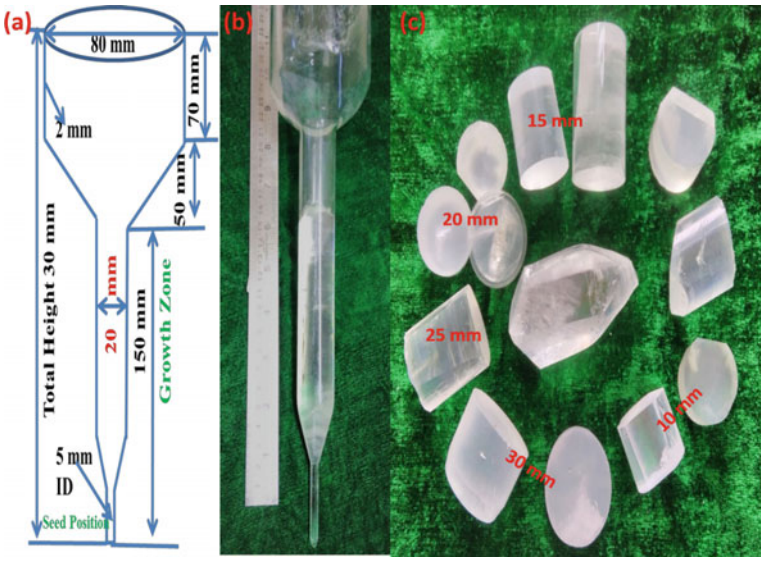

Fig. 5.1 **a** Glass ampoule design, **b** Unidirectional TPB single crystal with glass ampoule, **c** Cut and polished crystal cylinders grew from solution for usage as scintillator detectors setup

The experimental setup in Fig. 5.2 allows for two distinct varieties of transmission intensity, including closed aperture transmission, in which the transmitted beam from the crystal is gathered through a tiny pinhole (aperture). In contrast to the direct deduction of the full beam that passes through the crystal, the nonlinear refraction was captured and analysed using an open-aperture transmission. In addition, it provides details on the nonlinear absorption cross section. To analyse the *Z*-scan data is needed to compute the transmittance by determining the nonlinear equations for the transmission inside the crystal and the propagation between the crystal's outer surfaces to the aperture (Gaur et al. 2012).

The measurement was made with a He–Ne laser source with a wavelength of 632.8 nm. To transform the input laser beam into a Gaussian beam profile, the laser beam is narrowed using a Gaussian filter. The convex lens' focal length (f) at the focal point is 30 mm for the TEM00 mode Gaussian beam. The Gaussian beam waist (ω_0) has a diameter of 12.05 μm. The TPB single crystal was positioned in a crystal holder in a beam pathway and moved by the computer-aided translation stage in the + Z to −Z axial direction. A focal plane contains a tiny (0.67 mm) crystalline sample. The essential situation for this analysis is that the sample thickness must be less than Rayleigh diffraction length ($L < Z_R$) (Sheik-Bahae et al. April 1990). The small sample size (<1 mm) used for the Z-scan measurement will minimize the phase transition.

$$Z_R = \frac{K\omega_0}{2} \tag{5.1}$$

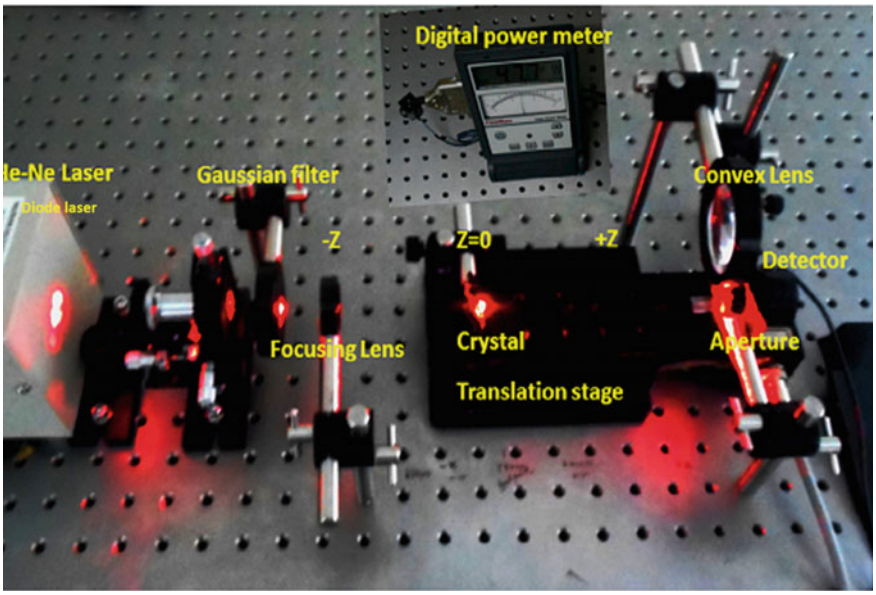

Fig. 5.2 Experimental arrangement for Z-scan measurement

where K is wave vector $\left(2\pi / \lambda = 9.92106\,\mathrm{m}^{-1}\right)$, ω_0 is the beam waist radius at a focus point computed by *1.27f/D*, where f is the focal length of a convex lens utilized and D is the laser beam radius (*2* mm) at the focal point, which can be used to derive the value of Rayleigh length as *0.72* mm.

An Nd:YAG laser has been used to calculate the LDT value for TPB. A variable attenuator was used to regulate the laser beam's energy before focussing on the convex lens with a 30 cm focal length. The unidirectional grown TPB single-crystal surface (<100> plane), which was positioned at the focal point of the lens, was exposed to a laser beam with a diameter of *1 mm* for this measurement.

Experimental Setup for Gamma Energy Measurement

The Philips photomultiplier tube (PMT) was attached with a cut and polished TPB crystal with dimensions of 30 mm in diameter and 40 mm in length. Dow Corning 200 (DC 200) silicon grease was used as scintillating glue to connect the crystal with PMT to transmit light from the crystal. Further, the crystal was encased with aluminium foil for scintillation light reflections and to avoid ambient light noise (Fig. 5.3). The output of the detector was processed and amplified through a spectroscopic amplifier so that the energy information of the output was retained. The analogue-to-digital converter (ADC) unit received the output signal from the amplifier, and a multichannel analyzer's histogram mode was used to collect data (MCA). Each radioactive source had enough time in the data collection period to provide a smooth

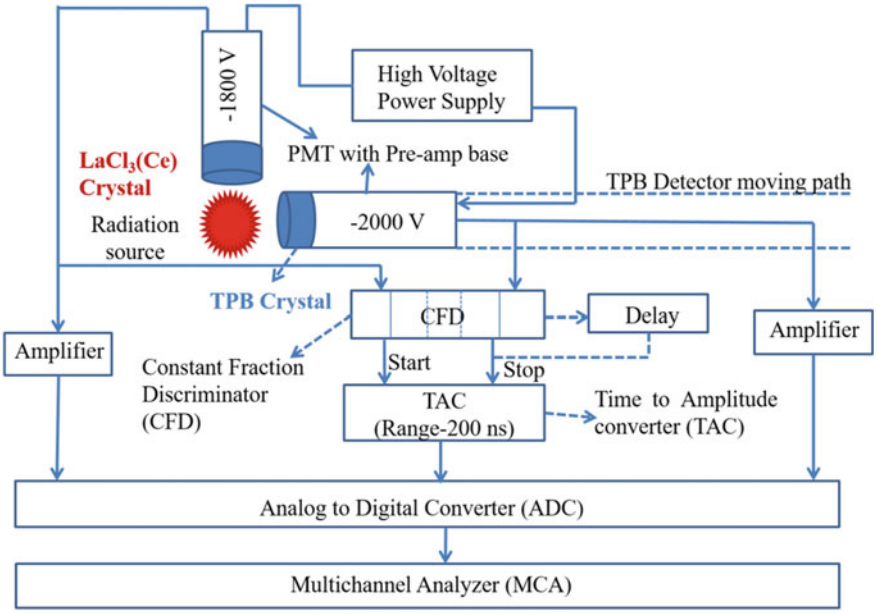

Fig. 5.3 Schematic diagram of Time of Flight (TOF) setup with the signal processing components for Neutron-gamma discrimination

spectrum. Figure 5.3 displays a schematic diagram of the experimental setup. Using ^{137}Cs, ^{60}Co, ^{22}Na and ^{133}Ba sources, the gamma-ray energy responses of the TPB crystal were studied. All measurements were taken under identical circumstances.

Time-Of-Flight (TOF) Setup

TOF is a basic particle discrimination technique based on its flight time to reach the detector from the source. This phenomenon can distinguish neutron and gamma particles over their flight path (Selvakumar et al. 2008). Figure 5.4a–d demonstrates the experimental setup and schematic block design for TOF measurements. Two detectors, cerium-doped lanthanum chloride ($LaCl_3$:Ce) and TPB, were used to make up the TOF arrangement for the current study. As a start detector, the $LaCl_3$:Ce detector was located extremely near the radioactive source (^{252}Cf) at a 90° angle to TPB. The TPB detector functioned as the stop detector and was placed at different distances relative to the source at 0° to measure the flight time of radioactive particles. The spontaneous emission of the californium (^{252}Cf) source was used for the detection of neutrons and gamma. A time-to-amplitude converter (TAC) circuit is used to save the signals from PMTs to construct the time difference spectrum and collect the energy information.

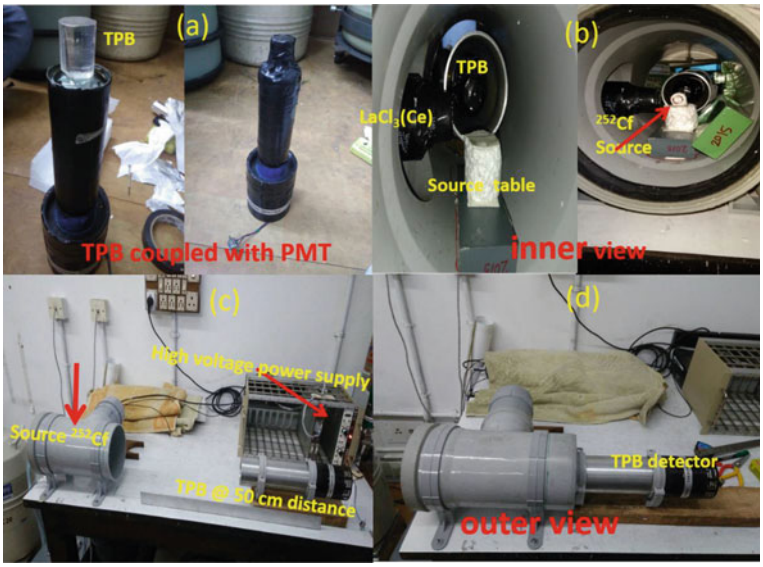

Fig. 5.4 3PB coupled with PMT; **(b)** Detectors positioning inner view; **(c)** 3PB detector at 50 cm from the source; **(d)**. Outer view of detectors close to 252Cf source.

Result and Discussions

Third Harmonic Generation

The closed aperture Z-scan curve of the TPB crystal is shown in Fig. 5.5a. In closed aperture mode, the normalized transmittance intensity curve showed a peak and a valley. The observed values shows that indication of negative nonlinearity, i.e. due to the absorption of light photons increases in local temperature in the crystal, which produces a solid self-defocusing refractive index (SDRI) effect (Rai et al. 2011). The self-defocusing effect occurs by increasing the beam divergence at the focal point.

The phase shift ($\Delta\phi$) is expressed in terms of the ratio between the difference in peak followed by valley transmittance intensity ($\Delta T_{(p-v)} = 2.95$) and aperture linear transmittance ($S = 0.088$) at the focus (Kanagasekaran et al. 2008)

$$|\Delta\phi| = \frac{\Delta T_{(P-V)}}{0.406(1-S)^{\frac{1}{4}}} \tag{5.2}$$

Here, $S = 1 - exp\left(\frac{2r_a^2}{\omega_a^2}\right)$, r_a is aperture radius and ω_a is beam radius. As a result, the grown TPB crystal's third-order nonlinear refractive index (n) can be determined by calculating it

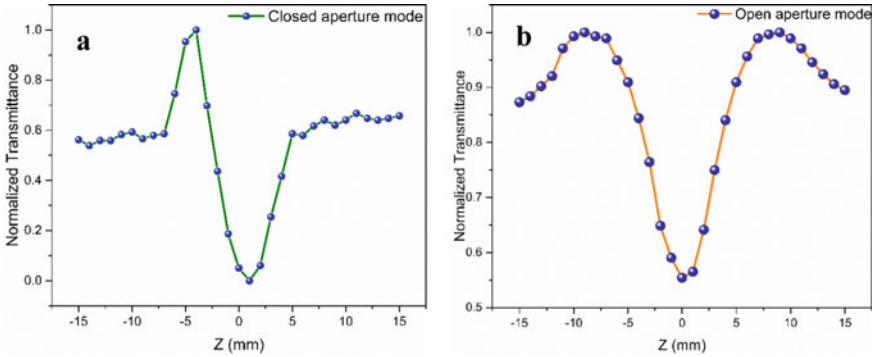

Fig. 5.5 Z-scan curve for TPB in (a) closed aperture mode; (b) open aperture mode

$$n = \frac{\Delta\phi}{L_{eff} I_0 K} \tag{5.3}$$

where L_{eff} is the effective thickness (1.73×10^{-3} m) of unidirectional grown TPB crystal assessed from $[1 - \exp(-\alpha L)]/\alpha$, where α (5.66×10^2) is the linear absorption coefficient, and I_0 is the intensity of the laser beam at the focal point.

Figure 5.5b depicts that in the Z-scan measurement of the crystal in an open-aperture mode, saturation absorption amplifies the peak followed by the valley, which is fallen the focal point along the optical path. It explains the reverse saturation absorption (RSA), which is indicated by the reduction in transmission with increasing input intensity. RSA describes that the absorption molecule in the ground state is lower than in the excited state (Henari 2001). From this curve, the nonlinear absorption coefficient (β) is able to be calculated using the following equation:

$$\beta = \frac{(2\sqrt{2})\Delta T}{L_{eff} I_0} \tag{5.4}$$

Here ΔT is (0.5545) valley value in an open-aperture curve. The calculated absorption coefficient $\left(\beta = 3.45 \times 10^{-5} \mathrm{mW}^{-1}\right)$ exposes that two-photon absorption process. The nonlinear refractive index (n) and absorption coefficient (β) were used to govern the TNLO susceptibility $\left(\chi^{(3)}\right)$ (Bharath and Kalainathan 2014)

$$\left|\chi^{(3)}\right| = \left[\left(\chi_{\mathrm{Im}}^{(3)}\right)^2 + \left(\chi_{\mathrm{Re}}^{(3)}\right)^2\right]^{\frac{1}{2}} \tag{5.5}$$

where $\chi_{Im}^{(3)}$ and $\chi_{Re}^{(3)}$ are the imaginary and real parts of nonlinear optical susceptibility, respectively. The imaginary and real parts of nonlinear optical susceptibility are calculated from the below derivations:

$$\chi_{Im}^{(3)}(esu) = \frac{\left(\lambda\beta C^2\varepsilon_0 n_0\right)10^{-2}}{4\pi^2} \tag{5.6}$$

and

$$\chi_{\mathrm{Re}}^{(3)}(esu) = \frac{\left(C^2 n\varepsilon_0 n_0\right)10^{-2}}{\pi} \tag{5.7}$$

Here $\varepsilon_0\left(8.854 \times 10^{-12}\mathrm{Fm}^{-1}\right)$ is the permittivity of free space, n_0 *(1.58) is* the linear refractive index of the TPB single crystal and C (3×10^8 m/s) is the velocity of light.

The coupling factor (ρ) is defined as the ratio between the imaginary and real parts of nonlinear optical susceptibility ($\chi_{Im,Re}^{(3)}$) (Senthil et al. 2014)

$$\text{i.e. } \rho = \frac{\chi_{Im}^{(3)}}{\chi_{Re}^{(3)}} \tag{5.8}$$

The expressed coupling factor (ρ) was calculated as 10.6. The coupling factor represents that the consequence of variation in NLO absorption of materials is more governing than the electronic nonlinearity and refractive index.

Also, the second-order hyperpolarizability (γ) is derived from the part of third-order large susceptibility ($\chi_{Re}^{(3)}$) to nonlinear polarization induced per molecule (Senthil et al. 2014)

$$\gamma_{Re} = \frac{\chi_{Re}^{(3)}}{f^4 N} \tag{5.9}$$

where f is the local field correction of Lorentz expression $f = \frac{(n_0^2+2)}{3}$ and N is the number of molecules per unit volume

The higher value of second-order hyperpolarizabilities (γ) was generally due to the higher conjugated π electron in the TPB molecules. The measured TNLO optical parameters such as nonlinear third-order nonlinear susceptibility $\left(\chi^{(3)}\right)$, refractive index (n), absorption coefficient (β) and second-order hyperpolarizabilities (γ) of the unidirectionally grown TPB single crystal are listed in Table 5.1.

The relatively higher value of $\chi^{(3)}$ can be ascribed to its molecule's electron density distribution and transfer between the acceptor and donor. Therefore, the

Table 5.1 Third-order nonlinear optical parameters by Z-Scan technique

S. No.	TNLO parameters of TPB by Z-Scan measurements	Values
1	Second-order molecular hyperpolarizability (γ)	8.6411×10^{-34} esu
2	Third-order nonlinear optical susceptibility ($\chi^{(3)}$)	1.103×10^{-4} esu
3	Nonlinear absorption coefficient (β)	3.454×10^{-5} mW^{-1}
4	Nonlinear refractive index (n)	1.649×10^{-11} m^{2}W^{-1}

Table 5.2 Comparison of third-order nonlinear optical susceptibility $\chi^{(3)}$ value of 3PB crystal with some well-known NLO crystals.

S. No.	Crystals	$\chi^{(3)}$ (esu)	References
1	1,3,5-triphenylbenzene (TPB)	1.103×10^{-4}	Durairaj et al. (2017)
2	Bis thiourea zinc acetate (BTZA)	1.679×10^{-6}	Pabitha and Dhanasekaran (2013)
3	Thiourea	5.6×10^{-6}	Girisun et al. (2011)
4	4-methyl-4′-N'-methylstilbazolium tosylate (MMST)	2.293×10^{-7}	Kumar et al. (2014)
5	l-alanine cadmium chloride (LACC)	0.9134×10^{-15}	Kalaiselvi et al. (2013)

conjugated π-electrons polarization will be high in the organic molecules and offer significant values of second-order hyperpolarizabilities (γ) and third-order nonlinear susceptibility $\left(\chi^{(3)}\right)$ for the TPB crystal. Consequently, the outcomes advise that the TPB single crystal could be a potential candidate for TNLO device applications.

Laser Damage Threshold (LDT)

The optical power density of the fundamental light beam is closely associated with crystal optical efficiency. When increasing power density causes optical materials to deteriorate. Therefore, the most advantageous attribute for device fabrications is that grown crystals should have high-energy surface damage tolerance. Low LDT values severely restrict the applications of the materials. A crystal's laser damage threshold is influenced by factors such as optical absorption, thermal conductivity and others. Although in high absorbing materials, the optical damage threshold throughout the crystal or surface is mainly instigated by temperature increase, which origins strain persuaded cracks. Hence the crystals have a higher specific heat capacity, then the crystal will have a high value of LDT (Saravanan et al. 2016). The LDT value of the unidirectional grown TPB crystal was determined by using the following formula:

$$\text{Power density } (P_d) = \frac{E}{\tau \pi r^2} \tag{5.10}$$

where τ is the laser pulse width in nanoseconds, E is laser energy in *milli-joule* and r is the radius of the circular spot size in millimetres. Therefore the calculated LDT value of TPB is 2.1612 GW/cm^2. Figure 5.6 displays the damaged TPB crystal's surface by the Nd:YAG laser source.

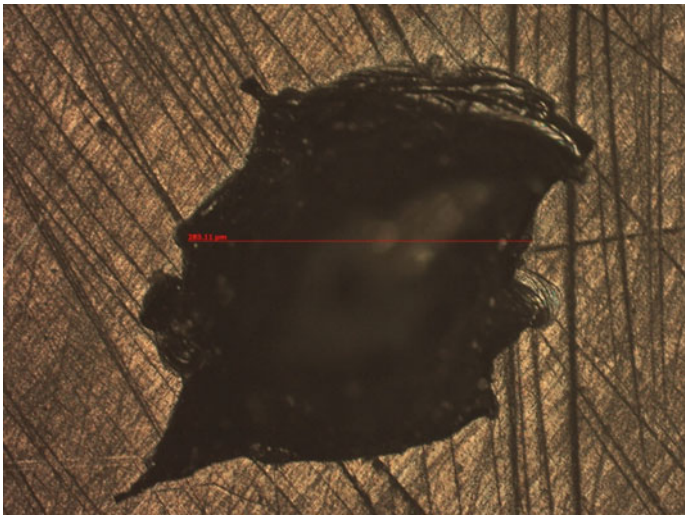

Fig. 5.6: Damaged TPB crystal surface by Nd:YAG laser

Gamma Energy Calibration

Before testing the neutron-gamma discrimination properties, the energy calibration was carried out for the TPB detector system. For detecting fast neutrons, organic compounds with low atomic numbers are preferable over inorganic ones. Due to their low atomic number (constitution of elements involving C and H primarily), the hydrocarbon molecules produce only the Compton continuum (amount of energy gained by electrons) for incident gammas (Sato et al. 2022; Yong-Hao et al. 2014; Ashrafi and Ghahremani Gol 2011). These detectors' energy calibrations are carried out using the energy at the Compton edge of the spectrum, resulting from the Compton scattering of an incident gamma photon by an electron at 180 degrees. During the Compton scattering, the energy gained by the scattered electron corresponding to the Compton continuum is calculated by the following equation:

$$E_c = \frac{2E^2}{E_0 + 2E} \tag{5.11}$$

where "E" is the incident photon energy and E_o–(0.511) is rest mass energy of the electron in MeV. The energy spectrum of TPB detector has been calibrated by using incident gamma rays of different energies from various sources, like ^{133}Ba (356 keV), ^{137}Cs (662 keV), ^{22}Na (511 keV), ^{60}Co (1252 keV average values of 1332 keV and 1173 keV) and 1275 keV (^{22}Na).

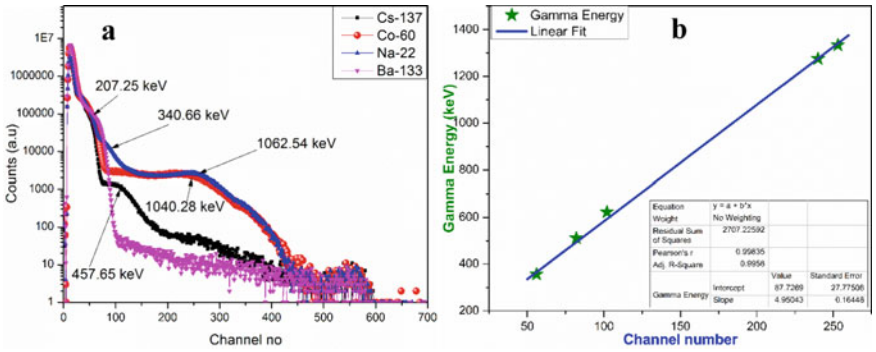

Fig. 5.7 **a** Coincidence energy spectrum of TPB crystal with different radioactive gamma energy sources and its respective Compton edges highlighted **b** Energy linearity of 3PB detector with different gamma energy sources

Corresponding Compton edge energies were calculated using the above relation (5.12) and used for calibration. As the Compton edge is not a discrete peak like a photo peak, an average channel number designating the edge in the spectrum has been used for calibration (Fig. 5.7a). The detector's calibration curve indicates the crystal's linear response to the gamma energies (Fig. 5.7a). The table shows the fit's extrapolated parameters (Fig. 5.7b inset). The errors replicate how well the generated parameters match linearly, according to the data.

Time Resolution of TPB Detector

To determine the time resolution of the TPB detector and a fast $LaCl_3$:Ce detector (commercially made) combination, a prompt time for the gamma source (^{60}Co) was generated. The stop detector (TPB) pulse was given known delays of 25, 33, 47, and 63 ns, and the resulting deviations in the response were noted to establish the time calibration (Fig. 7.8). With a prompt time resolution of ~1.5 ns, linearity of the time-to-amplitude converter (TAC) spectrum was detected (Fig. 7.8a). Figure 7.8b further illustrates that the $LaCl_3$:Ce and TPB crystal timing properties were in agreement.

The complex (alpha, gamma and neutron) radioactive source of ^{252}Cf was positioned at varying distances (d) ranging from 20 to 50 cm at intervals of 10 cm for the duration of flight measurement. The relatively high intense peaks belong to gamma and the remains belong to neutrons. These intensity differences are due to gamma-gamma and neutron-gamma events created in the LaCl:Ce and TPB detectors. When moving the TPB detector away from the source, the clear separation between gamma and neutron particles (Fig. 5.9a). The first peak from gamma events is basically in the same place. However, the peak from neutrons displays a clear shift towards upper channels. This shift indicates that the neutrons took longer to travel towards the TPB stop detector from a greater distance. The maximum distance for the stop detector

was kept at 50 cm because of the ^{252}Cf source's low intensity. The observed time taken for neutrons to reach the TPB detector is called flight time (t).

Fast Neutron Detection

The TOF spectrum has also been changed to the neutron energy spectrum using the relativistic energy Eq. (5.12) and integrating the flight time and path length from the observations (Fig. 5.9b) (Blain et al. 2017). The measurement was made at different distances (d) of 20, 30, 40 and 50 cm to determine the efficiency of the TPB detector. As a reference, the TOF's prompt gamma peak was used. This conversion has eliminated the gamma components from the neutron energy spectrum. Figure 5.8b shows that much error is introduced into the energy measurement due to the weak source strength at greater distances. The relativistic kinetic energy equation for moving neutrons is given by

$$E_n = m_0 c^2 \left(\left(1 - \frac{v^2}{c^2} \right)^{-\frac{1}{2}} - 1 \right) \tag{5.12}$$

where m_0 is the neutron rest mass (939.49 meV/c^2), c is the light velocity and v is the neutron velocity ($v = \frac{d}{t}$; d is the distance, t is time of flight).

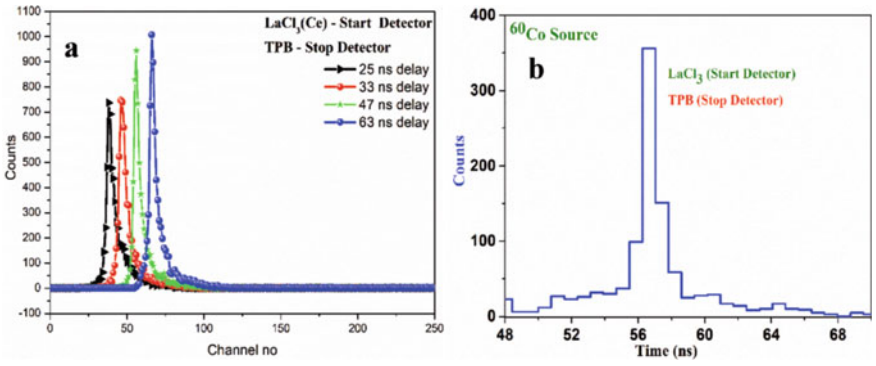

Fig. 5.8 **a** Change in peak location when the delay is altered; **b** The prompt TAC spectrum from a 60Co source without any energy selection.

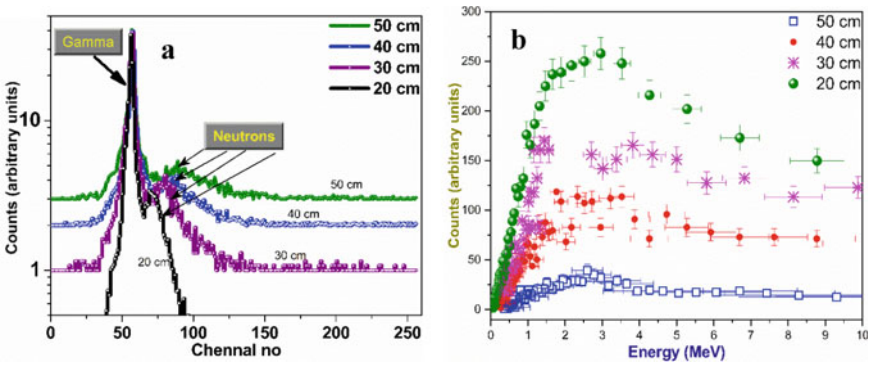

Fig. 5.9 **a** TAC spectra fixed 16 ns delay with a stop signal for 20–50 cm distances. The spectra for various distances are vertically moved to display the shift in the neutron peak; **b** Neutron energy spectrum at various distances.

Conclusion

The unidirectional TPB single crystal with different diameters in the cylindrical shape was grown along the <100> plane from the solution. The experimental arrangements of the TPB detector for energy and timing measurements have been discussed. The energy calibration utilized Compton edges in the gamma spectra corresponding to different radioactive sources. It shows a linear relationship between the pulse height and rising edge energies for various incident gamma-ray energies from radioactive sources. The single crystal formed using the unidirectional approach has good timing qualities, as evidenced by the timing resolution results. As a result, it operates dependably as a neutron detector and can discriminate against the gamma radiation background. Neutron energy spectra generated from the TOF measurements also agree with the spectra expected [47] from the ^{252}Cf source. The TPB crystal's high-energy particle discrimination property can be tested using the pulse shape discrimination (PSD) method. The findings will subsequently be enhanced by combining the PSD and TOF approaches. One can compare neutron-gamma discrimination and time resolution effectiveness with the TPB crystal made via conventional and unidirectional techniques. The PSD method can also test the TPB crystal to detect other radioactive particle sensitivity.

Acknowledgements The author Dr Durairaj. N would like to thank Dr. D.S. Kothari Postdoctoral Award (No. F. 4-2/2006 (BSR)/PH/20-21/0142 dated 14 September 2021) by the University Grants Commission (UGC), Government of India. He also thanks VIT University Vellore, IGCAR Kalpakkam and Saha Institute of Nuclear Physics (SINP) Kolkata for their constant support in utilizing the facilities.

References

Ashrafi S, Ghahremani Gol M (2011) Energy calibration of thin plastic scintillators using Compton scattered γ-rays. Nuc Inst Met Phys Res A 642:70–74

Baker JH, Galunov NZ, Tarasenko OA (2007) Neutron scintillation detectors for environmental, security and geological studies. IEEE Nucl. Sci. Symp. Conf. Rec. 2:1358–1364

Bharath D, Kalainathan S (2014) Synthesis, growth, thermal and optical studies on third-order nonlinear optical material (E)-2-{3-[2-(4-chlorophenyl) vinyl]-5, 5-dimethylcyclo-hex-2-en-1-ylidene} malononitrile for optoelectronic application. Spectrochim Acta Part A Mol Biomol Spectrosc 120:32–39

Blain E, Daskalakis A, Block RC, Danon Y (2014) Measurement of prompt fission neutron spectrum for spontaneous fission of 252Cf using γ multiplicity tagging. Phys Rev C 95:064615-1-7

Bourne MM, Clarke SD, Adamowicz N, Pozzi SA, Zaitseva N, Carman L (2016) Neutron detection in a high-gamma field using solution-grown stilbene. Nucl Inst Methods Phys Res A 806:348–355

Cieślak MJ, Gamage KAA, Glover R (2017) Pulse shape discrimination characteristics of stilbene crystal, pure and 6Li loaded plastic scintillators for a high resolution coded-aperture neutron imager. J Instrum 12(07):P07023

Clark J, Lanzani G (2010) Organic photonics for communications. Nat Photon 4:438–446. https://doi.org/10.1038/nphoton.2010.160

Clarke SD, Hamel MC, Pozzi SA (2017) Neutron and gamma-ray energy reconstruction for characterization of special nuclear material. Nucl Eng Technol 49(6):1354–1357

Dioni L et al (2018) Tests of a solution-grown stilbene scintillator in mono-energetic neutron beams of 565 keV and 5 MeV. Nucl Inst Methods Phys Res A 880:210–215

Durairaj N, Kalainathan S, Krishnaiah MV (2016) Investigation on unidirectional growth of 1,3,5-Triphenylbenzene by Sankaranarayanan-Ramasamy method and its characterization of lifetime, thermal analysis, hardness and etching studies. Mater Chem Phys 181:529–537

Durairaj N, Kalainathan S, Kumar R (2017) Optical and laser damage threshold studies on 1, 3, 5-triphenylbenzene scintillator crystal grown by Sankaranarayanan-Ramasamy (SR) technique. Optik 140:900–907

Gao L, Li B, Yi H, Cui J, Yang L, Song Y, Yang H-R, Zhou L, Fang S (2022) Nonlinear optical properties of pyrene derivatives based on a donor-acceptor structure and its polyurethane composites. ACS Omega 7(32):27959–27968

Gaur P, Sharma D, Singh N, Malik BP, Gaur A (2012) Determination of nonlinear absorption and refraction in direct and indirect band gap crystals by Z-scan method. Spectrochim Acta Part A: Mol Biomol Spectrosc 97:45–49

Girisun TCS, Dhanuskodi S, Vinitha G (2011) χ (3) measurement and optical limiting properties of metal complexes of thiourea using Z-scan. Mater Chem Phys 129(1–2):9–14

Hamel MC, Polack JK, Ruch ML, Marcath MJ, Clarke SD, Pozzi SA (2017) Active neutron and gamma-ray imaging of highly enriched uranium for treaty verification. Sci Rep 7:1–10

Henari FZ (2001) Optical switching in organometallic phthalocyanine. J Opt a: Pure Appl Opt 3(3):188

Jordan DV et al (2005) Methods and instruments for fast neutron detection. Pacific Northwest National Laboratory Richland, Washington, p 99352

Kalaiselvi P, Alfred Cecil Raj S, Vijayan N (2013) Linear and nonlinear optical properties of semiorganic single crystal: l-Alanine cadmium chloride (LACC). Optik 124(24):6978–6982

Kanagasekaran T, Mythili P, Srinivasan P, Nooraldeen AY, Palanisamy PK, Gopalakrishnan R (2008) Studies on the growth, optical, thermal, and mechanical properties of pure and o-Nitroaniline doped benzil crystals. Crystal Growth Design 8(7):2335–2339

Knoll GF (2010) Radiation detection and measurement. Wiley, New York

Krishna KM, Sudhahar S, Silambarasan A, Sornamurthy BM, Mohan Kumar R (2014) Crystal growth, structural, linear and nonlinear optical studies of 4-methyl-4′-N'-methylstilbazolium tosylate single crystals. Optik 125(2):751–755

Lawrence CC, Febbraro M, Flaska M, Pozzi SA, Becchetti FD (2016) Warhead verification as inverse problem: applications of neutron spectrum unfolding from organic-scintillator measurements. J Appl Phys 120(6):064501

Lecoq P (2020) Scintillation detectors for charged particles and photons. Part Phys Ref Libr: Detect Part Radiat 2:45–89

Ledoux I, Zyss J (1994) Nonlinear organic molecules and materials for optoelectronic devices. Int J Nonlinear Opt Phys 3(03):287–316

Marchi T, Pino F, Fontana CL, Quaranta A, Zanazzi E, Vesco M, Cinausero M et al (2019) Optical properties and pulse shape discrimination in siloxane-based scintillation detectors. Sci Rep 9(1):1–13

Matsuya Y et al (2022) Features of accelerator-based neutron source for boron neutron capture therapy calculated by particle and heavy ion transport code system (PHITS). AIP Adv 12(2):025013

Pabitha G, Dhanasekaran R (2013) Investigation on the linear and nonlinear optical properties of a metal-organic complex—Bis thiourea zinc acetate single crystal. Opt Laser Technol 50:150–154

Quang ND et al (2022) Measuring and unfolding fast neutron spectra using solution-grown trans-stilbene scintillation detector. Nucl Eng Technol

Rai RN, Mudunuri SR, Reddi RSB, Kumar Satuluri VSA, Ganeshmoorthy S, Gupta PK (2011) Crystal growth and nonlinear optical studies of m-dinitrobenzene doped urea. J Crystal Growth 321(1):72–77

Saravanan M, Senthil A, Abraham Rajasekar S (2016) Investigations on the low temperature solution growth, etching, laser damage threshold, photoluminescence, electrical characterization and nonlinear optical properties of organic material: ammonium hydrogen l-malate. Optik 127(4):1685–1689

Sato A, Koshimizu M, Fujimoto Y, Komatsuzaki S, Kishimoto S, Asaia K (2022) Novel class of organic crystal scintillators based on aggregation-induced emission. Mater Chem Front 6:1470–1476

Schuster P, Brubaker E (2016) Characterization of the scintillation anisotropy in crystalline stilbene scintillator detectors. Nucl Inst Methods Phys Res A. https://doi.org/10.1016/j.nima.2016.11.016

Selvakumar S, Arulchakkaravarthi A, Kumar R, Muralithar S, Sankar S, Sivaji K (2008) Enhanced energy resolution (22Na, 137Cs and 241Am) and alpha–gamma (241Am + 60Co) and neutron-gamma (241Am–Be) pulse shape discrimination properties of p-terphenyl crystals prepared by modified selective self-seeded vertical Bridgman technique (SSVBT). Solid State Commun 145:482–486

Semin S, Li X, Duan Y, Rasing T (2021) Nonlinear optical properties and applications of fluorenone molecular materials. Adv Opt Mater 9(23):2100327

Senthil K, Kalainathan S, Ruban Kumar A, Aravindan PG (2014) Investigation of synthesis, crystal structure and third-order NLO properties of a new stilbazolium derivative crystal: a promising material for nonlinear optical devices. RSC Adv 4(99):56112–56127

Shehata FM (1954) the structure of 1, 3, 5-Triphenylbenzene. Acta Crysta 7:117–121

Sheik-bahae M, Said AA, Van Stryland EW (1989) High-sensitivity, single-beam n2 measurements. Opt Lett 14:955–957

Sheik-Bahae M, Said AA, Wei TH, Hagan DJ, Van Stryland EW (1990) Sensitive measurement of optical nonlinearities using a single beam. IEEE J Quantum Electron 26(4):760–769. https://doi.org/10.1109/3.53394

Shin TH, Di Fulvio A, Clarke SD, Chichester DL, Pozzi SA (2017) Fast-neutron multiplicity counter for the detection of diversion scenarios. No. INL/CON-17–41062. Idaho National Lab.(INL), Idaho Falls, ID (United States)

Sosa CS et al (2019) Improved neutron–gamma discrimination at low-light output events using conical trans-stilbene. Nucl Instrum Methods Phys Res Sect A: Accel, Spectrometers, Detect Assoc Equip 916:42–46

Sun Q et al (2023) Dual discrimination of fast neutrons from strong γ noise using organic single-crystal scintillator. Matter 6(1):274–284

Wimmer-Schweingruber RF et al (2020) The lunar lander neutron and dosimetry (LND) experiment on Chang'E 4. Space Sci Rev 216:1–40

Xu W, Wang W, Li J, Wu Q, Zhao Y, Hou H, Song Y (2019) Two-photon absorption property and excellent optical limiting response of three Schiff base derivatives with large conjugated system. Dyes Pigments 160:1–8

Yong-Hao C et al (2014) Study of n-γ discrimination in low energy range above 40 keVee) by charge comparison method with a BC501A liquid scintillation detector. Chi Phys C 38(3):036001-1-036001-5

Zaitseva N, Carman L, Glenn A, Newby J, Faust M, Hamel S, Cherepy N, Payne S (2011) Application of solution techniques for rapid growth of organic crystals. J Cryst Growth 314:163–170

Zaitseva N, Glenn A, Carman L, Paul Martinez H, Hatarik R, Klapper H, Payne S (2015) Scintillation properties of solution-grown trans-stilbene single crystals. Nucl Instrum Methods Phys Res A 789:8–15

Chapter 6
Two-Dimensional Photonic Crystal-Based Filters Review

K. Rama Prabha and S. Robinson

Abstract This chapter deals with, initially, the introduction, history, types, and applications of photonic crystal-based filters. Optical filters are the devices used to pass the signal with various wavelengths. Filters are normally used to pass the desired wavelength. Typically, optical filters are used to transmit light signals. In general, the filters can be broadly classified into band pass, band stop, low-pass, and high-pass filters. The optical filter is generally classified into two types channel drop filter and add–drop filter. In most optical devices, channel drop filters are one of the most important components in designing photonic integrated circuits. This chapter analyzes the detailed survey of all optical filters, such as add–drop filters, channel drop filters, passband and band stop filters, and the different mechanisms, lattice structures, defects cavity types introduced into the waveguide, and different types of material characterization will be explained very clearly. Coupling efficiency, dropping efficiency, Q factor, and pass bandwidth are the device's structural and functional aspects that are taken into account. Also, a detailed analysis of the filter's coupled mode theory will be presented. The Q factor for the inner circular add–drop filter was calculated as 99.3 and the spectral width as 14 and, for the circular add–drop filter, the functional parameter Q factor accounted as 166.25 and the spectral width calculated as 8. The Q factor and transmission efficiency accounted for the fabrication of PC-based filters realized through SOI wafers and various types of fabrication techniques will be explored in this chapter. Finally, the important applications of photonic crystal-based optical filters will be presented.

Keywords Photonic crystals · Add–drop filters · Channel drop filters · Ring resonators

K. R. Prabha (✉) · S. Robinson
Department of Electronics and Communication Engineering, Mount Zion College of Engineering and Technology, Pudukkottai, Tamil Nadu, India
e-mail: ramaprabhakrishna8@gmail.com

© The Author(s), under exclusive license to Springer Nature Singapore Pte Ltd. 2023

S. S. Dhanabalan et al. (eds.), *Photonic Crystal and Its Applications for Next Generation Systems*, Springer Tracts in Electrical and Electronics Engineering,
https://doi.org/10.1007/978-981-99-2548-3_6

Introduction

Photonic Crystals (PCs) define the periodical arrangement of nanostructures that directly affect the photons. The refractive index of the photon affects the signal propagation of EM waves (PreetiRani and Sinha 2015). A PC-based light photon coupled inside the structure directly depends on wavelength. Initially, the wavelengths coupled inside are defined as modes. A group of allowed modes is called a band. The photonic band gap defines as the forbidden gap of photons. Disallowed bands of wavelengths are called photonic band gaps (Pirzadi et al. 2016; Sathyadevaki et al. 2017; Geerthana et al. 2015).

Photonic integrated circuits are used in many photonic crystal devices integrated with a single semiconductor chip. Many of the optical components used in photonic integrated circuits as lasers, modulators, detectors, filters, and multiplexers/demultiplexers. Generally, there are various materials used for improving the better performance of the device. Hence the silicon material is most widely used in PC-based filters to optimize high efficiency. Reliability and robustness are the two most important factors in silicon material. While using this material, the PIC drastically reduces the cost (Yablonovitch 1987).

Photonic Crystals in Nature

In the year 1887, Lord Rayleigh first studied the propagation of electromagnetic waves. Later in 1987, Eli Yablonovitch and Sanjeev John published two papers on photonic crystals. In Lord Rayleigh's study, he finds that the spectral range of large reflectivity is studied (Yablonovitch 1987). These structures are currently being used in a variety of applications, from reflective coatings to improving the efficiency of LED bulbs to highly reflective mirrors used in laser cavities. In recent research, similar structures are employed for a wide variety of purposes, including extremely reflecting mirrors in some laser cavities, reflective coatings, and improving LED efficiency. Instead of an electrical band gap, which prevents photon transmission for energies that fall within the gap, photonic band gap materials, also known as photonic crystals (PCs), are the optical equivalent of semiconductors (John 1987). A simple layered device, like a dielectric mirror, that might have a band gap for light that enters the structure perpendicular to the layers is a 1D photonic crystal. Photonic crystal broadly classified into one dimensional, two dimensional and three dimensional (Fig. 6.1).

Three different forms of PCs exist: (1DPCs), (2DPCs), and (3DPCs) (John 1987).

One-dimensional photonic crystal

Layers with various dielectric constants may be deposited or joined together to generate a band gap in a single direction in a one-dimensional photonic crystal.

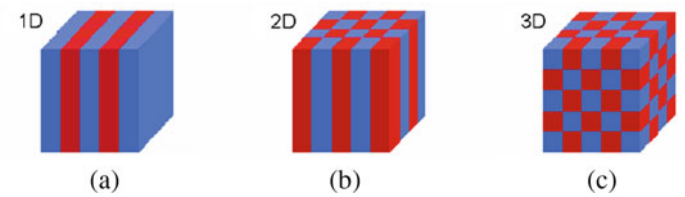

Fig. 6.1 **a** One-dimensional, **b** Two-dimensional, and **c** Three dimensional

An illustration of this kind of photonic crystal is a Bragg grating. Anisotropic one-dimensional photonic crystals have the potential to be used as optical switches and can be either isotropic or anisotropic.

Two-Dimensional Photonic Crystals

The sensor based on 2DPCs is receiving increased attention from the scientific community because it has a relatively simple structure, small size, better confinement of light, accurate band gap calculation, propagation loss is low, and easy integration compared to 1DPCs and 3DPCs. (Ashkan et al. 2015).

Figure 6.2 depicts the 2D photonic crystals of the rod and hole slab (Yablonovitch 1987). Transverse Magnetic (TM) mode with magnetic fields is perpendicular and TE mode is parallel to the rod axis. These modes are known as transverse electric (TE) and transverse magnetic (TM) modes, respectively.

Classifications of photonic crystal defects

The classification of PC-based defects is represented in Fig. 6.3 (Yablonovitch 1987). Photonic crystal defect is divided into three types, namely line defect, point defect, and surface defect.

- Point defects are specifically deleted rods in a structural design that are referred to as point defects. It is conceivable for a point defect to draw a light mode into the band gap when it forms in a photonic crystal.

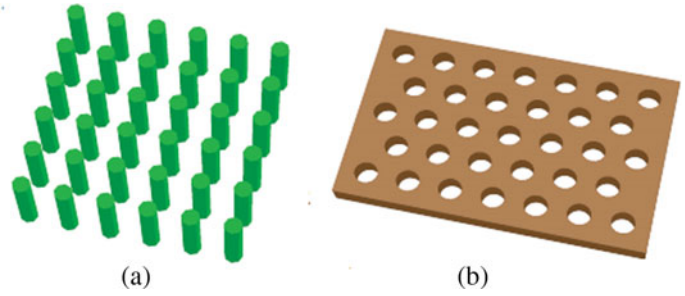

Fig. 6.2 Structure of 2D Photonic Crystals **a** Rod slab and **b** Hole slab

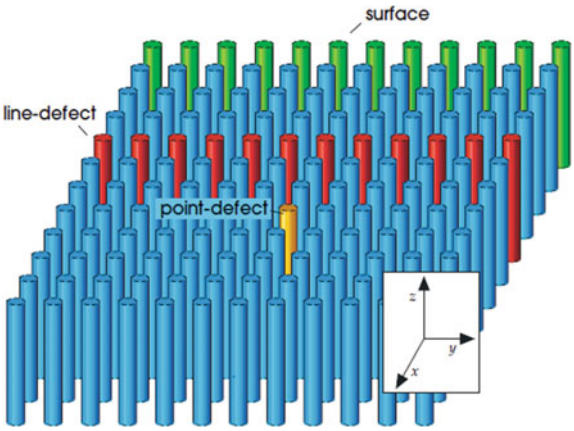

Fig. 6.3 Line and point defect

- Line defects are rows or columns of a rod that have been eliminated from a structural design. Depending on the structure's lattice constant and rod radius, two or three band gap areas are produced. No waves are allowed to pass through the gadget during these band gaps. Yet, some band gap wavelengths can only propagate inside the structure if a device flaw is introduced.
- Surface defects are defined as any rods from the surface rod that have been removed.

Point Defect

The light is captured by a point flaw. An optical cavity is another name for it. A point defect figure can be used to create the most basic type of photonic crystal cavity. Into the photonic crystal slab with perfect periodicity. The alteration of a single hole within the crystal constitutes a point defect.

Line Defect

A line defect is used to create a wave-guiding effect by transporting light from one place to another. A point defect cavity in the figure can be seen as extending into a line defect cavity. In this instance, the defect spans several consecutive lattice constants. Standing waves inside a line defect cavity are identical to the modes provided by that cavity.

Photonic Crystal-Based Filters

Specified wavelengths of light are the only ones that are transmitted via optical filters. They are commonly implemented as flat glass or plastic items in the optical path.

Optical channels specifically send light in a specific scope of frequencies, that is to say, colors, while impeding the rest of them. They can normally pass long

frequencies with just a long pass channel filter (LPF), short frequencies with just a short pass channel filter (SPF), or a band of frequencies, obstructing both longer and more limited frequencies with a bandpass channel filter (BPF). The passband might be smaller or more extensive, and the change or cutoff between maximal and negligible transmission can be sharp or slow (Fallahi et al. 2019; Rajalakshmi et al. 2015; Shanmuga Sundar et al. 2018a, b).

Optical Filter Classification

The optical filter can be classified into two types as depend on the wavelength absorptive filters.

Absorptive Filters

Absorptive channels send the limited frequencies by retaining undesirable ones. Figure 6.4 depicts the absorptive channel filter. These channels normally comprise colored glass or pigmented gelatin gums, and are moderately reasonable to fabricate and buy. The capacity of absorptive channels to weaken light depends on the channel's actual thickness and how much color or pigmentation is present in the filter.

Absorptive filters are relatively less precise when compared with dichroic types. They are regularly utilized in applications that require the transmission of a large number of frequencies as well as those that require the obstructing of short frequencies and the transmission of longer ones.

Thin-film interference Filters

Dichroic channels, otherwise called obstruction channels, channel light by dismissing every single undesired frequency, permitting chosen frequencies to go through. The expression "dichroic" is gotten from the Greek word díchros, signifying "of two different colors." These channels are built utilizing slight film innovation by saving a few layers of a dielectric film on one side of an optically level piece of straightforward glass. At the point when light strikes the covered side of the channel, the different layers of film amplify and communicate the ideal frequencies while reflecting and lessening the undesired ones.

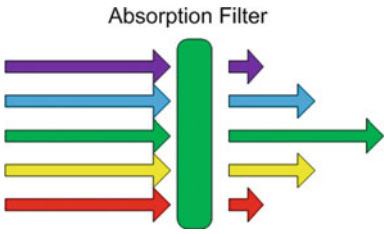

Fig. 6.4 Absorptive filters

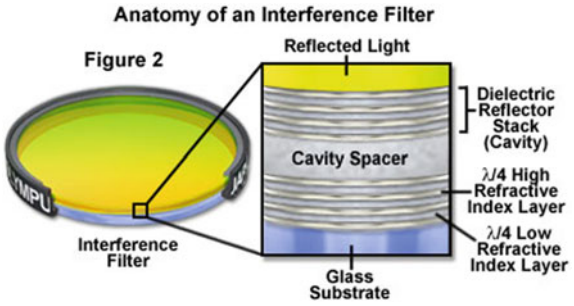

Fig. 6.5 Dichroic (Interference) filters

Figure 6.5 shown in the image above, dichroic filters rely on the series of reflective cavities between the film layers to achieve their precise filtering. Optical interference occurs when these cavities resonantly emit the appropriate wavelength frequencies while destroying or rejecting all others. Interference filters are far better suited to precision applications than absorptive ones due to their significantly improved selectivity.

There are many applications for using optical filters:

- Filters can eliminate some unwanted photons.
- For the gain equalization of fiber amplifiers used in optical fiber communications, wavelength-dependent losses are useful.
- In wavelength division multiplexing optical data transmission systems, filters in the form of fiber-optic add–drop multiplexers can extract or inject single channels.
- Neutral density filters can weaken optical signals without changing their spectrum characteristics.

All optical filters are designed to split an image into two identical images with different brightness levels, transmit or reflect particular wavelengths, attenuate or enhance an image, and more. Consider important terms, production methods, and the numerous types of filters on the market today to grasp the significance of selecting the right optical filter for any application. All filters, regardless of how they are made, pass, absorb, and/or reflect some amount of incident light, all have similar optical properties.

- Long pass channels: send frequencies over a cut-on frequency.
- Short pass channels: send frequencies under a cut-off frequency.
- Bandpass channels: send frequencies in a thin reach around a predefined frequency.
- Channel drop channels: sift looks over one little frequency range (channel) and reroutes (drops) it into another waveguide (called the drop waveguide).
- Add/drop channels: potentially drop (eliminate) at least one frequency, passing those signs to another waveguide.

Add–Drop Filters

When a filter is described as a "add and drop filter," it means that it can add one or more new wavelength channels to an existing multi-wavelength WDM network.

One important tool for coarse wavelength division multiplexing systems (CWDM) is the add–drop filter (ADF), which enables the addition and/or deletion of required output channels without interfering with other channels. Coupling efficiency, dropping efficiency, pass bandwidth, and quality factor are crucial ADF factors. Due to their small size, rapid operation, lengthy lifespan, suitability for photonic integrated circuits, and potential for use in future optical networks, photonic crystal (PC)-based optical devices have gained a lot of attention (Robinson and Nakkeeran 2012a).

The fundamental structure for a ring resonator-based ADF is given by an optical ring resonator sandwiched between two optical waveguides. In other words, the ring resonator causes the light to be ejected from the transmitted waveguide and drop into the base waveguide.

Figure 6.6 shows the schematic structure of the ring resonator-based add–drop filter which consists of bus and dropping waveguides and the ring resonator. Four ports are also included. The term "add-drop filter" refers to a device's capacity to build one and additional wavelength channels to an actual multi-wavelength signal and/or to eliminate the channels from one transmission channel to another. (Robinson and Nakkeeran 2013b).

In channel-dropping devices, resonators are used. In Fig. 6.8, a resonant cavity embedded between two parallel waveguides is displayed. The add/drop filter is the name of this structure. Several geometries, such as square, circular, and elliptical, are possible for the resonant cavity. The objective of dropping one channel by a filter without impacting the other channels can be accomplished if the resonators are small enough so that the spacing of the resonant frequencies fits the set of wavelength division multiplexing (WDM) channels within the communications window (Failed 2013).

The fundamental add/drop filter taken into account is made up of two identical and parallel single-mode slab waveguides that are connected by a resonant cavity with a variety of configurations. We took into consideration elliptical, circular, and

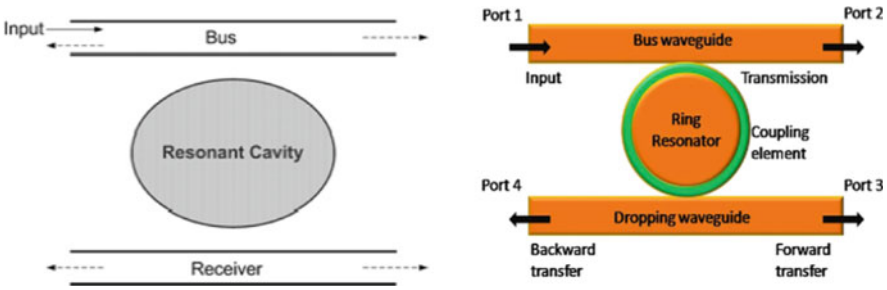

Fig. 6.6 Schematic structure of ring resonator and add–drop filter

square cavities of various sizes, as well as single and multiple square cavities. The add/drop efficiencies, spectrum widths, number of channels, and device power loss through radiations will all be examined with the various cavity shapes and sizes.

Dense Wavelength Division Multiplexing Add–drop Filter

A three-port multiplexing/demultiplexing device known as DWDM add/drop. It divides or joins together a single DWDM channel. The other channels in its operating wavelength range (C band or C + L bands). ITU DWDM wavelength grid is the chosen value for the central wavelength. Channel spacing options include 100 and 200 GHz. It is the fundamental component of multiple-channel DWDM mux/demux modules. This product enables the addition or removal of a single DWDM wavelength at any network node.

Features

- 100 GHz or 200 GHz channel distance
- Low insertion loss
- High channel insulation
- Epoxy resin-free optic path.

Applications

- DWDM frameworks
- Add/drop modules
- Lab Research and development
- CATV frameworks.

Coarse Wavelength Division Multiplexing Add–Drop Filter

At ITU CWDM grids, these add/drop filters have a center wavelength. Hence, the channel was eliminated or merged with other channels from the CWDM. Due to their unique property, these add/drop filters used a multimode CWDM network.

Features

- Based on proven thin-film filter technology
- Multimode fiber input and output
- Ultra flat and wide passband
- Low insertion loss
- High channel isolation
- High stability and durability.

Applications

- Systems using CWDM
- Optical passive Networks.

Parameters

- Transmission efficiency
- Dropping efficiency
- Quality factor
- Spectral width.

Transmission efficiency

The ratio of the power received over a transmission line to the power transmitted, as well as the ratio of a circuit or device's output to its input power, is known as transmission efficiency.

$$\text{Efficiency} \;=\; \text{Pout}/\text{Pin} * 100\%$$

Coupling efficiency

The effectiveness with which two optical components transfer optical power. the amount of power that can be transferred from one component to another.

Quality factor

A quality factor is a dimensionless parameter that measures a resonator's bandwidth with its center frequency and describes how under-damped an oscillator or resonator is.

$$\text{Q factor} \;= \lambda/\Delta\lambda$$
$$\Delta\lambda = \lambda_2 - \lambda_1$$

Spectral width

The spectral width is otherwise called pass bandwidth. The spectral width is a wavelength interval.

$$\Delta\lambda = \lambda_2 - \lambda_1$$

Pcrr-Based Optical Add–Drop Filter

The features of the circular PCRR-based add–drop filter, including transmission efficiency, dropping efficiency, spectral breadth, quality factor, and resonance wavelength, are studied. The resonant wavelength for the add–drop filter has been determined using the 2D FDTD approach. The most often used technique for figuring out a structure's band gap is called PWE.

Figure 6.7 sketches quasi square inner circular shaped PCRR-based add–drop filter, which consists of four ports. The ports are A (input), B (output), C (output), and D (output). The bus waveguide is part of the waveguide that is on top. The waveguide, also known as the bottom waveguide or drop waveguide, is so named. The bus waveguide contains port A (input) and Port B (input). The drop waveguide contains Port C (output) and Port D (output).

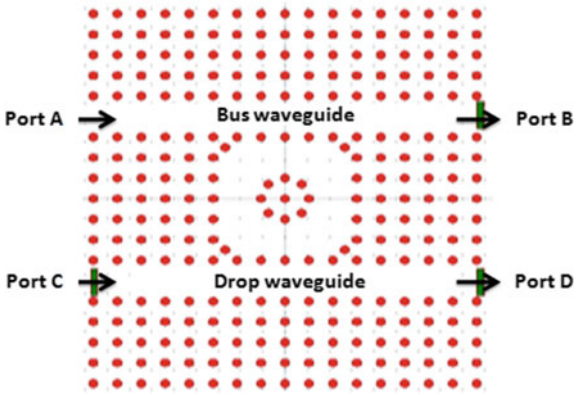

Fig. 6.7 Schematic structure of quasi square inner circular-shaped add–drop filter

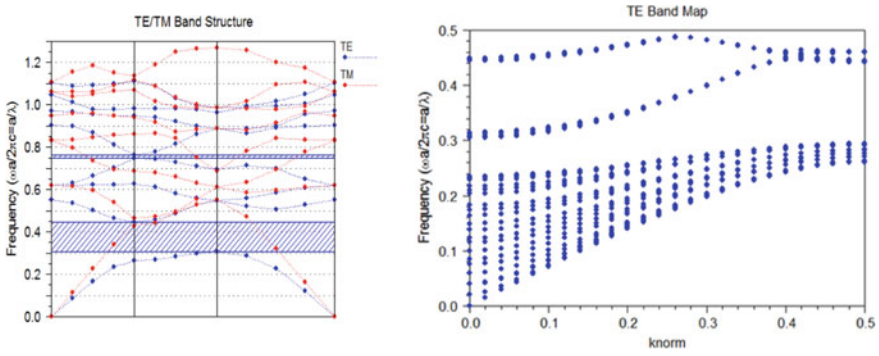

Fig. 6.8 Band structure diagram of Add–drop filter and Guided mode

The proposed structure has four channels, one of which is used to transmit power and signal from one waveguide to another. Suddenly signal is dropping at a particular wavelength and adds the channel or signal to a particular wavelength.

In contrast to the PCRR, which is molded by point defects to take on a circular shape, the bus waveguide is created through the introduction of line flaws. The PCRR is built by moving the inner and outer rods.

By altering the lattice constant, the position of the rods can be changed. The scatter rod is positioned in each of the four corners of the four sides to prevent forward dropping or propagation. It is employed to provide greater coupling and dropping efficiency.

The band structure diagrams for the fundamental 2 × 2 add–drop filter and guided mode are shown in Fig. 6.8. Here, the power has been adjusted with time. The structure's resonant wavelength is 1390 nm, its lattice constant is 540 nm, and its radius is 100 nm. Silicon serves as the substrate material.

The band diagram and guided mode are calculated above. Figure 6.9 shows that the output spectrum is taken by using the FDTD method of the proposed structure 2 × 2 add–drop filter and the transmission efficiency is 74% and dropping efficiency is 100%.

The output performance is calculated by using the dropping factor and transmission factor and the add–drop filter structure having one input and three outputs. The output performance is calculated when the input power enters another port as an output signal (Fig. 6.9).

The schematic representation of 3D view PCRR based on two 2 × 2 add–drop filters is shown in Fig. 6.10

Field Distribution

For the 2 × 2 circular ring resonator add–drop filter, at the output port, the fields estimated using the 2D FDTD approach are subjected to Fast Fourier Transform (FFT), which yields the normalized transmission spectra shown in Fig. 6.11.

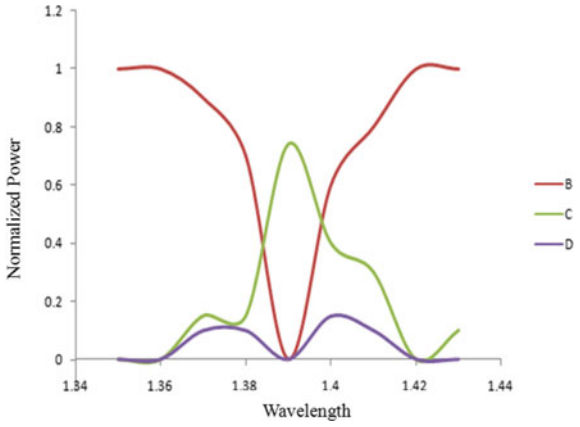

Fig. 6.9 Output response curve of add drop filter

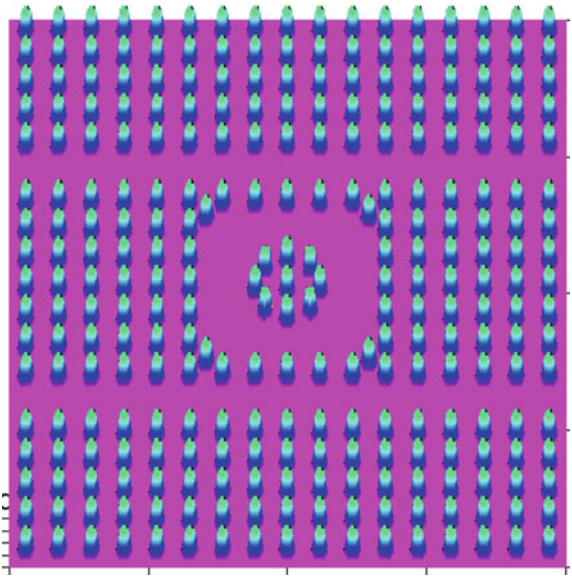

Fig. 6.10 3D view of PCRR-based add–drop filter

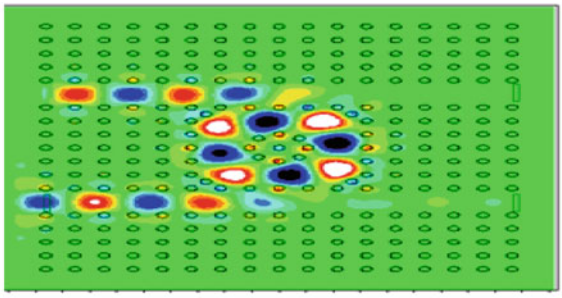

(a) On resonance-1390 nm

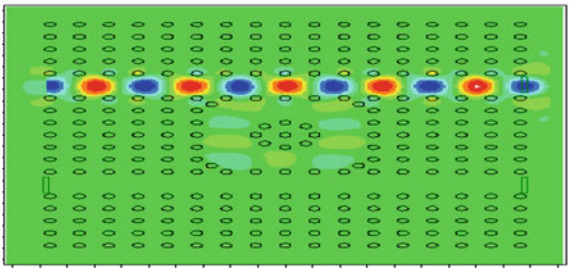

(b) Off resonance-1340 nm

Fig. 6.11 Signal Propagation of PCRR based optical add drop filter

Parameters calculations

Step1 Transmission efficiency

Transmission efficiency $= p_{out}/p_{in}*100$.

Efficiency $= 7.4/1*100$.

Efficiency $= 74\%$

Step 2 Spectral width

Spectral width $\Delta\lambda = \lambda_2 - \lambda_1$

Spectral width $\Delta\lambda = 1398-1384$.

Spectral width $\Delta\lambda = 14$.

Step 3 Quality factor

Quality factor $= \lambda/\Delta\lambda$.

Quality factor $= 1391/14$.

Quality factor $= 99.3$

Circular-Shaped Add–Drop Filter

Figure 6.12 sketches circular-shaped PCRR-based add–drop filter, which consists of four ports. The ports are A (input), B (output), C (output), and D (output). The bus waveguide is part of the waveguide that is on top. The waveguide, also known as the bottom waveguide or drop waveguide, bus waveguide contains port A (input) and Port B (input). The drop waveguide contains Port C (output) and Port D (output).

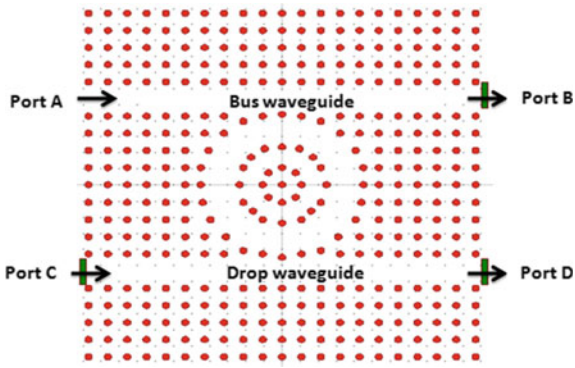

Fig. 6.12 Schematic structure of quasi-square inner circular-shaped add–drop filter

To transport power and signal from one waveguide to another, a quasi-square inner circular shape with four channels is used. Suddenly, a channel or signal is added at a specific wavelength while the signal at that wavelength drops.

Line defects are used to create the bus waveguide, whereas point defects, which are used to create a circular shape, are used to create the PCRR. The PCRR is built by adjusting the positions of the inner and outer rods.

By altering the lattice constant, the rods' positions can be altered. No dispersion rods are positioned in the corners of the four sides to prevent forward falling or propagation. To provide higher coupling and dropping efficiency, it is used.

The basic 2 × 2 add–drop filter's band structure diagrams are shown in Fig. 6.12. Here, the power is normalized to time. The structure's lattice constant is 540 nm, its resonant wavelength is 1330 nm, and its radius is 100 nm. Gallium phosphide is the substance of the substrate. The guided mode is depicted in Fig. 5.12.

The output performance is calculated by using the dropping factor and transmission factor and the add–drop filter structure having one input and three outputs. The output performance is calculated when the input signal is dropped into another port as an output signal (Fig. 6.13).

Field Distribution

For the 2 × 2 circular ring resonator, add–drop filters an input port receives the power. At the output port, the fields estimated using the 2D FDTD approach are subjected to FFT, which yields the normalized transmission spectra. Monitors placed at the input and output ports, as shown in Fig. 6.14, record the input and output powers.

Parameters calculations:

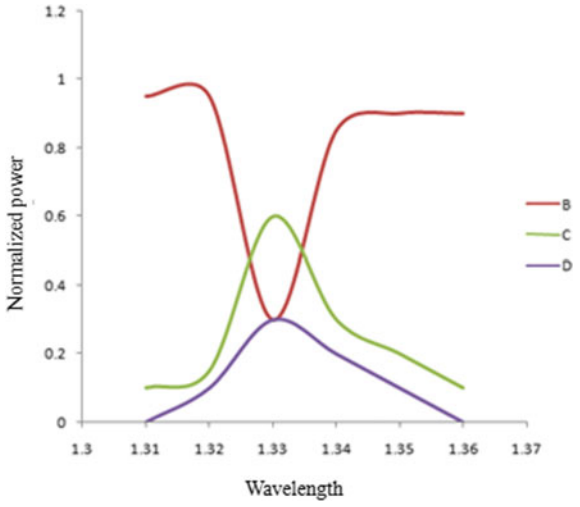

Fig. 6.13 Normalized transmission spectra of Circular-Shaped Add–Drop Filter

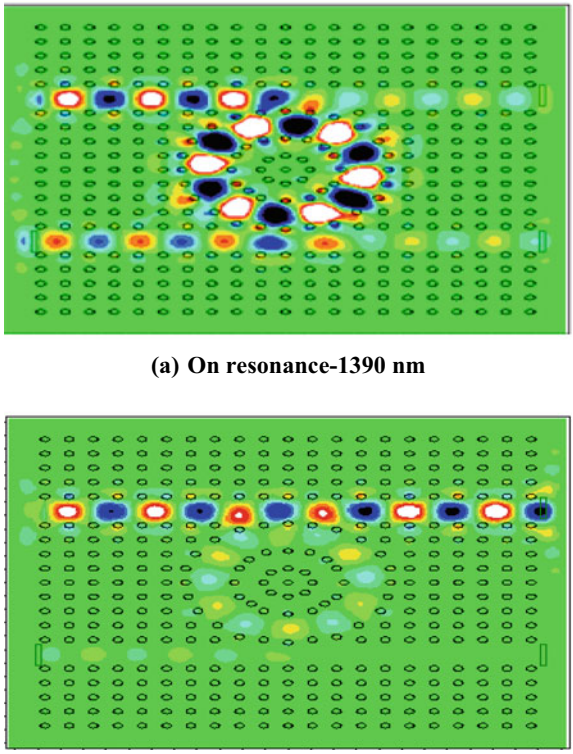

Fig. 6.14 Field distribution of Add-Drop Filter

(a) On resonance-1390 nm

(b) Resonance at OFF stat-1440 nm

Step1 Transmission efficiency

Transmission efficiency $= p_{out}/p_{in}*100$.

Efficiency $= 6.1/1*100$.

Efficiency $= 61\%$

Step 2 Spectral width

Spectral width $\Delta\lambda = \lambda_2 - \lambda_1$.

Spectral width $\Delta\lambda = 1334-1326$.

Spectral width $\Delta\lambda = 8$.

Step 3 Quality factor

Quality factor $= \lambda/\Delta\lambda$.

Quality factor $= 1402/8$.

Quality factor $= 166.25$.

Table 6.1 Functional parameter of add–drop filter

Components	Transmission efficiency (%)	Spectral width	Quality factor
Inner circular add–drop filter	74	14	99.3
Circular add–drop filter	61	8	166.25

The output performance is examined, and wavelengths for on- and off-resonance are computed. The resonant wavelength, quality factor, spectral width transmission efficiency, and dropping efficiency are all computed. Table 6.1 displays the output functionality of the three add–drop filters.

Multi-channel Tunable Filter

An electronic addressable solid-state random-access optical passband filter is known as an acousto-optic tunable filter (AOTF). Using a broadband or multi-line source can be used to quickly and dynamically choose a certain wavelength. Figure 6.15 shows a tunable multi-channel filter. Four dropping waveguides (B, C, D, and E), four hexagonal resonators (1, 2, 3, and 4), one bus waveguide (A), and five reflection structures make up the filter structure (RS1, RS2, RS3, RS4, RS5) (Cong et al. 2022).

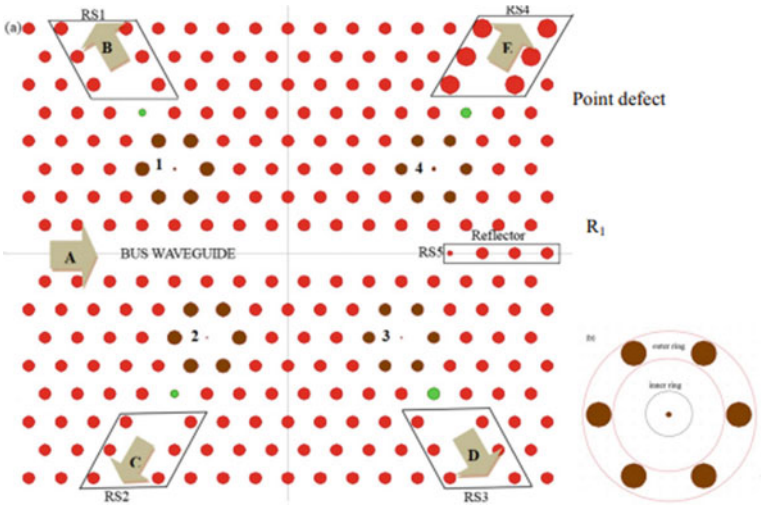

Fig. 6.15 Tunable multi-channel filter

In the PC lattice, 13 rods are removed to create the bus waveguide and 3 rods are removed to create the falling waveguides. The reflection structures are situated on both sides of the dropping waveguides and at the end of the bus waveguide to increase coupling efficiency.

Wavelength Filter with Dual Ring

Since most filters only have one ring on the resonator section, they have been successfully used for DWDM applications as well as C-band and L-band communications. The dual-ring wavelength filter is shown in Fig. 6.16 (Dangi et al. 2022).

Parameters calculations

Step1 Transmission efficiency

Transmission efficiency $= p_{out}/p_{in}*100$.

Efficiency $= 6.1/1*100$.

Efficiency $= 61\%$

Step 2 Spectral width

Spectral width $\Delta\lambda = \lambda_2 - \lambda_1$.

Spectral width $\Delta\lambda = 1334-1326$.

Spectral width $\Delta\lambda = 8$.

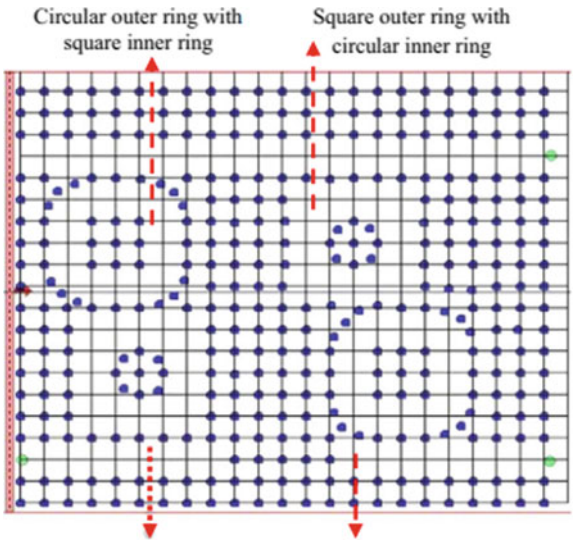

Fig. 6.16 Dual ring wavelength filter

Table 6.2 Functional parameter of Add–drop filter

Components	Transmission efficiency (%)	Spectral width	Quality factor
Inner circular add–drop filter	74	14	99.3
Circular add–drop filter	61	8	166.25

Step 3 Quality factor

Quality factor $= \lambda/\Delta\lambda$.

Quality factor $= 1402/8$.

Quality factor $= 166.25$.

The output performance is analyzed and on resonance, the wavelength is calculated, and of.

All optical filters' functional characteristics are compared. It can be seen from Table 6.2 above that the filters are created utilizing a ring resonator and square and triangular lattice via flaws. Functional factors like transmission efficiency and Q factor. According to the analysis above, optical filters using the aforementioned methods and various linear and nonlinear materials are reported. Nonlinear materials demand a high input power. The linear materials have a higher switching speed, a lower input power requirement, and improved performance metrics. Line defect and point defect ring resonators are used in the design of all-optical filters because they provide improved functional parameters like Q factor, coupling efficiency, footprint, and calculated wavelength. The comparison of all optical filters which depicts the complete analysis of all the functional parameter such as transmission efficiency, footprint, wavelength and Q factor respectively (Table 6.3).

Table 6.3 Comparison of all optical filters

Structure	Author	Lattice	Defect	Wavelength	Foot print	Transmission efficiency	Q factor	Coupling efficiency
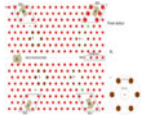	Cong et al. 2022)	Triangular	Line and point defect	1445.51 nm	74.05 μm^2	***	2251	***
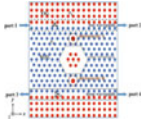	Tang et al. (2022)	Square	Ring resonator	***	***	***	***	***
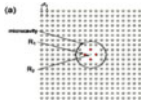	Liu et al. (2022)	Square	Line defect	1.5–1.6 μm)	27 $\mu m \times 17 \mu m$	90%	***	***
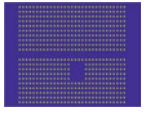	Singh et al. (2022)	Square	Linear defect	***	31 $\mu m \times 21 \mu m$	***	***	***
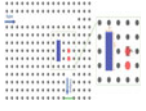	Dang et al. (2022)	Square	Line and point defect	***	60.86 μm^2	93.6%	20,549.3	***

Conclusion

In the FDTD method, a design and analysis of a photonic crystal ring resonator-based add–drop filter with all-round rings have been presented. These specially constructed add–drop filters can have their transmission efficiency, dropping efficiency, spectrum breadth, and quality factor changed by adjusting the index differences. The corresponding transmission efficiency is produced by adjusting the index differences of 2.1 and 2.3 in each zone of PCRR-based add–drop filters. One of the standout characteristics of this device is that the appropriate output power wavelength may be obtained by varying the index differences, lattice constants, and rod radius. That implies that adjusting the output wavelength is simple. The suggested switch's resonant wavelengths are 1390 nm and 1330 nm. Given these attributes, it appears that the device is appropriate for optical WDM systems, photonic integrated circuits, and upcoming optical networks that would be beneficial for a variety of real-time applications.

References

Andalib P, Granpayeh N (2008) Optical Add/Drop Filter Based on Dual Curved Photonic Crystal Resonator. Journal of Optoelectronics 47(2):249–250

Ashkan P, Zavvari M, HamedAlipour-Banaei (2015) All-optical AND/OR/NOT logic gates based on photonic crystal ring resonators. OptoElectrons 9(4):578–5843

Bendjelloul R, Bouchemat T, Bouchemat M (2016) An optical channel drop filter based on 2D photonic crystal ring resonator. Journal of Electromagnetic Waves and Applications 30(18):2402–2410

Cong Hu, Jinyue Jil, Tian Zhou, Chunting Wan, Chuanpei Xu, Aijun Zhu,(2022) "A Tunable Multichannel Filter Based on Photonic Crystal", Silicon, https://doi.org/10.1007/s12633-022-02159-8, pp. 1-10

Fallahi V, Seifouri M, Mohammadi M (2019) A new design of optical add/drop filters and multichannel filters based on hexagonal PhCRR for WDM systems. Journal of Photonic Network Communications 37(1):100–109

Gangchao Tang, Yuhao Huang, Jianfeng Chen, Zhi-Yuan Li, and Wenyao Liang, (2022)"Controllable one-way add-drop filter based on magneto-optical photonic crystal with ring resonator and microcavities", Optical Express, Vol. 30, No. 16, pp. 28762–28773.

Geerthana S, Sivanantha Raja A, Shanmuga Sundar D (2015) Design and optimization of photonic crystal fiber with improved optical characteristics. J Nonlinear Opt Phys Mater 24(04):1–11

Hadighorbanpour SM (2013) 2 channel All Optical De Multiplexer Based on Photonic Crystal Ring Resonators. Optik 6(2):224–227

Haisong Wang, Fanmin Kong, Kang Li, Liangmo Mei, (2007) "Highly efficient photonic crystal-based multi-channel drop filters "Journal of Optical Engineering, Vol.6781, No.4, pp.6781521–6.

Hamed, Pezeshki, and Vahid Ahmadi (2012) Nanoscale effects on multichannel add/drop filter based on 2-D photonic crystal ring-resonator Heterostructure. Journal of Theoretical and Applied Physics 47(11):1–6

Hongliang Ren, Hao Wena, Yali Qina, Shuqin Guoa, Weisheng Hub, Chun Jiangb Yaohui Jin,(2015) "Highly efficient channel drop filter based on photonic crystal one-way Waveguide "Journal of Optical Engineering, Vol.8308, No.5, pp.83081–6.

John S (1987) Strong localization of photons in certain disordered dielectric superlattices. Physics Review Letters. 58(23):2486–2489
Kuzma A, Frantisek Uherek J (2016) "Photonic crystal based add/drop filters for sensing. Optik 124(23):518–522
Lei W, Zang L, Zhang F (2022) (2021) "Performance Analysis of Three-Wavelength Multi-Channel Photonic Crystal Filters of Different Sizes." Crystals 1(1):1–12
Milad Moradi Dangi, Anwar Mohammadzadeh Aghdam, Rouhollah Karimzadeh, (2022)"Tunable optical filter with high performance based on 2D photonic crystal" , Journal of Computational Electronics, https://doi.org/10.1007/s10825-023-02020-0, pp. 1–7
Pirzadi M, Mir A, Bodaghi D (2016) Realization of Ultra-Accurate and Compact All-Optical Photonic Crystal OR Logic Gate. IEEE Photonics Technol Lett 282(1):2387–2390
PreetiRani YogitaKalra, Sinha RK (2015) Design of all-optical logic gates in photonic crystal waveguides. Optik 126(9):950–955
Qiu M, Mulot M, Swillo M, Anand S (2015) Optical add/drop filters using two-dimensional photonic crystals. Journal of Optical Engineering 5279(3):286–295
Rajalakshmi G, Sivanantha Raja A, Shanmuga Sundar D, (2015) Design and optimization of two-dimensional photonic crystal based optical filter. J Nonlinear Opt Phys Mater 24(03):1–8
Rakhshani MR, Mansouri-Birjandi MA (2013a) Wavelength De multiplexer Using Heterostructure Ring Resonators in Triangular Photonic crystals. J Telkomanika 11(4):1721–1724
Rakhshani MR, Mansouri-Birjandi MA (2013b) A new design of tunable four-port wavelength demultiplexer based on photonic crystal ring resonator. Optik 128(4):161–164
Rakhshani MR, Mansouri-Birjandi MA (2013c) Design of Six channel De multiplexer by heterostructure photonic crystal resonator cavity. J IRJABS 4(4):976–984
Rakhshani MR, Mansouri-Birjandi MA (2014) design and simulation of four channel wavelength demultiplexer based on photonic crystal circular ring resonators for optical communications. J Opt Commun 35(1):9–15
Rangaswamy Nakkeeran SR (2015) Coupled mode theory analysis for circular photonic crystal ring resonator based add-drop filter. Optoelectronics 6(2):224–227
Robinson S, Nakkeeran R (2011a) Photonic crystal ring resonator based add-drop filter using hexagonal rods for CWDM systems. Journal of Optoelectronics Letters 7(3):3430–3435
Robinson S, Nakkeeran R (2011b) Studies on Photonic Crystal based Add Drop Filter by Varying the Dimension of Inner Rods. Second International Conference on Sustainable Energy and Intelligent System 45(2):705–710
Robinson S, Nakkeeran R (2012a) Performance Evaluation of PCRR based Add Drop Filter with Different Rod Shapes. Journal of Microwaves, Optoelectronics and Electromagnetic Applications 11(1):26–38
Robinson S, Nakkeeran R (2013a) Characteristics of Add Drop Filter using single and dual PCRR in square lattice. Optik 124(25):5918–5922
Robinson S, Nakkeeran R (2013c) Photonic crystal ring resonator based add-drop filters: a review. Journal of Optical Engineering 52(6):60901–60907
S. Robinson, R. Nakkeeran,(2012b) " Investigation on two -dimensional photonic crystal resonant cavity based bandpass filter"Optik, Vol.123, No.4, pp.451–457.
S. Robinson, R. Nakkeeran, (2013) "Two-dimensional Photonic Crystal Ring Resonator based Add Drop Filter for CWDM systems" Optik, Vol.124, pp.3430–3435.
S.Robinson, R.Nakkeeran, (2013b) "PCRR based add-drop filter for ITU-T G.694.2 CWDM systems" Optik, Vol.124, NO.2, pp.393–398.
Sathyadevaki R, Sivanantha Raja A, Shanmuga Sundar D (2017) Photonic crystal-based optical filter: a brief investigation. Photonic Netw Commun 33:77–84
Sathyadevaki R. Shanmuga Sundar D, Sivanantha Raja A, (2016) Design of dual ring wavelength filters for WDM applications. Opt Commun 380(1):409–418
Shanmuga Sundar D, Sathyadevaki R, Sridarshini T, Sivanantha Raja A (2018a) Photonic crystal based routers for photonic integrated on-chip networks: a brief analysis. Opt Quantum Electron 50:1–15

Shanmuga Sundar D, Sathyadevaki R, Sivanantha Raja A (2018b) High-efficiency filters for photonic integrated networks: a brief analysis. Laser Phys 28:1–9

Sigalas MM, Flory CA, Wilson C (2017) Add-drop photonic crystals filters. Journal of Optical Engineering 4640(3):211–217

Singh R, Bhargava A (2022) Chalcogenide Photonic Crystal: Channel Drop Filter. IOP Conference Series: Materials Science and Engineering. https://doi.org/10.1088/1757-899X/1221/1/012056,pp.1-6

Tavousi A, Ali M, Mansouri-Birjandi MG, Ranjbar-Torkamani M (2017) Application of photonic crystal ring resonator nonlinear response for full-optical tunable add–drop filtering. J Photonic Netw Commun 34(1):131–139

Yablonovitch E (1987) Inhibited spontaneous emission on solid-state physics and electronics. Physics Review Letters. 58(20):2059–2062

Zexuan Qiang, Weidong Zhou, Richard A. Soref, "Optical add-drop filters based on photonic crystal ring resonators" Optics Express, vol.15, no.4, pp.1823–1831.

Chapter 7
Photonic Crystal-Based 2D Demultiplexer for DWDM Systems

V. R. Balaji, Richards Joe Stanislaus, M. A. Ibrar Jahan, R. G. Jesuwanth Sugesh, and Gopalkrishna Hegde

Abstract With the increasing number of internet users, Wavelength Division Multiplexing (WDM) technology is the most promising solution in optical communication systems. It enables multiple wavelength channels to be sent concurrently on a single fiber (SMF) rather than using separate SMF for each user. The WDM technology increases the carrying capacity of the physical medium, which is classified into Coarse WDM (CWDM) and Dense WDM (DWDM). The CWDM assigns large channel spacing to each user on a different wavelength. DWDM is similar, but it uses small channel spacing to support many users and alleviate the current bandwidth crisis, enabling the simultaneous transmission of more data. The demultiplexer is a prominent device in optical communication systems. The 2D photonic crystal (PC) is used to design the demultiplexer. The structural and performance parameters for the existing DWDM demultiplexer are studied. The future design considerations for the DWDM demultiplexer are reported in the survey paper.

Keywords Band gap · Demultiplexer · Resonant cavity · Quality factor · Defect · Quality factor · Transmission efficiency

V. R. Balaji (✉) · R. J. Stanislaus
School of Electronics Engineering, Vellore Institute of Technology, Chennai, Tamil Nadu 600127, India
e-mail: balaji.vr@vit.ac.in

M. A. I. Jahan
Department of ECE, RNS Institute of Technology, Bangalore 560098, India

R. G. J. Sugesh
Department of Electronics and Communication Engineering, School of Engineering Technology, CHRIST University, Bangalore 560029, India

G. Hegde
Centre for Nanoscience and Engineering, Indian Institute of Science, Bengaluru 560012, India

V. R. Balaji · R. J. Stanislaus · M. A. I. Jahan · R. G. J. Sugesh · G. Hegde
Mount Zion College of Engineering and Technology, Pudukkottai 622507, India

© The Author(s), under exclusive license to Springer Nature Singapore Pte Ltd. 2023

S. S. Dhanabalan et al. (eds.), *Photonic Crystal and Its Applications for Next Generation Systems*, Springer Tracts in Electrical and Electronics Engineering,
https://doi.org/10.1007/978-981-99-2548-3_7

Introduction

A photonic crystal (PC) is a man-made crystal composed of regular repetitions of dielectric materials with higher dielectric constants mounted on the air or air holes array on the dielectric materials. The periodic arrangement of dielectric material is fabricated with respect to three distinct types: 1D, 2D, and 3D. The 1D type is made up of a sequence of layers with different dielectric constants (Haret et al. 2009) as shown in Fig. 7.1.

The 2D PC (Akahane et al. 2003) is based on the arrangement of rods and holes in a dielectric slab that is in two dimensions as shown in Figs. 7.2 and 7.3.

Based on the arrangement of rods and holes in dielectric region categories into.

i. Etched air hole array-type PC with a high vertical index contrast,
ii. dielectric rods array-based PC with a high vertical index contrast,
iii. Etched air hole array-type PC with a low vertical index contrast,
iv. dielectric rod array-based PC with a low vertical index contrast.

The 3D PC (Braun et al. 2006) is an artificial arrangement of periodic dielectric variation in three dimensions.

PCs are distinguished by the existence of a Stop Band or Photonic Band Gap (PBG). The reason is that the region in PBG covers the conventional (C Band)

Fig. 7.1 1D PC

Fig. 7.2 Air hole in the dielectric (Si) slab

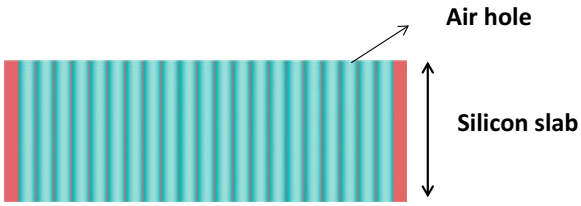

Fig. 7.3 Rods in the dielectric (Si)

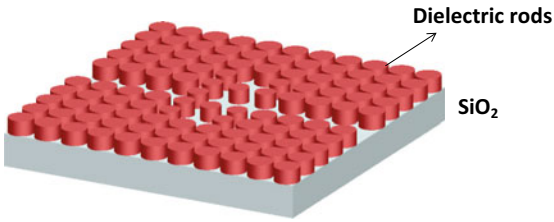

Table 7.1 Structural parameters of 2D PC device specifications

Parameter	Values
Dielectric rod radius (GaAs)	0.17a
Rod RI (n)	3.4
Rod Dielectric constant	11.56
Lattice Constant (a)	0.58 μm
Index difference	2.4

(1530 nm–1565 nm) and longer wavelength (L band) (1565 nm–1625 nm) in the optical communication systems (Dutton 1998) The PC can generate PBG at visible and infrared wavelengths, but the material losses will be higher than in the C and L bands (Campbell et al. 2000). The 2D PC can generate the PBG even at microwave frequency by changing the structural parameters in millimeters (Karthikeyan et al. 2022). The PBG acts as a stop band, not allowing the resonant frequencies to pass through in that band gap, introducing the defects in the PC that support an electromagnetic wave mode with a certain resonant frequency confined within the PC.

Among 1D, 2D, and 3D PC, the feasibly many applications are realized theoretically and practically analyzed in 2D PC due to fabrication simplicity and the presence of photonic bandgap (Yablonovitch 1993) in comparison with 1D and 3D PCs. We chose to study a 2D photonic crystal of dielectric rods in the air on a square array and a triangular array with the device specifications shown in Table 7.1.

Figure 7.4 shows the PBG structure for a square lattice (Anderson and Giapis 1996). The 14 dielectric rods of X and 14 dielectric rods of Z are placed in a square configuration as shown in Fig. 7.4. The polarization of the lattice is based on the geometry of the structure. The vertical crystal supports waveguide modes in TE polarization few modes in TM polarization are shown in Table 7.2.

Figure 7.5 shows the PBG structure for triangular lattice (Plihal and Maradudin 1991). The 14 dielectric rods are arranged in X and Z directions in a hexagonal pattern. The vertical alignment of rods supports the TE polarization few modes in TM polarization are shown in Table 7.3.

From Tables 7.2 and 7.3, it's inferred that a triangular lattice covers a larger PBG in comparison with a square lattice. The larger PBG is due to the triangular lattice's sixfold symmetry and the square lattice's fourfold symmetry.

After obtaining the PBG, the defects need to be introduced into the periodic structure to break the periodicity and allow the light or photon trapped in the reported PBG to localize the mode and allow the specific wavelength to pass. Defects in photonic integrated circuits (PIC) are classified as point and line defects (Anderson and Giapis 1996). Point defects are made by removing a single rod or modifying the structural parameter for a single rod, whereas line defects are produced by removing a series of rods or modifying their features.

The PC waveguide frequently uses defects to transmit electromagnetic waves without depending on total internal reflection. Based on the unique features of 2D PC, its development has led to enormous applications (Sridarshini et al. 2022) such

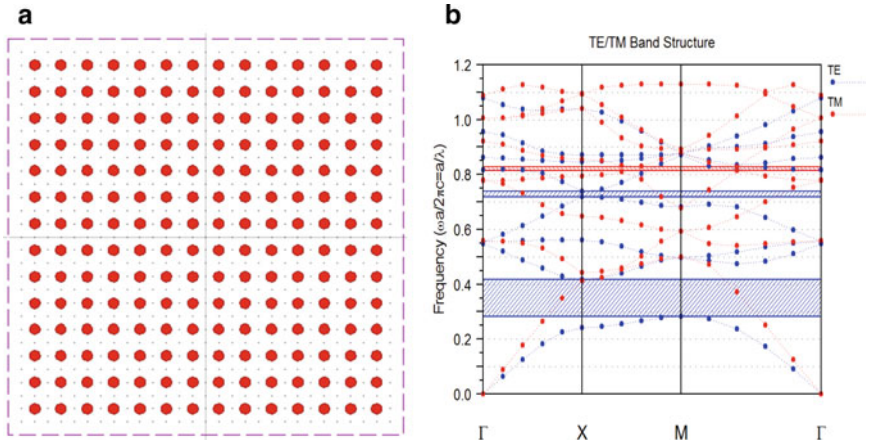

Fig. 7.4 **a** 14 × 14 2D dielectric rods Square Lattice **b** Bandgap structure for Square Lattice

Table 7.2 PBG for 14 × 14 PC (Square Lattice) structure

PBG	Frequency (a/λ)	Wavelength (nm)	Wavelength Band
TE 1 PBG	0.28289–0.41749	1389–2,050	Covering conventional window
TE 2 PBG	0.71863–0.73916	784–807	First window
TM PBG	0.77687–0.79254	731–746	ultraviolet-B

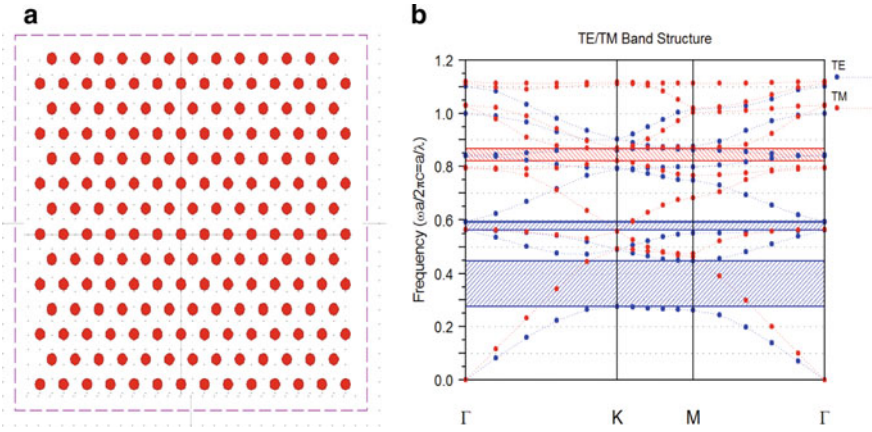

Fig. 7.5 **a** 14 × 14 2D Dielectric rods Triangular Lattice **b** Bandgap structure for Triangular Lattice

Table 7.3 PBG for 14 × 14 PC (Triangular Lattice) structure

PBG	Frequency (a/λ)	Wavelength (nm)	Wavelength band
TE 1 PBG	0.27605–0.44715	1297–2101	Covering conventional window
TE 2 PBG	0.5635–0.62913	921–1029	First window
TM PBG	0.81254–0.83254	696–713	Ultraviolet-B

as wavelength routers (Povinelli et al. 2001), filters (Thirumaran et al. 2021), logic gates (Sundar et al. 2018), power splitters (Geerthana et al. 2022), optical multiplexers (Ahmed et al. 2013), optical demultiplexer (Ghasemi et al. 2012), optical encoders (Balaji et al. 2022), decoders (Alipour-Banaei et al. 2016), antenna (Daghooghi et al. 2018), circulators (Sundar et al. 2019), and ADC converters (Youssefi et al. 2012).

The following is the outline for the paper: Sect. Literature Review explains the detailed survey analysis of existing reported demultiplexers. The future and design considerations and detailed fabrication steps are explained in Sect. Fabrication Steps of Air Holes Structure. The paper is concluded in Sect. Conclusion.

Literature Review

WDM technology allows multiple wavelength channels to be sent simultaneously on a single fiber (SMF) in optical communication systems to increase the number of internet users (Laude 2002). WDM technology uses two important devices to implement, such as a multiplexer and a demultiplexer. The SMF transfers information from one location to another, at one end, it multiplexes the different wavelengths through a multiplexer, and at the other end, an optical demultiplexer separates the wavelengths through a demultiplexer shown in Fig. 7.6.

WDM technology typically shifts the resonant wavelength towards higher and lower wavelength values, with 10–20 nm channel spacing for CWDM technology. Case 2 is resonant wavelength shifting towards a channel spacing of 0.1 nm or less and a maximum channel spacing of 1.6 nm using DWDM technology. Using DWDM, a larger number of users can utilize the bandwidth. The PC demultiplexer is realized with a Photonic Crystal Ring Resonator (PCRR), a resonant cavity mechanism used for DWDM systems. The basic resonator shapes are square, circular, rectangular, trapezoid, parelloid, quasi-shape, elliptical, diamond, dual-curved, X-shaped, and H-shaped to drop the desired wavelength from the cavity. The resonant cavity is designed with line defects and point defects. The literature review reveals the various cavities and waveguides used in the reported paper, as well as structural parameter changes such as defect size, rod or hole radius, coupling rods, scattering rods, and

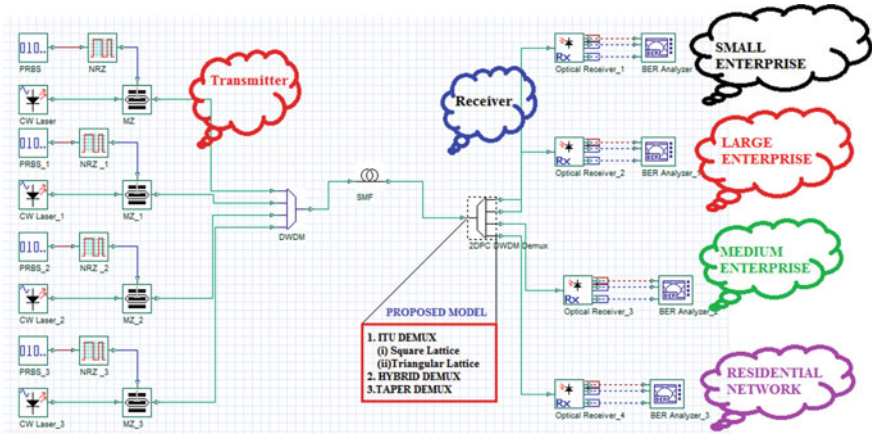

Fig. 7.6 Architecture for an optical fiber DWDM network

performance parameters such as low channel spacing, narrow spectral width, low crosstalk and, high-quality factor, which are reported in the extensive survey.

Photonic Crystal Ring Resonator Mechanism-Based DWDM Demultiplexer

A comparison of the performance and structural parameters of the Ring Resonator (PCRR) demultiplexer is shown in Table 7.4.

Photonic Crystal Ring Resonator: Based on a Two-Channel Optical Demultiplexer

Ghorbanpoura et al. (2013) reported a two-channel demultiplexer using a triangular lattice with dielectric rods. The demultiplexer uses the PCRR (octagon shape), a two-ring resonator used to drop different wavelengths using different radii of the dielectric rod. The reported demultiplexer drops the resonant wavelengths of 1590.8 and 1593.8 nm from channel 1 and channel 2. The quality factors and crosstalk values for channel 1 and channel 2 are 7954, 3984, −22 dB, and −11 dB, respectively. The footprint of the proposed structure was 681.36 μm^2. The spectral linewidth and channel spacing are not uniform in the design.

Table 7.4 Comparison of structural and performance parameters of Ring Resonator (PCRR) demultiplexer

Ref. No/ Year	Lattice cavity shape	Channel	Transmission efficiency (%) (Min.)	Q factor	Device (sm^2)	Cross talk (dB) (adjacent)	Channel spacing (nm)	Spectral width (nm)
23/ 2013	Triangular/ Octogen/ Rods	2	90	7954	681.36	−11	3.8	0.2
24/ 2013	Triangular X shape/Rods	4	45	1954	422	−7.5	2.7	0.8
28/ 2015	Square/ Octagon/ Rods	4	95	3943	***	−19	3	0.4
29/ 2015	Square/ Circular/ Rods	4	97	4862	790	−20.5	2	0.35
33/ 2016	Square/ Circular/ Rods	8	97	4862	434.16	−20.5	2	0.7
35/ 2017	Triangular/ Parellogram/ Holes	8	100	7777	434.56	−20	0.2	0.2
36/ 2017	Square/ Multilayer ring/Rods	8	86	7775	***	−20	1	0.2
37/ 2018	Triangular/ Hexoganal rings/holes	4	65.30	5472	500	−31	1	0.28
382,019	Square/ Homogenous ring resonators/ Rod	8	87	4206.2	737	−26	4	1.2

*** Not Applicable

Photonic Crystal Ring Resonator on Triangular Lattice: Based on a Four-Channel Demultiplexer

A four-channel wavelength division demultiplexer was designed with a 2D triangular lattice of the air rod by Alipour-Banaei et al. (2013a). To drop the specific wavelength, an X-shaped ring resonant cavity with scattering rods is used. The design drops the wavelengths 1563.5, 1566.2, 1569.7, and 1572.6 nm. The drawbacks of the reported design are low transmission efficiency, more crosstalk, high spectral width, and non-uniform channel spacing.

Photonic Crystal Ring Resonator on Square Lattice: Based on a Four-Channel Demultiplexer

Alipour-Banaei et al. (2013b) reported the four-channel optical demultiplexer using a square lattice, with the rods arranged in a square pattern. The PCRR mechanism was used to drop the desired wavelength. The inner rods in the ring resonant are arranged in an octagon shape core. Four-ring resonators are used with various radii in order to drop four wavelengths. The performance parameters are channel spacing of 3 nm, a spectral line width of 0.4 nm, maximum transmission efficiency of 95%, a quality factor of 2600, and a maximum crosstalk level of −19 dB. The design lacks a quality factor, non-uniform channel spacing, and spectral linewidth.

Three-Layer-Based Ring Resonator: Based on a Four-Channel Demultiplexer

A demultiplexer with four channels is designed using a square lattice with dielectric rods (n = 2.8) as reported by Talebzadeh et al. (2014). The desired wavelength is dropped by the resonator mechanism, which is a circular ring made of three layers with the inner ring RI differing from the outer ring RI and used to drop the desired wavelength with a quality factor of 4862 and a design efficiency of 100%. The design reported with low channel spacing is 2 nm, and the low spectral linewidth is 0.35 nm. The drawbacks are non-uniform channel spacing and spectral linewidth as per DWDM standards, and the footprint of the device is large.

Quasi-Square Ring Resonator: Based on an Eight-Channel Demultiplexer

Kannaiyan et al. (2016) designed the eight-channel demultiplexer using a square lattice with dielectric rods. Adjusting the size of the quasi-square ring resonator separates the desired wavelength. The resonator cavity size is varied by adjusting the radius of the inner rod. The design provides an average transmission efficiency of 90%, a Q factor of 1960, and a spectral linewidth of 1.8 nm, respectively. The drawbacks of this design are a lower quality factor, more crosstalk, and non-uniform channel spacing.

Parallelogram Ring Resonator: Based on an Eight-Channel Demultiplexer

Balaji et al. (2016) designed the eight-channel demultiplexer using a triangular lattice with air holes. A parallelogram resonator and a nanomicrocavity are used in the design. The resonator couples the electromagnetic waves from the bus waveguide to the cavity. A strong electric field is built around the cavity based on its circumference.

The desired wavelength was dropped based on the inner rod radius of the nanoring cavity. The transmission efficiency of the design is 100%, with a high-quality factor of 7777, a narrow spectral linewidth of 0.2 nm, and a channel spacing of 0.2 nm. The reported design has many advantages including uniform spectral line width and channel spacing designed as per DWDM standards.

Si/C Rod Crystal Multilayer Ring Resonator: Based on Six- and Eight-Channel Demultiplexers

Talebzadeh et al. (2017) reported a six-channel and a eight-channel demultiplexers using multilayer ring resonators in a square lattice with silicon rods. Each resonator's inner multilayer ring is made of carbon, and the radius of the rod in each resonator is varied to drop a specific desired wavelength. This design improves the coupling efficiency between the ring and waveguides, resulting in a rise in the quality factor of more than 7000, a channel spacing of 1 nm, and a spectral linewidth of 0.2 nm.

Hexagonal Ring Resonator: Based on a Four-Channel Demultiplexer

Sreenivasulu et al. (2017) reported the four-channel demultiplexer using a hexagonal ring resonator with a triangular lattice on air holes. By varying the inner central air hole, desired wavelengths are dropped. The design reported a good quality factor of 5472, a transmission efficiency of 65%, a channel spacing of 1 nm, and a spectral linewidth of 0.28 nm. The design is simple to realize and fabricate with current technology.

Homogeneous Ring Resonators: Based on an Eight-Channel Demultiplexer

Fallah et al. (2017) reported an eight-channel demultiplexer using a square lattice of dielectric rods. The design consists of an input waveguide, an output waveguide, and eight resonant rings, radius of the inner rods is varied to drop the desired wavelength. The design reported a low-quality factor, non-uniform spectral linewidth, and non-uniform channel also high crosstalk between the adjacent channels.

Photonic Crystal Resonant Cavity (Line/Point Defects) Mechanism-Based DWDM Demultiplexer

The comparison of performance and structural parameters of the resonant cavity (line/point defects) demultiplexer is shown in Table 7.5.

Table 7.5 Comparison of structural and performance parameters of resonant cavity (line/point defects) demultiplexer

Ref. No./ Year	Lattice/ Resonant Cavity	Channel	Transmission efficiency (%) (Min.)	Q factor	Device size (μm^2)	Cross talk (dB)	Channel spacing (nm) (Min.)	Spectral width (nm) (Min.)
25/ 2013	Square/ Point defect cavity/ Rods	32	40	3840	1519	−10	0.8	0.4
26/ 2014	Triangular/ Point defect cavity/ Rods	2	40	3840	1519	−10	0.8	0.4
27/ 2014	Square/ Point defect cavity/ Holes	2	0.3	7800	***	***	0.2	0.2
30/ 2015	Triangular/ Point defects/Air holes	2	99.61	7826.5	***	−20.98	0.1	0.2
31/ 2016	Square lattice/ Point defects/ Rods	8	99	3842	495	−11.2	2	0.4
33/ 2016	Square lattice/Line Point defects/ Rods	4	58.73	3487.8	360	−15.35	2	0.4
34/ 2015	Triangular/ Point defects/Air holes	4	73	6320	***	−27.6	12	0.2

*** Not Applicable

Point Defect Resonant Cavity: Based on 8-, 16-, and 32-Channel Demultiplexers

Alipour-Banaei (2013b) designed the 8-, 16-, and 32-DWDM demultiplexers using a square lattice with dielectric rods. The mechanism of a line and point defect-based resonant cavity is used in the design to drop the desired wavelength. The resonant cavity consists of one center rod and four surrounding rods. The varying radius of

the center rods and the desired wavelength is dropped. The design disadvantages are a 40% transmission efficiency, −10 dB crosstalk, non-uniform channel spacing, and spectral linewidth. The author designed for a maximum of 32 channels with a channel spacing of less than 1 nm.

Selective Wavelength Resonant Cavity: Based on a Two-Channel Demultiplexer

Mohammadi et al. (2013a) designed a two-channel demultiplexer using a triangular lattice with a dielectric rod. The selective wavelength is dropped by using a resonant cavity based on point defects and line defects. The resonant wavelengths are 1549.4 nm and 1551.2 nm. The performance parameters are transmission efficiency of 92%, maximum quality factor of 3021, channel spacing of 1.8 nm, and crosstalk of −10 dB.

Square Lattice with GaAs Holes: Based on a Four-Channel Demultiplexer

A four-channel demultiplexer was designed by Gupta et al. (2014). The demultiplexer design uses a square lattice with GaAs holes. The design consists of an input, an output waveguide, and cavity resonance. The desired wavelength is reduced by adjusting the radius of the cavity holes. The design to drop the narrow resonant wavelength is 0.2 nm, as are the uniform channel spacing and spectral linewidth. The drawbacks of the reported design are poor transmission efficiency and less than the standard threshold due to co-channel interference.

T-shaped with Point Defect Resonant Cavity: Based on a Two-Channel Demultiplexer

A triangular lattice with etched air holes is used to design a two-channel DWDM demultiplexer by Pashaei et al. (2016). The demultiplexer is designed as a T-shaped structure with a resonant cavity. The desired wavelength is obtained with a resonant cavity with middle and side defects. The design holds a transmission efficiency of 99.61%, a crosstalk of −24.59 dB, a spectral line width of 0.2 nm, and a quality factor of 79.

Three Central Rods Wall-Based Defect Cavity Based on an Eight-Channel Demultiplexer

Mehdizadeh et al. (2015) design an eight-channel demultiplexer using an array of dielectric rods with a square lattice. The resonant cavity acts as a wavelength filter to

drop the desired wavelength. The cavity consists of three central dielectric rods with different radii. The other three rods are placed above the central rods on the upper and lower walls of the cavity. The design reported a transmission efficiency of 94%, a crosstalk of −40 dB, and a quality factor of 2200. The drawback of this design is that it has a lower quality factor for working in DWDM systems, non-uniform spectral line width, and channel spacing.

L3 Cavity Line Defect Cavity: Based on a Four-Channel Demultiplexer

Talebzadeha et al. (2016) reported a four-channel DWDM demultiplexer based on a 2D photonic crystal using a rod structure. The desired wavelength is dropped based on the line defect resonant cavity. The design consists of input, L3 cavity-based, and four output vertical waveguides. The radius of the defect rod in the cavity is varied to drop the desired wavelength. The performance parameters for the design are transmission efficiency, crosstalk, quality factor, spectral width, and channel spacing of 93.45%, −27.33 dB, 4107, 0.4, and 2 nm, respectively. The drawbacks of this design are channel spacing and spectral line width which are not uniform as per DWDM standards.

Hexagonal Lattice with Defective Resonant Cavity: Based on a Four-Channel Demultiplexer

A four-channel PC demultiplexer designed in a hexagonal lattice of air holes by Mehdizade et al. (2015) The design consists of an input, an output, and a defective resonant cavity. By varying the radius of the defect air holes inside the cavity, the desired wavelength can be separated from the demultiplexer. The design has a minimum transmission efficiency of 73%, a crosstalk of −27.6 dB, and a quality factor of 6320. The design has a good quality factor and transmission efficiency, but the spectral linewidth and channel spacing are not uniform as per standards.

Fabrication Steps of Air Holes Structure

The PC demultiplexer can be designed with air holes in the silicon slab and dielectric rods in the air medium. The structure is completely periodic, with an arrangement of the lattice in square and hexagonal structures, which are preferable for optical device applications. The triangular lattice provides a broad PBG in the optical wavelength range compared to the square lattice structure, which helps to design many commercial applications in the optical network. The PC demultiplexer is designed and reported in both structures, but the majority of the simulation study and design are reported in the rod in the air medium structure; the flexibility in fabrication and

real implementation are reported in the air hole in the silicon slab structure due to the simplicity of fabrication (Jamois et al. 2003).

The fabrication step of air holes for the SOI platform is discussed. The PC based on a hexagonal lattice and a dielectric slab perforated with air is realized on a 100 nm thick silicon device which is integrated on a 600 nm SiO_2 layer underneath (Lončar et al. 2000; Bogaerts et al. 2002). The fabrication flow is illustrated in the following Fig. 7.7. (Step 1–Step 8).

Fabrication procedure for designing PC demultiplexer:

Step 1: Si/SiO2 bilayer is formed with Si slab of 100 nm and SiO_2 of 600 nm on the Si substrate.
Step 2: Oxidation/Mask layer is formed on the Si slab.
Step 3: SiO_2 is removed in order to define the thickness of the Si slab.
Step 4: Photoresist as it is the electron beam sensitive mask layer.
Step 5: E-Beam Lithography is used to define the PMMA pattern.
Step 6: Air holes etched on Si slab.
Step 7: Dry Etching (Removal of PMMA).
Step 8: SiO_2 underneath the Si slab is removed in order to improve vertical confinement of light.

Limitation of Existing Work and Future Enhancement

1. Based on a review of the literature on DWDM demultiplexer, it can be inferred that demultiplexer designed using

   i. dielectric rods array on square lattice (SiO_2),
   ii. dielectric rods array on Triangular lattice (SiO_2),
   iii. etched holes array on square lattice (Silicon slab),
   iv. etched holes array on Triangular lattice (Silicon slab).

2. Circular rings, square shape, quasi-square shape, rectangular shape, octagon shape, hexagonal shape, parallelogram shape, X shape, and T shape are the resonant cavity shapes.
3. Single-layer rings and multilayer rings are used in the reported work.
4. The single resonant wavelength drop from each resonator, but a few studies have reported dropping two wavelengths from a single resonator via a nanoring cavity.
5. Many published works reported better performance parameters such as high transmission efficiency, high-quality factor, transmission, narrow spectral line width, narrow channel spacing, and small foot print device size. Still, more flaws in DWDM systems remain unaddressed, such as

   i. The DWDM demultiplexer needs to have a high-quality factor for supporting DWDM standards of 0.1 nm or 0.2 nm.

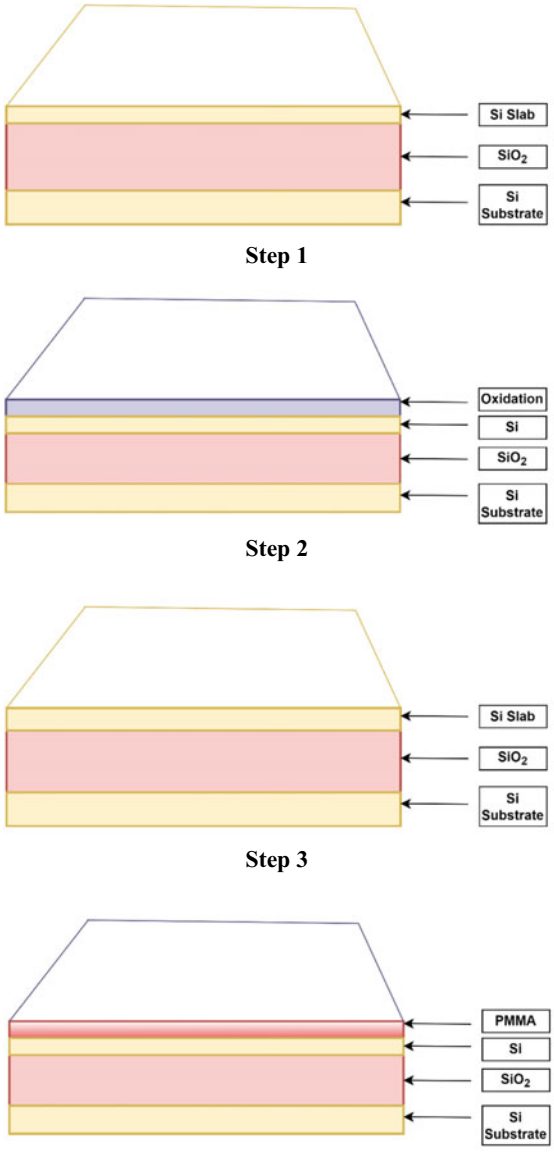

Fig. 7.7 Fabrication procedure for PC waveguides

ii. It is necessary to design the demultiplexer for DWDM standards (ITU-T-G 694.1 wavelength), standard defined equal spectral line width and channel spacing.
iii. In the future, hybrid-type DWDM demultiplexers will be required for flexible DWDM systems with different spectral line widths.

Fig. 7.7 (continued)

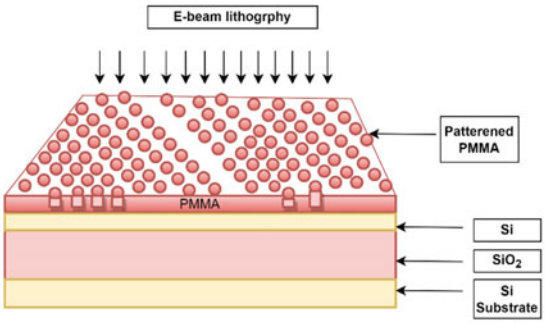

Step 5

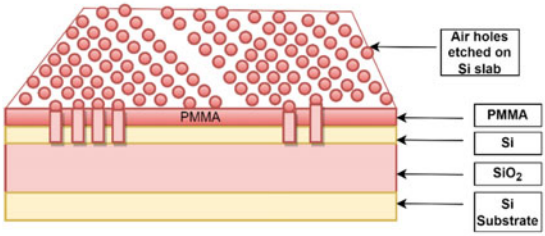

Step 6

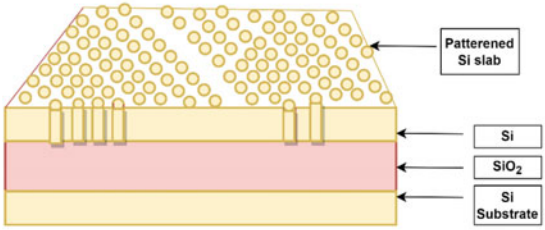

Step 7

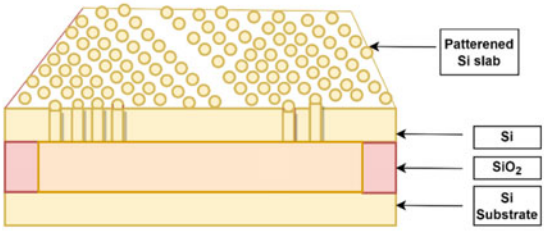

Step 8

iv. For PC devices to carry the signal in a different geometric shape from a waveguide to a 2D PC, a taper design is required.
v. DWDM demultiplexers need to be designed to support more channels, like 32, 64, and 128 channels, to support more internet users.

6. According to the literature review, square and triangular rods are more commonly reported in demultiplexer design, but in the fabrication concern in real-time systems, air holes are simple to fabricate and realize. The triangular air holes provide a higher bandgap compared to a square lattice. It is recommended to design the demultiplexer with air holes in a triangular pattern.
7. The desired wavelengths are dropped by varying the refractive index of the specific region, the radius of the rods, and the position of the holes. By taking into account the survey points, fabrication difficulties and tolerances can be reduced.

i. Rather than using multiple RI materials in a single design, it is simpler to use a single RI material for the entire design.
ii. The desired wavelength is dropped by varying only the center rod in the wavelength selection cavity.
iii. For easy fabrication and alignment, the radius of the rod or hole size should not be less than 100 nm.
iv. When designing the resonator rings, avoid changing the position of the rod for easy fabrication and realization, and also ensure the proper circumference for creating the circular modes inside the cavity.

Conclusion

This chapter gives a complete idea and a detailed survey of structural and performance parameters in the DWDM demultiplexer. The DWDM demultiplexer is needed for present and future communication networks to support more existing users and avoid a bandwidth crisis in the network. The majority of the reported papers did not follow the DWDM standards, the importance of designing the demultiplexer with DWDM standards is discussed. The difficulties of fabrication and how they can be reduced are discussed.

Acknowledgements This work was performed on Lumerical software/R SOFT BandSOLVE provided by Vellore Institute of Technology, Chennai. The authors are grateful to the institution.

References

Ahmed R, Khan MM, Ahmmed R, Ahad A (2013) Design, simulation and optimization of 2D photonic crystal power splitter

Akahane Y, Asano T, Song BS, Noda S (2003) High-Q photonic nanocavity in a two-dimensional photonic crystal. Nature 425(6961):944–947

Alipour-Banaei H, Rabati MG, Abdollahzadeh-Badelbou P, Mehdizadeh F (2016) Application of self-collimated beams to realization of all optical photonic crystal encoder. Physica E 75:77–85

Alipour-Banaei H, Mehdizadeh F, Serajmohammadi S (2013a) A novel 4-channel demultiplexer based on photonic crystal ring resonators. Optik 124(23):5964–5967

Alipour-Banaei H, Mehdizadeh F, Hassangholizadeh-Kashtiban M (2013b) A novel proposal for all optical PhC-based demultiplexers suitable for DWDM applications. Opt Quant Electron 45(10):1063–1075

Alipour-Banaei H, Serajmohammadi S, Mehdizadeh F (2015) Optical wavelength demultiplexer based on photonic crystal ring resonators. Photon Netw Commun 29(2):146–150

Anderson CM, Giapis KP (1996) Larger two-dimensional photonic band gaps. Phys Rev Lett 77(14):2949

Balaji VR, Murugan M, Robinson S, Hegde G (2022) A novel hybrid channel DWDM demultiplexer using two dimensional photonic crystals meeting ITU standards. SILICON 14(2):617–628

Balaji VR, Murugan M, Robinson S, Nakkeeran R (2017) Design and optimization of photonic crystal based eight channel dense wavelength division multiplexing demultiplexer using conjugate radiant neural network. Opt Quant Electron 49(5):1–15

Bogaerts W, Wiaux V, Taillaert D, Beckx S, Luyssaert B, Bienstman P, Baets R (2002) Fabrication of photonic crystals in silicon-on-insulator using 248-nm deep UV lithography. IEEE J Sel Top Quantum Electron 8(4):928–934

Braun PV, Rinne SA, García-Santamaría F (2006) Introducing defects in 3D photonic crystals: state of the art. Adv Mater 18(20):2665–2678

Campbell MTHRGDM, Sharp DN, Harrison MT, Denning RG, Turberfield AJ (2000) Fabrication of photonic crystals for the visible spectrum by holographic lithography. Nature 404(6773):53–56

Daghooghi T, Soroosh M, Ansari-Asl K (2018) A novel proposal for all-optical decoder based on photonic crystals. Photon Netw Commun 35(3):335–341

Dutton HJ (1998) Understanding optical communications, vol 1. Prentice Hall PTR, New Jersey

Fallahi V, Mohammadi M, Seifouri M (2019) Design of two 8-channel optical demultiplexers using 2D photonic crystal homogeneous ring resonators. Fiber Integr Opt 38(5):271–284

Geerthana S, Syedakbar S, Sridarshini T, Balaji VR, Sitharthan R, Sundar DS (2022) 2D-PhC based all optical AND, OR and EX-OR logic gates with high contrast ratio operating at C band. Laser Phys 32(10):106201

Ghasemi MA, Khodadadi R, Banaei HA (2012) Design and simulation of all optical multiplexer based on one-dimensional photonic crystal for optical communications systems. Int J Eng Res Appl 2(6):960–968

Ghorbanpour H, Makouei S (2013) 2-channel all optical demultiplexer based on photonic crystal ring resonator. Frontiers Optoelectron 6(2):224–227

Gupta ND, Janyani V (2014) Dense wavelength division demultiplexing using photonic crystal waveguides based on cavity resonance. Optik 125(19):5833–5836

Haret LD, Tanabe T, Kuramochi E, Notomi M (2009) Extremely low power optical bistability in silicon demonstrated using 1D photonic crystal nanocavity. Opt Express 17(23):21108–21117

Jamois C, Wehrspohn RB, Andreani LC, Hermann C, Hess O, Gösele U (2003) Silicon-based two-dimensional photonic crystal waveguides. Photonics Nanostructures-Fundam Appl 1(1):1–13

Kannaiyan V, Dhamodharan SK, Savarimuthu R (2016) Investigation on modified quasi-square PCRR based demultiplexer for WDM applications. Opt Quant Electron 48(8):1–12

Karthikeyan M, Jayabala P, Ramachandran S, Dhanabalan SS, Sivanesan T, Ponnusamy M (2022) Tunable optimal dual band metamaterial absorber for high sensitivity THz refractive index sensing. Nanomaterials 12(15):2693

Laude JP (2002) DWDM fundamentals, components, and applications. Artech House, Norwood, MA, pp 19–82
Lončar M, Doll T, Vučković J, Scherer A (2000) Design and fabrication of silicon photonic crystal optical waveguides. J Lightwave Technol 18(10):1402
Mehdizadeh F, Soroosh M (2016) A new proposal for eight-channel optical demultiplexer based on photonic crystal resonant cavities. Photon Netw Commun 31(1):65–70
Mehdizadeh F, Soroosh M (2015) A novel proposal for all optical demultiplexers based on photonic crystal. Optoelectron Adv Mater Commun 9:324–328
Mohammadi B, Soroosh M, Kovsarian A, Mehdizadeh F (2014) A proposed dual channel optical demultiplexer based on photonic crystals. Majlesi J Telecommun Dev 3(4)
Plihal M, Maradudin AA (1991) Photonic band structure of two-dimensional systems: the triangular lattice. Phys Rev B 44(16):8565
Povinelli ML, Johnson SG, Fan S, Joannopoulos JD (2001) Emulation of two-dimensional photonic crystal defect modes in a photonic crystal with a three-dimensional photonic band gap. Phys Rev B 64(7):075313
Rastegarnia A (2015) Designing optimal filter with hexagonal structure to reduce two-channel communication demultiplexer crosstalk phenomenon with optical wavelengths resolution technology in structure of photonic crystal. Majlesi J Telecommun Dev 4(2)
Sreenivasulu T, Bhowmick K, Samad SA, Yadunath TIR, Badrinarayana T, Hegde GM, Srinivas T (2018) Photonic crystal ring resonator-based four-channel dense wavelength division multiplexing demultiplexer on silicon on insulator platform: design and analysis. Opt Eng 57(4):046109
Sridarshini T, Chidambaram P, Geerthana S, Balaji VR, Thirumurugan A, Sitharthan R, Dhanabalan SS (2022) Current and future horizon of Optics and Photonics in Environmental sustainability. Sustain Comput Inf Syst 100815
Sundar DS, Sathyadevaki R, Raja AS (2018) High-efficiency filters for photonic integrated networks: a brief analysis. Laser Phys 28(11):116203
Sundar DS, Umamaheswari C, Sridarshini T, Karthikeyan M, Sitharthan R, Raja AS, Carrasco MF (2019) Compact four-port circulator based on 2D photonic crystals with a 90° rotation of the light wave for photonic integrated circuits applications. Laser Phys 29(6):066201
Talebzadeh R, Soroosh M (2015) High quality complete coupling 4-channel demultiplexer based on photonic crystal ring resonators. Optoelectron Adv Mater-Rapid Commun 9(1–2):5–9
Talebzadeh R, Soroosh M, Daghooghi T (2016) A 4-channel demultiplexer based on 2D photonic crystal using line defect resonant cavity. IETE J Res 62(6):866–872
Talebzadeh R, Soroosh M, Kavian YS, Mehdizadeh F (2017) All-optical 6-and 8-channel demultiplexers based on photonic crystal multilayer ring resonators in Si/C rods. Photon Netw Commun 34(2):248–257
Thirumaran S, Dhanabalan SS, Sannasi IG (2021) Design and analysis of photonic crystal ring resonator based 6× 6 wavelength router for photonic integrated circuits. IET Optoelectron 15(1):40–47
Yablonovitch EJJB (1993) Photonic band-gap structures. JOSA B 10(2):283–295
Youssefi B, Moravvej-Farshi MK, Granpayeh N (2012) Two bit all-optical analog-to-digital converter based on nonlinear Kerr effect in 2D photonic crystals. Opt Commun 285(13–14):3228–3233

Chapter 8
Investigation of Ultra-Small and Efficient Encoders and Decoders for High-Speed Optical Communication Systems

R. Arunkumar and S. Robinson

Abstract Optical encoders and decoders are becoming increasingly crucial in optical communication and computing applications. Due to its exceptional capacity to route optical signals and the intense light–matter interaction on a sub-wavelength scale, which has been extensively employed in realization, photonic crystal-based logic devices are frequently used for such applications. For effective information processing, optical encoders and decoders drastically minimize the number of optical switches and interconnections in a dense optical communication network. Combinational circuits, like encoders and decoders, are logic devices with many inputs and multiple outputs that translate a collection of input signals into their corresponding output signals following the input state and control signals, as we have covered in this chapter. The evaluation of the 2D PC-based optical Encoder and decoder is done in such a way that several performance metrics, including normalized output power, operating speed, delay time, response time, steady state time, fall time, power requirements, footprint, contrast ratio, insertion loss, and crosstalk between output logic levels, are taken into account. Also, we have included a thorough analysis of several mechanisms and approaches for introducing an all-optical encoder and decoder.

Keywords Photonic Crystals · Finite Difference Time Domain · Photonic Band Gap · Plane-Wave Expansion · All-optical encoder · All-optical decoder

R. Arunkumar (✉) · S. Robinson
Department Of Electronics and Communication Engineering, Mount Zion College of Engineering and Technology, Pudukkottai, TamilNadu, India
e-mail: arunec002@gmail.com

© The Author(s), under exclusive license to Springer Nature Singapore Pte Ltd. 2023

S. S. Dhanabalan et al. (eds.), *Photonic Crystal and Its Applications for Next Generation Systems*, Springer Tracts in Electrical and Electronics Engineering,
https://doi.org/10.1007/978-981-99-2548-3_8

Introduction

One of the cutting-edge research fields is the downsizing of optical devices with high speed, extended life, and low power dissipation. Microelectromechanical systems and planar lightwave circuits have proven instrumental in the miniaturization of optical devices. Generally, the optical devices based on planar lightwave circuits are typically in the centimeter range. Devices made of microelectromechanical systems are prone to bending and radiation losses, which reduce sensitivity at higher speeds. Moreover, the shorter life span of this technology is brought on by moving parts. Hence, it may not be effectively suitable for photonic integrated circuits (PICs). By employing photonic crystals in the optical device design, the problems mentioned above can be resolved. A photonic crystal structure is explicitly made to alter how light behaves. Generally, it is made up of a set of features that are arranged in a regular pattern and have periodicities that are roughly equivalent to the wavelength of the light of interest. The photonic crystal's interaction with light is influenced by the precise positioning and spacing of these features, enabling it to regulate photons' propagation and emission (Yablonovitch 1987; John 1987).

A periodic structure of materials with a regular dielectric constant fluctuation is known as a photonic crystal. The ability of the material to block specific wavelength ranges of electromagnetic radiation (i.e., the photonic band gap), which makes them practical for regulating the transmission of light, is a result of the periodicity in the dielectric constant. When defects (point defects, line defects, or both) are added to these periodic structures, the periodicity and, thus, the completeness of the PBG are damaged, allowing for the manipulation and control of the light. In order to enable the development of PC-based optical devices, it makes sure that light is localized in the PBG zone. Photonic crystals allow novel sensors, lasers, waveguides for optical communications, and sophisticated data storage materials. This chapter is an introduction to photonic crystals and their classification. Then, topics like the photonic band diagram, numerical techniques, operational parameters, and photonic crystal-based encoder and decoder are explored.

Introduction of Photonic Crystal and Its Classification

We can now explore quickly that the PCs have only recently gained significant attention; the initial hypothesis regarding the ability to control light propagation using a photonic structure dates back to 1887. These were the 1D photonic structure investigations. Scientist V. P. Bykov of the Soviet Union presented a study in 1972 that highlighted the idea of using periodic structures to suppress spontaneous emissions over 100 years earlier (Joannopoulos et al. 2008; Yi and Youn 2016).

Nonetheless, the works of E. Yablonovitch and S. John, published in Physical Review Letters in 1987, are the first to begin PC's intensive advancement. Each year,

the number of papers devoted to the potential management of spontaneous emission and the possible direction of radiation propagation utilizing periodic structure doubles.

In 1996, Thomas Krauss first demonstrated a 2DPC at optical wavelengths. This opened up the modern way of fabricating PCs in semiconductor materials using the semiconductor industry methods. Optical filters (Fan et al. 1998; Wang et al. 2010), multiplexers (Mohmoud et al. 2012), demultiplexers (Rawal and Sinha 2009), switches (Benisty et al. 2010), directional couplers (Moghaddam et al. 2010), power dividers/splitters (Gannat et al. 2009), and sensors (Abdel Malek 2011; Joannopoulos et al. 1995) are only a few examples of the PCs-based optical components that have been created and documented for commercial applications.

Types of photonic crystals

A block can be assembled in a lattice pattern to create a photonic crystal. The photons will travel through areas with a high index of refraction—the dielectric—scattered with regions with a low index of refraction—the air holes (Joannopoulos et al. 1995). According to the periodicity of their structures, PCs are primarily divided into 1DPCs, 2DPCs, and 3DPCs (Yue and Gong 2015) (Fig. 8.1).

The PC structure gets its name from the dielectric material's periodicity along one or more axes. If the refractive indices of the two locations are different, the dielectric material or the air holes can contain most of the light. Due to this confinement, the so-called photonic band gap, an area of forbidden energy, separates permissible energy areas. A lattice of high-refractive-index material placed within a medium with a lower refractive index can also create photonic band gap structures. Gemstone is one such naturally occurring example of a substance. Periodic nanostructures inside give it its luminescence, which resembles a rainbow.

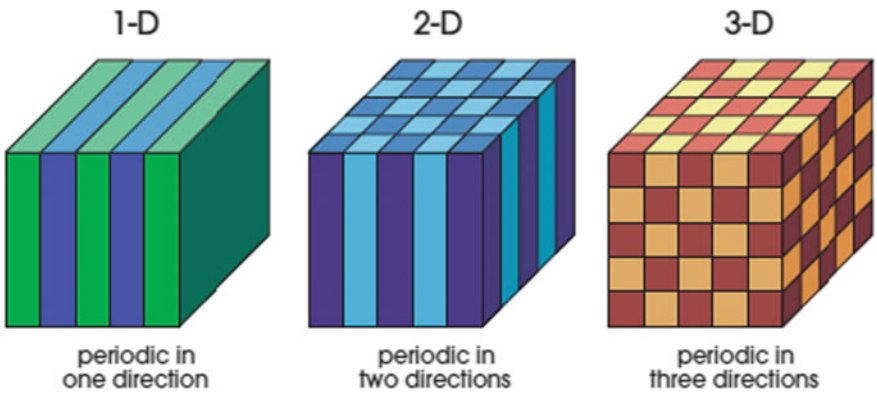

Fig. 8.1 Types of photonic crystal

Photonic Band Diagram

In theory, a band diagram would be required to account for all potential directions of PC propagation. The plane wave expansion (PWE) method can be used to calculate the propagation modes (dispersion characteristics) and PBGs in the band diagram for both periodic and nonperiodic structures (Lu et al. 2011; Fermi and Houdre 2003; Pendry 1996). The wavevector values "k" for the initial Brillouin zone, a constrained region with highly symmetric points, are determined to determine the entire structure's propagation modes. The first Brillouin zone is the portion of the initial lattice's Fourier transform created by points that are more closely spaced from the origin than any other periodic lattice vertex.

Numerical investigations of photonic crystals are presented in this chapter. Band structures and state densities for square, hexagonal, and circular 2D lattices of silicon's air columns are calculated using a "plane wave expansion" and Maxwell's equations as a foundation. The primary subject of this chapter is the analysis of band gap changes (TM- and TE-polarization) for pores with declining roundness that are approximated by ellipses with changing eccentricities.

Depending on the shape of the lattice, the structural parameter and no of TE and TM modes in PBG are different accordingly. Due to the unique properties of the lattice structure, the TE and TM methods are different. In the case of TM polarization, it is assumed that the electric waves that satisfy the criterion G = 0 s provide the most significant coupling in the Brillouin zone's center point for square lattice photonic crystal cavities. The coupling process in the 2D square lattice PC-like resonator with TE polarization is mainly carried out by magnetic waves that satisfy G = 0 and G = 20. Similarly, higher-order Bloch modes are not included in the coupling process in the triangular lattice photonic crystal cavity with TM polarization, which only involves waves satisfying the following condition: G = 0. The coupling procedure for TE polarization will be in TM mode. In high-speed optical communication, the selection of PBG is focused on third-generation optical windows, and operating wavelength is used as a particular value.

Figure 8.2a, b depict the band architectures of rod-type PC in square and triangular lattices. The rod radius and lattice constants are 0.1 m and 540 nm, respectively, where the rods (n1 = 3.46) in the air (n2 = 1) serve as hosts. By eliminating a line of rods (line defects) or a single rod (point defects), altering the size and shape of the rods already present in the structure, or changing the structural parameters, flaws disrupt the periodicity of the structure. Two PBG of TE modes are shown in the band diagram in Fig. 8.2a, b, whereas a PBG of TE and TM modes are offered at various wavelength ranges. As the normalized frequency of the initial TE PBG is detected between 0.445 a/λ and 0.25 a/λ, with corresponding wavelengths between 1260 and 1675 nm for third-generation optical window applications, that region is shown in blue, it is taken into consideration for further investigation.

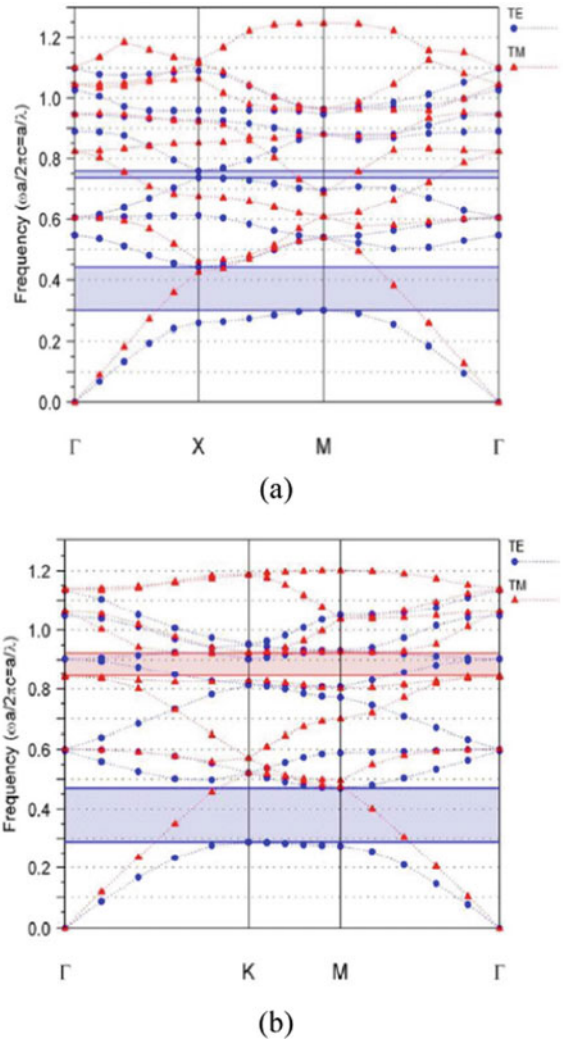

Fig. 8.2 Band diagram for **a** circular rods in the square lattice **b** circular rods in triangular

Defects in a 2D photonic crystal lattice

Defects are utilized in photonic crystals to open the photonic band gap and let electromagnetic waves pass through the structure. Defects can be created by removing or altering structural characteristics such as the lattice constant, rod radius, and refractive index differential. There are three defects: a point defect, a line defect, and a surface defect.

Numerical Methods

In both the design and study of photonic crystal structures, numerical approaches are indispensable. Dielectric materials arranged in periodic arrays called photonic crystals can affect how light travels through space. These structures have significant uses in optical sensing, light-emitting diodes, photovoltaic, and telecommunications, among other fields of photonics.

The behavior of photonic crystals has been modeled using various numerical techniques. The transfer matrix method (Pendry and MacKinnon 1992), PWE method (Pendry 1996), finite element method (Pelosi et al. 1997), finite difference time domain (FDTD) method (Taflove 2005), etc., approaches are the most often employed techniques. Dielectric materials arranged in periodic arrays called photonic crystals can affect how light travels through space. These structures have significant uses in optical sensing, light-emitting diodes, photovoltaic, and telecommunications, among other fields of photonics. Numerical approaches are indispensable in designing and studying photonic crystal structures.

The behavior of photonic crystals has been modeled using various numerical techniques. The transfer matrix method (Pendry and MacKinnon 1992), PWE method (Pendry 1996), finite element method (Pelosi et al. 1997), finite difference time domain (FDTD) method (Taflove 2005), etc., approaches are the most often employed techniques.

Every method has advantages and disadvantages. Regarding performance and ability to meet the need for PC-based device analysis, PWE and FDTD approach stands out among the rest. Because periodic structures' eigenmodes can be described as a superposition of several plane waves, the PWE approach was developed initially for the theoretical analysis of PC structures.

Using Maxwell's equations, electromagnetic wave propagation in PCs is described. When the material is considered to be linear, isotropic, periodic with a lattice vector, and lossless, Maxwell's equations adopt the following form Taflove (2005).

$$\frac{\partial E}{\partial t} = -\frac{1}{\mu}\nabla \times E \tag{8.1}$$

$$\frac{\partial E}{\partial t} = -\frac{1}{\varepsilon}\nabla \times H \tag{8.2}$$

PWE method

For the analysis of periodic structures, such as photonic crystals, the PWE method is an exacting numerical method that is precisely formulated. Using Bloch's theorem to determine the crystal's band structure, this approach expands the electromagnetic fields in the structure as a sum of plane waves. Modeling the movement of light in photonic crystals with the PWE approach yields exceptionally accurate results, but it only applies to systems with periodic geometries (Taflove 2005; Yee 1996).

$$\nabla \times \left(\frac{1}{\varepsilon(r)} \nabla \times E(r) \right) = \frac{\omega^2}{c^2} E(r) \tag{8.3}$$

Here,

- c—Speed of light
- ω—Angular frequency
- ε(r)—Dielectric constant (relative permittivity)
- E(r)—Electric field of the periodic function.

Periodic Eigen problems with solutions are given by the Bloch–Floquet theorem and can take the following form:

$$(ik + \nabla) \times \frac{1}{\varepsilon(r)} (ik + \nabla) \times u_k(r) = \frac{\omega(k)^2}{c^2} u_k(r) \tag{8.4}$$

The discretization of the eigenvalue equation in Eq. (8.4) into a plane wave basis results in an algebraic eigenvalue issue for a given Bloch vector k. It is resolved for the modes' permitted frequencies, defined by their eigenvectors. The band diagram is created by scanning k over the Brillouin zone.

FDTD method

A popular numerical method for analyzing electromagnetic wave propagation in photonic crystal structures is the FDTD approach. This approach divides the space into tiny cells, and Maxwell's equations are approximated using finite differences in each cell. Anisotropic and dispersive media can be simulated using the FDTD approach, which also enables the simulation of the time-domain response of photonic crystals (Yee 1996).

The fields in the 2D situation can be separated into the E and H polarizations, two transversely polarized modes. Using Yee-cell techniques, Maxwell's equations can be discretized in space and time (Li et al. 1310). Equations (8.5) and (8.6) are discretized spatially and temporally on a discrete 2D mesh using the XY-coordinate system for the E-polarization in the following FDTD time stepping formulas:

$$E_x \Big|_{i,\,j}^{n+1} = E_x \Big|_{i,\,j}^{n} - \frac{c\Delta t}{\varepsilon_0} \left[\frac{H_z \Big|_{i,\,j+1/2}^{n+1/2} - H_z \Big|_{i,\,j-1/2}^{n+1/2}}{\Delta y} \right] \tag{8.5}$$

$$E_y \Big|_{i,\,j}^{n+1} = E_y \Big|_{i,\,j}^{n} - \frac{c\Delta t}{\varepsilon_0} \left[\frac{H_z \Big|_{i+1/2,\,j}^{n+1/2} - H_z \Big|_{i-1/2,\,j}^{n+1/2}}{\Delta x} \right] \tag{8.6}$$

$$H_z\Big|_{i,\,j}^{n+1/2} = E_z\Big|_{i,\,j}^{n-1/2} + \frac{c\Delta t}{\mu_0}\left[\left(\frac{E_x\Big|_{i,\,j+1/2}^{n+1/2} - E_x\Big|_{i,\,j-1/2}^{n}}{\Delta y}\right) - \left(\frac{E_y\Big|_{i+1/2,\,j}^{n} - E_y\Big|_{i+1/2,\,j}^{n}}{\Delta x}\right)\right] \tag{8.7}$$

The spatial grid must be as small as necessary to discern the minor aspect of the simulated field to generate an accurate simulation. To obtain a stable simulation, one must meet the following requirement related to the spatial and temporal step size.

$$\Delta t \leq \frac{1}{c\sqrt{\frac{1}{\Delta x^2} + \frac{1}{\Delta y^2}}} \tag{8.8}$$

- c—Speed of the light.

Into the input port is launched a broad Gaussian pulse. Then, to gauge the time-varying electric field, a time monitor (detector) was inserted into each waveguide channel. The power that follows through the domain along the Z-direction is recorded using the time monitor as a function of time. Each port's output power is determined by integrating the power over the output ports' cells, as stated in Eq. (8.7):

$$P(t) = \frac{\mathrm{Re}\left[\int_A [E(t) \times H*(t)]dA\right]}{\mathrm{Re}\left[\int_A [E(t_0) \times H*(t_0)]dA\right]}$$

- E— Electric magnetic fields,
- H—Magnetic fields,
- A—The plane located within the domain of the time monitor.

Functional Parameters

The performance of the photonic crystal-based optical devices is analyzed using the following functional parameters,

Transmission efficiency (η)

One crucial factor in photonic crystal-based encoders and decoders is transmission efficiency, utilized to estimate output signal power or signal intensity level. The equation is used to calculate the transmission efficiency.

$$\text{Transmission efficiency} = \frac{P_o}{P_i}$$

- P_o is the resonant peak output power, and P_i is the wavelength-corresponding input power.

Contrast ratio

The following formula calculates the contrast ratio, determining how well an optical switch performs.

$$C = 10\log\left(P_{ON}/P_{OFF}\right)$$

- P_{ON} and P_{OFF} represent the output power in the ON and OFF states, respectively.

Response time and bit rate

The two parts that make up the response time are the transmission delay for t_1 to reach 0.1% of the average and the transmission delay for t_2 to reach 90% of the power average. Following are the anticipated response time and bit rate:

$$R = 4t2$$

$$BitRate(B_T) = \frac{1}{\text{Re}sponse\,Time}$$

Insertion loss

Insertion loss (IL), which is the ratio of the difference between normalized input and output powers to input power and is computed using the equation below, is another crucial characteristic of optical switches.

$$Insertion\,Loss(dB) = 10\log\frac{P_{in} - P_{out}}{P_{in}}$$

Propagation loss

The insertion loss to waveguide length ratio is used to define propagation loss. It is provided by $\text{Pr}\,opagation\,Loss = \frac{Insertion\,Loss}{Length\,of\,the\,Wavelength}$.

Crosstalk

Crosstalk (CR), measured between the output ports, is typically used to rate an optical switch's performance.

$$Cross\ Talk = 10 \log \frac{P_{low}}{P_{high}}$$

- P_{low} represents the lowest normalized power at the output port, while P_{high} represents the highest power at the output port.

Data Rate

The time response of the output signal can be used to calculate the rate of data transmission. The reciprocal of the steady-state time is the data rate.

Photonic Crystal-Based Encoder

A device that uses photonic crystals to encode data is called a photonic crystal-based encoder. Artificial materials with a periodic structure known as photonic crystals can influence the movement of light. They are suitable for optically encoding information because of this characteristic. The diffraction principle underlies the operation of a photonic crystal-based encoder. A photonic crystal's periodic structure interacts with an incident light beam to cause the beam to be diffracted. Information can be encoded using the resulting diffraction pattern. The encoding method employed in photonic crystal-based encoders is commonly based on a binary code, in which the presence of a diffraction spot corresponds to a logical one, and the absence of an area corresponds to a logical zero. The number of diffraction spots generated relies on the photonic crystal's element count and light's incidence angle. Some applications of photonic crystal-based encoders include data storage, optical communications, and sensing. They also fabricate advanced optical components such as filter resonators and lasers.

The overall block diagram of the encoder is shown in Fig. 8.3. The encoders, which produced N-bit binary codes with 2n inputs, were principally created utilizing various techniques to switch between the operational states of "OFF" and "ON". These techniques included adjusting design or structural parameters, altering the PC's materials and refractive index, changing the electromagnetic signal's input launch angle, and utilizing various defect mechanisms, including self-collimated effects (Zhang et al. 2007), interference-based defects (Nirmala Maria D'souza 2016), and multimode interference. Bit rate, reaction time/delay time, switching speed, footprint, operating wavelength, and contrast ratio are among the predicted functional parameters.

Design of 4 × 2 Encoder

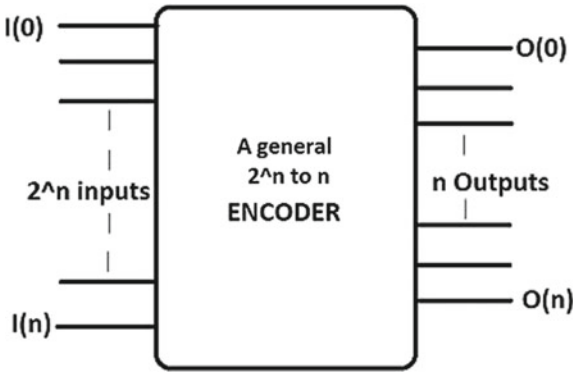

Fig. 8.3 The General block diagram of the Encoder

Figure 8.4 depicts the schematic arrangement of a 4 × 2 encoder, and Table 8.1 lists the design parameters. Four linear waveguide inputs (A0, A1, A2, and A3) and two Y-shaped output waveguides comprise the encoder's design (B0 and B1). By removing crystal rods from the structure in a plane direction and connecting them to binary code input A0, the A0 waveguide is created. When the binary code input A0 is high, both outputs must be zero, so the waveguide is constructed with a minimum short dimension and is not connected to the output port.

Similarly to that, the parallel of A0 constructed the waveguides A1, A2, and A3, and those waveguides served as input ports. The output waveguide and the input waveguide are bridged by the nanocoupling rods are named N1, N2, N3, and N4. To distribute the input power equally across all states, the silicon rods' radius is reduced by 50 nm to create the coupling rods. An encoder's output power can be

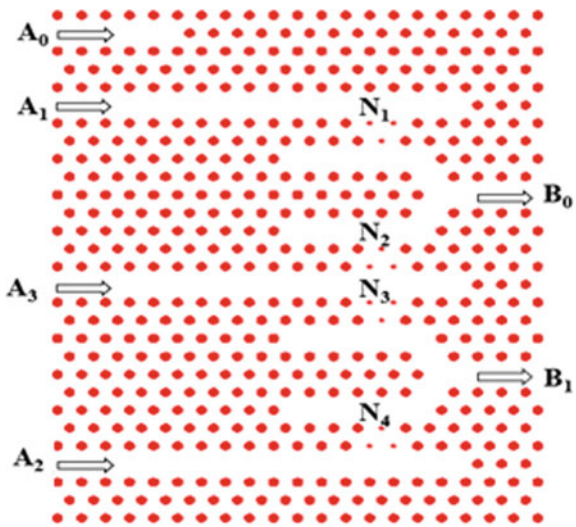

Fig. 8.4 The 4 × 2 encoder schematic layout

Table 8.1 Design parameters of 4 × 2 encoder

Description	Materials	Radius (nm)	Refractive index	Lattice structure	Structure type and defect mechanism
4 × 2 Encoder	Silicon (Si)	100	3.46	Triangular lattice	Line and Point defect—Y-shaped waveguides
Nano coupling rods N1, N_2, N_3	Silicon (Si)	50	3.46	Triangular lattice	Line and point defect

increased by using nanorods to improve the coupling between the input and output signal transmission, which also lowers reflection losses.

There are four input ports that receive the Gaussian optical waves. For simulation, 1550 nm of the resonance wavelength and 1 mW of input power are used. The 2D FDTD approach is used to simulate the proposed encoder structure and analyze the performance metrics. By acting as a digital switch between the input and output waveguides, the nanocoupling rods (N1, N2, N3, and N4) were introduced in the proposed structure to improve coupling between the input and output ports. The power input in this simulation is considered to be Pi, the power output to be Po, and the normalized power to be Pn = Po/Pi. In this instance, the output port's normalized power level yields a logical level, such as an "ON" or "OFF" state. P_o is believed to be logic "1" if directly above 0.25mW and logic "0" if it is directly below that level.

State 1: In the case of a given logic input of 1000, where A0 = 1 is "ON" and A1, A2, and A3 are "OFF," the Gaussian input signal is not entered within the waveguide. In this instance, the waveguide A0 configuration blocks the input signal after it enters the A0 input port. As a result, as illustrated in Fig. 8.5, no power is sent to output ports B0 and B1 (00). The normalized transmission power is 0% since Po output power is 0.0062 at B0 and 0.0001 at B1. Figure 8.5 inset shows the electromagnetic field distribution.

State 2: A0, A2, and A3 inputs are in the "OFF" state for the logic input 0100, but A1 is in the "ON" state. The input signal is sent through the N1 Nano coupling rods and into the A1 input port. So, as illustrated in Fig. 8.5, the output port B0 is in the "ON" state, whereas B1 is in the "OFF" state. The output port B0's normalized power level is around 99.8%, and the field distribution is depicted as an inset in Fig. 8.5. A power level of 0.0052% was attained by output port B1 as well.

State 3: The input port A2 = 1 is in the "ON" state, the logic input 0010 is provided, and the remaining inputs are left in the "OFF" condition. The field distribution when the input is 0010 is depicted in the inset of Fig. 8.5c. With the input power provided to port A2, the input signal coupled through the N4 coupling rods in the B1 output port, and the input power supplied to port A2, the encoder produces output 01 as illustrated in Fig. 8.5. B0 has a power level of 0.0052%, while B1 has a power level of 99.8%.

State 4:A3 is "ON" for logic input 0001 and "OFF" for A0, A1, and A2 inputs. The input signal is fed to port A3, as seen in the inset of Fig. 8.5d, and after that, light flows through both Y-shaped waveguides while being coupled through the N2

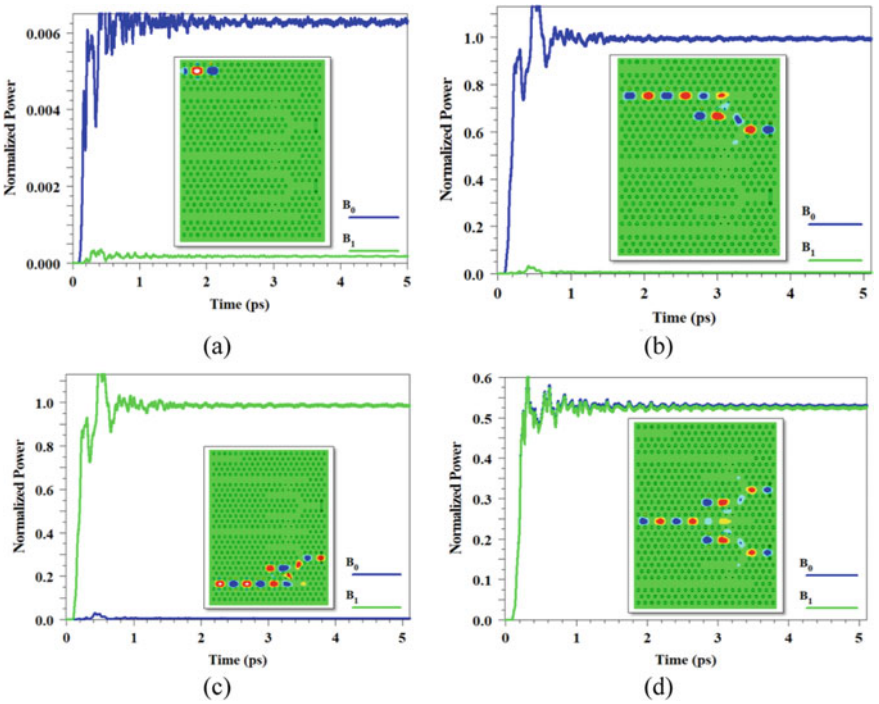

Fig. 8.5 Signal transmission and output responses of the proposed 4 × 2 encoder design

and N3 coupling rods, creating high output power in both output ports B0 and B1. In this case, the Encoder generates the output 11, which is shown in Fig. 8.5. According to Fig. 8.5, the normalized transmission power is 53.11% and the normalized power level at B0 and B1 is 0.5311 Pi.

The output for the "ON" and "OFF" states remain the same when the input is either 1000 or 0001, hence the contrast ratio is approximated for the inputs 0100 and 0010. When the output power levels of 0.9980 and 0.0052 are compared to the input levels of 0100 and 0010 for different logic levels, the resulting contrast ratio is 22.83 dB, respectively. For logic outputs 01 and 10, the response time and data rate are 0.228 ps and 4.38Tbps, respectively. For logic output 11, the response time and data rate are 0.235 ps and 4.25Tbps, respectively. The proposed optical encoder's minimum contrast ratio, maximum delay time, and minimum data rate are 22.83 dB, 0.235 ps, and 4.25Tbps, respectively.

Design OF 8 × 3 Encoder

The suggested 8*3 Encoder's schematic construction is shown in Fig. 8.6. There are eight input ports and three output ports on this 8*3 Encoder. To increase the output power, a defect rod with a radius of 40 nm is introduced in the center of the output

waveguide. Eight input ports and three output ports make up the proposed 8 × 3 Encoder. The Truth Table in Table 8.2 analyzes the Encoder's output.

Figure 8.7a–h displays the field distribution and output response of the proposed 8*3 Encoder for various input scenarios. The 1mW of input power is applied when

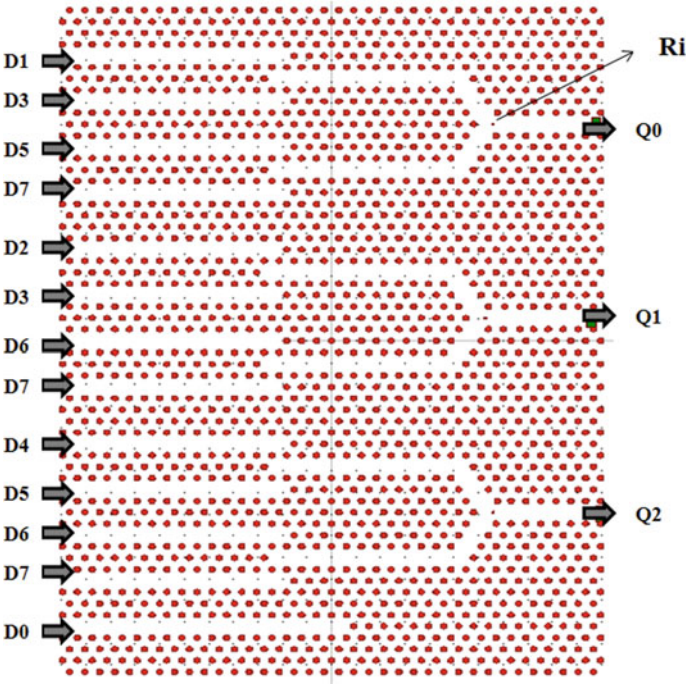

Fig. 8.6 Schematic structure of proposed 8*3 encoder

Table 8.2 Truth table of 8*3 encoder

Inputs									Outputs			
Input Logic	D0	D1	D2	D3	D4	D5	D6	D7	Output Logic	Q2	Q1	Q0
Input Logic 1	1	0	0	0	0	0	0	0	Output Logic 1	0	0	0
Input Logic 2	0	1	0	0	0	0	0	0	Output Logic 2	0	0	1
Input Logic 3	0	0	1	0	0	0	0	0	Output Logic 3	0	1	0
Input Logic 4	0	0	0	1	0	0	0	0	Output Logic 4	0	1	1
Input Logic 5	0	0	0	0	1	0	0	0	Output Logic 5	1	0	0
Input Logic 6	0	0	0	0	0	1	0	0	Output Logic 6	1	0	1
Input Logic 7	0	0	0	0	0	0	1	0	Output Logic 7	1	1	0
Input Logic 8	0	0	0	0	0	0	0	1	Output Logic 8	1	1	1

the input port is turned on. If the output power is greater than 50%, the output is considered 1 (ON); otherwise, the output is considered 0.

The field distribution and the output response curve for the proposed 8*3 Encoder for different logic gates are depicted in Fig. 8.7. From the above figure, there are

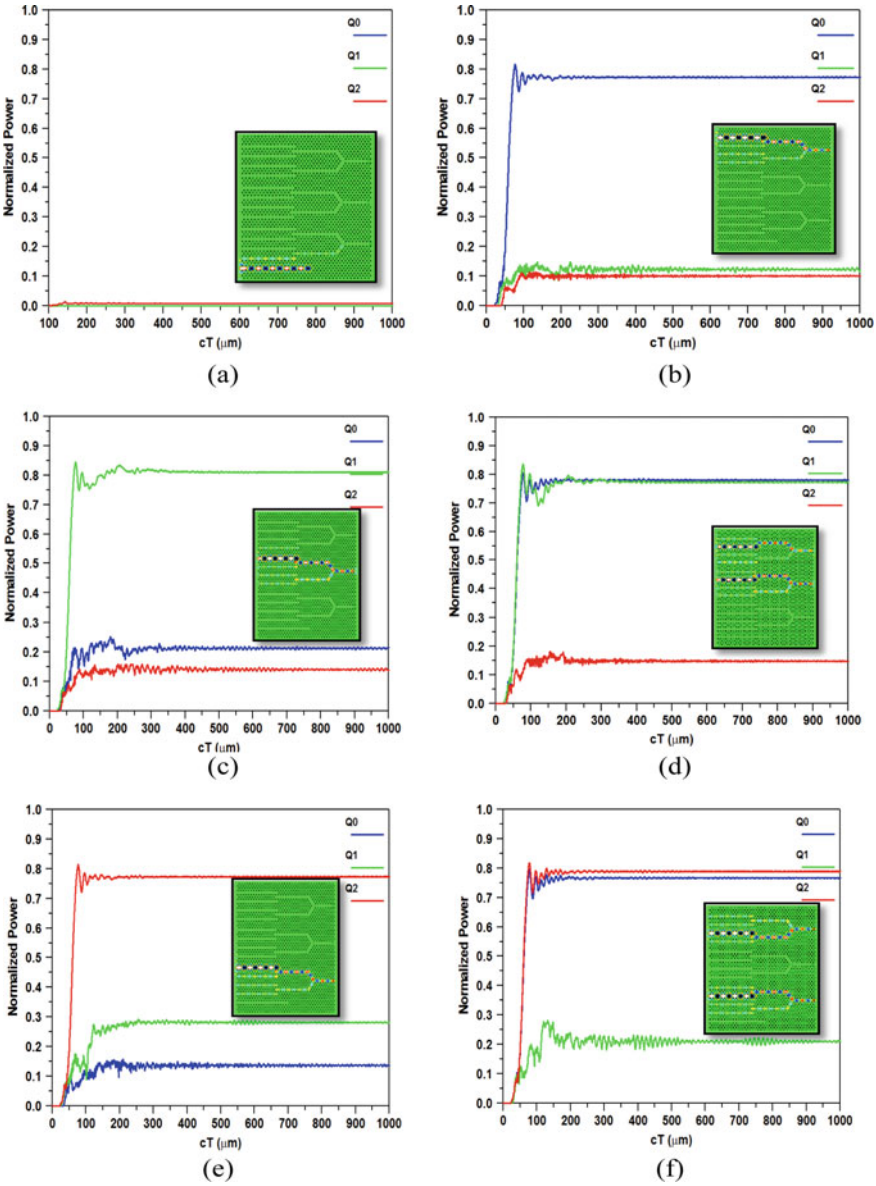

Fig. 8.7 Output response and Signal propagation of 8*3 Encoder for different logic state

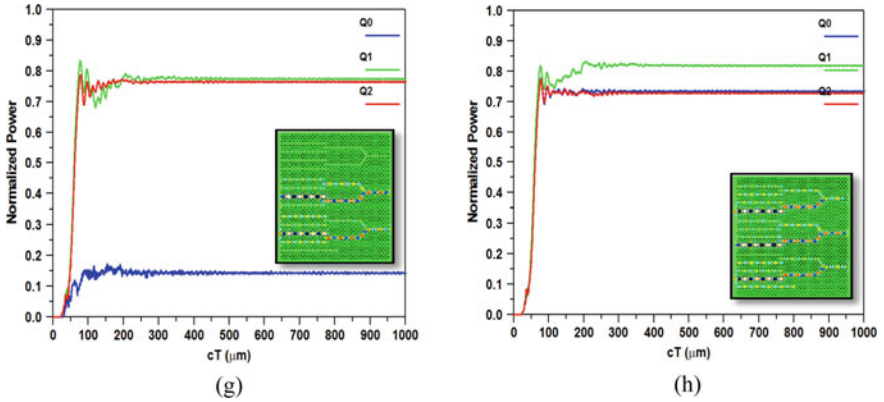

Fig. 8.7 (continued)

eight inputs, such as D0–D7 and three outputs Q0–Q2 were estimated. In Fig. 8.7a when input D0 is ON and D1, D2, D3, D4, D5, D6, D7 are OFF, the logic represented as 1,000,000 in Fig. 8.7b; hence, there is no output power at output ports Q0, Q1, Q2. In Fig. 8.7b, when input D1 is ON and D0, D2, D3, D4, D5, D6, D7 are OFF, the logic represented as 0,100,000; hence, the output port Q0 is ON. In Fig. 8.7c, if the input D2 is ON, then D0, D1, D3, D4, D5, D6, D7 are OFF; at this condition, the output port Q1 is ON. Hence, the field distribution is represented as 0,010,000. The maximum amount of power resonates in both output ports Q1 & Q2. When input D3 is ON and D0, D1, D2, D4, D5, D6, D7 are OFF, the logic for this state as 0,001,000 in Fig. 8.7d. The maximum amount of power resonates in both output ports Q1 & Q2. If the input D4 is ON then D0, D1, D2, D3, D5, D6, D7 are OFF, the output port Q2 is ON and Q1 & Q2 are OFF condition the logic for this state is noted as 0,000,100 in Fig. 8.7e, the power reaches the output port Q2. If the input port D5 is ON and D0, D1, D2, D3, D4, D6, D7 are OFF, the first and third Y-shaped waveguides are enabled. Therefore, the output ports Q0 and Q2 are ON and Q1 is OFF condition. Figure 8.7f represents the logic 00,001,000 the input power applied to port D5, the maximum power reached at the output port as Q0 and Q2. When the input port D6 is ON and D0, D1, D2, D3, D4, D5, D7 are OFF, the output ports Q1, Q2 are ON and Q0 is OFF, the signal propagation for the logic noted as 0,000,010 in Fig. 8.7g; hence, the power reaches the output port in Q1 and Q2. When input port D7 is ON and D0, D1, D2, D3, D4, D5, D6 are OFF, all the three output ports such as Q0, Q1, and Q2 are ON. Figure 8.7h represents the electric field distribution for logic 00,000,001; the maximum power reached at the output port as Q0, Q1, Q3.

With the output as mentioned above response, the contract radio, response time, and bit rate are computed. The contrast ratio is determined using the logarithmic function for logic 1 and 0 values. 9.08 dB is the contrast ratio value. Similar to this, $t = 0.25$ ps, $t1 = 0.217$ ps, and $t2 = 0.33$ ps are used to investigate the response time of 0.132 ps. The calculated bit rate is 7.5 Tbps. Table 8.3 displays the 8*3 Encoder's output performance.

Table 8.3 Logic functional parameter of the proposed 8*3 encoder

Input logic	Outputs			Functional parameters
	Port 2	Port 1	Port 0	
Input Logic 1	0	0	0	Contrast ratio = 9.08 dB Response time = 0.132 ps Bit rate = 7.5Tbps
Input Logic 2	0.1	0.14	0.78	
Input Logic 3	0.22	0.82	0.14	
Input Logic 4	0.15	0.78	0.78	
Input Logic 5	0.78	0.23	0.15	
Input Logic 6	0.78	0.22	0.79	
Input Logic 7	0.78	0.78	0.14	
Input Logic 8	0.81	0.74	0.74	

Comparing the functional properties of the suggested encoders to those of the reported encoders mentioned in Table 8.4 regarding contrast ratio, reaction time, and bit rate. From the table, it is determined that the response time decreases as the contrast ratio rises. At the same time, if the response time is faster, it instead restricts the contrast ratio. The same encoder will yield poor structural dimensions even if other functional parameters like contrast ratio, bit rate, and reaction time are excellent. Yet, compared to the previously reported encoders, the proposed encoder offers a noticeable improvement in all parameters with a smaller size. The proposed encoders are therefore employed in photonic integrated circuits for high-speed computing, communication, and data storage.

Photonic Crystal-Based Decoder

Based on the specific logic state of the input and the existing control signals, a decoder is a logic device that transforms a collection of input signals into matching output signals. A decoder is a combinational logic circuit that converts binary data or binary code from "N" bit input lines to a "2N" bit unique output line at the most while stimulating only one output line for all possible combinations of input (Sharma et al. 2022). Figure 8.8. demonstrates the encoder's overall block diagram (Rostamizadeh et al. n.d.).

Design Of 4 × 2 Decoder

A two-dimensional grid of chalcogenide rods organized in a square array makes up the basic structure. In the shape of a lattice with a spatial period (a) of 530 nm, it is assumed that there are 23 and 14 rods, respectively, with air spaces along the x- and z-directions. The dielectric rods' estimated refractive index is 3.1. A photonic band gap can be obtained by matching the structure to the optical system so that the third optical communication window falls within the range of 1215–1710 nm

Table 8.4 Functional parameter comparison between proposed and reported encoders

References	Type	Lattice	Defects	Footprint	Contrast ratio (dB)	Response time (ps)	Bit rate (Tbps)
HamedSeif-Dargahi (2018)	4*2	Square	Ring resonator	***	9.2	1.8	0.5
SiamakGholamnejad (2017)	4*2	Square	Ring resonator	***	***	1	1
FarhadMehdizadeh (2017)	4*2	Square	Line and Point	880 μm^2	***	0.2	5
Salimzadeh (2018)	8*3	Square	Ring resonator	***	***	2	0.5
Monisha et al. (2018)	4*2	Square	Ring resonator	***	11.5	***	***
Naghizade et al. (2018)	8*3	Square	Line and Point	1418 μm^2	***	0.16	6.25
Mostafa et al. (2018)	4*2	Square	Ring resonator	128.52 μm^2	7.11	0.1	10
Jayabharathan et al. (2018)	8*3	Triangular	Ring resonator	1674 μm^2	***	0.33	3
FatemehHaddadan (2018)	8*3	Square	Line and Point	510 μm2	***	3	0.33
Rajasekar et al. (2019)	4*2	Square	Line and Point	***	***	5	0.2
RaminYaghoobi and Sahel Javahernia (2018)	4*2	Triangular	Point and Line		25.82	0.28	3.5
Proposed work							
This work	8*3	Triangular	Line and Point	705.12 μm^2	9.08	0.132	7.5

*** Not Mentioned

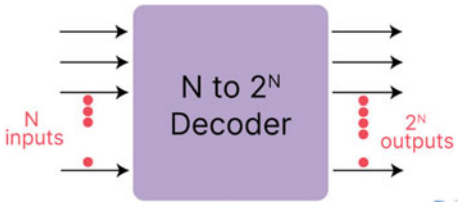

Fig. 8.8 The general block diagram of decoder

(JavadMaleki et al. 2019). Eight waveguides make up the suggested structure for decoding operation, which links two input ports (X and Y) to four output ports (O0, O1, O2, and O3). As a result, the lowering operations for the various intensities

through the holes are made possible by exploiting the various radii in the cavities in addition to the optical Kerr effect.

In Fig. 8.9, the radius of the green, yellow, blue, and black rods in waveguides W5, W6, W7, and W8 was assumed to be 118, 111, 104, and 97 nm, respectively, by adjusting the values of the radii for nonlinear rods with a step of 1 nm and calculating the power at output ports. In order to achieve decoding operation, different optical intensities into waveguide W4 in response to varied states of input ports will be dropped through waveguides W5W8. In Fig. 8.2b, the radii of a few rods in waveguides W1W3 are shown. These rods, which resemble the fundamental ones, are constructed of chalcogenide and have been painted red. Two 64 nm-radius rods have been inserted into the corners of waveguides W2 and W3 to improve optical wave transmission at bends. In waveguides W1 and W3, four rods with a radius of 74 nm and one rod with a radius of 70 nm are taken into consideration for achieving the appropriate interferences at the cross-connect.

By using various intensities on waveguide W4 and computing the normalized powers at output ports, the dropping action was further assessed. Figure 8.10 demonstrates that, for I0 equal to 10, the maximum dropping through waveguides W5, W6, W7, and W8 will occur approximately for I0, 2I0, 3I0, and 4I0, respectively.

Detailed information on the power analysis and timing assessment is provided in Table 8.6 contains comprehensive information on the power analysis and time evaluation. In the scenario when $X = Y = 1$, the highest normalized power value for logic 0 is around 4%. The lowest normalized power value for logic 1 is proportional to the scenario where $X = Y = 0$, where it equals 87%. The margins of error for logics 0 and 1 are therefore considered to be 4% and 87%, respectively. As can be observed, this structure's delay time is 220 fs, which is equivalent to the amount of

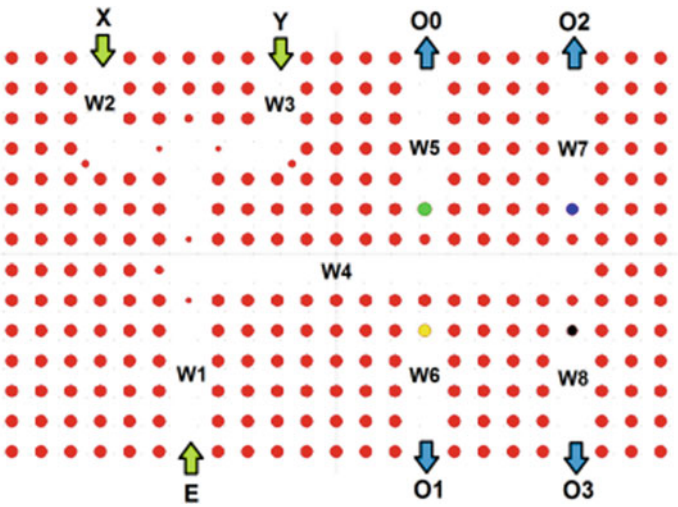

Fig. 8.9 The proposed structure for the optical 2-to-4 decoder

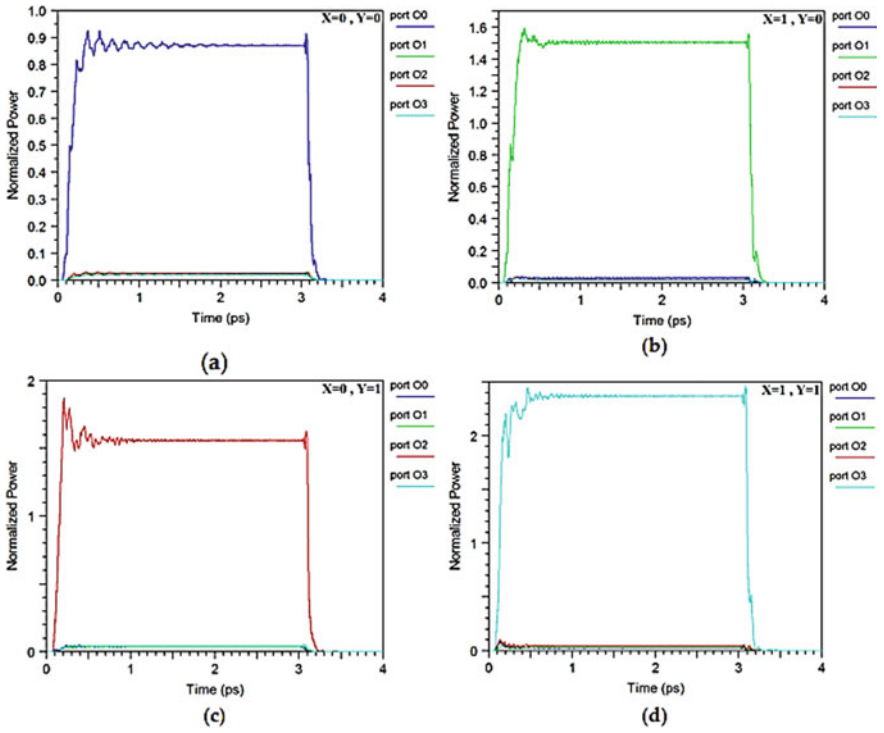

Fig. 8.10 The time response of the proposed structure for different states

time needed for a signal to reach 90% of its ultimate value. Moreover, for state X = Y = 1, the fall time (the length of time it takes for one cycle to fall in a 10% beginning value) is roughly 145 fs. Last but not least, 1.9 ps is the highest steady-state period in the 2% error band, as shown in Table 8.5.

Table 8.5 The time analysis's final results

Input		Output logic				Power (%)				Delay time (fs)	Fall time (fs)	Steady state time (ps)
X	Y	O0	O1	O2	O3	O0	O1	O2	O3			
0	0	1	0	0	0	87	3	3	2	200	130	1.9
1	0	0	1	0	0	3	151	3	2	210	125	1.6
0	1	0	0	1	0	3	3	155	3	205	120	1.7
1	1	0	0	0	1	3	4	4	239	220	145	1.6

Conclusion

The ideas, functionality, and specifications of encoders and decoders, which will be widely utilized for metro/access networks and enterprise networks, are discussed in this chapter. The encoder and decoder are made in a triangle or square lattice to allow optical computing applications that are used in real time. The photonic band gap for a row of rods before and after a defect is modeled using the PWE approach in the photonic crystal-based optical systems. The FDTD method is used to analyze 4*2 Encoder and 8*3 Encoder and the size of the devices are 178.1 μm^2 and 705.12 μm^2, respectively. The suggested encoder and decoder have high contrast ratio, a wide operational bandwidth, and low power consumption. The encoder and decoder are ideal for all high-speed optical communication, optical switching, and integrating devices due to their superior bit rate and response time.

References

Abdel Malek F (2011) Design of a novel left-handed photonic crystal sensor operating in aqueous environment, IEEE Photon. Technol Lett 23(3):188–190

Benisty H, Cambournac C, Laere FV, Thourhout DV (2010) Photonic crystal demultiplexer with improved crosstalk by second-order cavity filtering. J Lightwave Technol 28(8):1201–1208

Fan S, Villeneuve PR, Joannopoulos JD, Haus HA (1998) Channel drop tunneling through localized states. Phys Rev Lett 80(5):950–963

FatemehHaddadan MS (2018) Low-power all-optical 8-to-3 encoder using photonic crystal-based waveguides. Photon Netw Commun 36(1):1–7

Fermi R, Houdre R (2003) Radiation losses in planar photonic crystals: two dimensional representation of hole depth and shape by an imaginary dielectric constant. Opt Soc Am B 20:469–478

Gannat GA, Pinto D, Obayya SSA (2009) New configuration for optical waveguide power splitters. IET Optoelectron 3(2):105–111

Geerthana S (2022) S Syedakbar, T Sridarshini, V R Balaji, R Sitharthan and D Shanmuga Sundar, 2D- PhC based all optical AND, OR and EX-OR logic gates with high contrast ratio operating at C band. Laser Phys 32:10

Gholamnejad S, Zavvari M (2017) Design and analysis of all-optical 4–2 binary encoder based on photonic crystal. J Opt Quantum Electron 302(49)

Jayabharathan JK, Subhalakshmi G, Robinson S (2018) Design of all-optical 8*3 encoder using hexagonal shaped photonic crystal ring resonator. J Ovonic Res 14(5):351–358

Joannopoulos JD, Meade RD, Winn JN (1995) Photonic crystal: molding of flow of light. Princeton University Press, Princeton, NJ

Joannopoulos DJ, Steven Johnson G, Winn NJ, Meade RD (2008) Photonic crystals: modeling the flow of light, 2nd edn. Princeton University Press

John S (1987) Strong localization of photons in certain disordered dielectric superlattices. Phys Rev Lett 58(23):2486–2489

Li W, Xu XM, He YP, Tao L (2010) A ultra-short 1×2 double wavelength optical power splitter for 1310/1550 nm operation based on photonic crystal multimode interference. Proc SPIE Asia Commun Photon 7631:76312J1-J11

Lu TW, Chiu LH, Lin PT, Lee PT (2011) One-dimensional photonic crystal nanobeam lasers on a flexible substrate. Appl Phys Lett 99(7):071101–071101–3

Maleki MJ, Soroosh M, Mir A (2019) Improving the Performance of 2-To-4 OpticalDecoders Based on Photonic Crystal Structures. Crystals 9:635. https://doi.org/10.3390/cryst9120635
Martínez A, Sanchis P, Marti J (2005) Mach–Zehnder interferometers in photonic crystals. J Opt Quantum Electron 37:77–93
Mehdizadeh F, Soroosh M, Alipour-Banaei H (2017) A proposed for 4-to-2 optical encoder based on photonic crystals. IET Optoelectronics 11(1):29–35 (2017); Salimzadeh A, Alipour-Banaei H (2018) An all optical 8 to 3 encoder based o photonic crystal OR-gate ring resonators. J Opt Commun 410:793–798
Moghaddam MK, Attari AR, Mirsalehi MM (2010) Improved photonic crystal directional coupler with short length. Photon Nanostruct-Funda Appl 8(1):47–53
Mohmoud MY, Bassou ZM, Taalbi A, Chekroun ZM (2012) Optical channel drop filters based on photonic crystal ring resonators. Optics Commun 285(1):368–372
Monisha S, Saranya D, Rajesh A (2018) Design and analysis of multi—hexagonal reversible encoder using photonic crystals. J Opt Quantum Electron 51(1):1–12
Mostafa TS, Mohammed NA, El-Rabaie E-S (2018) Ultracompact ultrafast-switching-speed all-optical 4×2 encoder based on photonic crystal. J Comput Electron 17(1):1–14
Naghizade S, Mohammadi S, Khoshsima H (2018) Design and simulation of an all optical 8 to 3 binary encoder based on optimized photonic crystal OR gates. J Opt Commun 39(2)
Nirmala Maria D'souza (2016) Vincent Mathew, Interference based square lattice photonic crystal logic gates working with different wavelengths. J Opt Laser Technol 80:214–219
Pelosi G, Coccioli R, Selleri S (1997) Quick finite elements for electromagnetic waves. Artech House, Boston, London
Pendry JB, MacKinnon A (1992) Calculation of photon dispersion relation. Phys Rev Lett 69:2772–2775
Pendry JB (1996) Calculating photonic band structure. J Phys: Condensed Matter 8(9):1085–1108
Rajasekar R, Latha R, Robinson S (2019) Ultra-contrast ratio optical encoder using photonic crystal waveguide. J Mater Lett 251:144–147
RaminYaghoobi and Sahel Javahernia (2018) An optical majority gate using photonic crystal based nonlinear resonant cavity. J Opt Commun. https://doi.org/10.1515/joc-2018-0122
Rawal S, Sinha RK (2009) Design, analysis and optimization of silicon-on-insulator photonic crystal dual band wavelength demultiplexer. Opt Commun 282(19):3889–3894
Rostamizadeh A, Taghizadeh M, Jamali J, Andalib A, Application of photonic crystal based nonlinear ring resonators for realizing all optical 3-to-8 decoder. J Opt Commun https://doi.org/10.1515/joc-2020-0094
Saleh BEA, Teich MC (2019) Fundamentals of photonics, 3rd edn. Wiley, New Delhi, India
Salimzadeh A (2018) HamedAlipour-Banaei, "An all optical 8 to 3 encoder based o photonic crystal OR-gate ring resonators." J Opt Commun 410:793–798
Salmanpour A (2015) ShahramMohammadnejad, PedramTaghinejadOmran, All-optical photonic crystal NOT and OR logic gates using nonlinear Kerr effect and ring resonators. J Opt Quantum Electron 47(12):3689–3703
Sathyadevaki R, Sundar DS, Raja AS (2018) Photonic crystal 4×44×4 dynamic hitless routers for integrated photonic NoCs. Photon NetwCommun 36:82–95
Sathyadevaki R, Shanmugasundar D, SivananthaRaja A (2016) Design of dual ring wavelength filters for WDM applications. Opt Commun 380:409–418
Seif-Dargahi H (2018) Ultra-fast all-optical encoder using photonic crystal-based ring resonators. Photonic Netw Commun 36(2):272–277
ShanmugaSundar D, Sathyadevakiand R, SivananthaRaja A (2018) High-efficiency filters for photonic integrated networks: a brief analysis. Laser Phys 28:11
Shanmugasundar D, Sathyadevaki R, Sridarshini T et al, Photonic crystal based routers for photonic integrated on chip networks: a brief analysis. Opt Quant Electron 50:383
Sharma A, Goswami K, Mondal H, Datta T, Sen M (2022) A review on photonic crystal based all-optical logic decoder: linear and nonlinear perspectives. Opt Quantum Electron 54:90

Taflove A (2005) Computational electrodynamics: the finite- difference time-domain method. Artech House, Boston, London

Tang C (2014) XinyuDou, YuxiLin, HongxiYin, Bin Wu, Qingchun Zhao, Design of all-optical logic gates avoiding external phase shifters in a two-dimensional photonic crystal based on multimode interference for BPSK signals. J Opt Commun 316(1):49–55

Thirumaran S, Dhanabalan SS, Sannasi IG (2021) Design and analysis of photonic crystal ring resonator based 6 × 6 wavelength router for photonic integrated circuits. IET Optoelectronics 15:1

Wang Q, Cui Y, Zhang H, Yan C, Zhang L (2010) The position independence of heterostructure coupled waveguides in photonic-crystal switch. Optik Opt 121(8):684–688

Yablonovitch E (1987) Inhibited spontaneous emission on solid-state physics and electronics. Phys Rev Lett 58(20):2059–2062

Yee KS (1996) Numerical solution of initial boundary value problems involving Maxwell's equation in isotropic media. IEEE Trans Antenna Propag 14:302–307

Yi G, Youn BD (2016) A comprehensive survey on topology optimization of phononic crystals. J Struct Multidiscip Optim 54(5):1315–1344

Yue, Y, Gong, JP (2015) Tunable one-dimensional photonic crystals from soft materials. Journal of Photochemistry and Photobiology C: Photochemistry Reviews 23:45–67

Zhang Y, Zhang Y, Li B (2007) Optical switches and logic gates based on self-collimated beams in two-dimensional photonic crystals. J Opt Express 15(15):9287–9292

Chapter 9
Photonic Crystal Fibers for Sensing Applications

Daniel A. May-Arrioja, Natanael Cuando-Espitia, Amado M. Velázquez-Benítez, and Juan Hernández-Cordero

Abstract Optical fibers are cylindrical waveguides widely used in communications and sensing. These waveguides present important features for sensing applications, such as a reduced footprint, low toxicity, high sensitivity, and the ability for remote monitoring and multiplexing. Photonic crystal fibers (PCFs) offer several advantages over conventional fibers for developing sensors, improving their capabilities yet maintaining the biocompatibility features of their conventional counterparts. In PCFs, the light is confined by a periodic pattern of microstructured air holes running along the fiber, thus allowing lower losses. By engineering the geometric array of air holes, the response of PCFs can be optimized to use their unique features in sensing schemes. Different arrangements have been proposed to measure physical parameters such as refractive index, temperature, and bending using PCFs. In biomedical applications, they have been recognized as a key element for developing glucose detection devices and for designing gas sensors with high specificity and sensitivity. Additionally, the inherent compatibility of PCFs with fiber optic devices has allowed its integration with interferometric structures and other specialty fibers, thus enabling the generation of miniature, low-cost, high-efficiency, scalable, and multiparameter biosensors.

D. A. May-Arrioja (✉)
Centro de Investigaciones en Óptica A.C., Fracc. Reserva Loma Bonita, Prol. Constitución 607, Aguascalientes 20200, México
e-mail: darrioja@cio.mx

N. Cuando-Espitia
Applied Physics Group, CONACyT, DICIS, University of Guanajuato, Salamanca, Guanajuato 368850, México

A. M. Velázquez-Benítez
Instituto de Ciencias Aplicadas y Tecnología, Universidad Nacional Autónoma de México, Circuito Exterior S/N, Ciudad Universitaria, Mexico City 04510, México

J. Hernández-Cordero
Instituto de Investigaciones en Materiales, Universidad Nacional Autónoma de México, Circuito Exterior S/N, Ciudad Universitaria, Mexico City, Cd 04510, México

© The Author(s), under exclusive license to Springer Nature Singapore Pte Ltd. 2023

S. S. Dhanabalan et al. (eds.), *Photonic Crystal and Its Applications for Next Generation Systems*, Springer Tracts in Electrical and Electronics Engineering,
https://doi.org/10.1007/978-981-99-2548-3_9

Fundamentals of Photonic Crystal Fibers

It is highly recognized that optical fiber technology plays a key role for the incredible amount of data transmitted and received around the globe today. A single tiny silica thread of about 120 microns can support the same amount of information carried by hundreds of metal wires. It also exhibits lower noise and losses while carrying the information much faster. By the mid-1990s, several applications for this technology had been developed using conventional optical fibers, and physical limitations, such as confined cross-section areas of fundamental modes and limited operational wavelengths, restricted other applications. However, these and other limitations were greatly exceeded with the advent of Photonic Crystal Fibers (PCF) (Atkin et al. 1941). In short, PCFs can be seen as optical fibers in which a periodic structure of air holes runs along the fiber axis. By carefully engineering the periodic pattern, PCFs may permit monomodal operation in a wide range of wavelengths, generate wide modal areas, or enhance interesting nonlinear effects. PCFs have impacted areas such as supercontinuum generation and high-power laser delivery, and have been particularly exploited in optical sensing owing to their great flexibility.

The idea of generating a photonic lattice to reproduce prohibited band gaps analogous to the crystal lattices of semiconductors was motivated by the search for more efficient solid-state laser sources (Yablonovitch and Gmitter n.d.; John 1987). This idea was rapidly identified as a novel approach to guiding light within a fiber. The first report of a PCF was published in 1996 by the group of Phillip Russell, demonstrating a fiber structure with a solid core (Knight et al. 1996). In general, solid-core PCFs exhibit larger modal areas than conventional fibers. They can operate as single-mode waveguides over a large range of wavelengths and show very low intrinsic losses due to the lack of dopants in the core. The other main category of PCFs emerged a few years later with the publication, by the same group, of a hollow-core PCF in which the light was guided in the air (Cregan et al. n.d.). In contrast to conventional guiding mechanisms, this work demonstrates the Photonic Bandgap (PBG) as the key feature for trapping light in silica fiber. Since the appearance of these seminal papers and based on these two types of PCFs, various applications have been reported by different groups around the globe.

Figure 9.1 schematically shows the cross sections of solid-core and hollow-core PCFs. In a conventional optical fiber, light is confined at the core if and only if the core's refractive index (RI) is higher than that of the cladding. This condition imposes the need to use slightly different materials to fabricate an optical waveguide. However, a structure formed with a single material (silica) incorporating a periodic structure of air holes (diameter d and hole separation Λ) around a solid silica rod can exhibit an effective RI difference to achieve waveguiding conditions. Thus, a solid-core PCF can effectively guide light using a mechanism similar to conventional fibers. Moreover, the air holes act as a modal filter, allowing for the transmission of a fundamental mode with a typical cross-sectional area of twice the separation of

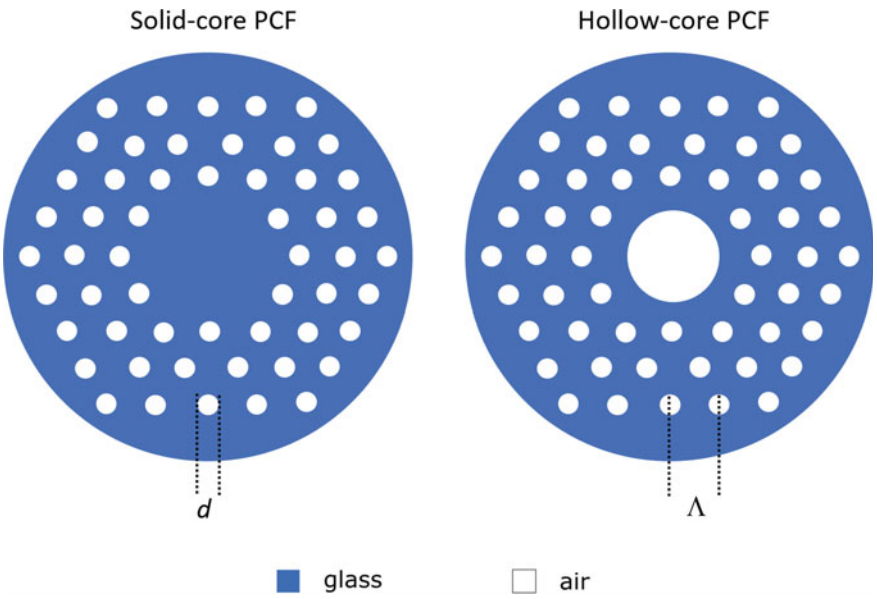

Fig. 9.1 Schematic representation of the cross-section of typical solid-core and hollow-core PCFs. In the figure, blue represents silica and white represents air holes. In this example, the cladding structure is identical with a hole diameter labeled as d and hole separation labeled as Λ. The separations, *d and* Λ and fiber diameter are not to scale and have been drawn to exemplify the basic idea of PCF structures

the air holes (2Λ). It has been shown that fundamental guiding occurs for a silica structure in which $d/\Lambda < 0.4$ (Mortensen et al. 2003).

Using a similar fabrication technology, one can design a PCF in which a relatively large air hole forms the fiber's core. For example, this PCF can be obtained by incorporating a glass capillary at the center of a honeycomb structure made upon stacking capillaries with smaller diameters than that at the center. The light-guiding mechanism for these structures relies on the fact that for certain optical frequencies, the honeycomb structure has gaps preventing energy from escaping the central hole of the fiber (i.e., the hollow core). In particular, the guiding condition for the hollow-core PCF is $\beta/k_0 < 1$ (where β is the propagation constant and k_0 is the free space wavenumber), which guarantees that no energy of the fundamental mode propagates through the cladding.

The main sources of losses in PCFs are related to OH impurities as well as imperfections in the air-hole structure. Typically, attenuation due to OH absorption in these fibers is within 0.01 dB/km and can be tackled by dehydration during the fabrication process (Saha et al. 2019). Meanwhile, imperfections in the periodic structure may arise as surface roughness or small variations in the geometry of the fiber structure. Hollow-core PCFs are especially sensitive to fiber imperfections since part of the energy can easily couple to cladding modes (Kurokawa et al. n.d.). Since the cross section of PCFs contains a finite number of air holes, modal leakage can occur;

by increasing the ratio d/Λ, one can increase the modal confinement, although this ratio should also be kept small enough to maintain monomodal operation. It has been shown that a minimum leakage loss is observed at the normalized wavelength $\lambda/\Lambda = 0.68$ (Vincetti 2003). Finally, bending loss is another factor arising during PCF fabrication. For solid-core PCFs, the bending loss mechanisms are related to coupling losses due to the misalignment of fiber sections. In contrast, hollow-core PCFs are less sensitive to bending loss as the main effect of curvature in these fibers is the narrowing of the PBG. This interesting feature has recently allowed for the development of laser pulse-handling systems based on hollow-core PCFs, delivering up to 4.9 kW of peak power at 3.4 μm over hundreds of meters (Fu et al. 2022).

The progress in fabrication capabilities, along with the inherent versatility of PCFs, has led to different designs impacting a variety of applications by tuning, for instance, birefringence, operational wavelength, modal cross-sectional area, and nonlinear effects. Moreover, as we will see in the following sections, PCF air channels can be filled with gasses and liquids to realize high-sensitivity sensors. In other words, PCFs have opened the door for integrating fiber optics with gasses and liquids, providing a means to probe these media by using PCFs as microchambers to perform optical tests such as fluorescence and optical absorption. PCFs detect physical or chemical parameters in a middle section between two single-mode fibers (SMFs) or at the end of an SMF spliced to the PCF. The most common configurations are shown in Fig. 9.2; in all cases, the parameter to be measured produces a change in the spectral features or intensity of the light guided by the fibers. These changes can be quantified, analyzed, or both, using standard transmission or reflection configurations such as those depicted in Fig. 9.2.

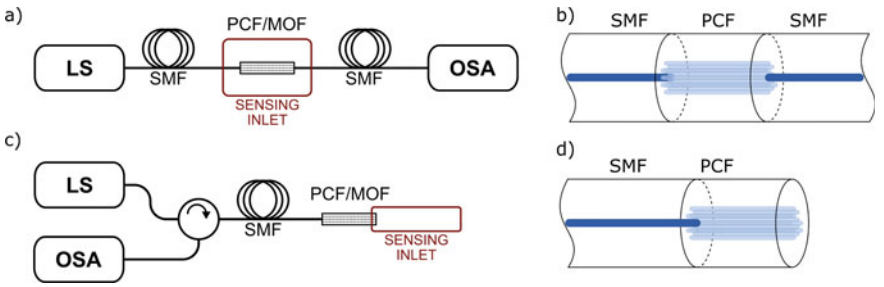

Fig. 9.2 Typical experimental setups for gas sensing with PCFs. **a** Transmission readout setup. **b** Reflection readout setup. Schematic detail of PCFs within fiber devices. **c** Typical SMF-PCF-SMF fiber device for transmission measurements. **d** Typical SMF-PCF fiber device for reflection measurements (MOF: Microstructured Optical Fiber)

Refractive Index Measurements

The main advantage of using PCFs for RI measurements relies on the possibility of introducing diverse materials inside the holes, thus serving as a micrometric container. Refractometers are commonly constructed by partially or completely filling the holes of the PCF with the material or substance to be analyzed (Liu et al. 2017; Algorri et al. 2018; Urrutia et al. 2019). Hence, incorporating the materials into the fibers is a suitable approach to facilitate the light–sample interaction, thereby inducing changes in the transmission features (Frazão et al. 2008; De et al. 2019).

Light confinement and the transmission features of PCFs are notably influenced by the RI of the material within the holes (Mortensen et al. 2003). Typically, liquid samples of single fluids or concentrations of solutes in mixes can be analyzed, quantified, or both, with these arrangements (De et al. 2020; Silva et al. 2014). The response of these compact refractometers is obtained by tracking amplitude changes of the optical wave or by monitoring the spectral shift at a characteristic wavelength. Generally, changes are measured in nm or dBs per RI unit (RIU), while the resolution is expressed in terms of the fraction of RI that can be detected.

Refractometers based on PCFs can be implemented upon inserting a section of this fiber in the middle of two SMFs or just at the end of an SMF, as previously depicted in Fig. 2. Devices incorporating pieces of PCFs in mid-sections use different schemes to measure the RI of the sample. Inlet and outlet channels at both ends of the PCF are commonly required to insert the liquid into the fibers, resembling a microfluidic system (Silva et al. 2014). An extensive number of possible configurations for inserting the fluid have been reported, although the essential principle is based on incorporating hollow elements with openings on the surface. These structures link the PCF with SMFs being located at the beginning and the end of the PCF, further granting selective filling of the inner holes (see Fig. 9.3) (Urrutia et al. 2019).

Devices using a section of PCF only at one end leave the microstructure of the fiber readily available for interaction with the liquid (Silva et al. 2014). For PCFs with small diameter holes, an additional hollow core fiber or glass capillary can be included between each SMF-PCF splice. In these arrangements, the capillaries can act as additional resonating cavities, as illustrated in Fig. 9.3b (Urrutia et al. 2019; Portosi et al. 2019). When the inner structure of the fiber is composed of larger diameter holes, interaction with liquids can occur directly (Urrutia et al. 2019); this is the case with microstructured optical fibers (MOFs). The most common configurations using PCFs for RI measurements are illustrated in Fig. 9.3c.

Selective filling of the holes of PCFs modifies the photonic bandgap and thus reshapes the transmission conditions. Analysis of the transmission spectrum hence provides a means to detect changes in the RI. Alternatively, tailored fibers in which the evanescent wave or the cladding modes extend outside the fiber can interact with external media (e.g., liquids or gasses). This interaction can be realized, for instance, through the cladding modes, which can be coupled to the outer structure of the fiber by splicing techniques (Jha et al. 2009).

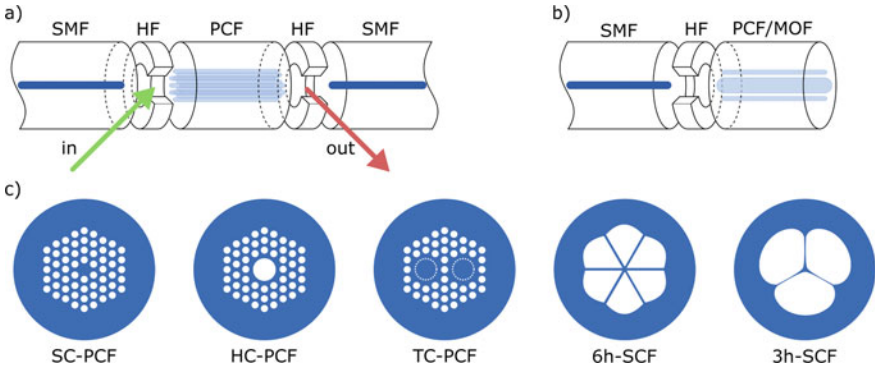

Fig. 9.3 Methods for measuring refractive index with PCFs. **a** General configuration for injecting liquids in PCFs spliced between two SMFs. **b** Use of PCFs spliced at only one end and leaving the inner microstructure in direct contact with the liquid. **c** Common PCFs used for refractive index measurement. SC-PCF: solid-core PCF; HC-PCF: hollow-core PCF; TC-PCF: two cores PCF; 6 h-SCF: six holes suspended-core fiber; 3 h-SCF: three holes suspended-core fiber

PCFs with two coupled cores have also been used for RI measurements. In this case, the coupling ratio between the cores changes upon sample insertion, and its RI can thus be obtained by monitoring the output intensity of the cores and through coupled-mode theory (Liu et al. 2017; Town et al. 2010; Wu et al. 2009). With this approach, both cores can be solid, and selected holes inside the fiber can be filled with the sample to be analyzed (Town et al. 2010). Alternatively, one of the cores can be hollow and is used to contain the sample (Wu et al. 2009). This configuration has achieved high sensitivities ranging from 38,000 nm/RIU (Town et al. 2010) to at least five times this number.

Although the effects generated by introducing the sample in PCFs are improved compared to those obtained with SMFs, additional enhancements are possible. An augmented response can be obtained by adding other devices to the PCF (see Fig. 9.3b). Resonant effects can be introduced using a Fabry–Pérot (FP) cavity located at the interfaces between the PCF and SMF (Frazão et al. 2008). Sensitivities in the range of 1,000–15,000 nm/RIU have been achieved using FP interferometers (Wu et al. 2013). Diffractive effects can also be produced either by incorporating long-period gratings (De et al. 2019), or by splicing single-mode to multimode (and vice versa) fibers (Frazão et al. 2008). Exciting cladding modes that interfere with the fundamental mode leads to modulation of the transmitted signal, which is also sensitive to RI changes. These approaches are depicted in Fig. 9.4; the sensitivities that can be achieved are typically in the range of hundreds to a couple of thousands of nm/RIU (Algorri et al. 2018; Urrutia et al. 2019). Plasmonic effects can also be obtained by coating or filling some inner holes with different metals, achieving sensitivities up to 63,000 nm/RIU (Danlard and Akowuah 2020). One last sensing mechanism is the four-wave mixing effect in PCFs, arising from normal and anomalous dispersion in these fibers (Nagarajan et al. 2018). This nonlinear effect is generated with nano-

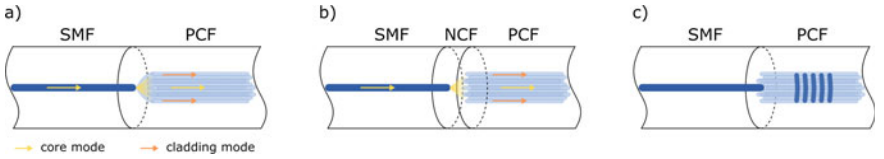

Fig. 9.4 Diffractive effects used in PCF devices. **a** Collapsed photonic structure upon splicing to SMF. **b** Use of intermediate no-core fiber (NCF) between SMF and PCF. **c** Inducing a long-period grating on PCF

and pico-second pulses, and the change in RI may be monitored upon tracking the Stokes and anti-Stokes shifts.

Gas Sensors

PCFs are attractive for gas sensing because they can serve as cells allocating the gas within the holes. Detection is generally based on optical absorption spectroscopy, and gas concentration can be thus obtained employing Beer–Lambert law (Monro et al. 1999; Hoo et al. 2003). Because of their size, the gas volumes housed by PCFs are small, and the interaction lengths can be of a few meters, thus providing adequate sensitivities for spectroscopic measurements. For example, a 1 m long hollow-core PCF with a core diameter of 10 μm can be filled with less than 100 nL of gas. The light sources used in these setups typically include either a tunable laser or a broadband emitter (e.g., superluminescent LEDs, ASE fiber laser sources) with spectral features coinciding with the absorption lines of the gas. A tunable filter may also be used together with a broadband emitter. Depending on the light source, the spectral absorption can be measured either with a photodetector or with a spectrometer. Light can be coupled into the PCF either with lenses, through butt coupling when the output of the source is fiber-coupled, or through a standard fiber spliced to one end of the PCF. Generic transmission and reflection setups used for gas sensing using these fibers are shown in Fig. 9.2a, c, respectively.

Evidently, the PCFs used for gas detection using absorption spectroscopy must be able to guide light in the spectral regions coinciding with the absorption bands of the gaseous species. Silica-based PCFs, for instance, can be constructed to operate in the near- or mid-infrared, a spectral region in which several gasses have absorption overtone bands (i.e., multiples of the fundamental absorption frequency) (Gayraud et al. 2008). Although in some cases, these bands may show low absorption levels, the large interaction lengths offered by PCFs allow for their detection with standard optical detectors and spectrometers. Gasses and volatile compounds can also be detected upon incorporating permeable membranes as coatings of tapered PCFs (Lopez-Torres et al. 2020). In this case, the fiber is modified (e.g., through heating and pulling) to increase the light's interaction with the cladding or to generate modal interference. Because in tapered fibers, light guiding is affected by the external medium,

interaction between the coating and the gas leads to a change in the transmission features of the PCF.

In general, sensors' response time using PCFs is defined in terms of the time required to fill the fiber with the gas. These filling times depend on the pressure, temperature, gas diffusion coefficient, and the capillary effect inherent to the size of the cladding holes. While a PCF of a few cm can be filled within a few minutes, a 1 m long fiber can take up to an hour to fill (Hoo et al. 2003; Gayraud et al. 2008). The response time can be reduced upon splicing the PCFs with tailored hollow glass structures with side gaps (C-shaped, see Fig. 9.3a, b) or through adjustments in the gas pressure at both ends of the fiber (Lopez-Torres et al. 2020). Control of the gas filling pressures also provides a means to inject more than one gas in the PCF, thereby allowing for multi-gas sensing through spectral analysis (Wynne et al. 2009). Side filling of the holes provides another means to reduce the filling times and thus reduce the response time. The hollow structure can be accessed through laser drilling using femtosecond pulsed lasers (Yu et al. 2020). In contrast, in arrangements using gas-sensitive coatings, the response time is limited by the diffusion time of the gas in the coating material.

For index-guided PCFs, the cladding holes surrounding the solid core are used to allocate the gas. An important parameter for this approach is the overlap between the field and the cladding, which can be estimated by the fraction of the power allocated in the holes (Monro et al. 1999). This parameter depends on the wavelength and geometry (hole size and pitch) of the PCF, and upon tailoring the structure, it can be optimized to increase the interaction between the optical wave and the gas. In general, for $\lambda > 2.2\Lambda$, this interaction becomes significant, and the PCF can serve as an evanescent wave gas sensor (Monro et al. 1999). For this condition to be fulfilled, the pitch must be small, which was difficult to achieve during the early days of PCFs. In contrast, fibers with a hollow core confining the light through a photonic bandgap offer direct interaction of the optical wave with the gas. Because more than 98% of the guided mode can be confined in the core, the light–gas interaction is significantly improved compared to index-guided PCFs (Hoo et al. 2003; Ritari et al. 2004). As a result, shorter lengths of fiber can be used, and weakly absorbing gasses can be readily detected (Ritari et al. 2004).

Aside from gas sensing applications, PCFs filled with gasses may serve as compact gas cells (Benabid et al. 2005). These gas cells are of interest for photonic applications in which a stable wavelength reference is required (e.g., an absorption line can be used as a reference to stabilize the emission wavelength of a laser) (Benabid et al. 2005). The nonlinear coefficient of some gasses is also larger than those observed in silica glasses, and thus, PCF gas cells may serve as a means to obtain highly nonlinear responses in all-fiber setups (Travers et al. 2011). As with other absorption cells for gas detection, setups using PCFs have also been combined with algorithms to identify absorption bands of different gasses with high precision (Cubillas et al. 2002). Simultaneous detection of multiple gaseous species and vapors contained in a single PCF has also been demonstrated using Raman spectroscopy (Yang et al. 2013). Furthermore, the long interaction lengths offered by hollow-core PCFs have enabled enhanced detection of intrinsically weak Raman signals. Spectroscopic detection

Table 9.1 Gasses detected using PCFs

Gas	References
Acetylene (C_2H_2)	Wynne et al. (2009), Ritari et al. (2004), Kassani et al. (2013)
Carbon dioxide (CO_2)	Wynne et al. (2009), Yang et al. (2013), Hanf et al. (2014)
Hydrogen cyanide ($H^{13}CN$)	Ritari et al. (2004)
Methane (CH_4)	Gayraud et al. (2008), Ritari et al. (2004), Cubillas et al. (2002), Hanf et al. (2014)
Nitrogen (N_2)	Yang et al. (2013), Hanf et al. (2014)
Oxygen (O_2)	Yang et al. (2013), Hanf et al. (2014)
Vapors (Toluene, Acetone)	Yang et al. (2013)

of multiple environmental gasses and even breath analysis have been reported with PCFs (Hanf et al. 2014). Other spectroscopic techniques, such as Fourier transform spectroscopy, have also been implemented using a PCF gas cell (Yu et al. 2020). Some examples of gasses detected using PCFs are included in Table 9.1.

Because of their compatibility with standard optical fibers and glass capillaries, PCFs can also be incorporated into fiber optic sensor arrangements. As an example, a hollow-core PCF can be incorporated in an FP fiber optic interferometer and thus serve as an intra-cavity gas cell. Double FP configurations have been shown to provide enough sensitivity to detect changes in air RI using the Vernier effect (Quan et al. 2015).

Fluorescence-Based Sensors

Fluorescent optical sensors are essential tools for detecting chemical, biochemical, environmental monitoring, and even chemical warfare, among other applications. Fluorescent detection is very useful for practical applications with respect to other optical sensing techniques due to its high sensitivity, strong selectivity, and accuracy (Schäferling 2012). In general, a fluorescent sensor either reads the fluorescence emitted by the molecule being measured or if the molecule does not fluoresce, an external fluorophore must be incorporated as a label and thus fluoresce when irradiated with light. The latter process can be better explained by describing the binding processes that occur in immunosensors. As shown in Fig. 9.5a, a surface is first functionalized with specific antibodies. This surface is then immersed in a solution containing antigens, which the antibodies will capture. Finally, detection antibodies, i.e., antibodies with fluorophores attached to them, are attached to the captured antigens. Shining light with a specific wavelength to the detection antibodies induces fluorescence that allows for the detection of the specific antigen. The functionalization surface antibodies can be eliminated since binding of the antigens to antibodies also occurs in their absence, and thus the antigen–antibody binding is free to move in a liquid solution.

Optical fibers have been widely used as fluorescence sensors because they exhibit some advantages compared to other optical techniques, such as small size, low cost, low transmission losses, and biocompatibility. The simplest use of an optical fiber as a fluorescence sensor is as a collector for the fluorescence signal. This is easily achieved by inserting the fiber tip into the fluorescent solution, and after the solution is irradiated with light, the fluorescence is then collected through the fiber tip. Since the amount of collected fluorescence is generally low due to the small fiber core diameter, a bundle of several fibers is used to increase the fluorescence signal-to-noise ratio rather than a single optical fiber. For instance, using a ring of six optical fibers, picric acid concentrations as low as 100 nM (25 ppb) were detected with excellent reproducibility (Dasary et al. 2018). Collecting light using the fiber tip is rather simple and has some advantages, such as the flexibility of the fiber probe and the need for small sample volumes given the diameter of 125 μm of standard optical fiber. Nevertheless, the amount of collected fluorescence is generally low, and a different approach is required to increase the amount of collected fluorescence.

Another way to increase the collected signal is to increase the effective acquisition area through which we acquire the fluorescence signal. This can be achieved by tapering an optical fiber and reducing its diameter even to nanometer scales, as shown in Fig. 9.5b (Yalla et al. 2012). Since fiber tapering systems can fabricate centimeter-long tapers, fluorescence detection is enhanced due to the large effective coupling area available from the tapered region. Under this configuration, either the tapered fiber can be immersed in the fluorescence solution, or its surface can be treated to attach the fluorescent material to the surface. The excitation source can be transmitted along the optical fiber to interact on the tapered section with the fluorophores, or excitation can also be achieved with external illumination over the tapered section. The advantage of the tapered configuration is that the fluorescence can be channeled into the guided mode, and the collected signal can thus be increased upon increasing the tapered length. The collection efficiency is improved to the point that the fluorescence from single quantum dots placed on the tapered surface can be measured (Yalla et al. 2012). A variation to this technique is to form a conical shape on the fiber tip, as shown in Fig. 9.5c (Ray et al. 2016). This conical shape can be fabricated precisely, either by using chemical etching methods or by cleaving the tapered section at the center. Since the tapered tip is manipulated from the non-modified optical fiber, it is more robust and less fragile than manipulating the entire tapered section.

The development of more complex optical fibers also provided a way to enhance the response of optical fiber fluorescence sensors. For instance, the development of MOFs with micrometer size holes running along the fiber to generate suspended cores became an ideal platform for improving fluorescence fiber sensors, see Fig. 9.3c (6 h-SCF and 3 h-SCF). MOFs have enhanced the performance of fluorescence fiber sensors because the holes can be infiltrated with a fluorescent solution. Thus, the holes provide small cells for sample allocation, also working as the delivery channels and light collectors with a long interaction path length. Additionally, the small core diameter allows for a large evanescent field overlapping between the propagating

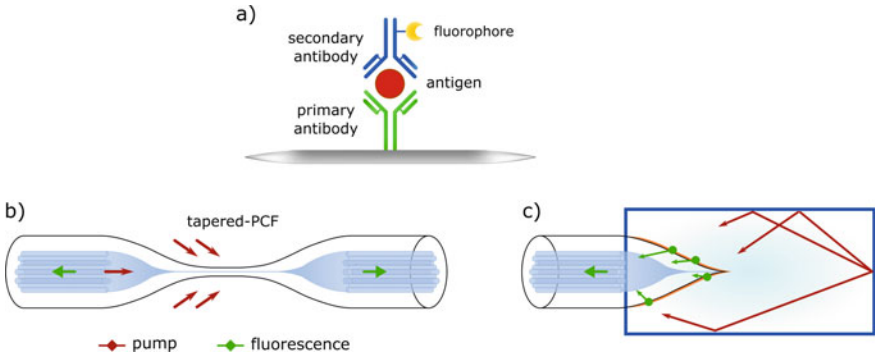

Fig. 9.5 **a** Schematic of surface functionalization steps for fluorescence immunosensors, **b** tapered optical fiber with fluorescent material surrounding the tapered region, and **c** tapered optical fiber tip with fluorescent material attached to the surface tip. The excitation source in both cases can be either external or propagating along the fiber core

mode from the excitation source and the fluorescent material, which also enhances fluorescence's coupling to the MOF core (Shahraam Afshar et al. 2007).

A major improvement can be obtained in the case of hollow-core PCFs such as that shown in Fig. 9.6a. Since hollow-core PCFs guide light in the central region due to resonant effects, this provides many air holes that can be filled with fluorescent material. In fact, the simplest realization of a hollow-core PCF fluorescent sensor is to infiltrate all the air holes with a fluorescent solution and pump externally with an excitation source perpendicularly to the hollow-core fiber. A different approach is to use the cladding structure as a waveguide for the excitation source (Jensen et al. 2004). As shown in Fig. 9.6b (red circles), the center of three adjacent holes forming a triangle comprises an air-suspended core similar to that of a MOF (see Fig. 9.3c). Since the width of these structures is only a couple of micrometers, we obtain a large penetration of the evanescent field into the fluorescent sample (orange circles in Fig. 9.6b) for visible excitation wavelengths. The main advantage of using a hollow-core PCF as a sample cell is that the interaction length is enhanced in the order of a centimeter with a sample volume of much less than 1 mL. This application is particularly important for tests requiring expensive reagents.

The required sample volume can be further reduced by infiltrating only the center hole of the hollow-core PCF while the holes in the cladding structure are left empty, as shown in Fig. 9.6a. This selective infiltration is achieved by collapsing the holes in the cladding crystal at one end of the hollow-core PCF while leaving the central hollow-core open. This process can be easily implemented using a commercial fusion splicer. Selectively filling the center hole of the hollow-core PCF with fluorescent material provides an overlap of nearly 100% between the guided excitation light and the sample material, which is significantly better compared to MOF. The sample measured volumes can be as low as 0.36 nL using this approach, which allows for the detection of molecules at concentrations ranging from only 0.1 nM and 0.02 pmol (Chen et al. 2019; Smolka et al. 2007a). Other approaches have selectively coated

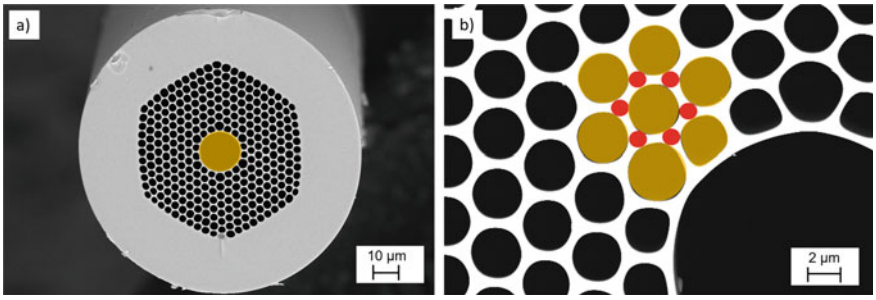

Fig. 9.6 **a** Scanning electron micrograph (SEM) of a hollow-core PCF and **b** zoom of the cladding crystal structure surrounding the hollow-core of the hollow-core PCF

the center hole inner wall of the hollow-core PCF with fluorophores, demonstrating the detection of molecules at concentrations in the order of μM and nM (Smolka et al. 2007b; Chi et al. 2022).

We can conclude by highlighting that hollow-core PCFs require very small amounts of liquid, in the order of a couple of nL. Regardless of the small amount of fluorescent material, a large enough fluorescence signal can be obtained from the end-facet of the hollow-core PCF. This efficiency is related to the strong confinement of the excitation light propagating along the hollow-core section, which enables almost 100% overlap between excitation light and fluorescent material. It is also worthwhile mentioning that since no etching or other structural modifications are required on the hollow-core PCFs, highly robust fluorescence sensors can be readily obtained. Finally, since the inner wall of the hollow core can be functionalized, hollow-core PCFs provide an ideal platform to study different chemical reactions or biological processes.

Glucose Detection

In the last decade, the risk of developing diabetes has significantly increased and is quickly evolving as one of the major concerns for human health. From the medical perspective, glucose levels between 100 and 126 mg/dL are classified as pre-diabetes, and beyond 126 mg/dL means the patient has diabetes. Therefore, the need for simple, sensitive, and cost-effective glucose sensors is of great interest in controlling diabetes. Although most methods for measuring glucose concentration are based on electrochemical systems, PCFs are of great interest due to the advantages inherent to optical fibers and the design flexibility that these fibers bring for sensor realization. Since the amount of glucose either in blood or serum will effectively increase their RI, in principle, any of the previously explained RI sensors could work to detect glucose. Nevertheless, because of the low concentration levels that have to be detected, SPR methods and solid-core PCFs with modified structures are preferred. Commercially

available solid-core PCFs have been modified into solid-core PCFs with a D-shape to enable SPR operation (Azab et al. 2022; Mumtaz et al. 2022). As shown in Fig. 9.7a, the D-shape allows the core to be exposed to the external medium, thereby creating a flat platform for the deposition of a metallic layer for SPR operation. In fact, regardless of the structure used for glucose detection, different materials have been investigated to enhance SPR operation for higher sensitivity. Experimental D-shaped glucose sensors with silver as the plasmonic layer have been demonstrated to achieve a sensitivity of 294.11 nm/RIU, with a resolution of $3.4 \times 10 - 4$ RIU (Azab et al. 2022). Simulations suggest that by using a different metallic layer as the plasmonic material (e.g., Au/Ti3C2Tx), a sensitivity enhancement of 1.7 times should be achieved. In this device, maximum sensitivities of 28,048 nm/RIU and 47,260 nm/RIU for a RI value of 1.42 were obtained while having the potential to measure over a wide range of bio-analytes (i.e., 1.30–1.43). The solid-core PCF hole lattice can also be modified to achieve a higher sensitivity. For instance, a square lattice was designed with indium tin oxide (ITO) as the plasmonic layer, detecting analytes with RI varying from 1.380 to 1.405. An average spectral sensitivity of 18,400 nm/RIU can be achieved with a resolution in the order of 10^{-6} (Liu et al. 2022).

Since side polishing a solid-core PCF can be complicated and time-consuming, solid-core PCFs with novel designs have also been proposed. As shown in Fig. 9.7b, the lattice is designed such that the core is at the periphery of the solid-core PCF. This allows for the coating of the metallic plasmonic layer without any modification of the solid-core PCF. This approach allows obtaining sensitivities from 6500 nm/RIU to 9000 nm/RIU for ranges of the analyte RI of 1.33–1.34 and 1.34–1.35, respectively. With a resolution in the order of 10^{-5}, these results correspond to a sensitivity of 0.81429 nm/g/L, within a glucose range from 10 g/L to 70 g/L (Das and Singh 2022). The lattice can also be modified to enhance the birefringence in the core, as shown in Fig. 9.7c. This large birefringence improves the multimode interference between the modes for each polarization and produces interference fringes in the output spectrum. Since these interference fringes depend on the effective RI of the polarization modes,

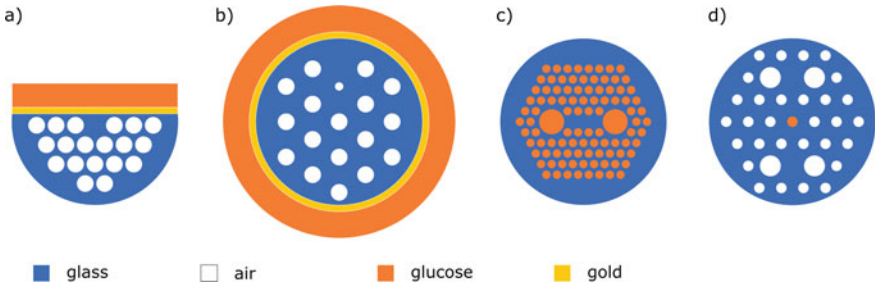

Fig. 9.7 Schematics of different solid-core PCF designs for glucose sensing. **a** D-shape solid-core PCF, **b** Solid-core PCF with an offset core close to the periphery of the fiber. **c** Solid-core PCF with a rectangular core and different hole diameters to obtain a large birefringence, and **d** Three core solid-core PCFs with a small hole in the central core. The three cores are aligned in the vertical direction

any changes in the air holes will modify the interference spectrum. Therefore, by filling the holes of the solid-core PCF with glucose solution, its concentration can be inferred from the spectral changes of the observed dips. In this approach, an average absolute sensitivity of 30,890 nm/RIU can be obtained, with a detection resolution of 0.54 mg/dL, which is lower than the 70 mg/dL required for the detection of hypoglycemia (Yousufali et al. 2021).

Other designs take advantage of the high sensitivity to effective index changes of coupled waveguides. As shown in Fig. 9.7d, the air holes can be modified to have three cores aligned vertically along the optical axis. In fact, in this design, the central core has a small hole that is filled with the glucose solution. Since the spectral response of the coupled waveguides is highly dependent on any effective index change, this kind of sensor can be very sensitive to small RI changes (Natesan et al. 2019). In yet another design, two coupled cores are formed by the air holes and separated by one air hole, which is also filled with the glucose solution (An et al. 2016). These configurations provide a maximum average sensitivity of 23,267.33 nm/RIU. A particular advantage of coupled waveguide systems is that their spectral response is sinusoidal. This sinusoidal response provides a simple way to operate them within the optical Vernier regime, which can easily enhance the device sensitivity by more than 30 times (Cuando-Espitia et al. 2021) and has yet to be explored for glucose measurements.

As a final remark, we should note that in most of the works described here, analysis is carried out using different glucose concentrations in buffered solutions. To the best of our knowledge, a more specific approach based on targeted functionalization has been studied only by one research group (An et al. 2016). In these works, the solid-core PCF surface was functionalized with glucose oxidase that reacts with glucose to produce secondary species of gluconic acid and H_2O_2. These by-products will significantly modify the RI around the solid-core PCF operating in a Mach–Zehnder configuration, and thus glucose concentration can be monitored (Li et al. 2021). Although this is the most reliable way to measure glucose, this approach needs to consider the RI of the surrounding solutions as well as the interaction of secondary species with sample components in more realistic clinical samples. Thus, PCF glucose sensors with extremely high specificity and sensitivity are yet to be designed and implemented to impact relevant biomedical sensing.

Conclusions

PCFs offer an excellent platform for developing versatile and highly sensitive fiber sensors for different applications. The periodic structure of air holes running along the fiber provides a simple way to design a specific PCF or modify a commercial PCF to measure different physical and biological parameters. The air hole distribution and diameter can be modified to design a PCF with certain waveguiding characteristics that enhance the interaction with the measurand or facilitate liquid flow along the fiber. In fact, one of the significant advantages of PCF for biological sensors is the

large interaction lengths that can be easily achieved by infiltrating the holes with target biomolecules or attaching the biomolecules to the hole's inner walls. Since air holes have small dimensions, this also translates into low sample consumption, which is ideal for highly expensive reagent procedures and examination of limited biological fluids. All these advantages make PCF sensors a promising technology for the detection and monitoring of different diseases with high specificity and sensitivity.

References

Algorri JF, Zografopoulos DC, Tapetado A, Poudereux D, Sánchez-Pena JM (2018) Sensors (Switzerland) 18
An G, Li S, Yan X, Zhang X, Yuan Z, Zhang Y (2016) J Opt Soc Am B 33:1330
Atkin DM, Shepherd TJ, Birks TA, Russell PSJ, Roberts PJ (1995) Electron Lett 31:1941
Azab MY, Hameed MFO, Mahdiraji GA, Adikan FRM, Obayya SSA (2022) Opt Quantum Electron 54:846
Benabid F, Couny F, Knight JC, Birks TA, Russell PSJ (2005) Nature 434:488
Chen HF, Jiang QJ, Qiu YQ, Chen XC, Fan B, Wang Y, Wang DN (2019) Anal Chem 91:780
Chi Z, Li M, Xu J, Yang L (2022) Anal Bioanal Chem 414:1641
Cregan RF, Mangan BJ, Knight JC, Birks TA, Russell PJS, Roberts PJ, Allan DC (n.d.) Single-mode photonic band gap guidance of light in air
Cuando-Espitia N, Fuentes-Fuentes MA, Velázquez-Benítez A, Amezcua R, Hernández-Cordero J, May-Arrioja DA (2021) Sci Rep 11:18383
Cubillas AM, Silva-Lopez M, Lazaro JM, Conde OM, Petrovich MN, Lopez-Higuera JM, Birks T, Roberts P, Russel PS, Atkin D, Sheperd T (2002) Methane detection at 1670-nm band using a hollow-core photonic bandgap fiber and a multiline algorithm. Wiley, New York
Danlard I, Akowuah EK (2020) Opt Fiber Technol 54
Das S, Singh VK (2022) IEEE Photonics Technol Lett 34:691
Dasary SSR, Singh AK, Lee KS, Yu H, Ray PC (2018) Sens Actuators B Chem 255:1646
De M, Gangopadhyay TK, Singh VK (2019) Sensors (Switzerland) 19
De M, Gangopadhyay TK, Singh VK (2020) Meas Sci Technol 31
Frazão O, Santos JL, Araújo FM, Ferreira LA (2008) Laser Photon Rev 2:449
Fu Q, Wu Y, Davidson IA, Xu L, Jasion GT, Liang S, Rikimi S, Poletti F, Wheeler NV, Richardson DJ (2022) Opt Lett 47:5301
Gayraud N, Kornaszewski ŁW, Stone JM, Knight JC, Reid DT, Hand DP, Macpherson WN (2008) Mid-infrared gas sensing using a photonic bandgap fiber
Hanf S, Keiner R, Yan D, Popp J, Frosch T (2014) Anal Chem 86:5278
Hoo YL, Jin W, Shi C, Ho HL, Wang DN, Ruan SC (2003) Appl Opt 42:3509
Jensen JB, Pedersen LH, Hoiby PE, Nielsen LB, Hansen TP, Folkenberg JR, Riishede J, Noordegraaf D, Nielsen K, Carlsen A, Bjarklev A (2004) Opt Lett 29:1974
Jha R, Villatoro J, Badenes G, Pruneri V (2009) Refractometry based on a photonic crystal fiber interferometer
John S (1987) Physical review letters strong localization of photons in certain disordered dielectric superlattices
Kassani SH, Park J, Jung Y, Kobelke J, Oh K (2013) Opt Express 21:14074
Knight JC, Birks TA, Atkin DM, Russell PSJ (1996) In: Optical fiber communication conference. Optica Publishing Group, PD3
Kurokawa K, Tajima K, Tsujikawa K, Nakajima K (n.d.) Reducing the losses in photonic crystal fibres
Li J, Zhang W, Tong Z, Liu J (2021) Opt Commun 492:126983

Liu Z, Tam HY, Htein L, Tse MLV, Lu C (2017) J Lightwave Technol 35:3425
Liu W, Hu C, Zhou L, Yi Z, Liu C, Lv J, Yang L, Chu PK (2022) Physica E Low Dimens Syst Nanostruct 138:115106
Lopez-Torres D, Elosua C, Arregui FJ (2020) Sensors (Switzerland) 20
Monro TM, Richardson DJ, Bennett PJ (1999) Electron Lett 35:1188
Mortensen NA, Folkenberg JR, Nielsen MD, Hansen KP (2003) Modal cutoff and the v parameter in photonic crystal fibers
Mumtaz F, Roman M, Zhang B, Abbas LG, Dai Y, Ashraf MA, Fiaz MA, Kumar A (2022) Photonics Nanostruct 52:101090
Nagarajan N, Yamunadevi R, Vasantha Jayakantha Raja R, Joshva Raj G (2018) IEEE Sens J 18:6607
Natesan A, Govindasamy KP, Gopal TR, Dhasarathan V, Aly AH (2019) IET Optoelectron 13:118
Portosi V, Laneve D, Falconi MC, Prudenzano F (2019) Sensors (Switzerland) 19
Quan M, Tian J, Yao Y (2015) Opt Lett 40:4891
Ray JC, Almas MS, Tao S (2016) Opt Lett 41:100
Ritari T, Tuominen J, Ludvigsen H, Petersen JC, Hansen TP, Simonsen HR (2004) Optical Society of America OCIS Codes: (060.2370) Fiber Optics Sensors, (230.3670) Light-Emitting Diodes
Saha R, Hossain MM, Rahaman ME, Mondal HS (2019) Frontiers Optoelectron 12:165
Schäferling M (2012) Angew Chem Int Ed 51:3532
Shahraam Afshar V, Warren-Smith SC, Monro TM (2007) Opt Express 15:17891
Silva S, Roriz P, Frazão O (2014) Photonics 1:516
Smolka S, Barth M, Benson O (2007a) Opt Express 15:12783
Smolka S, Barth M, Benson O (2007b) Appl Phys Lett 90:111101
Town GE, Yuan W, Mccosker R, Bang O (2010) Microstructured optical fiber refractive index sensor
Travers JC, Chang W, Nold J, Joly NY, Russell PSJ (2011) J Opt Soc Am B 28:A11
Urrutia A, del Villar I, Zubiate P, Zamarreño CR (2019) Laser Photon Rev 13
Vincetti L (2003) In: The proceedings of the ECOC-IOOC2003 Conference. Rimini, Italy
Wu DKC, Kuhlmey BT, Eggleton BJ (2009) Ultrasensitive photonic crystal fiber refractive index sensor
Wu DKC, Lee KJ, Pureur V, Kuhlmey BT (2013) J Lightwave Technol 31:3500
Wynne RM, Barabadi B, Creedon KJ, Ortega A (2009) J Lightwave Technol 27:1590
Yablonovitch E, Gmitter TJ (n.d.) Photonic band structure: the face-centered-cubic case
Yalla R, Nayak KP, Hakuta K (2012) Opt Express 20:2932
Yang X, Chang ASP, Chen B, Gu C, Bond TC (2013) Sens Actuators B Chem 176:64
Yousufali M, Mollah MA, Ahmed K (2021) Plasmonics 16:811
Yu R, Chen Y, Shui L, Xiao L (2020) Sensors (Switzerland) 20

Chapter 10
Photonic Crystal Biosensors for Healthcare and Pathologic Diagnostic Application

Amir Reza Sadrolhosseini, Seyedeh Mehri Hamidi, and Farnaz Amouyan

Abstract Recently, the application of photonic crystals was considered for recognizing chemical and biochemical molecules. A photonic crystal is a periodic dielectric structure, and it is categorized into one dimension, two dimensions, and three dimensions. The photonic band gap is a significant parameter in a photonic crystal. The photonic band gap manages the forbidden frequency and range of wavelength in the photonic crystal. Therefore, the response of photonic crystal can be adjusted using a photonic band gap and can be designed to detect biomolecules and chemical molecules. In this chapter, the various type of photonic crystals structure and the mechanism of a photonic crystal for biosensors have been considered for the detection and monitoring of biomolecules and biotargets, including nucleic acid (DNA or RNA) proteins, and cancer cells.

Keywords Photonic crystal · Biosensors · Resonators · Biomolecules · Photonic band gap · Pathologic

Introduction

Sensors and biosensors are emerging analytical tools for recognizing and detecting chemical and biochemical molecules. They can monitor the interactions of chemicals and biomolecules with the nanomaterial and they can depict the interaction of antibodies and antigens. The colorimetric, electrical, electrochemical, and optical, transducing systems are the based phenomena for converting the interaction effect to observable parameters (Monošík et al. 2012). So, these methods can convert the variation of a biological and chemical reaction into a measurable electrical or optical quantity (Chambers et al. 2008). Biosensors and sensors are used to detect the various chemical.

A. R. Sadrolhosseini · S. M. Hamidi (✉) · F. Amouyan
Magneto-Plasmonic Lab, Laser and Plasma Research Institute, Shahid Beheshti University, Tehran, Iran
e-mail: m_hamidi@sbu.ac.ir

© The Author(s), under exclusive license to Springer Nature Singapore Pte Ltd. 2023

S. S. Dhanabalan et al. (eds.), *Photonic Crystal and Its Applications for Next Generation Systems*, Springer Tracts in Electrical and Electronics Engineering,
https://doi.org/10.1007/978-981-99-2548-3_10

materials, toxic chemicals, and biological molecules including heavy metals, pesticide biological cells (Wang et al. 2012) proteins (Washburn et al. 2010), enzymes (Myung et al. 2012), viruses (Xu et al. 2007), hormones (Kirsch et al. 2013), and bacteria (Lissandrello et al. 2014).

The sample preparation and sample collection require measuring and detecting the mentioned molecules and the expert person should measure the parameters. Hence, human accuracy, and reliable readings are the significant factor to trust the results (Plebani 2010). Therefore, automated tools and instruments are necessary for detecting chemical and biochemical molecules (Cheung et al. 2015).

Recently, the in vitro test and diagnostic experiment devices have been improved to develop for recognition of the biomolecule including human immunodeficiency virus (HIV) and bacteria (Monošík et al. 2012). Therefore, affordable, sensitive, rapid, portable, label-free, and user-friendly are the main parameters to improve the new technology, and biosensors based on optical phenomena are a suitable candidate (Lifson et al. 2016).

To solve the mentioned problems, the application of microfluidics and nanotechnology is the best choice for biosensor platforms and they are a great promise to address the aforementioned challenges. The photonic crystal biosensor, localized surface plasmon resonance, informatic biosensor, and electrical biosensor can be employed as accurate tools and affordable diagnostic devices (Viswanathan et al. 2015). The photonic crystals have more applications in biotechnology and industry including biochemical sensors (Gowdhami et al. 2022), routers, (Shanmuga et al. 2018; Sathyadevaki et al. n.d.), wavelength filters (dynamic hitless routers for integrated photonic NoCs 2018), logic gates (Sathyadevaki et al. 2016), wide bandpass filters, and narrowband stop filters (Geerthana et al. 2022). The many structures of photonic crystals have been utilized to recognize a wide array of biomolecules in biotechnology and biological matrices, including urine, tears, blood, and sweat (Shanmuga et al. 2018). They are prepared using various inexpensive methods including hydrogels, mold-based replica imprinting, and colloidal self-assembly (Yetisen et al. 2014).

A photonic crystal arises from a periodic arrangement of a particular dielectric medium and a photonic band gap is created when a range of light beams cannot propagate due to the destructive interference of incident light with reflections at dielectric boundaries (Inan et al. 2017). There are a variety of structures and geometries for photonic crystals such as slabs, colloids, Bragg reflectors, opals, and microcavities. The simple Bragg structure is an optical phenomenon that can describe these structures. Figure 10.1a, b show the generic Bragg reflector structure and the band gap patterns. It contains alternating low and high refractive index thin dielectric layers. The thickness of layers is about ¼ wavelength of light Eq. (1). Light cannot propagate at normal incidence and it resides in a photonic band gap region (Fig. 10.1b) (Joannopoulos et al. 2008).

$$d_{max}n_{max} = d_{min}n_{min} = \frac{\lambda}{4}$$

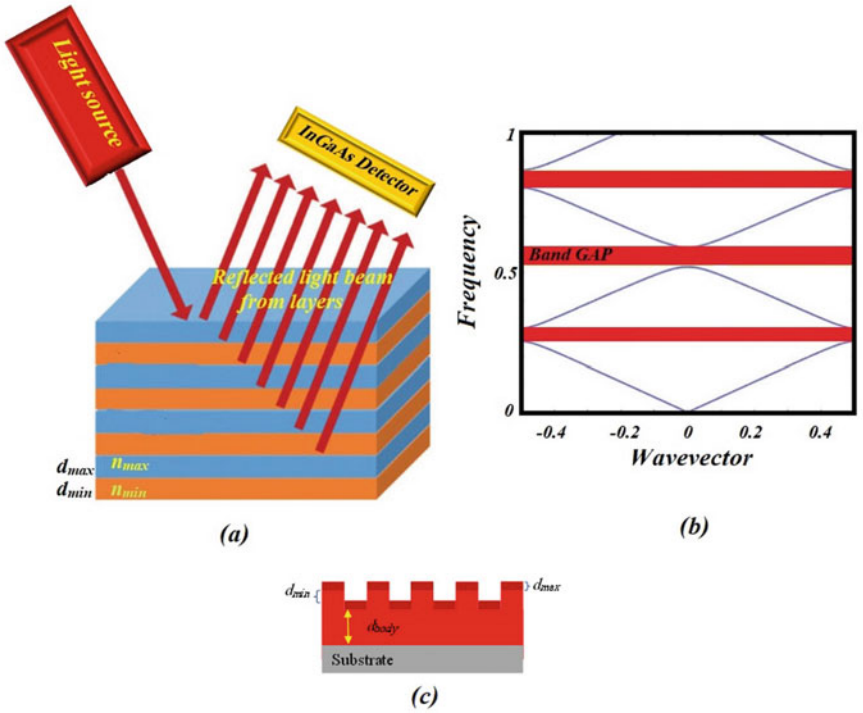

Fig. 10.1 **a** The generic Bragg reflector structure, **b** the band gap of structure, and **c** photonic crystal-based grating

where λ, d_{max}, n_{max}, d_{min}, and n_{min} are the wavelength, maximum thickness, maximum refractive index, minimum thickness, and maximum refractive index, respectively.

Figure 10.1c illuminates the photonic crystal structure based on low refractive index grating. The period of the grating (Λ) is smaller than the wavelength (visible and near-infrared ranges) of the incident light ($\Lambda < \lambda$). In order to fabricate the photonic crystal, high refractive index layers should be coated over a periodically arranged low refractive index grating layer. In this structure, higher order modes are confined at normal incidence and only the zeroth-order mode is permitted to propagate in the structure. These photonic crystal structures are known as subwavelength gratings and depict efficient optical resonances (Lee and Ryu 2002) and these can be used to reflect a narrowband of wavelengths and generate a sharp peak in the reflection spectrum (Magnusson and Ding 2003). In this case, the diffracted mode can couple to a weakly waveguide mode and the resonance occurs. The resonance ($\lambda_{Resonance}$) peak can be calculated from the period (Λ) of photonic crystal gratings and the effective refractive index (n_{eff}) depends on resonance conditions (Lee and Ryu 2002) as follows:

$$\lambda_{Resonance} = n_{eff}\Lambda \tag{10.2}$$

This structure shows the highly sensitive to variation of dielectric permittivity of the photonic crystal surface. Therefore, it is a suitable form of a photonic crystal for sensing and biosensing applications. It can be used as an important platform for environmental, chemical, and biochemical sensing (Liu et al. 1998). So, this platform can monitor the biochemical interaction (e.g., binding) on the surface of a photonic crystal because the effective refractive index can shift to a higher value due to binding the molecular on the surface of the photonic crystal or sensing layer which coated on the surface of photonic crystal (Fig. 10.1c). Consequently, photonic crystals can be used to detect and cap glucose (Fenzl et al. 2014), pathogens (Hu et al. 2013), proteins (Washburn et al. 2010), toxins (Shafiee et al. 2014), enzymes (Han et al. 2013), allergens (Kilian et al. 2009), biological cells (Tan et al. 2016), and DNA (Sharma et al. 2014).

In this chapter, the structure, main parameter, and application of photonic crystal for biosensors were considered.

The Photonic Crystal Structure for Sensor and Biosensor Applications

Sensors and biosensors based on photonic crystals are the significant configurations of nanosensor and micro-sensor. The physical quantity including pressure, temperature, humidity, chemical concentration, and refractive index can be measured using analysis of the reflection and transition of the light beam from photonic crystal. The photonic crystal sensors have a small size, short response time, and high sensitivity (Zhang et al. 2013). Therefore, the photonic crystal sensor and biosensor are attractive tools to investigate the contaminants materials in environment.

Figure 10.2 shows the general configuration of a photonic crystal sensor or biosensor. The photonic crystal sensor setup contains the photonic crystal chip (1D, 2D, or 3D structure) light source and photodetector. Recently, the broadband light source (visible to near-infrared spectrum), diode laser, and photodiode are the most common light sources, and the silicon detector or spectrometers based on fiber optics are the available optical detectors. The broadband light source can cover the wide range of visible and infrared spectra; hence, the broadband light source is one of the best light sources for photonic crystal. The photonic crystals are placed between the light source and the detector and they are the main role in sensing the physical and chemical quantity. The characteristics of photonic crystal change due to variations in the physical or chemical quantity. The detector can detect light spectrum and the spectrum analyzer show the absorption and spectrum part of light due to the interaction of the light beam with the photonic crystal in the presence of any analyte. Sometimes, a sensing layer as a gold layer was coated on the surface of the photonic crystal to increase the sensitivity and plasmonic properties of the photonic crystal. Therefore, the variation of light intensity or absorption spectrum occurred, when the analyte interacts with mentioned layer.

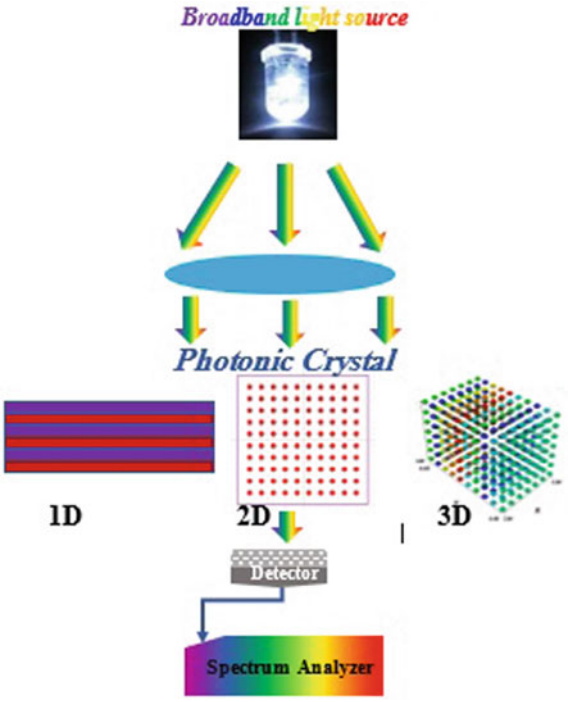

Fig. 10.2 The photonic crystal sensor contains the broadband light source, lens, photonic crystal, detector, and spectrum analyzer

The photonic crystal can confine the light beam; hence, the interaction of the light beam with the probed medium is very strong; therefore, the sensitivity, dynamic range, and response time of the sensor increase. Some biosensors and sensors work based on the interaction of evanescent electromagnetic waves with an analyte, but the photonic crystal can confine the evanescent and electrical field in the low refractive index area. Therefore, the photonic crystal sensor can be used to measure and detect the biomolecule with low refractive index and it is possible to detect and recognize the low variation of refractive index in the biological cell member (Rajesh and Nair 2010).

Recently, various type of photonic crystal biosensors has been presented to measure and recognize biomolecule including glucose (Fenzl et al. 2014), DNA (Sharma et al. 2014), virus (Xu 2007), toxic chemical (Cheung et al. 2015), and protein (Washburn et al. 2010). The photonic crystal waveguide, nanoring resonator, resonator, LX resonator, and fiber have been considered for biosensor and pathologic diagnostic applications.

The photonic crystal waveguide is a regular photonic crystal structure that can use for the detection of proteins. Figure 10.3a shows the sample of this structure. In this structure, the cutting wavelength assigns to detect the variation in the refractive index of the photonic crystal. The wide sensing area is the advantage sensor to detect large biomolecules (Rajesh and Nair 2010).

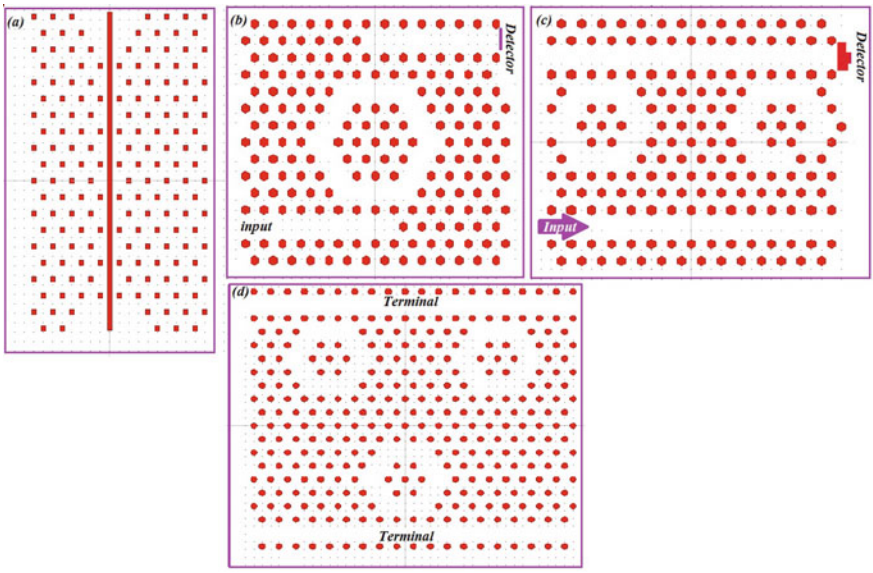

Fig. 10.3 Photonic crystal **a** waveguide, **b** nanoring resonator, **c** two-, and **d** three-resonator rings

The photonic crystal ring resonator and nanoring resonator have wide applications in the photonic integrated circuit (Thirumaran et al. 2021) and biosensor. The photonic crystal nanoring resonator is an attractive structure to detect biomolecules such as DNA. This structure is based on a resonance ring. In order to increase the sensitivity and quality factor, the radius of the resonator ring must be decreased. Therefore, the photonic crystal is the best candidate to activate the small resonance ring with low loss and high resonance. Various structures can be considered to prepare the biosensor. Figure 10.3b shows a biosensor for the detection of DNA based on the hexagonal ring and the two waveguide (one up, one down) was used to couple the light to the sensor. Sometimes, the area between the waveguide and resonator can be fulfilled with water for increasing the quality factor. Figure 10.3c, d show the two and three resonator rings in the photonic crystal structure. There are two or three areas for the interaction of biomolecules with the sensor. Therefore, the quality factor, redshift, and sensitivity increase, and they can be used for the detection of multi-biomolecule. The resonator rings have nanosize and the effective refractive index can change due to the interaction of biomolecules with the sensor area, therefore, the resonance wavelength is shifted to another value (Thirumaran 2021).

The photonic crystal resonator is another structure for biosensors. The photonic crystal resonator sensor contains the waveguide and resonator which formed like an air hole in the dielectric substrate. Figure 10.4a shows the photonic crystal resonator sensor, the micro-resonator formed in the middle of the photonic crystal when the dimension of the air hole was decreased. The quality factor and the resonance wavelength are about 400 and 1.5 μm, respectively. This structure is sensitive to variations

of refractive index about 2 × 10–3 a.u and the sensor was suitable for the detection of the protein. Figure 10.4b shows the photonic crystal resonator. It contains a waveguide and micro-resonator. The structure was formed by deleting two rows and decreasing the air hole in the middle. This structure has a high-quality factor, high sensitivity, and linear relationship between resonance wavelength and variation of refractive index; so, it is suitable for gas sensors and toxic chemical sensors (Jahns et al. 2014).

The photonic crystal LX resonator is the popular structure of biosensors. The X is the integer value and it is the number of holes that were removed from the middle of the photonic crystal.

Figure 10.4c depicts the Lx resonator and it can be used to detect biomaterials and ion metals such as Ca^{+2} the resonance wavelength, and quality factor are about 1.5 μm and 500, respectively (Hua et al. 2013).

The photonic crystal fiber is a promising photonic device such as a sensor. The air hole formed along the axis of fiber optics. The liquid sample can flow in the air holes

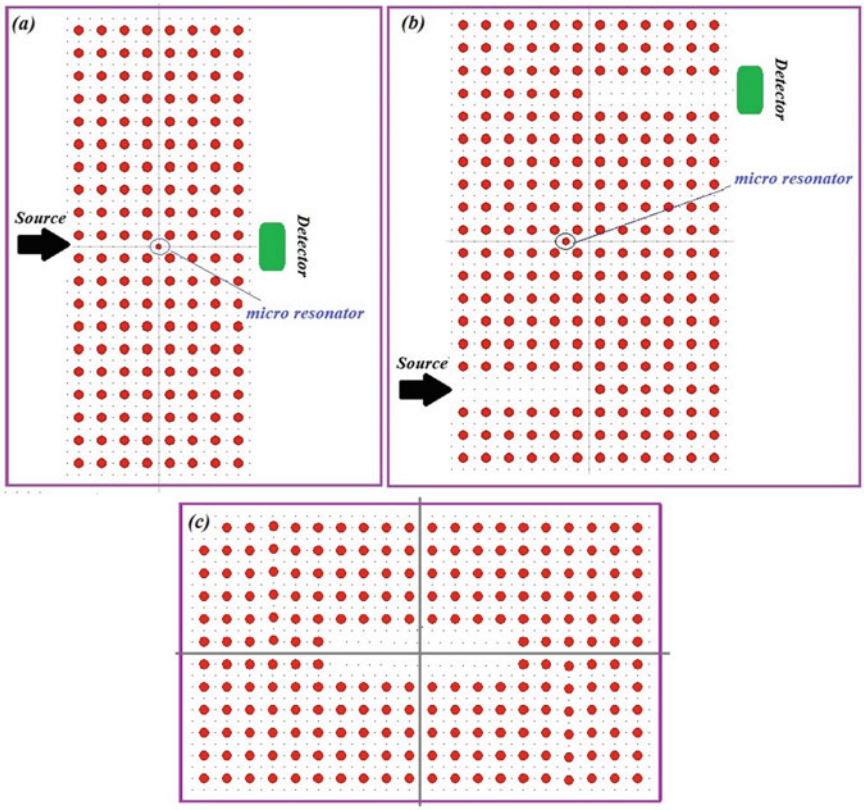

Fig. 10.4 Photonic crystal structure with **a** the micro-resonator, **b** the micro-resonator and waveguide, and **c** the LX resonator

and the light beam can interact with the sample. The main mechanism of photonic crystal fiber is based on the spectrum shift in the wavelength and the redshift occurs when the light interacts with the analyte. The sensing layer should be coated on the sensing area and increases the sensitivity and resolution (Kawasaki et al. 2020).

Sensing Mechanism of Photonic Crystal in Sensors and Biosensors

Fluorescent-based detection and label-free sensing are the main approaches for the detection and recognition of chemicals and biomolecules (Rifat et al. 2016). The mechanism of fluorescent detection is based on changes in emission intensity or wavelength shift appearing in the emission beam in the presence of biological molecules. In label-free sensing, the sensing layer can interact with the target biomolecules and the measurement parameters change. The free-label approach can be used for the detection of chemical and biological molecules using fiber, ring resonator sensor, photonic crystal biosensor, surface plasmon resonance sensor, and other optical methods (Rifat et al. 2016). Photonic crystal biosensors are an intense interest subject in biotechnology and nanophotonic. The main mechanism for the photonic crystal biosensors and sensors is based on refractive index (RI) and resonance wavelength change. The RI and variation of wavelength depend on the surface density and the binding of molecules on the surface of the photonic crystal. When the biomolecule interacts with the active layer (sensing layer), the refractive index of the layer changes; therefore, some of the characteristics of the transmission spectrum will be altered and it can be used to measure the concentration of biomolecules (Fan et al. 2008).

Sometimes, the variation of the refractive index is very small. The main mechanism of the optical biosensor or photonic crystal sensor is based on a variation of the real part of the refractive index and that causes the variation of transmission spectrum two methods can be used for detecting the sensor output. Sometimes, the variation of the refractive index is very small. The light beam is coupled to the photonic crystal from a broadband source and the wavelength modulation method is considered to detect and measure the physical and chemical quantities. Therefore, the wavelength shift should be measured to investigate the sensor output. In this particular case, the laser beam interacts with the photonic crystal and the intensity changes due to a small variation of the physical parameter of the analyte. Hence, the intensity of the light beam should be measured as the output of the sensor. In the mentioned case, the variation of wavelength and intensity beam is due to variations in refractive index and this is caused by the binding of the molecule or biomolecule to the photonic crystal (Fan et al. 2008).

Another method for biosensors is based on changes in the resonance wavelength in the presence of biomolecules. So, the variation of resonance wavelength should be used to detect the molecules. In this case, the narrow full width at half maximum

(FWHM) and the working wavelengths are important parameters and the sensitivity of the sensor depends on FWHM. Moreover, the intensity of resonance wavelength can measure to recognize the biomolecule. In this case, the small variation in the refractive index and resonance wavelength can be measured for the detection of low concentrations of biomolecules (Fan et al. 2008).

The photonic crystal biosensor or sensors actuate the photonic band gap or the Bragg reflection.

The advantages of photonic crystal sensors are surface waves and the surface waves over surface-plasmon polariton waves on the periodic structure of the sensor and on a metallic surface, respectively. It is fabricated using a thin film layer (Olyaee n.d.). These surface waves improved and enhanced the sensitivity of the structure and it can improve the characterization parameters of biosensors. The method based on interference of the long range of the photonic crystal surface waves is a mechanism for the sensor and the shift in the maximum peak position is a method to find the alter in the refractive index thickness of layer and resonance wavelength (Villa et al. 2002).

Significant Parameters and Structure of Photonic Crystal in Sensors and Biosensors

The photonic crystal sensors work based on variations in the optical parameters of the medium and photonic crystal. The interaction of the analyte with the sensing layer or photonic crystals causes the variation of optical parameters of the light beam including the phase, intensity, and polarization of the light beam. The optical parameters of the medium are the refractive index ($\hat{n} = n + ik$) and absorption coefficient. The significant parameters for evaluation of photonic crystal sensor are sensitivity, quality factor, limit of detection, full width at half maximum (FWHM), and free spectral range that are investigated as follows:

Sensitivity of Photonic Crystal Sensor

The sensitivity of the photonic crystal sensor is the ratio of change in the sensor output (wavelength shift or intensity shift) to the variation of refractive index or other optical parameters of the medium (measurand). Therefore, sensitivity (S) is a criterion to measure the interaction of light with the photonic crystal in the presence of the analyte. Hence, the sensitivity is a variation of wavelength shit ($\Delta\lambda$) to the variation of refractive index (Δn) or variation of intensity shift (ΔI) to the variation of refractive index. The variation of refractive index is corresponding to the molecular weight (m) of biomolecular or toxic chemicals which interact with photonic crystals. The sensitivity can calculate as follows (Fan et al. 2008):

$$S = \frac{\Delta\lambda}{\Delta n} = \frac{\Delta\lambda}{m} \tag{10.3}$$

$$S = \frac{\Delta I}{\Delta n} = \frac{\Delta I}{m} \tag{10.4}$$

Quality Factor

The significant parameter for the evaluation of a photonic crystal sensor is the quality factor when the output of the sensor is the wavelength shift and the sensor works with the broadband light source. The quality factor is the ratio of wavelength (λ_0) that was shifted due to the interaction of the molecule with the photonic crystal to the FWHM ($\Delta\lambda_{FWHM}$) of the spectrum. The spectrum of the light source and the coupling of light with the photonic crystal is important to obtain the optimum quality factor value (Fan et al. 2008).

$$Q = \frac{\lambda_0}{\Delta\lambda_{FWHM}} \tag{10.5}$$

Limit of Detection

The limit of detection is an important parameter to evaluate the detection of low concentrations of biomolecules or toxic chemicals. As a definition, the lowest concentration of an analyte that the response of the optical sensor can be observed and the variation of wavelength and intensity can be consistently measured with the high probability is limit of detection (LOD).

The sensor and biosensor contain receptors and transducers. The receptor can detect toxic chemicals and biomolecules, and it is sensitive to changes in the physical quantity. Some biomolecules can use as a receptor for particular biosensors and they can recognize the particular analyte including antibodies, enzymes, nucleic acid, and DNA (Sharma et al. 2014). The transducer can convert the effect of molecule interaction with receptors to physical parameters that are measurable. There are two sensor types that can be used to detect the biomolecule including a sensor with a particular label and a free label sensor (Fan et al. 2008).

Full Width at Half Maximum (FWHM)

The full width at half maximum is the significant characterization of the output sensor signal. This parameter is useful to evaluate the sensitivity and sensor design because it affects the limit of detection and quality factor or biosensor and sensor. To design the photonic crystal sensor, it is preferred to obtain the narrow FWHM because the free spectral range decreased.

Free Spectral Range (FSR)

The free spectral range is an important parameter that should be considered to design the photonic crystal sensor. The reliable results depend on the sufficient range of wavelength that resonant peaks do not overlap with the working resonant peak. The free spectral range is proportional to the square of the wavelength. Thus, the free spectral range is small in short wavelengths. Therefore, the sensor or biosensor should be designed for long wavelengths and this is the easiest idea for obtaining the optimum sensor (Fan et al. 2008).

Biosensor Application of Photonic Crystal

Recently, photonic crystals were used to detect biomolecules and macromolecules including nucleic acid, proteins, blood components, and cancer cells. In Sect. 2, the mechanism, and the various type of photonic crystal structures for biosensors were investigated. In this section, the particular photonic crystal biosensors are explained based on mentioned mechanism.

Photonic Crystal Biosensor for Detection of Nucleic Acids and Protein

The famous biomolecule is nucleic acids which are significant macromolecules in the cells of organisms and they have two categories including deoxyribonucleic acid (DNA) and ribonucleic acid (RNA). The nucleic acids are composed of nucleotides. The nucleotides are monomers that makeup nucleosides (5-carbon sugar, nitrogenous base) and a phosphate group. Consequently, RNA and DNA contain ribose and deoxyribose as a sugar part of nucleic acids. Nucleic acids have a main role in viruses and living cells and they are very large molecules, therefore, the investigation of their genetics and the detection of new nucleic acids are the intense interest subject in biology and biotechnology (Konopsky and Alieva 2007).

The photonic crystal nanoring resonators are the significant configuration for the detection of nucleic acid (DNA and RNA) (Roberts n.d.). The hexagonal and diamond nanoring resonator are the usual structures for nucleic acid biosensors. Figure 10.5a, b, c, d show the photonic crystal structures for the detection of particular nucleic acid. The diamond and hexagonal nanoring resonators formed in the dielectric so that the air holes in the ring are the suitable place for prob of nucleic acid (DNA, or RNA). The excitation wavelength is in the range of 1200–1600 nm and the hole size is about 100 nm. Figure 10.5c, d show the interaction of molecules with sensing layer that was coated on the surface of photonic crystal. When the prob molecule interacts with the target such as DNA, or RNA, the variation of wavelength should be measured. The main condition for using the sensor for the detection of nucleic acid is the linear response in the variation of wavelength and the wavelength of resonance must change in the sensing area (sensitivity of the sensor).

Figure 10.5e shows the hexagonal nanoring structure for the detection of DNA. In this structure, the hole hexagonal lattice formed on the surface of the silicon plate. The hole can be fulfilled with liquid like water. The hexagonal nanoring was sandwiched between two waveguides for coupling the Gaussian light beam to the photonic crystal structure and the detection of the light beam after resonance and interaction with the

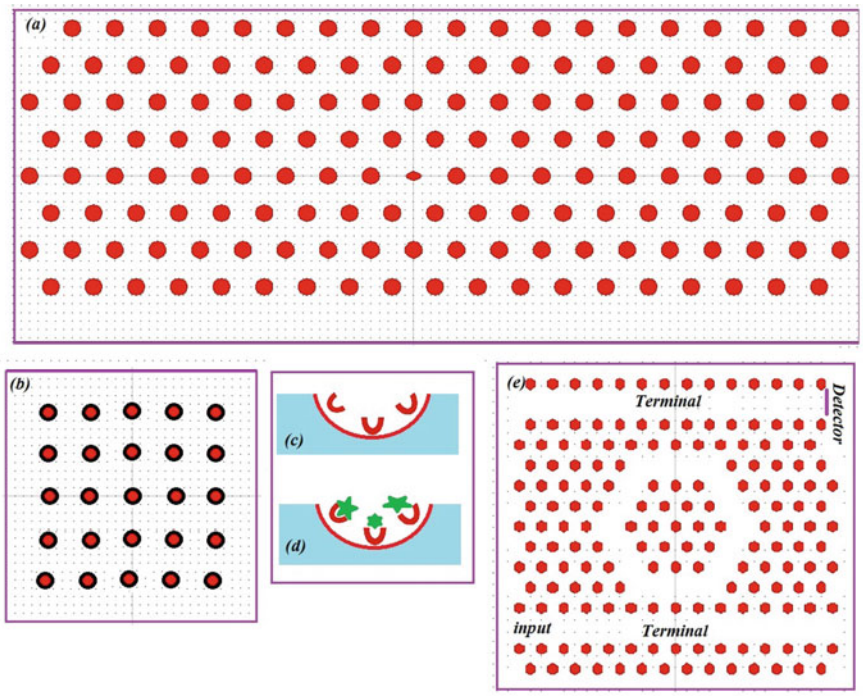

Fig. 10.5 The **a** and **b** photonic crystal structure to investigate the DNA interaction with probe medium, **c** and **d** the interaction of nucleic acid with prob, and **e** the structure of nanoring and waveguide for protein and nucleic acid biosensor

DNA or RNA using the InGaAs detector. The important parameters are the distance between the resonator ring and waveguide and the place of a hole for prob DNA. As a literature (Roberts n.d.; Benmerkhi et al. 2020), the best place is the corner (color) of the hexagonal near to input waveguide and the optimum number of holes between the nanoring and the resonator is about 3 raw.

Proteins are the main macromolecule in the human body and they are the large biomolecules they are made from amino acid chains using peptide bonds. Proteins are like a chain of a three-dimensional coil of polymers that are consisting of amino acids. The sequence of amino acids is determined by genes in the proteins. Although the genetic code introduces 20 standard amino acids, in some organisms the genetic code includes selenocysteine and in some archaebacteria it contains pyrrolysine. Proteins are the main source of energy, and the generation of hormones, enzymes, and antibodies. Hence, proteins are a significant research point in genetics, pharmacology, and microbiology (Hsiao and Lee 2010).

More configuration of photonic crystals was used to detect and measure the concentration of protein. The photonic crystal resonator or micro-resonator (Koshland n.d.) is the candidate to fabricate the biosensor for probing the proteins. Figure 10.5a, b show the sample of the photonic crystal resonator structure for detecting the protein. The sensing medium such as glutaraldehyde can be used to cap the protein (albumin) when the target protein contacts with the sensing layer the refractive index will be shifted to a higher value. Hence, the resonance wavelength which is about 1580 nm, changes to 1590 nm. On the other hand, the redshift appeared when the prob biomolecule interacted with the protein target (Fan et al. 2008).

Another structure for protein biosensors is the mix of the photonic crystal waveguide and photonic crystal resonator structures. The tunable laser in the near-infrared range should be used to arouse the resonance mode. Figure 10.4 also demonstrates the sample photonic crystal structure for protein biosensors. The stability, sensitivity, and quality factor were improved by about 30%. The minimum concentration of protein that can be detected using these structures was about 3 × 10–5 ppb and the minimum red shift is about 2 nm (Lee and Fauchet 2007).

Photonic Crystal Biosensor for Detection of Cancer Cell

The principal of photonic crystal biosensors for the diagnosis and detection of cancer are as same as the photonic crystal biosensor for the detection of nucleic acid and proteins. Hence, the photonic crystal resonator, photonic crystal wave, and photonic crystal nanoring resonator structures can be used to fabricate the cancer biosensor.

Simple biosensor cancer was reported based on the variation of refractive index in the 2D photonic crystal waveguide (Saeed and Najafgholinezhad 2013). This structure was fabricated on the 5 × 5 silicon wafer and the wavelength shift (blue shift) appeared in the presence of cancer cells. The sensitivity and quality factors were reported at about 2000 nm/RIU and 99, respectively. The real-time cancer

biosensor was prepared using a graphene layer on the 1D photonic crystal (Panda 2020). The sensor works based on shifts in the absorption and transmittance spectra in the resonance wavelength. The sensitivity, quality factor, and resolution were about 290 nm/RIU, 2200, and 0.07 nm, respectively. Another 1D photonic crystal biosensor was fabricated with Aly and Zaky using SiO2/GaAs system sequential layers to improve the sensitivity up to 2000 nm/RIU (Panda 2021). The diamond nanoring resonator was used to detect the cancer cell. In this structure, the body fluid can flow in the sensor and the variation of refractive index or nature of human cells in the urine, blood, or saliva can be recognized. The quality factor was reported in about 2000 (Arafa 2019).

Consequently, two dimensions of the photonic crystal sensor are the suitable structure for cancer biosensors and the cancer cell can be detected in the human fluid using photonic crystal sensor structure.

Conclusion

The photonic crystals were fabricated using periodic particular dielectric medium and the variety of photonic crystal structures are Bragg reflectors, microcavities, and low refractive index grating. The photonic crystals waveguide, resonator, nanoring resonator, LX resonator, and fiber are the primary candidate for biosensor and pathologic diagnostic applications. The sensitivity, quality factor, the limit of detection, full width at half maximum, and free spectral range are significant parameters for evaluating sensors and biosensors based on photonic crystals. The photonic crystal sensor based on a waveguide and resonator is more useful than other photonic crystal structures in biosensors. Photonic crystal sensors are sensitive, reliable, and accurate tools for detecting nucleic acids, proteins, sugar, and cancer cells. The photonic crystal sensor based on a waveguide and resonator are more useful than other photonic crystal structures in biosensors.

References

Aly AH, Zaky ZA (2019) Ultra-sensitive photonic crystal cancer cells sensor with a high-quality factor. Cryogenics 104:102991. https://doi.org/10.1016/j.cryogenics.2019.102991

Benmerkhi A, Bouchemat M, Bouchemat T (2020) Design of two-dimensional photonic crystal biosensor using DNA detection, pp 960–964. https://doi.org/10.1080/10426507.2020.1804206

Chambers JP, Arulanandam BP, Matta LL, Weis A, Valdes JJ (2008) Curr Issues Mol Biol 10:1–12 [PubMed: 18525101]

Cheung SF, Cheng SKL, Kamei DT (2015) J Lab Autom 20:316–333 [PubMed: 25787805]

Choko AT, Desmond N, Webb EL, Chavula K, Napierala-Mavedzenge S, Gaydos CA, Makombe SD, Chunda T, Squire SB, French N, Mwapasa V, Corbett EL (2011) PLoS Med 8:e1001102 [PubMed: 21990966]

Chopra H, Kaler RS, Painam B (2016) Photonic crystal waveguide-based biosensor for detection of diseases. J Nanophotonics 10(3). https://doi.org/10.1117/1.JNP.10.036011
D Shanmuga Sundar, R Sathyadevaki and A Sivanantha Raja, High-efficiency filters for photonic integrated networks: a brief analysis, 2018 Laser Phys. 28,11, 116203
Fan X, White IM, Shopova SI, Zhu H, Suter JD, Sun Y (2008) Sensitive optical biosensors for unlabeled targets: a review. Anal Chim Acta 620:8–26
Fenzl C, Hirsch T, Wolfbeis OS (2014) Angew Chem Int Ed 53:3318–3335
Geerthana S, Syedakbar S, Sridarshini T, Balaji VR, Sitharthan R, Shanmuga Sundar D (2022) 2D-PhC based all optical AND, OR and EX-OR logic gates with high contrast ratio operating at C band. Laser Phys 32(10):106201
Gowdhami D, Balaji VR, Murugan M, Robinson S, Hegde G (2022) Photonic crystal based biosensors: an overview. ISSS J Micro Smart Syst 11:147–167
Han JH, Kim HJ, Sudheendra L, Gee SJ, Hammock BD, Kennedy IM (2013) Anal Chem 85:3104–3109 [PubMed: 23418954]
Hsiao F-l, Lee C (2010) Computational study of photonic crystals nano-ring resonator for biochemical sensing. IEEE Sens J 10(7):1185–1191. https://doi.org/10.1109/JSEN.2010.2040172
Hu Y, Jiang X, Zhang L, Fan J, Wu W (2013) Biosens Bioelectron 48:94–99 [PubMed: 23651573]
Inan H, Poyraz M, Inci F, Lifson MA, Baday M, Cunningham BT, Demirci U (2017) Photonic crystals: emerging biosensors and their promise for point-of-care applications. Chem Soc Rev 46(2):366–388. https://doi.org/10.1039/c6cs00206d
Jahns S, von Oertzen F, Karrock T, Nazirizadeh Y, Gerken M (2014) Photonic crystal slabs for biosensing, progress. In: Electromagnetics research symposium proceedings. Guangzhou, China
Joannopoulos JD, Johnson SG, Winn JN, Meade RD (2008) Photonic crystals: molding the flow of light. Princeton University Press
Kawasaki D, Oishi R, Kobayashi N, Mizuta T, Sueyoshi K, Hisamoto H, Endo T (2020) Highly sensitive optical ion sensor with ionic liquid-based colorimetric membrane/photonic crystal hybrid structure. Sci Rep 10, Article number:16739
Kilian KA, Lai LMH, Magenau A, Cartland S, Böcking T, Di Girolamo N, Gal M, Gaus K, Gooding JJ (2009) Nano Lett 9:2021–2025 [PubMed: 19382766]
Kirsch J, Siltanen C, Zhou Q, Revzin A, Simonian A (2013) Chem Soc Rev 42:8733–8768 [PubMed: 23852443]
Konopsky VN, Alieva EV (2007) Anal Chem 79:4729–4735
Koshland DE, Felix Haurowitz, protein biochemistry. https://www.britannica.com/science/protein
Lee Y-H, Ryu HY (2002) IEEE Circuits Dev Mag 18:8–15
Lee M, Fauchet PM (2007) Two-dimensional silicon photonic crystal based biosensing platform for protein detection. 15(8):4530–4535. https://doi.org/10.1364/OE.15.004530
Lifson MA, Ozen MO, Inci F, Wang S, Inan H, Baday M, Henrich TJ, Demirci U (2016) Adv Drug Delivery Rev. 103:90–104
Lissandrello C, Inci F, Francom M, Paul MR, Demirci U, Ekinci KL (2014) Appl Phys Lett 105:113701 [PubMed: 25316924]
Liu ZS, Tibuleac S, Shin D, Young PP, Magnusson R (1998) Opt Lett 23:1556 [PubMed: 18091845]
Magnusson R, Ding Y (2003) Optical science and technology. In: SPIE's 48th annual meeting. International Society for Optics and Photonics
Mohebzadeh Bahabady A, Olyaee S (2015) Two-curve-shaped biosensor for detecting glucose concentration and salinity of seawater based on photonic crystal nano-ring resonator. Sens Lett 13(9):774–777(4)
Monošík R, Streanský M, Šturdík E (2012) Acta Chim Slovaca 5:109–120
Myung S, Yin PT, Kim C, Park J, Solanki A, Reyes PI, Lu Y, Kim KS, Lee KB (2012) Adv Mater 24:6081–6087 [PubMed: 22961629]
Olyaee S, Mohsenirad H, Mohebzadeh-Bahabady A, Photonic crystal chemical/biochemical sensors. https://doi.org/10.5772/63288

Panda A, Puspa Devi P (2020) Photonic crystal biosensor for refractive index based cancerous cell detection. Opt Fiber Technol 54:102123. https://doi.org/10.1016/j.yofte.2019.102123
Panda A, Pukhrambam PD, Wu F, Belhadj W (2021) Graphene-based 1D defective photonic crystal biosensor for real-time detection of cancer cells. Eur Phys J Plus 136, Article number:809
Plebani M (2010) Ann Clin Biochem 47:101–110 [PubMed: 19952034]
Rajesh V, Nair R (2010) Vijaya, Photonic crystal sensors: an overview. Prog Quantum Electron 34(3):89–134
Rifat AA Amouzad Mahdiraji G, Shee YG, Jubayer Shawon M, Mahamd Adikan FR (2016) A novel photonic crystal fiber biosensor using surface plasmon resonance. Procedia Eng 140:1–7
Roberts RJ, Nucleic acid, chemical compound. https://www.britannica.com/science/nucleic-acid
Saeed O, Najafgholinezhad S (2013) a high quality factor and wide measurement range biosensor based on photonic crystal nanocavity resonator. Sens Lett 11(3):483–488(6). https://doi.org/10.1166/sl.2013.2829
Sathyadevaki R, Shanmuga Sundar D, Sivanantha Raja A (2018) Photonic crystal 4×4 dynamic hitless routers for integrated photonic NoCs. Photonic Netw Commun 36:82–95
Sathyadevaki R, Shanmuga sundar D, Sivanantha Raja A (2016) Design of dual ring wavelength filters for WDM applications. Opt Commun 380:409–418
Shafiee H, Lidstone E, Jahangir M, Inci F, Hanhauser E, Henrich TJ, Kuritzkes DR, Cunningham BT, Demirci U (2014) Sci Rep 4:4116 [PubMed: 24576941]
Shanmuga Sundar D, Sathyadevaki R, Sridarshini T, Sivanantha Raja A (2018) Photonic crystal based routers for photonic integrated on chip networks: a brief analysis. Opt Quantum Electron 50, Article number:383
Sharma P, Roy SK, Sharan P (2014) IEEE TENSYMP 2014–2014 IEEE Region 10 Symposium, pp 171–176
Tan Y, Halsey JF, Tang T, Vande Wetering S, Taine E, Van Cleve M, Cunningham BT (2016) Biosens Bioelectron 77:194–201. [PubMed: 26406461]
Thirumaran S (2021) Shanmuga Sundar Dhanabalan, Indira Gandhi Sannasi, Design and analysis of photonic crystal ring resonator based 6 × 6 wavelength router for photonic integrated circuits. IET Optoelectron 15(1):40–47
Villa F, Regalado LE, Ramos-Mendieta F, Gaspar-Armenta J, Lopez-Rı´os J (2002) Opt Lett 27:646–648
Viswanathan S, Narayanan TN, Aran K, Fink KD, Paredes J, Ajayan PM, Filipek S, Miszta P, Tekin HC, Inci F (2015) Mater Today 18:513–522
Wang J, Wu C, Hu N, Zhou J, Du L, Wang P (2012) Biosensors 2:127–170 [PubMed: 25585708]
Washburn AL, Luchansky MS, Bowman AL, Bailey RC (2010) Anal Chem 82:69–72 [PubMed: 20000326]
Xu H, Wu P, Zhu C, Elbaz A, Gu ZZ (2013) Photonic crystal for gas sensing. J Mater Chem C 1:6087–6098
Xu J, Suarez D, Gottfried DS (2007) Anal Bioanal Chem 389:1193–1199 [PubMed: 17710386]
Yetisen AK, Montelongo Y, da Cruz VF, Martinez-Hurtado JL, Neupane S, Butt H, Qasim MM, Blyth J, Burling K, Carmody JB, Evans M, Wilkinson TD, Kubota LT, Monteiro MJ, Lowe CR (2014) Nano Lett 14:3587–3593 [PubMed: 24844116]
Zhang H, Jia Z, Lv X, Zhou J, Chen L, Liu R, Ma J (2013) Biosens Bioelectron 44:89–94 [PubMed: 23395728]

Chapter 11
High-Frequency Photonic Crystal-Based Terahertz Antenna for Medical Applications

Sathish Kumar Danasegaran, Elizabeth Caroline Britto, K. Sagadevan, and Susan Christina Xavier

Abstract The microstrip patch antenna plays a significant part in the medical domain. This chapter discusses a few descriptions of tiny medical antennas in the range of TeraHertz (THz) frequency. Small-size antennas are permitted to provide minimally invasive care. The proposed C-slotted THz patch antenna is used in and around the human body due to its miniaturized size. The slotted microstrip Photonic Crystal (PhC) antenna is intended for the THz frequency series, and it achieves better results of −44.63 dB return loss and 6.2 dBi directivity at 1.86 THz. The applications of the proposed antennas are body scanning, cancer treatment, DNA signatures, biomedical spectroscopy, etc.

Keywords THz frequency · Microstrip patch antenna · Medical field

Introduction

THz is well suited to the next-generation wireless communication devices capable of firing at a blistering 100 Gb/s (Hwu et al. 2013). The THz technique's utility in high-speed data transfer between electronic devices is very promising. There has been a growth in demand for unallocated frequency bandwidth in recent years, and future transmission networks will rely on the THz area for improved transmitter frequency, more powerful data rates, and large channel power. A transducer is a device that transforms a radio frequency (RF) electrical signal into a frequency-matched electromagnetic (EM) signal and vice versa (Failed 2019). It can work as a transmitter of signals as well as receiver. It is the interface among the radio waves

S. K. Danasegaran (✉) · E. C. Britto · K. Sagadevan
Department of ECE, IFET College of Engineering, Villupuram, Tamil Nadu, India
e-mail: dsathishh@yahoo.com

S. C. Xavier
Department of ECE, MAM College of Engineering & Technology, Trichy, Tamil Nadu, India

© The Author(s), under exclusive license to Springer Nature Singapore Pte Ltd. 2023

S. S. Dhanabalan et al. (eds.), *Photonic Crystal and Its Applications for Next Generation Systems*, Springer Tracts in Electrical and Electronics Engineering,
https://doi.org/10.1007/978-981-99-2548-3_11

propagating via area and electric powered current shifting in a metallic conductor, used with transmitter or receiver.

Antennas must be categorized to get their body shape and methodology extra. (Poonguzhali et al. 2022a) There are several antennas based on the applications:

1. Wire Antenna,
2. Aperture Antenna,
3. MicroStrip Antenna,
4. Array Antenna,
5. Reflector Antenna,
6. Lens Antenna.

Microstrip Patch Antenna

A microstrip patch antenna includes a very thin metal strip established on a ground plane and located among dielectric materials (Mohamed Nizar et al. 2021). Photo-etching is used to position the radiating element and feed lines on the dielectric material (Sharma and Singh 2009). For ease of inspection and fabrication, the patch or microstrip is typically rectangle, round, or rectangular (Son 2014) shown in Fig. 11.1.

To begin, some strategies for improving penetration deepness inside humid biological tissues are investigated (Vafapour et al. 2020). THz radiation has great potential in the medical field. The utmost promise of THz radioactivity in biomedical attention has so far been in cancer imaging since 1.65 THz radioactivity is appropriate for testing the surface soft tissues in which most maximum cancers happen (Jae 2009). In this context, the outlined state-of-the-art THz techniques are applicable in medical systems to develop sensing abilities and clean deeper into tissues.

The discussion of various imaging methods that are also available for investigation, but they are limited to either macroscopic or microscopic imaging (Siegel 2004). The microscope is used to find image information of tissues. The existing method of X-ray, macroscopic level, and MRI are used to give models of existing tissues, but they have much lower resolution and accuracy. In this article, the Ansys HFSS ver.14 tool was used to design and analyze a THz imaging antenna with a frequency range of 0.1–10 THz and a very low power of 3.58 mV (Sathish Kumar et al. 2021). It can detect a variety of tumors with high-resolution and non-ionizing radiation at a low cost, including surface cancer, chest cancer, cervical cancer, and colon cancer.

In non-ionizing radiation purposes applications like quality management, protein analysis, pharmaceuticals, and cancer therapy, biomedical imaging has confirmed promise. The frequency range is 0.960–20.0 THz, with a resonant at 0.6 THz, resulting in the UWB transparent antenna's high performance. The result of the reflection coefficient is −55 dB obtaining the maximum value of gain of 6.13 dB and 8.2 dBi value of directivity (Hu and Nuss 1995). As a result, it can be used in

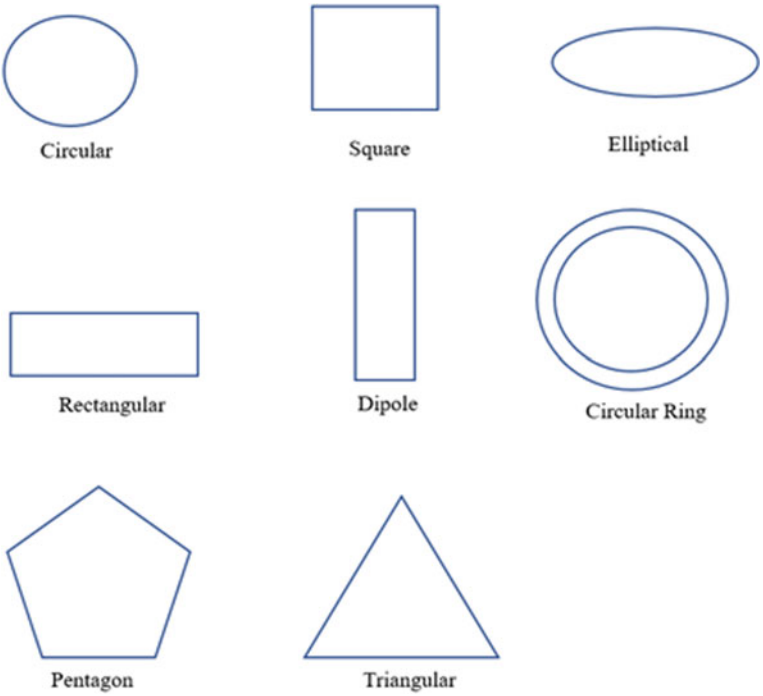

Fig. 11.1 Different shapes of patch

imaging and satellite communication applications that need a large BW at higher frequencies, such as the THz range.

An imaging system using the 0.3–3 THz range of EM spectrum is used for security, safety, and biomedical application (Mantsch and Naumann 2010). The connection between the living tissue and electromagnetic ranges has the extent to high absorbance of water this will find the tissues in different content of water. Also, spectroscopy in this THz region finds the number of proteins and molecules in the particular frequency spectrum (Chiu et al. 2009).

THz frequency has many features of non-ionizing, high penetration, and resolution (Britto et al. 2022). To determine the pathological tissues and superficial tissue using the signal-to-noise ratio of 0.1–10 THz frequency range for finding absorption peaks and identify the biological samples like tissue, blood, and urine depending on the substance like water protein, fat, and fiber (Denizhan Sirmaci et al. 2016).

Techniques for Feeding

Feeding systems are divided into two groups. One is contacting, and the other is non-contacting (Failed 2020). The coaxial observation, microstrip length, aperture joined, and proximity joined are the four varieties of feeding methods.

Coaxial Probe Feed

Coaxial-line feed or probe feed is an acquainted approach used for feeding microstrip patch antennas this day, in which the interior transmitter of the coaxial is prolonged via the dielectric and associated to the patch antenna, even though the exterior transmitter is hooked up to the floor plane, the most important advantage of this feed is that it can be connected via preferred vicinity within the patch to match with its far enter impedance of the patch (Maynard 2006). It is likewise smooth to build, and it becomes a feeble deceptive broadcast. The negative aspects are that it additionally has slender bandwidth and is extra hard to model.

Line Feed Microstrip

It's a method of feeding, wherein the microstrip patch is immediately related to the moving out microstrip feed line. The measurement of the feed line is one of a kind than a microstrip patch. It is straightforward to manufacture and match.

Feed with Aperture

This feed is made up of two substrates that are distributed by a ground plane and are separate from individual differences. The microstrip patch and feed line are compared into a slot in the ground plane in this process. The aperture-coupled feeding system has the benefits of minimized interference and pure polarization.

Proximity-Coupled Feed

In comparison, the manufacturing of this feeding process is a little more difficult. This technique employs two dielectric substrates. Between two substrates is the feed line and the microstrip patch is toward the topmost surface of the upper dielectric layer. It has the most comprehensive bandwidth which prevents stray radiation.

Different Substrates

The discovery of a suitable substrate is the first step in constructing an antenna. A variety of substrate materials, coated in copper, aluminum, or gold, are available. The dielectric constant of the substrate will vary as the substrate material is shaped. The antenna architecture for the microstrip patch antenna uses different substrates. The dielectric constant (permittivity) presents the main function in the overall representation of a patch antenna.

There is neither one prototypical substrate, the opportunity preferably depends on the form. Conformal microstrip antennas, for instance, require compressed substrates, while low-frequency demands require high dielectric constants to keep the size down. Low dielectric substrates are used in microstrip patch antennas. The list of materials is given below:

1. FR4 Lossy (4.4),
2. Roger 4350 (3.48),
3. Foam (1.05),
4. Nylon fabric (3.6),
5. Silicon (11.7).

Compare to other materials the FR4 Substrate has a suitable parameter for microstrip patch antenna. The advantages of choosing this material in the medical field for good flexibility, thin substrate, higher frequencies, good electrical features, low price, and easy availability.

Antenna in Medical World

Cancer is one of the most complex diseases, and if it is not detected early enough, it will lead to death (Ashworth et al. 2009). In this context, the microstrip patch antenna has a rectangular configuration with a microstrip feed, and the material substrate is FR4 with a dielectric constant of 4.4, which is inexpensive and readily available. Antennas have been researched thoroughly for several medical uses. Because these antennas are used in and around the human body, the C slotted patch antenna for THz medical applications. The medical domain is considerably enhanced in this virtual system due to seasoned biomedical technologies (Sun et al. 2011). Electromagnetism (Britto et al. 2022) has been transformed into radiofrequency and used in medical applications. In the area of biomedical applications, implanted technologies are gaining a lot of scrutinies. Medical implants that can connect with an external device through wireless technology are known as implantable medical devices (Kumar et al. 2020; Rubaek et al. July 2009). Too, certain necessities might be affected a person's safety, biocompatibility, low power intake, and lengthy life. The above-mentioned medical field was still used antenna systems that don't provide better efficiency. To overcome these problems the proposed system provides 1.86 THz frequency. Compact size and better return loss.

Procedure

The rectangular microstrip patch antenna is positioned above the ground on a fair substrate partition. Picking substrate materials for the antenna configuration is a strong, FR4 material with a dielectric constant estimate of 4.4. FR-4 is commonly available and inexpensive. For the proposed frequency, the substrate permittivity is nearly constant. Furthermore, the availability of FR-4 material in a wider range of thickness values than other materials, giving a greater design flexibility. The contribution of substrate FR-4 in the suggested design plays a crucial role in enhancing the antenna's bandwidth. The structure and form of the substrate are important parameters in antenna design, as are the dielectric constant and loss tangent. The inset feedline is one of the few feeding technologies that is chosen to achieve persuasive impedance matching and is made of copper. Silver has better conductivity than copper or gold. Copper, on the other hand, is much stronger than the other two metals. Unfortunately, copper is a highly reactive metal. Copper is an inexpensive metal. To determine the width (W) and length (L) of the patch by using the below formulas.

Evaluation of Extent (H) of the Patch

The calculation is used to measure the patch's height

$$pl = \frac{C_0}{2f_r\sqrt{\varepsilon_{reff}}} - 2\Delta L \tag{11.1}$$

where C = velocity of light, given as 3.0 × 108 m/s,
εr = the dielectric substrate.

Evaluation of Width (W) of the Patch

Figure 11.2 illustrates the patch antenna schematic and the value of patch's breadth is obtained from the subsequent formula:

$$pw = \frac{C_0}{2f_r}\sqrt{\frac{2}{\varepsilon_r + 1}} \tag{11.2}$$

The width, W, is in millimeters (mm).

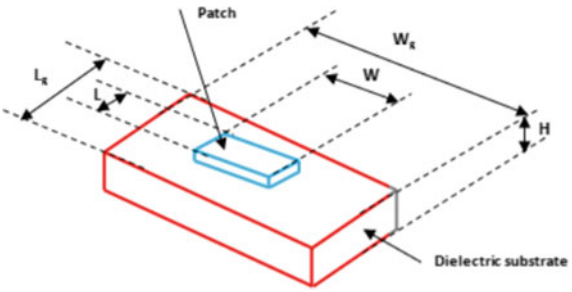

Fig. 11.2 Schematic diagram of a Rectangular Microstrip Patch Antenna

Evaluation of the Effective Dielectric Constant (εeff)

It is estimated using the following numerical relationship:

$$\varepsilon_{eff} = \frac{\varepsilon_r}{\sqrt{1 + \frac{12h}{fw}}} + 0.04\left(1 - \frac{fw}{h}\right)^2 \; if \; \frac{fw}{h} < 1 \tag{11.3}$$

Otherwise,

$$\varepsilon_{eff} = \left(\frac{\varepsilon_r + 1}{2} + \frac{\varepsilon_r - 1}{2}\right)\left[\frac{1}{1 + (12h)/fw}\right] \tag{11.4}$$

where H and W are the height and the width, respectively, of the patch in that other.

Evaluation of the Effective Length of the Patch (Leff)

The formula determines the patch's effective length:

$$L_{eff} = \frac{C}{2F_o\sqrt{\varepsilon_{eff}}} \tag{11.5}$$

Evaluation of the Length Extension (ΔL)

Length distance is the additional length on the end of the patch due to the fringing range with its width. It is estimated using the method given as

$$\frac{\Delta L}{h} = 0.412\frac{\left(\varepsilon_{reff} + 0.3\right)\left(\frac{pw}{h} + 0.264\right)}{\left(\varepsilon_{reff} - 0.258\right)\left(\frac{pw}{h} + 0.8\right)} \tag{11.6}$$

where ΔL is the millimeter expansion of the patch, H and W are the patch's height and width, respectively. εeff is the substrate's effective dielectric constant, which is dimensionless.

Evaluation of the Actual Length (L) of the Patch

The real length of the patch, L is the distinction within the patch's effective length and multiplies the patch's range expansion. Mathematically, it's written as

$$\mathrm{L} = \mathrm{Leff} - 2\Delta\mathrm{L} \tag{11.7}$$

Dimensions of the Ground Plane Are Calculation

The height and width of the ground flat dimensions were circumscribed. The height and width of the ground plane beat the height and width of the patch in that status by six points the width or height of the patch. They're evaluated utilizing the following formula:

$$\mathrm{L}g = \mathrm{L} + 6\mathrm{h} \tag{11.8}$$

$$\mathrm{W}g = \mathrm{W} + 6\mathrm{h} \tag{11.9}$$

where L and W are the length and the width of the patch antenna, respectively.

Feed Point Evaluation

Xf, Yf are the XY-coordinates of the feed point to the patch antenna. The following formulas used to measure the feed point positions by the coaxial method.

$$\boldsymbol{X}_f = \frac{L}{2\sqrt{\varepsilon_{eff}}} \tag{11.10}$$

$$\boldsymbol{Y}_f = \frac{\boldsymbol{W}}{2} \tag{11.11}$$

Table 11.1 Geometry of the proposed antenna

Antenna elements	Parameters	Dimensions in (μm)
Substrate	Length Sl	30
	Width Sw	91.89
	Height h	0.1
Patch	Length Pl	16.95
	Width Pw	91.29
Feed	Width Fw	5
	Length Fl	8

where XF and Yf are the feed point location along XY-coordinates. The calculated dimensions are publicized in Table 11.1.

Photonic Crystal Structure

A recurrent metallic sequence printable patch on such a dielectric material is used in microwave and millimeter-wave applications. Once the patch is used over a dielectric material with a high permittivity, this strives to couple too much power to the substrate due to surface wave outflow. Since the power does not make a contribution to the radiation pattern, it is assumed a loss mechanism. An actual solution is obtained whenever the PhC is utilized as an antenna substrate. When the commuting frequency of the antenna is within the bandgap, no power is radiated into the surface from any angle. The PhC suppresses surface waves to improve antenna efficiency. As PhC structural properties, the media of dielectric constants, the air hole radii (r), the lattice constant (a), and the r/a relation are investigated. The frequency in the dielectric permittivity of the media is clarified and the Bloch-Floquet theorem is exploited to resolve the issue in a regular diagonalized matrix for the eigenvectors and values. Generally, there are two types of lattices available in the PhC design such as square and triangle. The PhC substrate is designed using a square lattice structure with circular air holes in a diameter of 1.50 μm and a lattice constant of 5.0 μm.

Proposed Structure

In this chapter, rectangular C-slotted microstrip PhC antenna frequency is designed for medical applications. Along with PhC structure, the C-slotted patch is used to enhance the antenna characteristics. Microstrip antennas have various benefits, including low weight, compact length, and ease of fabrication shown in Fig. 11.3. The substrate and patch layer of the proposed patch antenna is exemplified in Fig. 11.4.

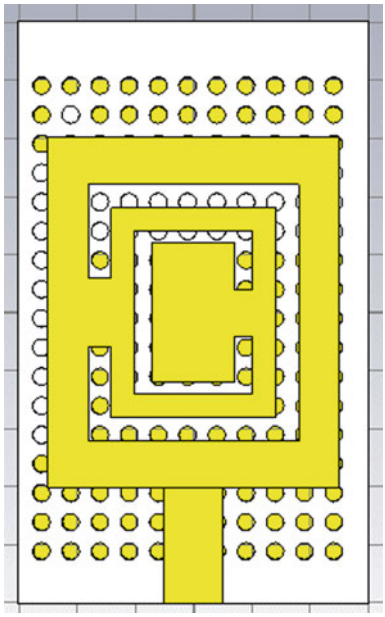

Fig. 11.3 Proposed C-slotted PhC antenna structure

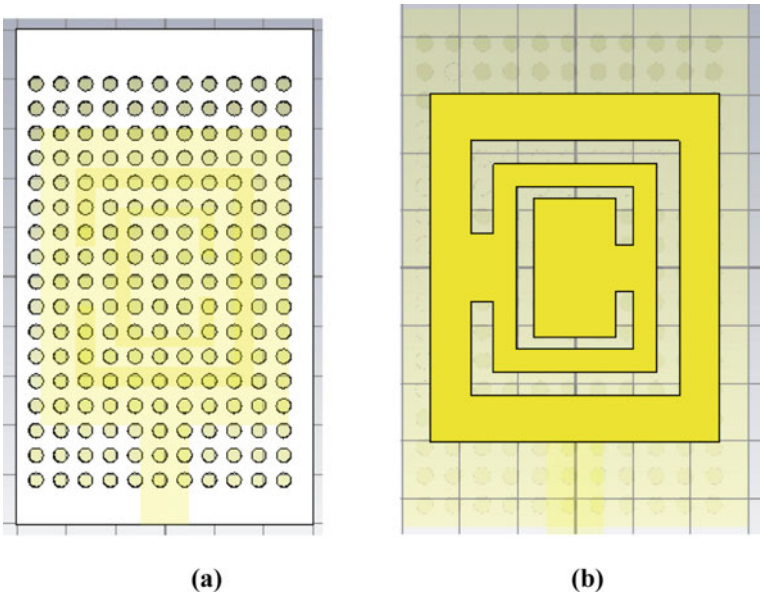

Fig. 11.4 Proposed PhC antenna **a** PhC Substrate and **b** Patch

Optimization of the Substrate Height "h"

In patch antenna, the output of return loss, gain, directivity, and VSWR will be depending on the substrate thickness "h". Another critical issue in the design of a patch antenna is determining the optimum substrate material thickness. To select an acceptable substrate thickness (h), a designer must first understand the consequences of modifying the substrate thickness. The simulation of antenna characteristics for an inset feed rectangular microstrip patch antenna by altering the substrate thickness (h) from 0.1 μm to 1 μm. which are listed in Table 11.2. It is observed that when the thickness is varied from 0.1 μm to 1 μm the antenna characteristics are decreases gradually. The proposed patch antenna is designed with an 'h' value of 0.1 μm and it yields a strong VSWR of 1.0117 dBi, 9.4 dB of gain, and an RL of −44.63 dB resonates at 1.86 THz. When the thickness is gradually increasing with the step value of 0.1 μm the simulated result of the various structure produces the return loss of –43.97 dB, –14.03 dB, –18. 6 dB, –33.93 dB, –22.33 dB, –33.5 dB, –32.47 dB, –24.48 dB, and –20.98 dB. It is observed that the antenna performances are degrading for large values of substrate height.

Return Loss

It's a parameter that shows how much power is "missing" to the weight and doesn't reflect as a reflection. As a result, the RL is a limitation that designates how to fit the wire and antenna that have been matched. The RL curve from an antenna is a graph of its s11 vs frequency. For better performance, such a graph would have a dip at the producing frequency and the smallest dB value at this frequency. When decreasing the height of the antenna the frequency level increase and also the output of the

Table 11.2 Impact of varying "h" values of substrate

"h" Value	Frequency (THz)	Return Loss (dB)	Directivity (dBi)	VSWR	Gain (dB)	Bandwidth (THz)
0.1	1.86	−44.63	6.20	1.011	9.4	0.067
0.2	1.85	−43.97	2.20	1.852	5.5	0.059
0.3	1.40	−14.03	1.07	1.495	5.2	0.023
0.4	1.51	−18.16	1.14	1.281	5.1	0.044
0.5	1.57	−33.93	1.17	1.041	4.1	0.013
0.6	1.40	−22.33	0.94	1.165	2.8	0.245
0.7	1.43	−33.50	0.95	1.403	2.5	0.167
0.8	1.46	−32.47	0.96	1.048	2	0.249
0.9	1.48	−24.48	0.97	1.126	1.5	0.378
1.0	1.50	−20.93	0.97	1.197	2.1	0.278

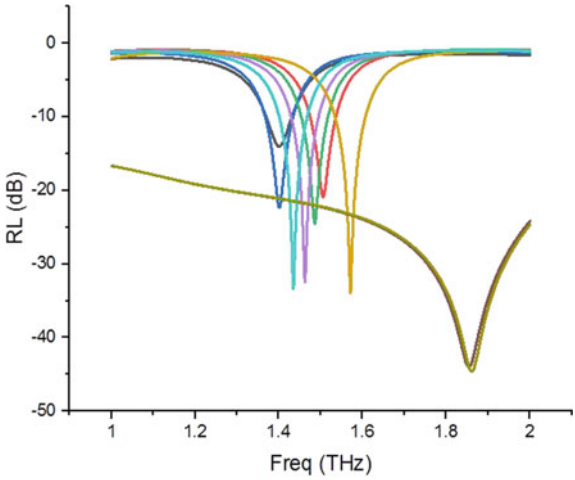

Fig. 11.5 Return loss curve for various proposed structures

return loss increase. Frequently, increasing the height of the antenna, the frequency and return loss gradually decrease. The below diagram has several frequencies. By varying the 'h' value with a frequency of 1.86 THz and return loss (RL) of 44.63 dB shown in Fig. 11.5, the system delivered a good result.

Vswr

The VSWR (voltage standing wave ratio) or reflection coefficient, which defines the energy transmitted from an antenna, restricts the VSWR. The VSWR is determined by the following formula if the reflection coefficient is given by s11 or return loss. By varying the 'h' value with a frequency of 1.86 THz and VSWR 1.0117 dBi shown in Fig. 11.6, the system delivered a good result.

Directivity

The attention of radiation in the region of the origin is defined by directivity.

$$\boldsymbol{Directivity} = \frac{U_{\max}}{U_o} \tag{11.12}$$

The directivity is described as the ratio of the material antenna's maximal radiation power to that of an isotropic or source antenna transmitting the corresponding entire power shown in Fig. 11.7.

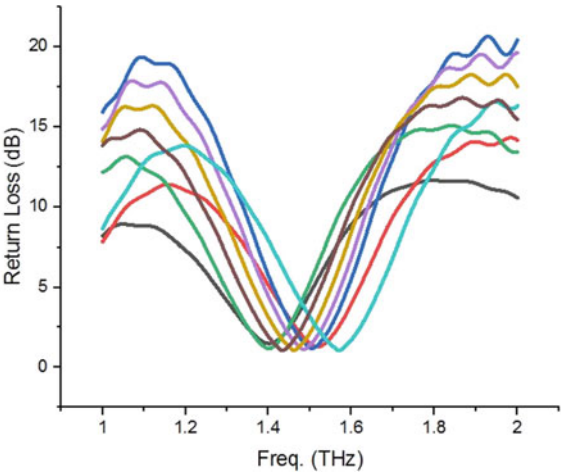

Fig. 11.6 VSWR

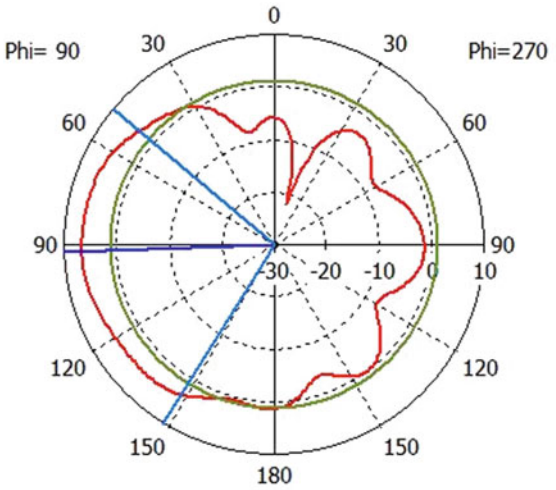

Fig. 11.7 Directivity curve

Gain

The gain of an antenna tells us the energy transferred by an antenna in a special route in connection to an isotropic antenna. This description defines the most signal strength that an antenna can broadcast or receive in a given region. Antenna gain is an added significant measure than directivity since it holds all losses.

$$\textbf{Antenna gain} = \textbf{Directivity} * \textbf{Efficiency} \tag{11.13}$$

The maximum gain value will be obtained by varying the "h" value on the degree 60. When compared to 30 and 90°, the output will be a maximum range of 60° as shown in Fig. 11.8. Better performance has been achieved using the "h" value of 0.1. Figure 11.9 illustrates the surface current distribution of the proposed C-slotted patch antenna.

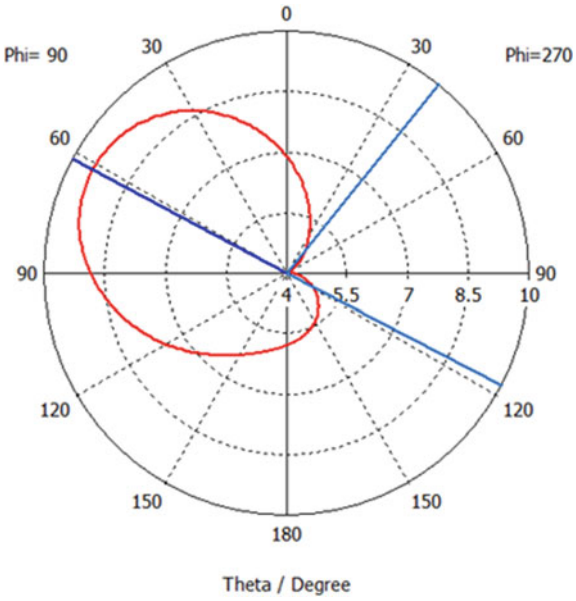

Fig. 11.8 Plot of gain value

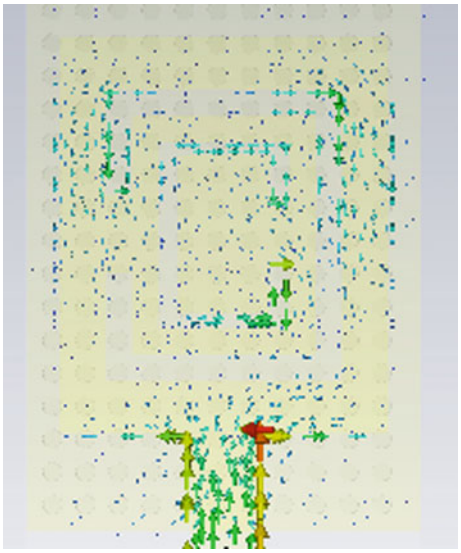

Fig. 11.9 Surface current distribution of the proposed antenna

Comparison of Proposed Work with Existing Results

Table 11.3 shows the results of different existing patch antennae premised on THz frequency. It is observed that the antenna performances of various PhC-based antennas are moderate. The existing antenna structures used different substrate materials like Polyamide, GaAs, Silicon, and Rogers, whereas the proposed antenna utilized FR-4 substrate.

When compared to the current investigation, the effectiveness of the proposed THz antenna performance is greater. It is due to the PhC structure, the PhC lattice endorses both TM and TE modus transmission which makes virtually confined and connecting lattices in the region of high dielectric. As a result of the circular Brillouin zone, the TE mode transmission increases which tends to enhance the antenna performances like return loss, gain, and directivity. Also, the proposed C-slotted PhC-based patch antenna is more effective and it is suitable for various THz filters, sensors, and high-speed wireless devices (Sivasangari et al. 2022; Sathish Kumar 2022; Poonguzhali et al. 2022b; Sridarshini et al. 2022; Geerthana et al. 2022; Karthikeyan et al. 2022; Karthikeyan and Sitharthan 2022; Dhanabalan et al. 2022).

Table 11.3 Comparison of proposed work with existing works

Works	Substrate material	Frequency (THz)	Return Loss (dB)	Directivity (dBi)	VSWR	Gain (dB)
Proposed antenna	FR4	1.86	−44.63	6.20	1.011	9.4
Zubair et al. (2022)	Polyamide	3.65	−29	6.06	–	5.01
Rana and Rahman Smieee (2022)	Rogers 5880	0.028	−38.34	–	1.024	8.2
Adel et al. (2023)	Polyamide	1.1	−35	–	-	-
Shihzad et al. (2022)	Polyamide	0.714	−23.57	–	1.14	–
Dhillon (2017)	Polyamide	0.67	–	5.08	–	5.22
Kumar et al. (2020)	GaAs		−25	–	1.17	–
Sathish Kumar et al. (2021)	Polyamide	1.5	−21.35	–	1.18	2.88
Vahdati and Parandin (2019)	Silicon	3.98	−36	–	<1.5	–
Kushwaha et al. (2018)	Rogers 5880	1.4	−28.5	–	–	–

Conclusion

This chapter demonstrates the C-slotted patch antenna in THz technology based on PhC substrate. The proposed PhC antenna structure is analyzed by varying the substrate thickness values. The optimal PhC antenna provides the efficient output of −44.63 dB return loss and directivity 6.2 dBi at the operating frequency of 1.86 THz. These antennas are perfectly suitable for all wireless communication, material spectroscopy, especially in the field of medical like imaging and scanning, sensing breast and skin cancers, hyperthermia treatments, dental care, and more commercial use of THz devices.

Acknowledgements Authors are sincerely thankful to the reviewers and editors for their critical comments and suggestions to improve the quality of the chapter.

Conflict of Interest The authors declare that there is no conflict of interest

References

Amarveer, Singh Dhillon (2017) Divesh Mittal, Ekambir Sidhu,THz rectangular microstrip patch antenna employing polyimide substrate for video rate imaging and homeland defence applications. Optik 144:634–641

Ashworth PC, Pickwell-MacPherson E, Provenzano E, Pinder SE, Purushotham AD, Pepper M, Wallace VP (2009) THz pulsed spectroscopy of freshly excised human breast cancer. Opt Express 17(15):12444–12454

Ashyap AY, Inam M, Kamarudin MR, Dahri MH, Shamsan ZA, Almuhanna K, Alorifi F (2023) Multi-band metamaterial antenna for terahertz applications. Comput Mater Continua 74(1)

Caroline BE, Danasegaran SK**,** Xavier SC, Lalithakumari S (2022) Investigation of electromagnetic wave propagation in a defected photonic crystal square lattice structure. J Electron Mater. https://doi.org/10.1007/s11664-022-10058-2

Chiu C, Chen H, Huang Y, Lee W, Hwang Y, Huang H, Sun C (2009) All-THz fiber-scanning near-field microscopy. Opt Lett 34(7):1084–1086

Danasegaran SK, Caroline BE, Poonguzhali S (2022) Smart gas sensor based on photonic crystal for sensing perilous gases: industrial and mining applications. Energy Sources, Part A: Recover, Util, Environ Eff 44(3):7564–7572. https://doi.org/10.1080/15567036.2022.2115583

Denizhan Sirmaci Y, Akin CK, Sabah C (2016) Fishnet based metamaterial loaded THz patch antenna. Opt Quantum Electron 48(2):1–10

Geerthana S, Syedakbar S, Sridarshini T, Balaji VR, Sitharthan R, Shanmuga Sundar D (2022) 2D-PhC based all optical AND, OR and EX-OR logic gates with high contrast ratio operating at C band. Laser Phys 32(10)

Hu BB, Nuss MC (1995) Imaging with THz waves. Opt Lett 20(16):1716

Hwu SU, DeSilva KB, Jih CT (2013) THz (THz) wireless systems for space applications. In: 2013 IEEE sensors applications symposium proceedings, pp 171–175. https://doi.org/10.1109/SAS.2013.6493580.J; Son (2009) THz electromagnetic interactions with biological matter and their applications. J Appl Phys 105(10):102033

Karthikeyan M, Jayabala P, Ramachandran S, Dhanabalan SS, Sivanesan T, Ponnusamy M (2022) Tunable optimal dual band metamaterial absorber for high Sensitivity THz refractive index sensing. Nanomaterials 12(15):2693. https://doi.org/10.3390/nano12152693

Karthikeyan M, Sitharthan R, Ali T, Pathan S, Anguera J, Shanmuga Sundar D (2022) Stacked T-shaped strips compact antenna for WLAN and WiMAX Applications. Wirel Pers Commun 123:1523–1536

Kumar DS, Caroline BE, Sagadevan K, Sakthiganesh G, Saravanan R (2020) Investigation of high directional gain pentagonal shaped patch antenna. In: 2020 7th international conference on smart structures and systems (ICSSS), pp 1–6. https://doi.org/10.1109/ICSSS49621.2020.9202223

Kumar DS, Prithika P, Caroline BE (2019) Investigating the performance of microstrip patch antenna with photonic crystal on different substrate. In: 2019 IEEE international conference on system, computation, automation and networking (ICSCAN), pp 1–5, https://doi.org/10.1109/ICSCAN.2019.8878861

Kumar DS, Caroline BE, Thilagavathi S (2020) Investigation of equilateral triangular microstrip patch antenna using photonic Crystal. In: 2020 international conference on system, computation, automation and networking (ICSCAN), pp 1–6. https://doi.org/10.1109/ICSCAN49426.2020.9262319

Kushwaha RK, Karuppanan P, Malviya L (2018) Design and analysis of novel microstrip patch antenna on photonic crystal in THz. Phys B Condens Matter 545:107–112

Mantsch HH, Naumann D (2010) THz spectroscopy: The renaissance of far infrared spectroscopy. J Mol Struct 964(1–3):1–4

Maynard C (2006) Evolving and experimental technologies in medical imaging. Yearb Diagn Radiol 2006:201–203

Mohamed Nizar S, Rafi Ahamed S, Priyanka E, Jayasri R, Kesavaraman B (2021) Comparison of different photonic crystal fiber structure: a review. J Phys Conf Ser 1717(1). IOP Publishing

Oh SJ, Kang J, Maeng I, Suh J-S, Huh Y-M, Haam S, Son J-H (2009) Nanoparticle-enabled THz imaging for cancer diagnosis. Opt Express 17:3469–3475

Poonguzhali S, Sivasangari A, Lalithakumari S, Sathish Kumar D (2022a) A novel reconfigurable antenna architecture for wireless applications. In: 2022a international conference on smart technologies and systems for next generation computing (ICSTSN), pp 1–4

Poonguzhali S, Sivasangari A, Ajitha P, Lalithakumari S, Sridevi A, Danasegaran SK (2022b) Design and performance analysis of smart photonic sensors for industrial applications. Curr Appl Phys 39:183–189

Rubaek T, Kim OS, Meincke P (2009) Computational validation of a 3-D microwave imaging system for breast-cancer screening. IEEE Trans Antennas Propag 57(7):2105–2115. https://doi.org/10.1109/TAP.2009.2021879

Sathish Kumar D, Caroline BE, Shanmuga Preethi N, Lokeshwar M (2021) Design and analysis of high pace terahertz antenna. In: International conference on system, computation, automation and networking (ICSCAN)

Shanmuga Sundar D, Hanabalan, SR, Madurakavi K, Thirumurugan A, Rajesh M, Avaninathan SR, Carrasco MF (2022) Flexible compact system for wearable health monitoring applications. Comput Electri Eng 102:108130. ISSN 0045–7906

Sharma A, Singh G (2009) Rectangular microstirp patch antenna design at THz frequency for short distance wireless communication systems. J Infrared Milli Terahz Waves 30:1

Shihzad W, Ullah S, Ahmad A, Abbasi NA, Choi D-Y (2022) Design and analysis of dual-band high-gain THz antenna array for THz space applications. Appl Sci 12(9231):1–20

Siegel P (2004) THz technology in biology and medicine. IEEE Trans Microw Theory Tech 52(10):2438–2447

Sivasangari A, Ajitha P, Poonguzhali S, Danasegaran SK, Rajkumar I (2022) High performance photonic nanostructured sensors for smart industries: design and analysis. Braz J Phys 52(5):1–6, 180. https://doi.org/10.1007/s13538-022-01184-7

Sohel Rana M, Mostafizur Rahman Smieee M (2022) Design and analysis of microstrip patch antenna for 5G wireless communication systems. Bull Electr Eng Inform 11(6):3329–3337

Son J-H (2014) THz biomedical science and technology. CRC Press, Boca Raton, FL

Sridarshini T, Chidambaram P, Geerthana S, Balaji VR, Thirumurugan A, Sitharthan KM, Shanmuga Sundar D (2022) Current and future horizon of optics and photonics in environmental sustainability. Sustain Comput: Inf Syst 36

Sun Y, Sy MY, Wang YX, Ahuja AT, Zhang YT, Pickwell-Macpherson E (2011) A promising diagnostic method: THz pulsed imaging and spectroscopy. World J Radiol 3(3):55–65. https://doi.org/10.4329/wjr.v3.i3.55

Vafapour Z, Keshavarz A, Ghahraloud H (2020) The potential of THz sensing for cancer diagnosis. Heliyon 6(12)

Vahdati, Parandin F (2019) Antenna patch design using a photonic crystal substrate at a frequency of 1.6 THz. Wirel Person Commun 109:2213–2219. https://doi.org/10.1007/s11277-019-06676-5

Zubair M, Jabbar A, Akinsolu MO, Ali Imran M, Liu B, Abbasi QH (2022) Design of truncated microstrip square patch antenna for terahertz communication. In: 2022 IEEE international symposium on antennas and propagation and USNC-URSI radio science meeting (AP-S/URSI). Denver, CO, USA. pp 1558–1559. https://doi.org/10.1109/AP-S/USNC-URSI47032.2022.9886809

Chapter 12
Role of Photonics in Energy Crisis

L. Jerart Julus, A. Andrew Roobert, and J. Joshan Athanesious

Abstract There are currently challenges in the fields of photonics and electronics regarding energy harvesting, light emission, renewable energies, and the development of environmentally friendly materials. Recent years have seen an increase in the demand for environmentally friendly technologies as a result of global concerns about environmental degradation. The development of eco-friendly, renewable materials has become increasingly important as current electronics and photonics technology rely heavily on hazardous chemicals. It is increasingly important to develop renewable and eco-friendly materials to replace the hazardous chemicals present in the current technology used to create electronics and photonics devices based on semiconductors. Using optics to help protect the environment is stressed by the importance of Green Photonics.

Keywords Energy · Nanostructure · Photonic crystal · Biosensor · Photovoltaics · Solar cell

Introduction

It has recently attracted increasing attention that solar energy can be employed to address global issues that relate to energy and the environment, and there are a variety of techniques that can be utilized to do so. Photovoltaics, photoelectrochemical cells, and photocatalysis, respectively, are methods of directly converting solar energy into electrical and chemical energy. In general, these processes are administered by four

L. J. Julus (✉)
School of Information Technology & Engineering (SITE), Vellore Institute of Technology, Vellore, India
e-mail: jerartjulus@gmail.com

A. A. Roobert
Department of ECE, Francis Xavier Engineering College, Tirunelveli, India

J. J. Athanesious
SCOPE, VIT, Chennai, India

© The Author(s), under exclusive license to Springer Nature Singapore Pte Ltd. 2023

S. S. Dhanabalan et al. (eds.), *Photonic Crystal and Its Applications for Next Generation Systems*, Springer Tracts in Electrical and Electronics Engineering,
https://doi.org/10.1007/978-981-99-2548-3_12

steps: absorption of light, charge separation, charge migration, and charge recombination. Solar conversion is currently very inefficient due to the fact that separate semiconductor resources cannot be optimized for all four processes, resulting in very low overall efficiency, which limits their use in practical applications. Solar energy conversion is low in efficiency due to two main factors: limited light absorption and high charge carrier recombination rates. As a result of the limitations of current semiconductors, a number of approaches have been proposed. Biomolecular research and biomedical applications benefit greatly from photonic and plasmonic platforms. In recent years, PC-based nanostructures have been widely used in diagnostic applications due to their single structural and optical properties that have proven to be effective tools for controlling infectious diseases (Hasan et al. 2018).

The purpose of this article is to review the advantages of photonic and plasmonic nanostructures in conserving solar energy conversion and biosensing. Photovoltaic, photothermal, and photocatalytic applications are discussed in relation to solar energy conversion. The application of photonic, plasmonic, or hybridized photonic–plasmonic nanostructures to semiconductors is discussed in order to increase solar energy conversion efficiency. Solar energy can be generated using photonic–plasmonic technology, and biosensors for the future can be developed using this technology.

A wide range of dye-sensitized solar cells, as well as silicon solar cells, are currently using self-assembled photonic crystals to manage photons. It is possible to enhance the power conversion efficiency of solar cells by integrating them into the electrodes or implementing them as the back reflector without compromising the efficiency of the solar cells if they are incorporated into the electrodes or implemented as the back reflector. Photonic crystal-based solar cells have been extensively discussed in terms of the underlying mechanisms influencing power conversion efficiency enhancement.

Electrification Through Photovoltaics

Antireflective Surfaces Made with Photonic Crystals

The conversion of solar energy into electricity is carried out by photovoltaic (PV) devices. A thin-film solar cell's conversion efficiency is greatly influenced by the degree of light absorption. Understanding nanostructure types and their optimal spatial arrangement is crucial to improving light trapping. Solar cells have a high reflection loss, which degrades the performance of a solar cell due to the high reflection loss at the glass–air interface (Thompson et al. 2018). An antireflective coating can help to reduce the reflection loss. As the AR bandwidth of conventional AR coatings is narrow and the incidence angle range is small, they restrict the performance of solar cells. It has been noted that several types of solar cells have widely implemented alternative approaches for suppressing reflection losses across a broad

range of wavelengths. During this procedure, the refractive index of the solar cell is gradually reduced away from the top surface of the cell.

Optical Crystal Surfaces with Omnidirectional Antireflection

It has been possible to reconstruct the exquisite structure thanks to a lot of excellent biological materials provided by nature. In order to fabricate AR materials, we usually divide them into two types: bottom-up and top-down. Top-down fabrication involves wet or dry etching, sol–gel processing, physical vapor deposition, and chemical vapor deposition. For fabricating AR materials, the sol–gel method is commonly used. In order to maximize these raw materials when in liquid form, a high chemically active ingredient was compounded as a precursor. Following the slow polymerization of the sol, a particle used to gel will be introduced. With sol–gel, a three-dimensional net structure is formed without any solvent flowing (Lin et al. 2020).

Solar Cell Systems Based on Plasmonic Nanostructures

In recent years, researchers have been exploring the concept of incorporating nanoparticles (NPs) into different sites of solar cells in order to enhance light-trapping efficiency. As Au and Ag NPs exhibit SPR peaks in the visible spectrum, this review emphasizes that understanding the plasmonic effects of metal nanostructures on OSCs based on important parameters such as surface plasmon resonance (SPR) or localized surface plasmon resonance (LSPR) is crucial (John and Wang 2008). The EM field of an incident light generates a combined oscillation of conduction electrons. As electrons are bounded within a 3D structure in Metallic Nanoparticles (MNPs), this phenomenon can only be observed. Therefore, the EM field generated around NPs would be many orders of magnitude greater than that generated by incident light (Yeganegi et al. 2014). Nanoscale size effects are observed in SPR NPs but not in bulk metal particles. A dipole is generated by dividing and mobilizing opposite charges to different parts of a surface as a result of the EM field incidence. Dipoles are resistant to the EM field of incisor light because they produce their own internal electric field. Light scattering is thus enhanced by the LSPR induced by MNPs distributed randomly or homogeneously around them.

Geometrical Effects of Particles and Their Surroundings

A plasmonic nanostructure's size and morphology can be modified to modify the scattering direction, with 30 and 60 nm being the most suitable sizes for forward scattering effects. The 50-nm-sized MNPs scatter photons both backwards and forwards.

A larger diameter of MNPs scatters more radiation backwards, whereas a smaller diameter results in weak scattering and serves as near-field enhancers when absorption is insufficient due to weak scattering. A large nanostructure is also harmful since it allows the particle to absorb light unhindered, reducing conversion efficiency. The active and buffer layers of Wang et al. (2004) were simulated using different sizes of Ag NPs. NPs with small sizes perform best when embedded within active layers, while NPs with large sizes perform best inactive layers. Thus, plasmonic behavior in solar cells can be predicted by reducing reflections and improving optical absorption. In the same way, the shape of MNPs has a distinct effect on their resonance. By selecting the right MNP shape, it is possible to adjust the resonance wavelength to meet any specific application requirement. Additionally, MNPs are affected by their surrounding medium. In addition to controlling the electric field geometry around MNPs, the surrounding dielectric medium also tunes the wavelength of the resonance.

Excitation of Excitons by Light Absorption

The PSC consists of an active layer and a layer for electron charge transport. Active layers, which are made up of a hybrid of p-type and n-type materials, serve two distinct purposes. As an optical harvester, it is able to separate charges. To enhance light transmission into the active layer, it is necessary to reduce the loss of optical light caused by reflections at the interface between the air and substrate. To achieve the highest level of transparency in the device structure, the first material to absorb incident light should be as transparent as possible. A thin layer at a particular wavelength can effectively be applied to organic materials since they possess a higher absorption coefficient than inorganic/crystalline or multi-crystalline silicon (Forati 2022). Polymer materials, on the other hand, typically have narrow absorption spectra with no optical absorption in the red and near-infrared wavelengths.

Photocurrent Generation in PSCs

Consequently, light absorption generates electrically neutral excitons inside the active layer. Researchers are currently modifying the bandgap and enlarging the absorption region in order to improve efficiency.

The electron–hole pairs contribute to the subduing of electrostatic binding energy by converting excitons into free charge carriers, which requires the subduing of electrostatic binding energy. As a result, the potential energy undergoes radical transformation due to a highly intense and discrete electric field generated at the interfaces (Qi and Liu 2017). There can be two types of free charge carrier losses, namely geminate recombination and non-geminate recombination, if the EM field generated is too weak to permit separation beyond electrostatic attraction. Recombination of

dissociated electrons and holes, and regeneration of excitonic states, is the basis for gemstone recombination.

Researchers currently believe that a number of physical mechanisms are responsible for the increased efficiency of cells. By lowering the potential barrier of the cathode and hindering the quenching of excited states in polymer films, the deposition of Au/Ag NPs on ITO can help improve hole injection. In Fig. 12.1b, small NPs with small diameters induce LSPR, enhancing active layer absorption, charge carrier transfer efficiency, and reducing recombination losses. It is possible to convert metal nanoparticles into charge recombination centers by embedding them into the organic photoactive layers reported from Aftab et al. (2023) with permission from Elsevier. This will result in a quenching of excitons and transferring non-radiative energy from the organic photoactive layers to the metal nanoparticles. There are many people who prefer designs described in Fig. 12.2a, b, c, since they are more likely to be effective in absorbing and releasing the gas at the interface reported by Alkhalayfeh et al. (2021) with permission from Elsevier. Furthermore, morphology (shape), size, and dispersion of the NPs have a great effect on absorption. It is due to the roughness of PEDOT:PSS embedded with decahedron-shaped Ag NPs that allows for better hole collection compared to PEDOT:PSS/Ag-icosahedron. When Ag NPs were sized larger, the efficiency of OPV was reported to increase from 0.663% to 0.925%. Au NPs have a lower scattering efficiency than their self-absorption intensity. Ag NPs, on the other hand, exhibit high scattering efficiency, although the LSPR region is designed to be within a wavelength range of 400–500 nm, so maintaining the broad wavelength range is a challenge. In terms of technology, LEDs are distinct semiconductor devices with a narrowband emission that may be made to emit in the ultraviolet (UV), visible, or infrared portions of the spectrum in Fig. 12.3. These LED dies are unable to produce the white light required for applications involving broad illumination. There are two typical methods for transforming the LED emission's narrow spectral band (Alkhalayfeh et al. 2021). Phosphor conversion and discrete color mixing are two examples (Fig. 12.4.). Moreover, there are a few hybrid LED luminaries that combine these two approaches to produce white light.

The LED die emits at a wavelength of about 460 nm after phosphor conversion. In order to create white light LED packages, some of this light is released directly, while some of it is down-converted by the phosphor to longer wavelengths with white band emissions that blend with the blue. Since 1997, these have been manufactured on a large scale. Yet, one of the issues is the challenge of keeping constant light quality because of the phosphor's and LED's (blue of UV) inherent fluctuations in wavelength (Giuliano et al. 2016). White light is sensitive to changes in temperature, optical properties, peak emission wavelength, and LED optical power, among other things. This could result in hue discrepancies between pieces, which could be quite problematic in lighting applications. The efficiency of phosphor conversion-based white LEDs is also fundamentally constrained by Stokes loss (caused by the phosphor's down-conversion of wavelength). LED packages that blend colors have the potential to produce devices with improved efficacy. Yet, because the production process is more complicated, it is also less cost-effective. To accommodate the

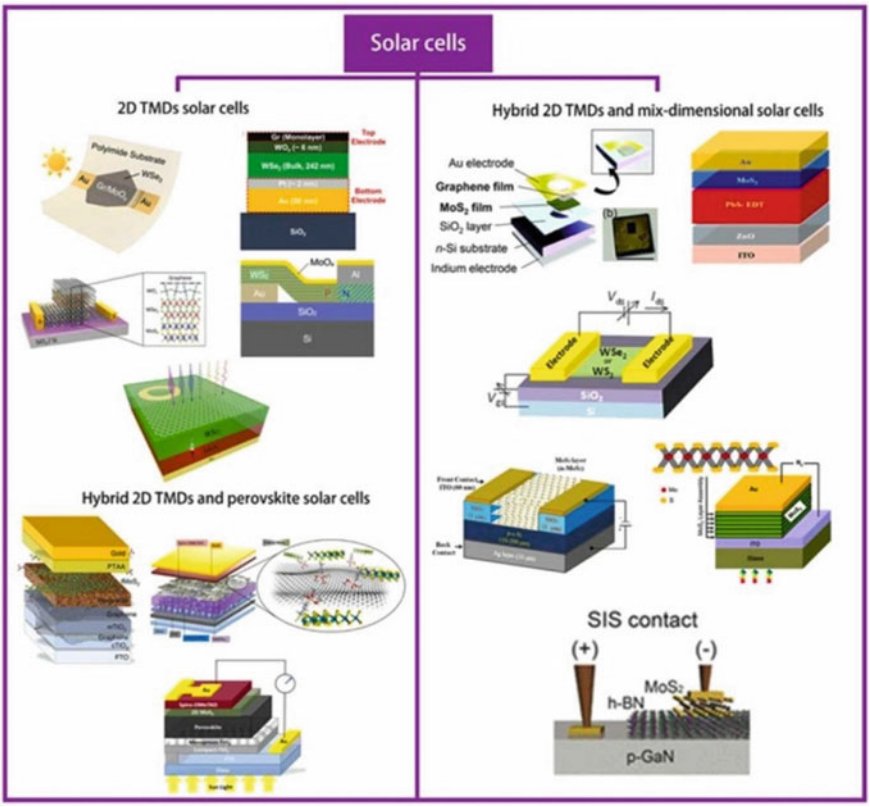

Fig. 12.1 Photocurrent generation in PSCs is shown as a two-dimensional energy diagram

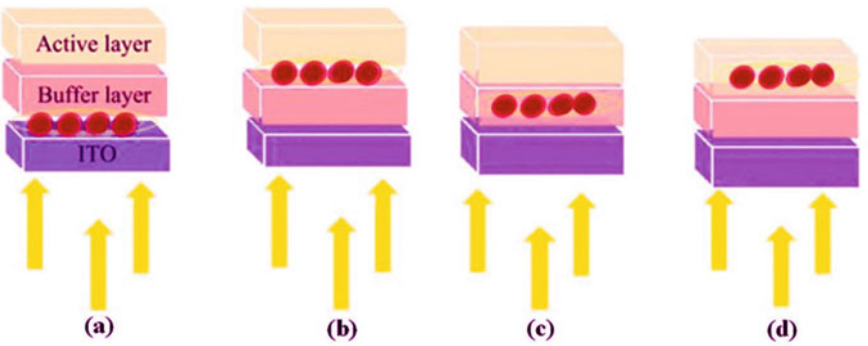

Fig. 12.2 OPVs designed using different plasmonic light trapping strategies

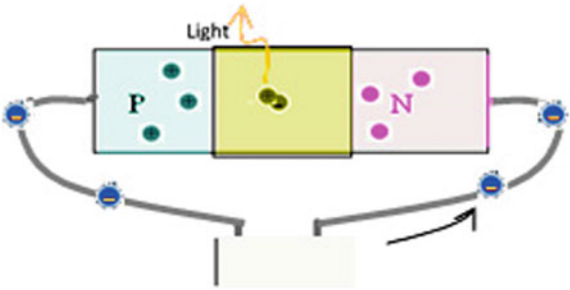

Fig. 12.3 Light emission in LED

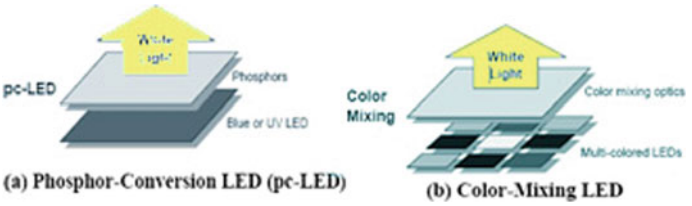

Fig. 12.4 LED packages for white light

various deterioration and thermal characteristics of the individual LED dies, the technique requires multi-die mounting, complex optics, and maybe color control feedback circuitry as well. Another issue is the lack of effective green emitters (Holguín-Lerma et al. 2019).

OLEDs are multi-layer thin-film electronics made of organic carbon molecules or polymers. They are made up of the following layers: a rigid or flexible substrate foil, sheet, or plate; an electrode layer; layers of active materials; a counter electrode layer; and a productive barrier layer. The electrodes must all be transparent to light at least one of them. In Fig. 12.5, OLED component materials have wider emission spectra. It could be feasible to adjust the emission peak by making small modifications to the chemical composition. This raises hope that white light produced by OLEDs may be of high quality. OLED technology for common lighting applications is in its infancy but still needs to advance. By 2015 or 2020, white light OLED sources are expected to be commercially viable.

Also, a lot of OLED research is being conducted in nations like China, Japan, Korea, Taiwan, etc. Researchers in Taiwan have developed OLEDs with a full range of color temperatures to mimic the sunlight spectrum which could be useful. This sunlight-style OLED is said to have a relatively simple design consisting of nanometer-thick layers of various color-emitting materials, electron transport layers, and electron injection layers. The limited life and aging of OLEDs, as with all LEDs, is a significant problem (Xiu et al. 2020).

There is still a lot of creative work being done in the research fields. LEDs with photonic crystals engraved on them have the ability to direct light emission at specific

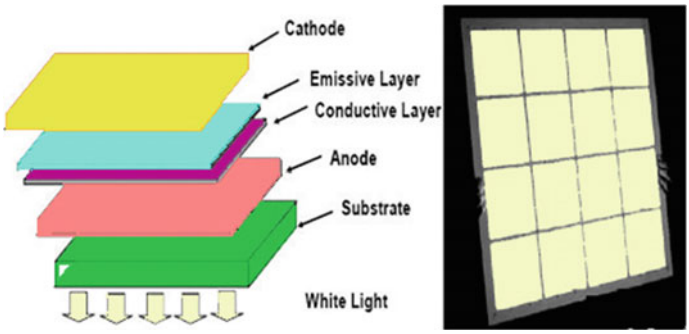

Fig. 12.5 Diagram of OLED device structure and photo of OLED panel

angles and increase brightness without using additional power. These gadgets could transform the lighting sector and encourage the use of greenlighting solutions thanks to the development of economical production procedures (Miyoshi et al. 2009). One of the first significant advances in LED structure was the addition of quantum wells, which could confine charge carriers so they could recombine more effectively. In order to prevent the internally created light from being constrained by the refractive index difference between the semiconductor material and the surrounding air, the brightness also depends on surface texturing in addition to the increase in the number of photons generated internally. Blue LEDs made of GaN have a RI of 2.3 at 450 nm. By total internal reflection at semiconductor–air interfaces, this high RI effectively traps light. Usually, fewer than 20% escapes, which results in low external quantum efficiency. Commercial devices typically use surface texturing by forming facets—surface angles on exterior faces—to improve the likelihood that a light beam would strike the facet at an angle where it can escape.

Nonetheless, many LED applications may need a specific angular distribution of light intensity and can profit from the light-emitting face's ordered patterning. To achieve this, a photonic crystal structure is created on top of the LED, increasing its surface brightness and modifying its spatial emission profile (Rao et al. 2019). Commercial LED technology has the potential to be more effective than traditional light sources. Although the efficacy of commercial LEDs now ranges from 63 to 101 l m/W, research may increase LED efficacy to around 230 l m/W. OLED laboratory efficiencies are starting to outperform those of traditional technologies. Currently, an OLED device's greatest laboratory efficacy is around 102 l m/W. The potential of this technology for producing effective white light requires further study. SSL (Solid-State Lighting) has the potential to revolutionize lighting efficiency, attractiveness, and quality while cutting down on greenhouse gas emissions by millions of metric tons.

The deployment of energy efficiency, the most affordable, cleanest, and fastest energy source, is mandated by President Obama's energy and environmental strategy. By 2012, it is anticipated that lighting in the USA will use almost 10 quads of primary energy (one quad is equal to the energy in 171–172 barrels of oil, or roughly 1015

BTUs). Between 2012 and 2027, a nationwide switch to SSL for general illumination might result in a 32.5 quad reduction. By the development of semiconductor technologies, the objective is to establish a new US-led market for high-efficiency general illumination products in order to conserve energy, cut costs, and improve the quality of the lit environment (Lin et al. 2019). Global SSL is no longer the future of illumination technology. It already embodies modern technology. Production is a multi-billion dollar industry. New goods are created every week, and milestones are continually reached.

A significant and critical practical barrier to adopting this energy-efficient technology is that building contractors and developers, who may not ultimately be responsible for paying the electricity bill, frequently decide whether to acquire lighting systems. As a result, cheaper lighting may frequently be chosen instead of more expensive but energy-saving lighting options that might result in longer term savings for the consumer. An initiative called SSL Quality Advocates has been established to improve the quality and develop rules for labeling product performance in a consistent manner in order to avoid a repetition of the errors made in the CFL market introduction. Lumen output, luminaire efficacy, power input, associated color temperature, and color rendering index are the five categories in which the label will provide critical performance data. A voluntary pledge initiative has been proposed by the DOE (Department of Energy, USA) to create a growing network of SSL Quality Advocates throughout the lighting supply chain.

Participating Producers Will Consent to Utilize the Label and Adhere to the Rules

Retailers, utilities, contractors, designers, and other buyers who are taking part will commit to search for and to acquire products bearing this label (Ji et al. 2020). There has been significant development in the commercialization of OLED lighting technology over the past few months. OLED lighting technology, which is anticipated to become commercially accessible this year, is being actively developed by all of the main lighting firms, including Philips Lighting, Osram, GE, Panasonic, and Thorn Lighting (2010). The significance of OLED lighting technology was emphasized in two plenary lectures given by Panasonic's Takuya Komoda and Mike Simpson of Philips Lighting UK (Pedruzzi et al. 2022). Work on SSL is ongoing on several levels in India as well. BPL Techno Vision announced the "Study Lite" rechargeable study lamp in January 2009. This lamp was created in association with Sankara Nethralaya, an eye hospital situated in Chennai, to provide students what it dubbed the "perfect lighting". Study Lite uses a 24 set of light-emitting-diode (LED) bulbs as its light source to produce flicker-free, white light that does not emit any ultraviolet or infrared rays. Furthermore, LEDs are extremely efficient because they typically only require 10% of the electricity used by regular light bulbs. Moreover, the lifespan of an LED is up to 50 times greater than that of an incandescent or compact fluorescent lamp

(CFL). Dual-power sources are used by Study Lite. It can be powered by a solar panel that BPL offers as an additional accessory or by a mains power supply. The lamp first became available in Chennai and Bangalore for Rs. 1,690. It is currently accessible throughout India (Bett et al. 2014).

Another cutting-edge LED-based Indian business, Lucifer Lights, has set numerous industry standards. The most recent of these is India's Central Power Research Report on efficiency (CPRI). The creation of proprietary technology that makes use of the benefits of LEDs in practical lighting has made it possible for Lucifer to provide very energy-efficient products. One important marketing strategy that has helped their products be used widely is the ongoing price decrease of their products (Gjessing et al. 2010). The government is very interested in solid-state lighting. Several institutions have been conducting research into LEDs and OLEDs. All significant lighting manufacturers have expressed interest in converting to SSL. They will be in competition with businesses in the display technology sector that are already experienced with the production of LEDs and OLEDs.

Energy-Efficient Photonic Systems Using Green Photonic

Silicon Photonics

The OIDA's new Green Photonics energy-efficienct strategy includes silicon photonics. The future of Silicon Photonics, according to Dr. Lebby, OIDA President, will be in energy-efficient Photonic integrated circuits rather than the extremely high data rates being exhibited by the research community. He stressed the value of goods for datacom and consumer applications where lower power consumption is a crucial feature (Raj and Thomas 2023). The issue of the exponentially growing energy requirement as bandwidth requirements may be solved through silicon photonics (Darshan et al. 2023a). The urgent need to address the electrical power consumption of routers and find more energy-efficient, compact, and cooler methods for directing the flow of optical databits was one issue raised by most of the speakers at the first technology transfer, which Nature Photonics organized in Tokyo in October 2007 to discuss questions about the future of optical communication (Darshan et al. 2023b). It was mentioned that 9% of Japan's electricity use in 2015 would be accounted for by routers. We need to reduce the amount of energy we need for transmission from about 100 pJ per bit to just 10 pJ per bit. Investigating photonic technology, which facilitates this, needs to happen quickly. Power usage has significantly increased as a result of the rapidly expanding internet traffic. For ever-shorter distances, optical interconnects have been proposed to replace electrical interconnects in order to speed up communication. The energy efficiency of photonic components is crucial because 15% of the electricity used in a country like the USA is used for computing-related purposes (Jiang et al. 2022). Because of its compatibility with many materials and manufacturing processes, silicon is becoming the preferred material for photonic

components. Electronics on a microscale. Modulators, amplifiers, and photodetectors are examples of active devices that can be incorporated on a chip. Copper interconnects might alternatively be replaced by silicon optical interconnects. Yet, it's likely that the key deciding variables will be energy consumption and heat dissipation. Third-order optical nonlinearities, such as Kerr and Raman effects, are the foundation for silicon photonic devices like amplifiers and wavelength converters. They call for high optical intensities, which result in significant energy loss through two-photon and free carrier absorption. By Bahram Jalali et al. (2022), the two-photon photovoltaic action in silicon has been thoroughly explained. He contends that electrical power can be generated while optical losses are being reduced by recovering the optical energy lost to two-photon absorption in silicon devices.

Fiber Lasers

Future technologies for photonic systems will be differentiated by their levels of energy efficiency and environmental impact. For instance, fiber lasers, which are highly effective at turning electrical energy into photons and are not based on chemical reactions, are anticipated to displace traditional lasers in many applications (Qi et al. 2022). They assert that their operation is fifteen times more effective than that of a typical laser. Moreover, they use less electricity and require less cooling.

Sensing

While photovoltaics, SSL, and energy savings in communication are the well-known elements of green photonics, there are numerous more, less well known but no less fascinating, applications in sensing, optics instruction, and light pollution. For more than 40 years, people have anticipated that optical sensors, particularly those based on fiber optics, will become quite significant. But after a thorough investigation, few have lived up to the high expectations. Yet, a fresh window of opportunity is opening in the field of green photonics. Environmental sensing makes use of a wide range of optical technologies. Sophisticated monitoring programs are being developed in response to the need to collect trustworthy scientific data for environmental sensing. The objective is to identify ecological changes brought on by climate change. There is a need for monitoring programs that provide data that adheres to certain scientific standards and quality control procedures. Government funding for sensor research has significantly risen on a global scale. The 2009 Economic Recovery Act in the USA allocates a sizable amount of funds towards environmental monitor and sensor research (Julus et al. 2020).

According to a report released in June 2009 by BCC research (Priya et al. 2023), the global market for environmental sensing and monitoring technology is anticipated to grow to $13 billion in 2014 from $9.1 billion in 2008 and an estimated $10.1

billion in 2009. The use of photonic-based sensors for water processing and wastewater treatment, as well as photonic devices for biosensing, are among the fastest-growing new fields according to the rate of development in revenues. Multi-angle light scattering and other photonic methods are preferable in this situation. These techniques can identify and categorize radiation, chemical, biotoxin, and radioactive substances as well as bacteria and spores. When used in water treatment, photonics provides real-time warnings, whereas conventional laboratory tests might take up to 72 h that optical sensors, particularly those based on fiber optics, will become quite significant. But after a thorough investigation, few have lived up to the high expectations. Yet, a fresh window of opportunity is opening in the field of green photonics. Environmental sensing makes use of a wide range of optical technologies. Sophisticated monitoring programs are being developed in response to the need to collect trustworthy scientific data for environmental sensing. The objective is to identify ecological changes brought on by climate change. There is a need for monitoring programs that provide data that adheres to certain scientific standards and quality control procedures. Government funding for sensor research has significantly risen on a global scale. The 2009 Economic Recovery Act in the USA allocates a sizable amount of funds towards environmental monitor and sensor research.

Silicon Photonic Integrated Circuits

New photonic technologies, such as silicon photonic integrated circuits, are used in remote sensing. Substantial funds have been invested in the development of optical techniques for the distant or stand-off detection of environmental contaminants, trace compounds, etc. These methods use sophisticated Raman scattering-based laser remote sensing or laser-induced fluorescence from a target sample. The development of new types of sensors with extremely extended operational lifetimes is made possible by the use of specific classes of nanoparticles that exhibit very strong photostability in fluorescence emission. The ability to sense air pollution and network numerous devices to measure is enabled by photonic-based technology. Siemens has created a method for monitoring carbon monoxide levels that uses a laser and is significantly more accurate than traditional sensors (Moscoso-Mártir et al. 2022). Kenneth Suslick describes the intriguing concept of an "Artificial nose" that can identify toxins (Lee et al. 2022a). This is based on colorimetry's most basic photonic principle. The sensor array, which resembles a dotty postage stamp, may be helpful in identifying chemical exposure that poses major health hazards. A digital, multidimensional extension of litmus paper is how the gadget is defined. It is made up of a 6×6 array of several nanoporous pigments, the color of which changes depending on the surrounding chemical environment. The poisonous gas and its concentration are identified by the pattern of color change.

Photonic Fence

Space-borne lidar sensors have advanced over the past 40 years beyond their initial application in astronomy. They are now being used to detect snow on Mars, measure wind speeds, and monitor glacier melting (Lee et al. 2022b). Researchers will be able to track how a changing surface, such as a multi-glacier, varies its heights over time with the use of a functioning lidar system aboard a spacecraft. The laser is also being considered as a potential tool for creating a "Photonic Fence" that may kill mosquitoes by telling them apart from other beneficial insects. The high-speed CMOS camera sensor on the prototype fence employs a retro-reflective backdrop to image mosquitoes 100 feet away. The imaging system can distinguish between the particular height, speed, and trajectories of a mosquito as well as its distinctive wing-beat speed (Wang et al. 2022).

Many sensor technologies connected to photonics:

(1) Laser-induced incandescence for UV and IR vehicle emission monitoring.
(2) A multiparameter fiber optic sensing system that tracks the combustion of fossil fuels employing a sapphire fiber grating as the sensing element.
(3) Raman spectroscopy detectors, which can identify specific chemical groups, can be used in agriculture to monitor pollution.
(4) The usage of optical fiber-mounted porous silicon photonic crystal for remote sensing of environmental toxins has been adopted for the disposal of industrial and mine waste.
(5) Imaging laser fluoro sensors and IR/UV microwave radiometers can be utilized to detect ocean spills and dumping.
(6) Measurement of tiny levels of a specific atom or molecule, such as oxygen, carbon dioxide, or water vapor, using optical spectroscopic techniques is relevant for tracking climate change. Relevant gases include oxygen, carbon dioxide, and water vapor.

Education in Optics

Optics is the fundamental science for comprehending and solving issues like the Greenhouse Effect, improving light collection and subsequently solar energy generation efficiency, saving energy through solid-state lighting, and less power-hungry opto-electronic systems. The architecture of the "Green Building" would be heavily influenced by optical engineering (Murphy et al. 2022). Focus should be placed on optics education as a result of the Green Photonics industry's rapid rise in prominence. Some of the energy that the sun uses to warm the earth's surface is radiated again as infrared light. This light is absorbed by some gases in the atmosphere, preventing the energy from escaping into space. The precise balance between the energy that the earth radiates and the energy that is reflected back keeps our planet's

environment comfortable and habitable. Esposito and Radetsky (2023) reports on an intriguing experiment conducted at the classroom level. Young pupils are taught about the greenhouse effect using inexpensive tools like plastic bags, balloons, a few clear glasses or glass panes, and an infrared camera. The plastic bags and balloons will transmit visible and infrared light, but the water container will absorb infrared light and appear black on the infrared camera screen. The glass panels will reflect infrared light but transmit visible light.

Light Pollution

The concept of light pollution is very new, despite the fact that topics like air pollution, water pollution, noise pollution, etc., have received much study. Light produced by humans that is unneeded or obtrusive is known as light pollution. Light pollution primarily comes in three flavors.

(1) **Sky Glow**: Light that is transmitted into the sky and is reflected by clouds or other atmospheric constituents. In this sense, increased dispersion brought on by air pollution also contributes to light pollution.
(2) **Light Trespass**: When a source of light from your property encroaches on another person's property.
(3) **Glare**: Lights that is too bright to comfortably view or that impairs night vision. Several branches of research, including biology, engineering, and astronomy, are impacted by light pollution.

According to estimates, photons directed upwards into the environment or excessive illumination squander 30% of outdoor lighting. This amounts to a waste of $10.4 billion annually in the USA alone and results in the production of 38 million metric tons of carbon dioxide that are unneeded. By using energy-efficient low-light pollution outdoor lighting fixtures, Green Photonics can offer solutions to this issue (Green et al. 2022).

An outdoor light that is both energy-efficient and low-light pollution should emit light at an angle between the astronomical horizon and the nadir, which is the line perpendicular to the ground. Light pollution is the term used to describe any light that is produced or reflected above this astronomical horizon (Menéndez-Velázquez et al. 2022). Bagheri et al. (2022) provides an informative description of the issues raised by light pollution and some straightforward fixes What's the problem with light pollution?

- Unshielded light entering the eyes impairs vision, which is hazardous. A good light source illuminates the scene but obscures it from view. Misdirected light that shines into people's eyes, onto other people's property, or into the night sky wastes electricity. That results in increased electricity costs and needless air pollution.
- It is annoying when unintentional light shines onto someone else's property. The visual equivalent of dueling boom boxes can be created by too much light, which

also lends the neighborhood an industrial appearance. It is difficult to look into surrounding darker areas with overly bright lighting.
- Foreground objects become silhouettes against a bright background.
- Slowly moving from strong light to lower light levels causes eyes to readjust, briefly reducing vision. An excessively lit shop looks like a prison yard and is just as intrusive as a big sign.
- Light that shines upward into the night sky blocks out half of our perspective of the natural world. Artificially brightened night skies make astronomical observatories less useful and prevent us from all experiencing the awe-inspiring and relaxing wonder of the stars and the calming and inspiring wonder of the heavens to all of us.

Simple Light Pollution Solutions

Employ only lighting fixtures that focus light downward, not above or into your eyes, to reduce light pollution. Fittings that produce hazardous glare should either be covered or uninstalled.

By first demanding that these superior lighting standards only apply to new fixtures, existing fixtures that need maintenance, and dangerous lighting, significant capital expenditures can be avoided.

- Establish limits on how bright lights can be, re-direct moveable fixtures to avoid glare, and require lighting solutions that enable unnecessary lights to be switched off.
- For security, use motion-activated lighting.
- Employ illumination that is actuated by motion sensors for security purposes.

Artificial Photosynthesis

An "Artificial Leaf" is produced using the novel idea of artificial photosynthesis, which substitutes synthetic material for the chlorophyll molecule. The green dream of producing electricity using synthetic photosynthesis is starting to take shape. The only source of energy for grass and all other green plants is sunlight to produce sugar from carbon dioxide, water, and chlorophyll (giving off oxygen as a byproduct). It has always been intriguing to consider the idea of reproducing it as a source of electricity.

Global Energy Crisis

Following the global energy crisis and widespread urbanization, considerable efforts have been directed towards building integrated photovoltaics (BIPVs). We have focused our attention on next-generation (zero-energy) buildings, which consume the same amount of electricity as they produce. Solar cells (SCs) based on conventional photovoltaics display dull or black colors, which makes BIPV based on them unattractive. As a result of their enormous market prospects, color-controlled SCs are attracting increasing interest since they can display a wide range of colors and vivid patterns in addition to generating electricity. The optical responses of SCs can be controlled using a variety of photonic approaches, such as (1) introducing a Fabry–Perot filter to control color and purity by tailoring the resonance of the F–P filter upon the SCs, and (2) adding a color-adjusting layer (CAL) above (or behind) the transparent conducting oxide (TCO) or replacing the TCO with CAL entirely. The complex multi-domain behaviors of highly nanostructured SCs pose a challenge to comprehensive device-level simulations. The a-Si:H SC proposed in Fig. 12.6 is a schematic diagram.

A-Si:H SC is composed of ARC layers, DBR stack, buffer layer, and ARC stack. Thin n-type (p-type) doping zones of 30 nm (50 nm) are present in the a-Si:H active layer here, and the thickness of the layer is 500 nm. The rear (front) electrode for electron (hole) transport is made from ZnO (ITO) and has a thickness of 100 nm (20 nm). Using 55 nm TiO_2 as a buffer layer reduces the reflection of light (McWilliams et al. 2022) and enhances color purity. There are six ZnS/ZnO pairs in the DBR, and each pair has a quarter-wavelength thickness. Spectral width and reflectivity play a very important role in determining color quality. Thin-film optics requires careful designing of DBR thicknesses to display RGB colors localized differently in the visible spectrum.

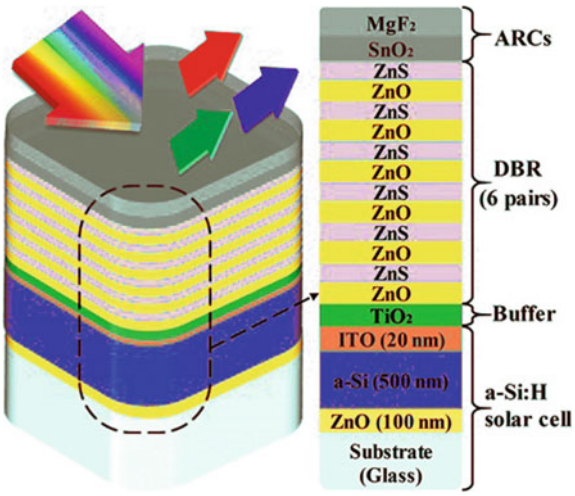

Fig. 12.6 SC proposed with different layers

References

Aftab S, Iqbal MZ, Hussain S, Hegazy HH, Saeed MA (2023) Transition metal dichalcogenides solar cells and integration with perovskites: a review. Nano Energy 108249

Alkhalayfeh MA, Aziz AA, Pakhuruddin MZ (2021) An overview of enhanced polymer solar cells with embedded plasmonic nanoparticles. Renew Sustain Energy Rev 141:110726

Bagheri S, Karimzadeh S, Feizizadeh B (2022) Investigation and modeling of physical development of urban areas and its effects on light pollution using night light data. Int J Eng Geosci 8(1):98–110

Bett A, Eisenlohr J, Höhn O, Bläsi B, Benick J, Repo P, Hermle M(2014) Front side antireflection concepts for silicon solar cells with diffractive rear side structures. In: 29th European photovoltaic solar energy conference and exhibition, vol 987

Darshan GP, Lavanya DR, Prasad BD, Sharma SC, Nagabhushana H (2023a) Quantum dots-based solar cells: futuristic green technology to accomplish the energy crisis. In: Quantum dots. Woodhead Publishing, pp 157–188

Darshan GP, Lavanya DR, Prasad BD, Sharma SC, Nagabhushana H (2023b) Quantum dots-based solar cells: futuristic green technology to accomplish the energy crisis. In: Quantum dots. Woodhead Publishing, pp 157–188

Esposito T, Radetsky LC (2023) Specifying non-white light sources in outdoor applications to reduce light pollution. LEUKOS 1–25

Forati E (2022) Density of Bloch states inside a one-dimensional photonic crystal. Phys Scr 97(4):045814

Giuliano G, Viola S, Watson S, Laycock L, Rowe D, Kelly AE (2016) Laser based underwater communication systems. In: 2016 18th international conference on transparent optical networks (ICTON). IEEE, pp 1–4

Gjessing J, Marstein ES, Sudbø A (2010) 2D back-side diffraction grating for improved light trapping in thin silicon solar cells. Opt Express 18(6):5481–5495

Green RF, Luginbuhl CB, Wainscoat RJ, Duriscoe D (2022) The growing threat of light pollution to ground-based observatories. Astron Astrophys Rev 30(1):1

Hasan SB, Mosk AP, Vos WL, Lagendijk A (2018) Finite-size scaling of the density of states in photonic band gap crystals. Phys Rev Lett 120(23):237402

Holguín-Lerma JA, Ng TK, Ooi BS (2019) Narrow-line InGaN/GaN green laser diode with high-order distributed-feedback surface grating. Appl Phys Express 12(4):042007

Ji S, Lin X, Chen M, Rong X, Xu H, Li W, Cai Z (2020) Green wavelength-tunable and high power Ho 3+-doped upconversion fiber lasers. IEEE Photonics Technol Lett 32(6):313–316

Jiang M, Wu H, An Y, Hou T, Chang Q, Huang L et al (2022) Fiber laser development enabled by machine learning: review and prospect. PhotoniX 3(1):16

John S, Wang R (2008) Metallic photonic-band-gap filament architectures for optimized incandescent lighting. Phys Rev A 78(4):043809

Julus LJ, Manimegalai D, Chakkaravarthy SS (2020) FBMC-based dispersion compensation using artificial neural network equalization for long reach-passive optical network. Int J Wavelets Multiresolut Inf Process 18(01):1941011

Lee W, Han S, Moon SR, Park J, Yoo S, Park H et al (2022a) Coherent terahertz wireless communication using dual-parallel MZM-based silicon photonic integrated circuits. Opt Express 30(2):2547–2563

Lee C, Kim S, Cho YH (2022b) Silk and paper: progress and prospects in green photonics and electronics. Adv Sustain Syst 6(2):2000216

Lin TY, Lin JH, Lin JD, Hsu CC, Lee CR (2019) All-optical and polarization-independent tunable guided-mode resonance filter based on a dye-doped liquid crystal incorporated with photonic crystal nanostructure. J Lightwave Technol 38(4):820–826

Lin SY, Hsieh ML, John S, Frey B, Bur JA, Luk TS, Narayanan S (2020) An in-situ and direct confirmation of super-planckian thermal radiation emitted from a metallic photonic-crystal at optical wavelengths. Sci Rep 10(1):5209

McWilliams B, Sgaravatti G, Tagliapietra S, Zachmann G (2022) A grand bargain to steer through the European union's energy crisis. 22(14). Bruegel

Menéndez-Velázquez A, Morales D, García-Delgado AB (2022) Light pollution and circadian misalignment: a healthy, blue-free, white light-emitting diode to avoid chronodisruption. Int J Environ Res Public Health 19(3):1849

Miyoshi T, Masui S, Okada T, Yanamoto T, Kozaki T, Nagahama SI, Mukai T (2009) 510–515 nm InGaN-based green laser diodes on c-plane GaN substrate. Appl Phys Express 2(6):062201

Moscoso-Mártir A, Koch J, Schulz O, Müller J, Mashayekh AT, Das AD et al (2022) Silicon photonic integrated circuits for soliton based long haul optical communication. J Light Technol 40(10):3210–3222

Murphy SM, Vyas DK, Sher AA, Grenis K (2022) Light pollution affects invasive and native plant traits important to plant competition and herbivorous insects. Biol Invasions 1–4

Pedruzzi E, Silva LC, Leal-Junior AG, Castellani CE (2022) Generation of a multi-wavelength Brillouin erbium fiber laser with low threshold in multiple frequency spacing configurations. Opt Fiber Technol 69:102832

Piels M, Bowers JE (2023) Photodetectors for silicon photonic integrated circuits. Photodetectors 419–436

Priya GL, Saran P, Padhy SK, Agarwal P, Andrew Roobert A, Julus LJ (2023) Novel low power cross-coupled FET-based sense amplifier design for high-speed SRAM circuits. Micromachines 14(3):581

Qi Y, Yang S, Wang J, Li L, Bai Z, Wang Y, Lv Z (2022) Recent advance of emerging low-dimensional materials for vector soliton generation in fiber lasers. Mater Today Phys 100622

Qi L, Liu C (2017) Complex band structures of 1D anisotropic graphene photonic crystal. Photonics Res 5(6):543–551

Raj A, Thomas RK (2023) Green energy applications of carbon nanotubes. In: Carbon nanotubes for energy and environmental applications. Apple Academic Press, pp 161–190

Rao A, Abdelsalam K, Sjaardema T, Honardoost A, Camacho-Gonzalez GF, Fathpour S (2019) Actively-monitored periodic-poling in thin-film lithium niobate photonic waveguides with ultra-high nonlinear conversion efficiency of 4600% W−1 cm−2. Opt Express 27(18):25920–25930

Thompson D, Zhu L, Mittapally R, Sadat S, Xing Z, McArdle P, Meyhofer E (2018) Hundred-fold enhancement in far-field radiative heat transfer over the blackbody limit. Nature 561(7722):216–221

Wang J, Chen W, Yang D, Fang Z, Liu W, Xiang T, Qiu X (2022) Photonic lignin with tunable and stimuli-responsive structural color. ACS Nano

Wubs M, Suttorp LG, Lagendijk A (2004) Spontaneous-emission rates in finite photonic crystals of plane scatterers. Phys Rev E 69(1):016616

Xiu H, Xu P, Wen P, Zhang Y, Yang J (2020) Rapid degradation of InGaN/GaN green laser diodes. Superlattices Microstruct 142:106517

Yeganegi E, Lagendijk A, Mosk AP, Vos WL (2014) Local density of optical states in the band gap of a finite one-dimensional photonic crystal. Phys Rev B 89(4):045123